國立交通大學
土木工程學系碩士班
碩士論文

擋土牆背側存在堅硬岩層對主動土壓力之影響

Active Earth Pressure on Retaining Walls near Rock Faces

研 究 生：黃聖峯

指導教授：方永壽 博士

中華民國 九十八年 九月

擋土牆背側存在堅硬岩層對主動土壓力之影響

Active Earth Pressure on Retaining Walls near Rock Faces

研 究 生：黃聖峯　　Student：Sheng-Feng Huang

指導教授：方永壽 博士　Advisor：Dr. Yung-Show Fang

國立交通大學土木工程學系碩士班

碩士論文

A Thesis

Submitted to the Department of Civil Engineering

College of Engineering

National Chiao Tung University

in Partial Fulfillment of the Requirements

for the Degree of

Master of Engineering

in Civil Engineering

September, 2009

Hsinchu, Taiwan, Republic of China

中華民國九十八年九月

擋土牆背側存堅硬岩層對主動土壓力之影響

研究生 ： 黃聖峯　　指導教授 ： 方永壽 博士

國立交通大學土木工程學系碩士班

摘要

本論文探討擋土牆背側存堅硬岩層對主動土壓力之影響。本研究以渥太華砂作為回填土，回填土高 0.5 公尺。量測於鬆砂 ($D_r = 35\%$) 狀態下作用於剛性擋土牆的側向土壓力。本研究利用國立交通大學模型擋土牆設備來探討堅硬介面以不同界面傾角β及距擋土牆不同距離 b，侵入回填土對擋土牆主動土壓力影響。為了模擬堅硬的岩層介面，本研究使用一片鋼製傾斜介面板，及其支撐系統。本研究共執行三種距牆距離 b = 0、50 mm、100 mm，五種堅硬界面傾角 β = 0^o、50^o、60^o、70^o、80^o、90^o 等多組實驗。依模型擋土牆試驗結果，獲得以下結論：

1、 當模擬無岩石介面傾角存在時 ($\beta = 0$)，主動土壓力係數 $K_{a,h}$ 與 Coulomb 解相符合，而主動合力作用點位置大約作用於擋土牆底部 0.333H 處，與理論值吻合。

2、 當模擬岩石介面傾角 β 越大，受界面板的影響越大，所造成主動土壓力合力 $K_{a,h}$ 越小；在相同角度，岩石介面距擋土牆距離越近 (b 越小)，則所受岩石介面的影響越大，主動土壓力合力 $K_{a,h}$ 也越小。

3、 主動土壓力合力 $K_{a,h}$ 隨介面傾角越大、或距離牆距離越小而逐漸變小，其合力作用點位置則會漸漸高於理論值 0.333H。

4、 當傾角等於 90 度時 (擋土牆與介面板相互平行)，主動土壓力係數隨著深

度增加而減少，而 Coulomb、Rankine 理論值的預估則過於保守。

5、 當傾斜岩石介面入侵到主動土楔時，造成擋土牆抗滑動之安全係數增加，因此根據 Coulomb 理論所求解的安全係數會偏向安全。

6、 當傾斜岩石介面入侵到主動土楔時，也會造成擋土牆抗傾覆之安全係數增加，因此根據 Coulomb 理論所求解的安全係數也會偏向安全。

關鍵字：砂土、模型試驗、主動土壓力、岩層介面

Active Earth Pressure on Retaining Walls near Rock Faces

Student : Sheng-Feng Huang Advisor : Dr. Yung-Show Fang

Department of Civil Engineering

National Chiao Tung University

Abstract

In this paper, the active earth pressure on retaining walls near an inclined rock face into backfill for loose sand is studied. The instrumented model retaining wall facilities at National Chiao Tung University was used to investigate the active earth pressure induced by different interface inclination angles β and spacing b. The loose Ottawa silica sand was used as backfill material. To simulate an inclined rock face, a steel interface plate and its supporting system were used. The main parameters considered for this study were the rock face inclination angles β = 0°, 50°, 60°, 70°, 80°, 90°and the horizontal spacing b = 0, 50 mm, 100 mm. Base on the test results, the following conclusions can be drawn:

1. Without the interface plate (β = 0^o), the active earth pressure coefficient $K_{a,h}$ is in good agreement with Coulomb's solution. The point of application h/H of the active soil thrust is located at about 0.333 H above the base of the wall.
2. With the approaching of the interface plate, the soil mass behind the wall decreased, the active earth pressure coefficient $K_{a,h}$ decreased with increasing stiff interface inclination angle β or decreasing spacing b.
3. As the interface angle β increased or spacing b decreased (the rock face approached the wall face), the inclined rock face intruded the active soil wedge, the earth pressure decreased near the base of the wall. This change of earth pressure distribution caused the active thrust to rise to a slightly higher location.

4. For $\beta = 90°$ (parallel vertical walls), the lateral pressure coefficient was not a constant with depth as assumed by Coulomb and Rankine. The pressure coefficient decreased with depth. It is obvious that, the evaluation of σ_h with Coulomb's and Rankine's theory would be on the safe side.
5. For all b = 0, b = 0.1H, and b = 0.2H, the horizontal component of active soil thrust $P_{a,h}$ would decrease with increasing β angle. The intrusion of the inclined rock face would actually increase the FS against sliding of the wall. The evaluation of FS against sliding with Coulomb's theory would be on the safe side.
6. For all b = 0, 0.1H, 0.2H, the normalized driving moment would decrease with increasing β angle. The intrusion of an inclined rock face into the active soil wedge would increase the F.S. against overturning of the retaining wall. The evaluation of F.S. against overturning with Coulomb's theory would also be safe.

Keywords: sand, model test, active earth pressure, rock face

Acknowledgements

The author wishes to give his sincere appreciation to his advisor, Dr. Yung-Show Fang for his enthusiastic advice and continuous encouragement in the past two years. If there is not the guidance from him, the thesis can not be accomplished.

Very special thanks are extended to Dr. Yi-Wen Pan, Dr. Jhih-Jhong Liao, Dr. An-Bin Huang, Dr. Shen-Yu Shan and Dr. Chih-Ping Lin for their teaching and valuable suggestions. In addition, the author also felt a great gratitude to the members of his supervisory committee, Dr. Chia-Cheng Fan and Dr. Huei-Wen Chang for their suggestions and discussions.

The author must extend his gratitude to Dr. Tsang-Jiang Chen, Mr. Kuo-Hua Li, Mr. Shih-Ta Hsu and Mr. Yu-Lun Chien for their support and encouragement. Appreciation is extended to all my friends and classmates, especially for Miss Yi-Jhen Jiang, Mr. Cho-Min Lin, Mr. Wei-Ting Chen, Miss Yu-Fen Hsu, Mr. Kuan-Yu Chen, Mr. Ting-Yuen Huang and Mr. Li-Chun Chen for their encouragement and assistance.

Finally, the author would dedicate this thesis to his grandfather, grandmother, parents, sister and girlfriend for their continuing encouragement and moral support.

Table of Contents

List of Tables

List of Figures

List of Symbols

C_u = Uniformity Coefficient

b = Distance between Interface Plate and Model Wall

D_r = Relative density

D_{10} = Diameter of Ottawa Sand whose Percent finer is 10%

D_{60} = Diameter of Ottawa Sand whose Percent finer is 60%

e_{max} = Maximum Void Ratio of Soil

e_{min} = Minimum Void Ratio of Soil

F = Force

G_s = Specific Gravity of Soil

h = Location of Total Thrust

$(h/H)_a$ = Point of application of active soil thrust

H = Effective Wall Height

i = Slop of Ground Surface behind Wall

K_o = Coefficient of Earth Pressure At-Rest

K_a = Coefficient of Active Earth Pressure

K_h = Coefficient of Horizontal Earth Pressure

$K_{a,h}$ = Coefficient of Horizontal Active Earth Pressure

P_a = Total Active Force

RT = Rotation about Wall Top

RTT = Rotation about a Point above Wall Top

RB = Rotation about Wall Base

RBT = Rotation about a Point below Wall Base

S = Wall Displacement

T = Translation

z = Depth from Surface

β = Angle of inclination Rock Face

σ_h = Horizontal Earth Pressure

σ_N = Normal Stress

γ = Unit Weight of Soil

ϕ = Angle of Internal Friction of Soil

δ_i = Angle of Interface Friction

δ_{sw} = Angle of Side-Wall Friction

δ_w = Angle of Wall Friction

Chapter 1

Introduction

This thesis studies the active earth pressure on a retaining wall near an inclined rock face as shown in Fig. 1.1. In the figure the inclined rock face intruded the Rankine active soil wedge. Under such a condition, can Coulomb's or Rankine's theories be used to evaluate the earth pressure acting on the retaining walls? Would the distribution of active earth pressure still be linear with depth? Would the point of application of the active soil thrust still be located at H/3 above the base of the wall (H is the height of backfill behind the wall)? It is important to investigate how would the nearby inclined rock face influence the Factor of Safety against sliding and overturning of the retaining wall.

1.1 Objectives of Study

In tradition, active earth pressure behind a gravity-type retaining wall is estimated with either Coulomb's or Rankine's theory. However, if the retaining wall is constructed adjacent to an inclined rock face as shown in Fig. 1.1, the rock face intrudes the active soil wedge behind the wall. For gravity-type retaining walls, the Rankine's active failure wedge is bounded by the wall and the failure plane with an inclination angle of $(45°+ \phi/2)$ with the horizontal, as shown in Fig. 1.1. It is clear in the figure that the nearby rock face may interfere the development of the Rankine's active failure wedge as the wall moves away from the backfill. The distribution of active earth pressure on the retaining structure adjacent to an inclined stiff interface is investigated in this study. In Fig. 1.1, the horizontal spacing between the inclined rock face and the base of the wall is expressed as b, and the inclination angle of the rock face with the horizontal is defined as β.

1.2 Research Outline

To study the effects of an adjacent inclined rock face on the active earth pressure on the retaining wall, the National Chiao Tung University (NCTU) model retaining wall facility was used. Fig. 1.2 shows a steel interface plate covered with a layer of "SAFETY-WALK" was designed to simulate the rock face. Air-dry Ottawa sand was used as the backfill material. The soil was placed between the wall and the interface plate with the air-pluviaiton method to achieve a relative density of 35%. The main parameters considered for this study were the rock face inclination angles β = 0°, 50°, 60°, 70°, 80°, 90°and the horizontal spacing b = 0, 50 mm, 100 mm as in Fig. 1.2, 1.3 and 1.4. For all tests, the height of the backfill H was 0.5 m. The variation of lateral earth pressure σ_h was measured with the soil pressure transducers (SPT) on the surface of the model wall. Based on experimental results, the variation of horizontal earth pressure was obtained.

Based on the test results, the magnitude of active soil thrust and the location of the active thrust were calculated. These results were compared with Coulomb's theoretical solution, numerical solution reported by Fan and Fang (2009) and the centrifuge test results reported by Frydman and Keissar (1987). It is hoped that this study would provide valuable information for the design of a retaining wall near an inclined rock face.

1.3 Organization of Thesis

This paper is divided into the following parts:

Chapter 1: Introduction of the subject

Chapter 2: Review of past investigations regarding the active earth pressure theories, numerical studies and laboratory test results

Chapter 3: Description of experimental apparatus

Chapter 4: Description of the Interface plate and supporting system

Chapter 5: Characteristics of the backfill and the interfaces

Chapter 6: Test results regarding horizontal earth pressure and active soil thrust

Chapter 7: Conclusions and design recommendations

Chapter 2

Literature Review

Geotechnical engineers frequently use the Coulomb and Rankine's earth pressure theories to calculate the active earth pressure behind retaining structures. These theories are discussed in the following sections. Mackey and Kirk (1967), Fang and Ishibashi (1986), Frydman and Keissar (1987), and Take and Valsangkar (2001) made experimental investigations regarding active earth pressure. Numerical investigation was made by Leshchinsky, et al. (2004) regarding the change of earth pressure from the at-rest to the active condition for a retaining wall near a vertical rock face. Fan and Fang (2009) used the non-linear finite element program PLAXIS (PLAXIS BV, 2002) to investigate the active earth pressure against a rigid wall near a stable rock face. Their major findings are introduced in this chapter.

2.1 Active Earth Pressure Theories

2.1.1 Coulomb Earth Pressure Theory

Coulomb (1776) proposed a method of analysis that determines the resultant horizontal force on a retaining system for any slope of wall, wall friction, and slope of backfill. The Coulomb theory is based on the assumption that soil shear resistance develops along the wall and the failure plane. Detailed assumptions are made as the followings:

1. The backfill is isotropic and homogeneous.
2. The rupture surface is plane, as plane BC in Fig. 2.1(a). The backfill surface AC is a plane surface as well.

3. The frictional resistance is distributed uniformly along the rupture surface BC.
4. Failure wedge is a rigid body.
5. There is a friction force between soil and wall when the failure wedge moves toward the wall.
6. Failure is a plane strain condition.

To create an active state, the wall is designed moved away from the soil mass. If the wedge ABC in Fig. 2.1(a) moves down relatively to the wall, and the wall friction angle δ will develop at the interface between the soil and wall. Let the weight of wedge ABC be W and the force on BC be F. With the given value θ, and the summation of verticle forces and horizontal forces, the resultant soil thrust P can be calculated as shown in Fig. 2.1(b).

To test different wedge scenarios, the corresponding values of P can be acquired. The upper part of Fig. 2.2 illustrates the curve of P according to different wedge scenarios. And the maximum P is the Coulomb's active force P_a as Eq. (2.1).

$$P_a = \frac{1}{2}\gamma H^2 K_a \tag{2.1}$$

where

P_a = total active force per unit length of wall

K_a = coefficient of active earth pressure

γ = unit weight of soil

H = height of wall

And

$$K_a = \frac{\sin^2(\phi+\beta)}{\sin^2\beta\sin(\beta-\delta)\left\{1+\sqrt{\frac{\sin(\phi+\delta)\sin(\phi-i)}{\sin(\beta-\delta)\sin(\beta+i)}}\right\}^2} \tag{2.2}$$

where

ϕ = internal friction angle of soil

δ = wall friction angle

β = slope of back of the wall to horizontal

i = slope of ground surface behind wall

2.1.2 Rankine Earth Pressure Theory

Rankine (1875) considered the soil in a state of plastic equilibrium and used essentially the same assumptions as Coulomb. The Rankine theory assumes that there is no wall friction and failure surfaces are straight planes, and that the resultant force acts parallel to the backfill slope. Detailed assumptions are made as the followings:

1. The backfill is isotropic and homogeneous.
2. Retaining wall is a rigid body. The wall surface is vertical to the ground and the friction force between the wall and the soil is neglected.
3. Elastic equilbrium is not applicable to the stress condition in the failure wedge.

Rankine assumed no friction between wall surface and backfill, and the backfill is cohesionless. The earth pressure on plane AB of Fig. 2.3(a) is the same as that on plane AB inside a semi-infinite soil mass in Fig. 2.3(b). For active condition, the active earth pressure σ_a at a given depth z can be expressed as:

$$\sigma_a = \gamma z K_a \tag{2.3}$$

The total active force P_a per unit length of the wall is equal to

$$P_a = \frac{1}{2}\gamma H^2 K_a \tag{2.4}$$

The direction of resultant force P_a is parallel to the ground surface as Fig. 2.3(b),

where

$$K_a = \cos i \frac{\cos i - \sqrt{(\cos^2 i - \cos^2 \phi)}}{\cos i + \sqrt{(\cos^2 i - \cos^2 \phi)}} \tag{2.5}$$

2.1.3 Terzaghi General Wedge Theory

The assumption of plane failure surface made by Coulomb and Rankine, however, does not apply in practice. Terzaghi (1941) suggested that the failure surface in the backfill under an active condition was a log spiral curve, like the curve bd in Fig. 2.4, but the failure surface dc is still assumed a plane.

The illustration in Fig. 2.5 shows how Terzaghi and Peck (1967) calculated the active resistance with trial wedge method. The line d_1c_1 makes an angle of $45^\circ + \phi/2$ with the surface of the backfill. The arc bd_1 of trial wedge abd_1c_1 is a logarithmic spiral formulated as the following equation

$$r_1 = r_0 e^{\theta \tan \phi} \tag{2.6}$$

O_1 is the center of the log spiral curve in Fig. 2.5, where $O_1b = r_1$, $O_1d_1 = r_0$, and $\angle bO_1d_1 = \theta$. For the equilibrium and the stability of the soil mass abd_1f_1 in Fig. 2.6, the following forces per unit width of the wall are considered.

1. Soil weight per unit width in abd_1f_1: $W_1 = \gamma \times$ (area of abd_1f_1)
2. The vertical face d_1f_1 is in the zone of Rankine's active state; hence, the force P_{d1} acting on the face is

$$P_{d1} = \frac{1}{2}\gamma (H_{d1})^2 \tan^2 (45^\circ - \frac{\phi}{2}) \tag{2.7}$$

where

$H_{d1} = d_1 f_1$

P_{d1} acts horizontally at a distance of $H_{d1}/3$ measured vertically upward form d_1.

3. The resultant force of the shear and normal forces dF, acting along the surface of sliding bd_1. At any point of the curve, according to the property of the logarithmic spiral, a radial line makes an angle ϕ with the normal. Since the resultant dF makes an angle ϕ with the normal to the spiral at its point of application, its line of application will coincide with a radial line and will pass through the point O_1.
4. The active force per unit width of the wall P_1. P_1 acts at a distance of H/3 measured vertically form the bottom of the wall. The direction of the force P_1 is inclined at an angle δ with the normal drawn to the back face of the wall.
5. Moment equilibrium of W_1, Pd_1, dF and P_1 about the point O_1:

$$W_1[l_2] + P_{d1}[l_3] + dF\ (0) = P_1[l_1] \tag{2.8}$$

or

$$P_1 = \frac{1}{l_1}[W_1 l_2 + P_{d1} l_3] \tag{2.9}$$

where l_2, l_3, and l_1 are the moment arms for forces W_1, P_{d1}, and P_1, respectively.

The trial active forces per unit width in various trial wedges are shown in Fig. 2.7. Let P_1, P_2, P_3, …, and P_n be the forces that respectively correspond to the trial wedges 1, 2, 3, …, and n. The forces are plotted to the same scale as shown in the upper part of the figure. A smooth curve is plotted through the points 1, 2, 3, …, n. The maximum P_1 of the smooth curve defines the active force P_a per unit width of the wall.

2.1.4 Spangler and Handy's Theory

Spangler and Handy (1984) have applied Janssen's theory (1895) to design problem of fascia retaining walls. Fig. 2.8 defines the soils with a width B bounded by two unyielding frictional boundaries (the rock face and wall face). The vertical force equilibrium of the thin horizontal soil element in Fig. 2.9 requires

$$(V + dV) + 2K\mu \frac{V}{B} dh = V + \gamma B dh \tag{2.10}$$

This is a linear differential equation, the solution for which is

$$V = \gamma B^2 \frac{1 - e^{-2K\mu(h/B)}}{2K\mu} \tag{2.11}$$

where

μ = tan δ, the coefficient of friction between the soil and the wall

γ = unit weight of the soil

B = backfill width

h = backfill depth

K = the coefficient of lateral earth pressure

V = the vertical force

From the solution of eq.(2.11), an equation for lateral earth pressure σ_h can be calculated

$$\sigma_h = \frac{\gamma B}{2\mu}\left[1 - e^{-2K\mu\left(h/B\right)}\right] \tag{2.12}$$

Some solutions for different values of B are shown in Fig. 2.10. The soil pressure, instead of continuing to increase with increasing values of h, levels off at a maximum value $\sigma_{h,max}$ defined as follows.

$$\sigma_{h_{\max}} = \frac{\gamma B}{2\mu} = \frac{\gamma B}{2\tan\delta} \tag{2.13}$$

2.2 Laboratory Model Retaining Wall Tests

2.2.1 Model Study by Mackey and Kirk

Mackey and Kirk (1967) experimented on lateral earth pressure by using a steel model wall. This soil tank was made of steel with internal dimensions of 36 in. × 16 in. × 15 in. (914 mm × 406 mm × 381 mm) as shown in Fig. 2.11. In this investigation, when the wall moves away from the soil, the earth pressure decreases (see Fig. 2.12) and then increases slightly until it reaches a constant value. Mackey and Kirk reported that if the backfill is loose, the active earth pressure obtained experimentally are within 14 percent off those obtained theoretically from almost any of the methods list in Table 2.1.

Mackey and Kirk utilized a powerful beam of light to observe the failure surface in the backfill. It could trace the position of the shadow, formed by changes of the sand surface in different level. It was found that the failure surface due to the translational wall movement was a curve in the backfill (Fig. 2.13), rather than a plane assumed by Coulomb.

2.2.2 Model Study by Fang and Ishibashi

Fang and Ishibashi (1986) conducted laboratory model experiments to investigate the distribution of the active stresses due to three different wall movement modes: (1) rotation about top, (2) rotation about base, and (3) translation. The experiments were conducted at the University of Washington.

Fig. 2.14 shows lateral earth pressures measured at various depths decreased rapidly with the translational active wall displacement. Most measurements reach

the minimum value at approximately 10×10^{-3} in (0.25 mm, 0.00025H) wall displacement and stay steady thereafter. Table 2.2 shows the range of wall displacement reported by previous researchers for translational wall movement mode to achieve an active state of stress.

Fig. 2.15 shows the horizontal earth pressure distributions at different translational wall movements. The measured active stress is slightly higher than Coulomb's solution at the upper one-third of wall height, approximately in agreement with Coulomb's prediction in the middle one-third, and lower than Coulomb' at the lower one-third of wall surface. However, the magnitude of the active total thrust P_a at S = 20×10^{-3} in. (0.5 mm) is nearly the same as that calculated from Coulomb's theory.

Fig. 2.16 shows the K_a as a function of soil density and internal friction angle. In this figure, the K_a value decreases with increasing ϕ. angle, and the Coulomb's solution would possible underestimate the coefficient K_a for rotational wall movement.

2.2.3 Centrifuge Model Study by Frydman and Keissar

Frydman and Keissar (1987) used the centrifuge modeling technique to test a small model wall near a vertical rock face as shown in Fig. 2.17, and changes in pressure from the at-rest to the active condition was observed. The centrifuge system has a mean radius of 1.5 m, and can develop a maximum acceleration of 100 g, where g is acceleration due to gravity. The models are built in an aluminum box of inside dimensions 327 × 210 × 100 mm. Each model includes a retaining wall made from aluminum (195 mm high × 100 mm wide × 20 mm thick) as shown in Fig. 2.18. The rock face is modeled by a wooden block, which can, through a screw arrangement, be positioned at varying distances b from the wall. Face of the block is coated with the sand used as fill, so that the friction between the rock and the fill is equal to the angle of internal friction of the fill.

Frydman and Keissar (1987) found that Spangler and Handy (1984) developed an equation, base on Janssen's (1895) arching theory, for calculating the lateral pressure acting on the wall of the silo. The lateral pressure at any given depth, z, is given as (silo pressure equation).

$$\sigma_x = \frac{\gamma b}{2\tan\delta}\left[1-\exp\left(-2K\frac{z}{b}\tan\delta\right)\right] \tag{2.14}$$

where

σ_x = the lateral pressure acting on the wall

b = the distance between the wall

z = depth from wall top at which σ_x is required

K = the coefficient of lateral earth pressure

γ = the unit weight of the backfill

δ = the angle of friction between the wall and the backfill

σ_v is the mean vertical pressure at a given depth. The coefficient K value depends on the movement of the wall. For walls without any movement, the Jaky's equation was suggested for estimating the K value. In the active condition, Frydman and Keissar further derived the K value by taking into account the friction between the wall and the fill and assuming that the soil near the wall reached a state of failure .The K value is given by

$$K = \frac{(\sin^2\phi+1)-\sqrt{(\sin^2\phi+1)^2-(1-\sin^2\phi)(4\tan^2\delta-\sin^2\phi+1)}}{(4\tan^2\delta-\sin^2\phi+1)} \tag{2.15}$$

Where ϕ = the angle of internal friction of the fill. The coefficient of lateral earth pressure in the active condition at given depth z can be determined as the ratio of σ_x over $\sigma_v(=\gamma z)$, and is expressed as

$$K_a = \frac{1}{2\tan\delta}\frac{b}{z}\left[1-\exp\left(-2K\frac{z}{b}\tan\delta\right)\right] \qquad (2.16)$$

The coefficient of active earth pressures at given depth z for a retaining wall near a vertical rock face can be theoretically estimated by substituting Eq. 2.15 into Eq. 2.16. The distribution of K_a value with the depth in Eq. 2.16 was verified using the experimental data obtained from the centrifuge model test, which the wall rotated about its base (RB model). The K_a value obtained decreased considerably with depth. Additionally, the measured K_a value was significantly less than the Rankine's or Coulomb's coefficient of active earth pressure. Fig. 2.19 shows the measured coefficient K_a value was in a range from 0.22 to 0.25 at z/b = 2, while it was about 0.14 at z/b = 6.5.

2.2.4 Centrifuge Model Study by Take and Valsangkar

Take and Valsangkar (2001) conducted the centrifuge model tests to investigate the reduction of earth pressures behind retaining walls of narrow backfill width. A series of tests has been performed to a using flexible subminiature earth pressure cells, to measure the lateral earth pressures behind the unyielding model retaining walls. Fig. 2.20 showed the fascia retaining wall which represented one such case of narrow backfill width retaining wall.

In Fig. 2.21(b), the earth pressure cells were mounted with epoxy on the 254-mm-wide, 150-mm-high (the effective wall height H is only 140 mm), 12.5-mm-thick aluminum unyielding model wall. The cavities were fabricated in such a manner as to ensure that the diaphragm of each pressure cell was flush with the wall surface. During the calibration of the pressure cells, the model retaining wall was bolted to the base of the centrifuge package (Fig. 2.21(a)). Once the calibration phase of the experimental program was competed, the model retaining wall was bolted in a vertical position onto one end of the centrifuge package with a variable spacing B to

the model rock face (Fig. 2.21(b)). The model backfill material is classified as a poorly graded sand with little or no fines as shown in Fig. 2.22, the backfill material has a uniformity coefficient of 2.2, a coefficient of curvature of 1.0, and a mean particle size of 0.4 mm.

To investigate the effect of dissimilar boundary frictional characteristics (δ = 22° and 30°) tests were performed with a loose soil sample for backfill widths of B = 38 mm and 15 mm. The results of these tests were shown in Fig. 2.23(a) and Fig. 2.23(b), respectively. With a reduction in backfill width, arching was observed to truncate lateral earth pressure. As predicted by arching theory, the z/B ratio has a dominant effect on the magnitude of the reduction of earth pressure within the narrow backfill (Fig. 2.24).

2.3 Numerical Studies

2.3.1 Numerical Study by Leshchinsky, et al.

Leshchinsky, Hu, and Han (2004) used the limit equilibrium method with computer program ReSSA 2.0 (ADAMA, 2003) to numerically investigate the lateral earth acting on a MSE wall. A baseline 5m-high wall was specified, the geometrical modeling was shown in Fig. 2.25(a). A single layer of reinforcement at 1/3 of the height of the wall was simulated in the analysis. In Fig. 2.25 the foundation was considered as competent bedrock to eliminate external effects on its stability. Various types of reinforced cohesionless fill were used in the analysis, all having a unit weight of γ = 20 kN/m^3 and the internal angle of friction ϕ of the fill varying from 20° to 45°.

Fig. 2.25(b) showed the base width of the fill was B, and the slope of the rear section of the fill was m. Fig. 2.26 represented the variation of active earth pressure coefficient K_a as a function of the rock face slope m. For B = 0, K'_a rapidly decreased with an increase in m (i.e., as the space between the wall and bedrock was

very small). K_a' was determined with the numerical analysis, and K_a was calculated with Rankine theory $K_a = \tan^2(45^\circ - \phi/2)$. For B = 0, 0.1H,and 0.2H, K_a' decreases with an increase in m, as the space between the wall face and the bed-rock slope was wider.

2.3.2 Numerical Study by Fan and Fang

Fan and Fang (2009) used the non-linear finite element program PLAXIS (PLAXIS BV, 2002) to investigate the earth pressure from the at-rest to the active condition for a rigid wall close to an inclined rock face (Fig. 2.27). The wall used for analysis is 5 m high, the back of the wall is vertical, and the surface of the backfill is horizontal. Typical geometry of the backfill zone used in the study is shown in Fig. 2.27. To investigate the influence of the adjacent rock face on the behavior of earth pressure, the inclination angle β of the rock face and the spacing b between the wall and the foot of the rock face were the parameters for numerical analysis. The wall was prevented from any movement during the placing of the fill. After the filling process, active wall movement was allowed until the earth pressure behind the wall reached the active condition. The finite element mesh, which has been examined to eliminate the influence of size effect and boundary on the results of the analyses, for a retaining wall with limited backfill space (β = 70° and b = 0.5m) is shown in Fig. 2.28. The finite element mesh consists of 1,512 elements, 3,580 nodes, and 4,536 stress points.

Base on the numerical analysis, distributions of horizontal earth pressures with the depth (z/H) at various wall displacements for b = 0.5 m and β = 80° are shown in Fig. 2.29. In the figure, the distribution of active earth pressure with depth is non-linear. Due to the nearby rock face, the calculated active pressure is considerably less than that computed using the Coulomb's theory.

Fig. 2.30 shows the variation of the active earth pressure coefficient ($K_{a(Computed)} / K_{a(Coulomb)}$) computed with finite element analysis, as a function of the

inclination of the rock face and rock face-wall spacing b, for walls under T mode. For $\beta > 60°$, the analytical active K values are less than those calculated with Coulomb's solution. The analytical K value decreased with increasing β angle, for β angles greater than 60°. Fig. 2.31 shows the variation of the $K_{a(Computed)}/K_{a(Coulomb)}$ with the β angle for T(traslation), RT(rotation about top) and RB(rotation about base) wall movement modes.

Fig. 2.32 shows the variation of the location of resultant of active earth pressures with the β angles at various fill widths (b) for walls in T mode. The h/H value increased with increasing β angles, and it increased with decreasing fill widths (b). For walls moving in T mode, the h/H value reached up to 0.41, 0.38, and 0.34 for β angles of 90°, 80°, and 70°, respectively, at a fill width (b) of 0.5 m. In addition, the h/H value reached up to 0.46 for β angles 90° at a fill width b = 0 m.

Fig. 2.33 shows the variation of the point of application of the active soil thrust with the β angle for b = 0.5 m. The variation of the h/H value with the β for walls in RB and T modes are similar. For $\beta < 60°$, h/H = 0.333 was calculated for both T and RB modes. For $\beta > 60°$, for walls in RB and T modes, the h/H increased with increasing β angles. For walls in RT mode, due to the arching stress near the top of the wall, the h/H value is considerably higher than those in RB and T modes.

Chapter 3

Experimental Apparatus

In order to study the earth pressure behind retaining structures, the National Chiao Tung University (NCTU) has built a model retaining wall system which can simulate different kinds of wall movement. All of the investigations described in the thesis were conducted in this model wall, which will be carefully discussed in this chapter. The entire facility consists of four components, namely, model retaining wall, soil bin, driving system, and data acquisition system. The arrangement of the NCTU model retaining wall system is shown in Fig. 3.1.

3.1 Model Retaining Wall

The movable model retaining wall and its driving systems are illustrated in Fig. 3.1. The model wall is a 1000-mm-wide, 550-mm-high, and 120-mm-thick solid plate, and is made of steel. Note that in Fig. 3.1 the effective wall height H is only 500 mm. The retaining wall is vertically supported by two unidirectional rollers , and is laterally supported by four driving rods. Two sets of wall-driving mechanisms, one for the upper rods and the other for the lower rods, provide various kinds of movements for the wall. A picture of the NCTU model wall facility is shown in Fig. 3.2.

Each wall driving system is powered by variable-speed motor. The motors turn the worm driving rods which cause the driving rods to move the wall back and forth. Two displacement transducers (Kyowa DT-20D) are installed at the back of retaining wall and their sensors are attached to the movable wall. Such an arrangement of displacement transducers would be effective in describing the wall

translation.

To investigate the distribution of earth pressure, nine earth pressure transducers were attached to the model wall. The arrangement of the earth pressure cells should be able to closely monitor the variation of the earth pressure of the wall with depth. Base on this reason, the earth pressure transducers SPT1 through SPT9 have been arranged at two vertical columns as shown in Fig. 3.3.

A total of nine earth pressure transducers have been arranged within a narrow central zone to avoid the friction that might exist near the side walls of the soil bin as shown in Fig. 3.4. The Kyowa model PGM-02KG (19.62 kN/m^2 capacity) transducer shown in Fig. 3.5 was used for these experiments. To reduce the soil-arching effect, earth pressure transducers with a stiff sensing face are installed flush with the face of the wall. They provide closely spaced data points for determining variation of the earth pressure distribution with depth.

3.2 Soil Bin

The soil bin is fabricated of steel members with inside dimensions of 2,000 mm × 1,000 mm × 1,000 mm (see Fig. 3.1). Both sidewalls of the soil bin are made of 30-mm-thick transparent acrylic plates through which the behavior of backfill can be observed. Outside the acrylic plates, steel beams and columns are used to confine the side walls to ensure a plane strain condition.

The end wall that sits opposite to the model retaining wall is made of 100 mm thick steel plates. All corners, edges and screw-holes in the soil bin have been carefully sealed to prevent soil leakage. The bottom of the soil bin is covered with a layer of SAFETY-WALK to provide adequate friction between the soil and the base of the soil bin.

In order to constitute a plane strain condition, the soil bin is built very rigid so that the lateral deformations of the side walls will be negligible. The friction between the backfill and the side walls is to be minimized to nearly frictionless, so that shear

stress induced on the side walls will be negligible. To eliminate the friction between backfill and sidewall, a lubrication layer with 3 layers of plastic sheets was furnished for all model wall experiments. The “thick” plastic sheet was 0.152 mm thick, and it is commonly used for construction, landscaping, and concrete curing. The “thin” plastic sheet was 0.009 mm thick, and it is widely used for protection during painting, and therefore it is sometimes called painter’s plastic. Both plastic sheets are readily available and neither is very expensive. The lubrication layer consists of one thick and two thin plastic sheets were hung vertically on each sidewall of the soil bin before the backfill was deposited. The thick sheet was placed next to the soil particles. It is expected that the thick sheet would help to smooth out the rough interface as a result of plastic-sheet penetration under normal stress. Two thin sheets were placed next to the steel sidewall to provide possible sliding planes. For more information regarding the reduction of boundary friction with the plastic-sheet method, the reader is referred to Fang et al. (2004).

3.3 Driving System

As illustrated in Fig. 3.1, the variable speed motors M1 and M2 (Electro, M4621AB) are employed to compel the upper and lower driving rods, respectively. The shaft rotation compels the worm gear linear actuators, while the actuator would push the model wall. Since only the variation of earth pressure caused by the translational wall movement is investigated, the motor speeds at M1 and M2 were kept the same for all experiments in this study.

3.4 Data Acquisition System

Due to the considerable amount of data collected by the soil-pressure transducers, a data acquisition system was used shown in Fig. 3.6. It is composed of the following four parts: (1) dynamic strain amplifiers (Kyowa: DPM601A and

DPM711B); (2) NI adaptor card; (3) AD/DA card; and (4) personal computers shown in Fig. 3.7. An analog-to-digital converter digitized the analog signals from the sensors. The digital data were then stored and processed by a personal computer. For more details regarding the NCTU retaining-wall facility, the reader is referred to Wu (1992) and Fang et al. (1994).

Chapter 4

Interface Plate and Supporting System

A steel interface plate is designed and constructed to simulate inclined rock face near the retaining structure shown in Fig. 1.1. In Fig. 4.1, the plate and its supporting system are developed by Zheng (2008) to fit in the NCTU model retaining-wall facility. The interface plate consists of two parts: (1) steel plate; and (2) reinforcing steel beams. The supporting system consists of the following three parts: (1) top supporting beam; (2) base supporting block; and (3) base supporting boards. Details of the interface plate and its supporting system are introduced in the following sections.

4.1 Interface Plate

4.1.1 Steel Plate

The steel plate is 1.370 m-long, 0.998 m-wide, and 5 mm-thick as shown in Fig. 4.2. The unit weight of the steel plate is 76.52 kN/m^3 and its total mass is 83 kg (0.814 kN). A layer of anti-slip material (SAFETY-WALK, 3M) is attached on the steel plate to simulate the friction that acts between the backfill and rock face as illustrated in Fig. 4.2 (c) and Fig. 4.3 (a). For the inclination angle $\beta = 50^o$ shown in Fig. 1.2, the length of the interface plate should be at least 1.370 m. On the other hand, the inside width of the soil bin of the NCTU retaining wall facility is 1 m. In order to put the interface plate into the soil bin, the width of the steel plate has to less than 1.0 m. As a result, the steel plate was designed to be 1.370 m-long and 0.998 m-wide.

4.1.2 Reinforcement with Steel Beams

To simulate the stiffness of the rock face shown in Fig. 1.1, the steel interface plate should be nearly rigid. To increase the rigidity of the 5 mm-thick steel plate, Fig. 4.2 (b) and Fig. 4.3 (b) shows 5 longitudinal and 5 transverse steel L-beams were welded to the back of steel plate. Section of the steel L-beam (30 mm × 30 mm × 3 mm) was chosen as the reinforced material for the thin steel plate. On top of the interface plate, a 65 mm × 65 mm × 8 mm steel L-beam was welded to reinforce the connection between the plate and the hoist ring shown in Fig. 4.3 (b).

4.2 Supporting System

To keep the steel interface plate in the soil bin stable during testing, a supporting system for the interface plate was designed and constructed by Zheng (2008). A top-view of the base supporting frame is illustrated in Fig. 4.4. The supporting system composed of the following three parts: (1) base supporting block; (2) top supporting beam;and (3) base boards. These parts are discussed in following sections.

4.2.1 Top Supporting Beam

In Fig. 4.5, the top supporting steel beam is placed at the back of the interface plate and fixed at the bolt slot on the side wall of the soil bin. Details of top supporting beam are illustrated in Fig. 4.7. The section of supporting steel beam is 65 mm × 65 mm × 8 mm and its length is 1700 mm. Fig. 4.4 shows four bolt slots were drilled on each side of the U-shape steel beam on the side wall of the soil bin. Fig. 4.6 shows the top supporting beam was fixed at the slots with bolts.

4.2.2 Base Supporting Block

The base supporting block used to support the steel interface plate is shown in Fig. 4.8. The base supporting block is 1.0 m-long, 0.14 m-wide, and 0.113 m-thick. Fig. 4.8 (b) shows three trapezoidal grooves were carved to the face of the base supporting block. Fig. 1.2 shows the foot of the interface plate could be inserted into the groove at different distance from base of the model wall. For this study, different horizontal spacing d adopted for testing includes: (1) d = 0 mm; (2) d = 50 mm; and (3) d = 100 mm. Fig. 4.5 shows 6 pieces of base boards are stacked between the base supporting block and the end wall to keep the base block stable. The base board shown in Fig. 4.9 is 1860 mm-long, 1000 mm-wide and 113 mm-thick. The surface of the top base board was cover with a layer of anti-slip material SAFETY-WALK.

Chapter 5

Backfill and Interface Characteristics

This chapter introduces the properties of the backfill, and the interface characteristics between the backfill and the wall. Laboratory experiments have been conducted to investigate the following subjects: (1) backfill properties; (2) model wall friction; (3) side wall friction; (4) interface plate friction; and (5) distribution of soil density in the soil bin.

5.1 Backfill Properties

Air-dry Ottawa sand (ASTM C-778) was used throughout this investigation. Physical properties of the soil include G_s= 2.65, e_{max}= 0.76, e_{min}= 0.50, D_{60}= 0.315 mm, and D_{10}= 0.213 mm. Grain-size distribution of the backfill is shown in Fig. 5.1. Major factors considered in choosing Ottawa sand as the backfill material are summarized as follows.

1. Its round shape, which avoids effect of angularity of soil grains.
2. Its uniform distribution of grain size (coefficient of uniformity C_u=1.48), which avoids the effects due to soil gradation.
3. High rigidity of solid grains, which reduces possible disintegration of soil particles under loading.
4. Its high permeability, which allows fast drainage of pore water and therefore reduces water pressure behind the wall.

To establish the relationship between unit weight γ of backfill and its internal friction angle ϕ, direct shear tests have been conducted. The shear box used has a square (60 mm×60 mm) cross-section, and its arrangement are shown in Fig. 5.2.

Chang (2000) established the relationship between the internal friction angle ϕ and unit weight γ of the ASTM C-778 Ottawa sand as shown in Fig. 5.3. It is obvious from the figure that soil strength increases with increasing soil density. For the air-pluviated backfill, the empirical relationship between soil unit weight γ and ϕ angle can be formulated as follows

$$\phi = 6.43\gamma - 68.99 \tag{5.1}$$

where

ϕ =angle of internal friction of soil (degree)

γ =unit weight of backfill (kN/m^3)

Eqn. (5.1) is applicable for γ = 15.45 ~ 17.4 kN/m^3 only.

5.2 Model Wall Friction

To evaluate the wall friction angle δ_w between the backfill and model wall, special direct shear tests have been conducted. A 88 mm × 88 mm × 25 mm smooth steel plate, made of the same material as the model wall, was used as the lower shear box. Ottawa sand was placed into the upper shear box and vertical load was applied on the soil specimen. The arrangement of this test is shown in Fig. 5.4.

To establish the wall friction angles δ_w developed between the steel plate and sand, soil specimens with different unit weight were tested. Air-pluviation methods was used to achieve different soil density, and the test result is shown in Fig. 5.5. For air-pluviation Ottawa sand, Lee (1998) suggested the following relationship:

$$\delta_w = 2.33\gamma - 17.8 \tag{5.2}$$

Eqn. (5.2) is applicable for γ = 15.5~17.5 kN/m^3 only. The ϕ angle and δ angle obtained in section 5.1 and 5.2 are used for calculation of active earth pressure based

on Coulomb, and Rankine's theories.

5.3 Side Wall Friction

To constitute a plane strain condition for model wall experiments, the shear stress between the backfill and sidewall should be eliminated. A lubrication layer fabricated with plastic sheets was equipped for all experiments to reduce the interface friction between the sidewall and the backfill. The lubrication layer consists of one thick and two thin plastic sheets as suggested by Fang et al. (2004). All plastic sheets had been vertically placed next to both side-walls as shown in Fig. 5.6.

The friction angle between the plastic sheets and the sidewall was determined by the sliding block tests. The schematic diagram and the photograph of the sliding block test by Fang et al. (2004) are illustrated in Fig. 5.7 and Fig. 5.8. The sidewall friction angle δ_{sw} is determined based on basic physics principles. Fig. 5.9 shows the variation of interface friction angle δ_{sw} with normal stress σ based on the plastic sheet lubrication tests. The friction angle measured was 7.5°. With the plastic – sheet lubrication method, the interface friction angle is almost independent of the applied normal stress. The angle of wall friction for smooth concrete is about $\phi/2$ to $2\phi/3$, with the $\phi = 31.3°$ for loose sand, the wall friction angle should be $\delta = 15.7°\sim20.9°$. The shear stress between the acrylic side-wall and backfill has been effectively reduced with the plastic-sheet lubrication layer.

5.4 Interface Plate Friction

To evaluate the interface friction between the interface plate and the backfill special, direct shear tests were conducted as shown in Fig. 5.10. In Fig. 5.10(b), a 80

mm × 80 mm × 15 mm steel plate was covered with a layer of anti-slip material "SAFETY-WALK" to simulate the surface of the interface plate. The interface-plate was used to simulate the inclined rock face near the wall as shown in Fig. 1.1. Dry Ottawa sand was placed into the upper shear box and vertical stress was applied on the soil specimen as shown in Fig. 5.10(a).

To establish the relationship between the unit weight γ of the backfill and the interface-plate friction angle δ_i, soil specimens with different unit weight were tested. Air-pluviation methods was used to achieve different soil density, and the test result is shown in Fig. 5.11. For air-pluviation Ottawa sand, Wang (2005) suggested the following empirical relationship:

$$\delta_i = 2.7\,\gamma - 21.39 \tag{5.3}$$

where

δ_i = interface-plate friction angle (degree)

γ = unit weight of backfill (kN/m^3)

Eqn. (5.3) is applicable for γ = 15.1 ~16.36 kN/m^3 only.

The relationships between backfill unit weight γ and different friction angles are illustrated in Fig. 5.12. The internal friction angle of Ottawa sand ϕ, model wall-soil friction angle δ_w, interface-plate friction angle δ_i, and sidewall friction angle δ_{sw} as a function of soil unit weight γ are compared in the figure. It is clear in Fig. 5.12 that, with the same unit weight, the order of the four different friction angles is $\phi > \delta_i > \delta_w > \delta_{sw}$.

5.5 Control of Soil Density

5.5.1 Air-Pluviation of Backfill

To achieve a uniform soil density in the backfill, dry Ottawa sand was

deposited by air-pluviation method into the soil bin. The air-pluviation method had been widely used for a long period of time to reconstitute laboratory sand specimens. Rad and Tumay (1987) reported that pluviation is the method that provides reasonably homogeneous specimens with desired relative density. Lo Presti et al. (1992) reported that the pluviation method could be performed for greater specimens in less time. As indicated in Fig. 5.13, the soil hopper that lets the sand pass through a calibrated slot opening at the lower end was used for the spreading of sand. A picture showing air-pluviation of the Ottawa sand into soil bin is indicated in Fig. 5.14. Air-dry Ottawa sand was shoveled from the soil storage bin to the sand hopper, weighted on the electric scale, then pluviated into the soil bin. As indicated in Fig. 5.15, four types of slot openings (5 mm, 7 mm, 10 mm and 15 mm) were adopted by Ho (1999), and the drop height of soil varied from 0.25 m to 2.5 m.

Das (1994) suggested that the granular soil with a relative density of 15% ~ 50% is defined as loose. In this study, the drop height of 1.0 m and the slot opening of 15 mm were selected to achieve the loose backfill with a relative density of 35%.

5.5.2 Distribution of Soil Density

To investigate the distribution of soil density in the soil bin, soil density measurements were made. The soil density control cup made of acrylic is illustrated in Fig. 5.16 and Fig. 5.17. For the air-pluviated backfill, the density cups were used to measure the soil density at different elevations and locations.

In Fig. 5.18, a layer of 100 mm-thick Ottawa sand was placed in the soil bin as a soil blanket. Four density-control cups were then put into the soil bin on the surface of soil blanket. Locations of the cups are illustrated in Fig.5.18. Then Ottawa sand was placed layer by layer into the soil bin up to 0.5 m thick.

After the soil has been poured to the top, the soil cups were dug out of the backfill carefully. Soil density in the box can be found by dividing the mass of soil

in the box by the inside volume of the cup. To investigate the variation of density with depth, another group of tests were conducted. As shown in Fig. 5.19, four density control cups were put into the soil bin at different depths near the center of the soil bin. After the soil was poured into the soil bin up to 0.5 m thick from base board, the cups were dug out of the soil mass carefully, and the soil in the cups were determined. The distributions of relative density of loose sand measured at different elevations are shown in Fig. 5.20. For experimental result, the relative density average with depth was 35.4%. Standard deviation of relative density was 1.04%. From a practical point of view, it may be concluded from these data that the soil density in the soil bin is quite uniform.

Chapter 6

Test Results

This chapter reports the experimental results regarding effects of an adjacent inclined rock face on the active earth pressure against a retaining wall filled with loose sand. The rock face interface inclination angles $\beta = 0^o$, 50^o, 60^o, 70^o, 80^o, 90^o and spacing b = 0, 50 mm, 100 mm are illustrated in Fig. 1.2 to Fig. 1.4. The height of backfill H is 0.5 m and the air-pluviation method was used to prepare the backfill. The loose Ottawa sand (D_r = 35%) with the unit weight γ = 15.6 kN/m^3 was prepared as the backfill material. Based on direct shear tests (Ho, 1999) the internal friction angle ϕ for the loose backfill would be 31.3^o. The γ and ϕ values are used to calculate earth pressures based on the Jaky and Coulomb theories. The testing program is listed in Table 6.1

6.1 Horizontal Earth without Interface Plate

The variation of lateral earth pressure as function of active wall movement was investigated. After the loose backfill and had been placed into the soil bin as shown in Fig. 6.1 (a) (b), the model wall slowly moved away from the soil mass in a translation mode at a constant speed of 0.015 mm/s. No compaction was applied to the loose backfill.

Distributions of horizontal earth pressure σ_h measured at different stages of wall displacements S/H (S : wall displacement, H : backfill height) for Test 1215-3 and 1229-1 are illustrated in Fig. 6.2 and Fig. 6.3. As the wall started to move, the earth pressure decrease, and eventually a limit limiting active pressure was reached. The pressure distributions are essentially linear at each stage of wall movement. Active earth pressures calculated with Rankine and Coulomb theories are also

indicated in the figure. The ultimate experiment active pressure distribution at S/H = 0.04 is in fairly good agreement with that estimated with Coulomb and Rankine theories.

The variation of horizontal earth-pressure coefficient K_h as a function of wall displacement is shown in Fig. 6.4. The coefficient K_h is defined as the ratio of the horizontal component of total soil thrust P_h to $\gamma H^2/2$. The horizontal soil thrust P_h was calculated by summing the pressure diagram shown in Fig. 6.3. The coefficient K_h decreased with increasing wall movement S/H until a minimum value was reached, then remained approximately a constant. The ultimate value of K_h is defined as the horizontal active earth-pressure coefficient $K_{a,h}$. In Fig. 6.4, the active condition was reached at approximately S/H = 0.00375~0.004. In Fig. 6.4, it may not be an easy task to define the point of active wall movement S_a. For a wall that moved away from a loose sandy backfill in a translational mode, Mackey and Kirk concluded the wall displacement required to reach an active state is S_a = 0.004 H. The S_a values recommended by Mackey and Kirk (1967), Bros. (1972), Fang and Ishibashi (1986) Fang et al. (1997) were summarized in Table 2.2 and illustrated in Fig. 6.4. In this study the active wall movement is assumed to be S_a = 0.004 H.

It may be observed in Fig. 6.4 that the Coulomb theory ($\delta = \phi/2$) provide a good estimate of the active earth pressure. In the actual design of retaining walls, the wall friction angle δ is generally assumed to be between $\phi/2$ (smooth concrete) and ϕ (rough stone) (Sowers, 1979). The steel piles against the following clean sand : δ = 17° (NAVFAC DM-7.2, 1982) The model wall used for this study is made of steel. For this reason, $\delta = \phi/2$ was used in the theoretical Coulomb solutions in this study.

In Fig. 6.3, the distribution of earth pressure with depth at different wall movements is nearly linear. As a result, the point of application of the total thrust should act at about H/3 above the wall base (h/H = 0.333). Test results in Fig. 6.5 show that the point of application of soil thrust are located at about 0.33 H ~ 0.36 H above the wall base.

6.2 Horizontal Earth Pressure for b = 0

Fig. 6.6 to Fig. 6.9 show the steel interface plate was placed in the soil bin for β = 50°, 60°, 70° and 80°, and dry Ottawa sand was pluviated behind the model wall for b = 0. It should be mentioned that, to clearly show the position of the interface plate, the picture in Fig. 6.6 was taken without the plastic-sheet lubrication layer. During testing, the lubrication layers were hung vertically between the acrylic side-wall and backfill. Fig. 6.10 to Fig. 6.17 show the distribution of earth pressure at different stages of wall movement with presence of a stiff interface plate for an inclination angle β = 50°,60°, 70° and 80°. In Fig. 6.10 and Fig. 6.11 (β = 50°), the measured horizontal stress at S/H = 0 is lower than Jaky's solution at lower H/3 of the wall. At the wall movement S/H = 0.004, the active earth pressure is less than that of Coulomb's solution at the lower H/3 of the wall. In Fig. 6.6(a), for the upper part of the model wall, the interface plate is relatively far from the SPT. It is reasonable to expect the measured σ_h to be close to Coulomb's prediction. However, for the lower part of the model wall, the interface plate is relatively close to the soil pressure transducers. As a result, the active earth pressure measured would be affected by the approaching of the interface plate.

In Fig. 6.12 to Fig. 6.15 (β = 60° and 70°), the measured σ_h was significantly lower than Jaky's solution at S/H = 0. At S/H = 0.004, the σ_h measured at lower H/2 of wall was lower than Coulomb's solution. It may be observed in Fig. 6.7 and Fig. 6.8, with increasing β angle (β = 60° to 70°), the horizontal distance between the model wall and interface plate was reduced. In Fig. 6.16 and Fig. 6.17 (β = 80°), the measured at-rest pressure distribution is not linearly with depth. and it is significantly less than the Jaky solution at S/H = 0. Fig. 6.9 shows, for β = 80°, the interface plate was quite close to the wall surface. The amount of backfill soil sandwiched between the rock face and the wall was very little. In this Fig. 6.16 and Fig. 6.17, the earth pressure slightly decreased with the active wall movement.

Fig. 6.18 to Fig. 6.21 presented the variation of lateral soil thrust as a function of active wall movement for β = 50°, 60°, 70°, and 80°. As the wall started to move, the lateral soil thrust decreased with increasing wall movement until a stable value is reached, K_h then remained approximately a constant. The ultimate value of K_h is defined as the horizontal active earth pressure coefficient $K_{a,h}$. For b = 0, the active condition was observed at approximately S/H = 0.004.

The Fig. 6.22 to Fig. 6.25 showed the variation of the point of application of the soil thrust as a function of active wall movement for β = 50°, 60°, 70°, and 80°. At the active wall movement of 0.004 H, for β = 50^o, 60^o and 70^o, the $(h/H)_a$ values reached 0.35, 0.38 and 0.40, respectively. For β = 80^o, experimental results showed that the active soil thrust was located at about 0.46 H ~ 0.47 H above the base of the wall. As compared to Fig. 6.4 and Fig. 6.5 (without interface plate), it is clear that the magnitude and the point of application of the active soil thrust are significantly affected by the presence of the nearby rock face.

6.3 Horizontal Earth Pressure for b = 50 mm

Fig. 6.26 to Fig. 6.30 showed the steel interface plate was placed in the soil bin for β = 50°, 60°, 70°, 80° and 90° and dry Ottawa sand was pluviated behind the model wall. In the figures ,the horizontal spacing between the base of the interface plate and the base of the wall b = 50 mm. Fig. 6.31 to Fig. 6.40 showed the distribution of earth pressure at different stages of active wall movement with the presence of a stiff interface plate with the inclination angle β = 50°, 60°, 70°, 80° and 90°. In Fig. 6.31 to Fig. 6.34 (β = 50° and 60°), the measured stress σ_h at S/H = 0 is lower than Jaky's prediction at lower H/3 of the wall. At the wall movement of 0.004 H, the active earth pressure was less than Coulomb's solution at the lower part of the wall. In Fig. 6.35 to Fig. 6.38 (β = 70° and 80°), the active earth pressure

measured at lower H/3 of the wall was lower than Coulomb's solution. In Fig. 6.39 and Fig. 6.40 (β = 90°), it was found that theoretical solutions apparently overestimated the test results in both at-rest and active conditions. In Fig. 6.30, the interface plate was parallel to the model wall, the interface plate is quite close to the soil transducers on the wall. As the result, the at-rest and active earth pressure measured would be significantly affected by the nearby interface plate, especially for $\beta = 90^o$.

The Fig. 6.41 to Fig. 6.45 presented the variation of total soil thrust as a function of active wall movement. As the wall started to move, the lateral soil thrust decreased with increasing wall movement until a stable value was reached, then remained approximately a constant. The ultimate value of K_h was defined as the horizontal active earth pressure coefficient $K_{a,h}$. For b = 50 mm, the active condition was reached at the wall movement of 0.004 H.

Fig. 6.46 to Fig. 6.50 showed the point of application of the active soil thrust as a function of active wall movement. At the wall movement of 0.004 H for $\beta = 50^o$, 60^o and 70^o, the $(h/H)_a$ values reached 0.34, 0.35 and 0.36, respectively. For $\beta = 80^o$ and 90^o, experimental results show that the points of application of the active soil thrusts were located at about 0.40 H and 0.42 H above the wall base.

6.4 Horizontal Earth Pressure for b = 100 mm

Fig. 6.51 to Fig. 6.55 showed the steel interface plate was placed in the soil bin for β = 50°, 60°, 70°, 80° and 90° and dry Ottawa sand was pluviated behind the model wall. The horizontal distance brtween the base of the interface plate and the base of the wall was b = 100 mm. Fig. 6.56 to Fig. 6.65 showed the distribution of earth pressure at different stages of wall movement with presence of a stiff interface plate for an inclination angle $\beta = 50^o$~90^o. In Fig. 6.56 and Fig. 6.57 (β = 50°), the stress measured at S/H = 0 was lower than Jaky's solution near the bottom of the

wall. However, the active earth pressure in Fig. 6.56 was close to Coulomb's solution. It was clear in Fig. 6.51 that with β = 50° and b = 100 mm, the interface plate was relatively far from the wall face and did not intrude the Rankine active soil wedge behind the retaining wall. As a result, the measured active earth pressure was not strongly affected by the presence of the rock face. A similar active pressure distribution can be observed in Fig. 6.58 and Fig. 6.59 for β = 60°.

In Fig. 6.60 to Fig. 6.63 (β = 70°~80°), the active earth pressure measured at H/3 above wall base was lower than Coulomb's solution. In Fig. 6.64 and Fig. 6.65 (β = 90°), at S/H = 0 the measured at-rest pressure distribution was not linear with depth. The distribution of at-rest and active earth pressures at the lower half of the wall were less than Jaky's solution and Coulomb's solution, respectively. It is clear in Fig. 6.55 that the rock face and wall were parallel and it was not possible for the active soil wedge to develop behind the wall.

In Fig. 6.66 to Fig. 6.70, the horizontal earth pressure coefficient K_h decreased with increase wall movement, eventually a constant value $K_{a,h}$ was observed. In Fig. 6.70 (β = 90°), the interface plate was only 0.1 m from the SPT, (Fig. 6.55), and the constant value $K_{a,h}$ was significantly lower than the value estimated with the Coulomb's theory. For β = 50° (Fig. 6.51), the interface plate was relatively far from the soil pressure transducers. As a result, the active earth pressure measured would not be affected by the interface plate.

The location of the total soil thrust versus active wall movements was shown in Fig. 6.71. to Fig. 6.75 for β = 50°, 60°, 70°, 80° and 90°. Experimental results showed that the point of application of the active soil thrusts were located at about 0.38 H above the wall base for $\beta = 90^o$. For $\beta = 50^o$, 60^o, 70^o and 80^o, the $(h/H)_a$ values reached 0.336, 0.340, 0.344 and 0.356, respectively.

6.5 Active Soil Thrust

The distributions of active earth pressure at the interface inclination angle $\beta = 0°$, 50°, 60°, 70° and 80°, for b = 0, were shown in Fig. 6.76. For b = 50 mm and b = 100 mm, the distributions of active earth pressure for $\beta = 0°$, 50°, 60°, 70°, 80° and 90° were shown in Fig. 6.77 and Fig. 6.78. In Fig. 6.76, the active earth pressure decreased with increasing β angle. It would be reasonable to expect that the magnitude of active soil thrust to decrease with increasing β angle (approaching of rock face). In Fig. 6.76, the shape of the active pressure distribution implied that the point of application of the active soil thrust would rise with increasing rock face inclination angle β.

The variation of horizontal earth pressure coefficient K_h as a function of active wall movement S/H for b = 0, b = 50 mm, b = 100 mm are shown in Fig. 6.79 to Fig. 6.81. Without the interface plate ($\beta = 0°$), the active earth pressure coefficient $K_{a,h}$ was in fairly good agreement with Coulomb's equation ($\delta = \phi/2$). However, with the approaching of the interface plate, the soil mass behind the wall decreased, the active earth pressure coefficient $K_{a,h}$ decreased with increasing stiff interface inclination angle β.

The point of application of the soil thrust as a function of wall movement was discussed in this paragraph. Fig. 6.82 to Fig. 6.84 showed, without the interface plate ($\beta = 0°$), the point of application of the earth pressure resultant was located at about 0.333 H above the base of the wall. In Fig. 6.82, as the interface angle β increased up to 70°, the inclined rock face intruded the active soil wedge, the earth pressure decreased near the base of the wall. This change of earth pressure distribution caused the active thrust to rise to a slightly higher location as shown in Fig. 6.82 to Fig. 6.84.

6.5.1 Magnitude of Active Soil Thrust

The active earth pressure coefficient $K_{a,h}$ as a function of interface inclination angle β for b = 0, b = 0.1H and b = 0.2H was shown in Fig. 6.85. For comparison purposes, the analytical results reported by Fan and Fang (2009) were also plotted in Fig. 6.85. Without the interface plate (β = 0°), the experimental coefficient $K_{a,h}$ values were similar Coulomb's prediction. For b = 0.1H and b = 0.2H, the coefficient $K_{a,h}$ values were in good agreement with numerical $K_{a,h}$ values. With the intrusion of the rock face into the active soil wedge, the active earth pressure coefficient $K_{a,h}$ decreased with increasing rock face angle β. Although the tend was the same, for b = 0, the experimental $K_{a,h}$ coefficient was lower than the numerical $K_{a,h}$ values.

Fig. 6.86 showed a circular storage silo filled with granular material. It is important for the designer to know how much lateral pressure is acting on the inside of silo walls. The granular material in the silo was restrained by parallel vertical walls which is similar to the b = 100 mm and β = 90° condition shown in Fig. 6.55. For β = 90°, Fig. 6.87 showed the active horizontal pressures based on the theoretic solution (Spangler and Handy, 1982), numerical solution (Fan and Fang, 2009), data measured from the centrifuge model test (Frydman and Keissar, 1987), and the data measured from the model retaining wall test. In Fig. 6.87 the lateral pressure coefficient was not a constant with depth as assumed by Coulomb and Rankine. The pressure coefficient decreased with depth. The tend was the same, for results based on numerical analysis and experiments. It is obvious that, the evaluation of σ_h with Coulomb's and Rankine's theory would be on the safe side.

6.5.2 Point of Application of Active Soil Thrust

Fig. 6.88 showed the point of application of active soil thrust with the β angles for b = 0, b = 50 mm and b = 100 mm. For comparison purposes, the numerical results reported by Fan and Fang (2009) were also plotted in Fig. 6.88. For β = 0°, which indicated no rock face was near the retaining wall, the $(h/H)_a$

value was located at about 0.333 H above the base of the wall. As the interface angle β increased the rock face approach the wall face, the earth pressure measured near the base of the wall decreased. This change of earth pressure distribution caused the active total thrust to move to a slightly higher location as shown in Fig. 6.88. For b = 0, β = 80°, the point of application of the active soil thrust was located at 0.463H above the base of the wall. For b = 100 mm, since the rock face was distanced 0.1 m horizontally, the influence of the inclined rock face on the wall became less significant.

6.6 Design Considerations

In the design of a retaining structure, it is often necessary to check its adequacy. It is important to investigate how would the nearby inclined rock face influence the Factor of Safety (F.S.) against sliding and overturning of the retaining wall.

6.6.1 Factor of Safety against Sliding

The Factor of Safety against sliding of the retaining structure is defined as:

$$FS_{sliding} = \frac{\sum \text{Resisting Force}}{\sum \text{Driving Force}} \tag{6.1}$$

For the retaining wall shown in Fig. 1.1, the driving force came from the active earth pressure acting on the face of the wall. Fig. 6.85 indicated, for all b = 0, b = 0.1H, and b = 0.2H, the horizontal component of active soil thrust $P_{a,h}$ would decrease with increasing β angle. The presence of the inclined rock face would decrease the active earth pressure acting on the wall to a value lower than Coulomb's estimation. In equation 6.1, if the driving force on the wall is reduced, and the resisting force remained the same, the F.S. against sliding would increase.

The intrusion of the inclined rock face would actually increase the FS against sliding of the wall. In other words, the evaluation of F.S. against sliding with Coulomb's theory would be on the safe side.

6.6.2 Factor of Safety against Overturning

The Factor of Safety against overturning of the retaining wall is defined as:

$$FS_{overturning} = \frac{\sum \text{Resisting moment}}{\sum \text{Driving moment}} \tag{6.2}$$

The driving moment in equation 6.2 is the product of the horizontal soil thrust $P_{a,h} = K_{a,h} \times 0.5\, rH^2$ and the moment arm h. Fig. 6.85 showed, for β =50°~80°, coefficient $K_{a,h}$ would decrease with increasing β angle. However, Fig. 6.88 showed, for β =50°~90°, the moment arm h increased with increasing β angle. Fig. 6.89 showed the normalized driving moment $K_{a,h} \times \left(h/H\right)$ as a function of the rock face inclination angle β. It is clear that, for the result obtained with both the experimental and analytical methods, for all b = 0, 0.1H, 0.2H, the normalized driving moment would decrease with increasing β angle. In equation 6.2, if the driving moment is reduced, while the resisting moment remained the same, the FS against overturning would increase. The intrusion of an inclined rock face into the active soil wedge would increase the F.S. against overturning of the retaining wall. In other words, the evaluation of F.S. against overturning with Coulomb's theory would also be safe.

Chapter 7

Conclusions

In this study, the effects of a nearby inclined rock face on the active earth against a model retaining wall were investigated. The loose back fill was prepared with the air-pluviation method. Based on the experimental data, the major findings of this study are summarized as follows:

1、 Without the interface plate ($\beta = 0^o$), the active earth pressure coefficient $K_{a,h}$ is in good agreement with Coulomb's solution. The point of application h/H of the active soil thrust is located at about 0.333 H above the base of the wall.

2、 With the approaching of the interface plate, the soil mass behind the wall decreased, the active earth pressure coefficient $K_{a,h}$ decreased with increasing stiff interface inclination angle β or decreasing spacing b.

3、 As the interface angle β increased or spacing b decreased (the rock face approached the wall face), the inclined rock face intruded the active soil wedge, the earth pressure decreased near the base of the wall. This change of earth pressure distribution caused the active thrust to rise to a slightly higher location.

4、 For $\beta = 90°$ (parallel vertical walls), the lateral pressure coefficient was not a constant with depth as assumed by Coulomb and Rankine. The pressure coefficient decreased with depth. It is obvious that, the evaluation of σ_h with Coulomb's and Rankine's theory would be on the safe side.

5、 For all b = 0, b = 0.1H, and b = 0.2H, the horizontal component of active soil thrust $P_{a,h}$ would decrease with increasing β angle. The intrusion of the inclined rock face would actually increase the FS against sliding of the wall. The evaluation of FS against sliding with Coulomb's theory would be on the safe side.

6、 For all b = 0, 0.1H, 0.2H, the normalized driving moment would decrease with

increasing β angle. The intrusion of an inclined rock face into the active soil wedge would increase the F.S. against overturning of the retaining wall. The evaluation of F.S. against overturning with Coulomb's theory would also be safe.

References

1. Ang, A. H., and Tang, W. H., (1975) “Probability Concepts in Engineering Planning and Design Volumn Ⅰ - Basic Principles,” John Wiley and Sons, Inc, New York, N.Y., pp. 286-294.
2. Brinch Hansen, J., (1953), “Earth Pressure Calculation,” Danish Technical Press, Copenhagen.
3. Bros, B., (1972), “The Influence of Model Retaining Wall Displacements on Active and Passive Earth Pressure in Sand,“ Proceedings, 5th European Conference on Soil Mechanics, Vol.1, Madrid, Spain, pp. 241-249.
4. Chen, C. Y., (1995), “Active Earth Pressure with Inclined Backfill,” Master of Engineering Thesis, National Chiao Tung University, Hsinchu, Taiwan.
5. Chang, S. Y., (2000), “Effect of Backfill Density on Active Earth Pressure,” Master of Engineering Thesis, Dept. of of Civil Engineering, National Chiao Tung University, Hsinchu, Taiwan.
6. Chen, H. R., (1997), “Earth Pressure At-Rest with Different Soil Densities and Backfill Inclinations,” Master of Engineering Thesis, National Chiao Tung University, Hsinchu, Taiwan.
7. Chen, T. J., (2003). “Earth Pressures Due to Vibratory Compaction.” Ph.D. dissertation, National Chiao Tung University, Hsinchu, Taiwan.
8. Clough, G. W., and Duncan, J. M., (1971), “Finite Element Analysis of Retaining Wall Behavior,” Journal of Geotechnical Engineering, ASCE, Vol. 87, No. SM12, pp. 1657-1673.
9. Das, B. M., (1994), “ Principal of Geotechnical Engineering,” PWS Publishing Company, Boston.
10. Dubrova, G. A., (1963), “Interaction of Soil and Structures,” Izd. “Rechonoy Transport, ” Moxcow.
11. Fan, C. C., and Chen K. H, (2006), “Earth Pressure of Retaining Walls near

Faces" Master of Engineering Thesis, Department of Construction Engineering, National Kaohsiung First University of Science and Technology, Taiwan.

12. Fan, C. C., and Fang, Y. S., (2009), "Active Earth Pressure on Rigid Retaining Walls Built at Constrained Fill Space." Soils and Foundations, Japanese Geotechnical Society.

13. Fang, Y. S. (1983). "Dynamic Earth Pressures Against Rotating Walls." Ph.D. dissertation, Department of Civil Engineering, University of Washington, Seattle, Washington.

14. Fang, Y. S., and Ishibashi, I., (1986), "Static Earth Pressures with Various Wall Movements," Journal of Geotechnical Engineering, ASCE, Vol. 112, No. 3, Mar., pp. 317-333.

15. Fang, Y. S., Cheng F. P., Cheng, R. T., and Fan, C. C., (1993), "Earth Pressure under General Wall Movements," Geotechnical Engineering, SEAGS, Vol. 24, No. 2, December., pp. 113-131.(NSC 77-0101-E-009-06)

16. Fang Y. S., Chen, T. J., and Wu, B. F.,d (1994), "Passive Earth Pressure with Various Wall Movements," Journal of Geotechnical Engineering, Vol. 120, No. 8, Aug., pp. 1307-1323.

17. Fang, Y. S., Chen, J. J., Holtz, R. D., and Lee, W. F. (2004), "Reduction of Boundary Friction in Model Tests.", ASTM Geotechnical Testing Journal, 27(1), 1-10.

18. Frydman. S., and Keissar, I. (1987). "Earth Pressure on Retaining Walls near Rock Faces." Journal of Geotechnical Engineering, ASCE, 113(6), 586-599

19. Ho, Y. C., (1999), "Effects of Backfill Compaction on Passive Earth Pressure," Master of Engineering Thesis, National Chaio Tung University, Hsinchu, Taiwan.

20. Hou. P. H., (2006) "Design and Construction of NCTU KA Model Retaining Wall" Master of Engineering Thesis, National Chiao Tung University, Hsinchu, Taiwan.

21. Ishibashi, I., and Fang, Y. S., (1987), "Dynamic Earth Pressures with Different

Wall Movements Modes," Soils and Foundations, Japanese Society of Soil Mechanics and Foundations Engineering, Vol. 27, No. 4, Dec., pp. 11-22.

22. Ichihara, M., and Matsuzawa, H., (1973), "Earth Pressure during Earthquake," Soils and Foundations, Japanese Society of Soil Mechanics and Foundations Engineering, Vol. 13, No. 4, Dec., pp. 75-86.

23. Janbu, N., (1957), "Earth Pressure and Bearing Capacity Calculation by Gerneral Procedure of Slices," Proceedings, 4th Int. Conf. Soil Mechs. Found. Eng., 2, pp. 207-212.

24. Janssen, H. A., (1895), "Versuche uber Getreidedruck in Silozenllen," Aeitschrift, Verein Deutscher Ingenieure, 39: 1045-1049. (Partial English Translation in Proceedings of Institute of Civil Engineers, London, England, 1896)

25. Lee, C. C., (1998), "Passive Earth Pressure with Various Backfill Densities," Master of Engineering Thesis, National Chiao Tung University, Hsinchu, Taiwan.

26. Leshchinsky, D., Hu, Y.,and Han, J. (2003). "Limited reinforced space in segmental retaining walls."Geotextiles and Geomembranes, 22(6),543-553.

27. Lo Presti, D. C. F., Pedroni, S., and Crippa, V. (1992). "Maximum dry density of cohesionless soils by pluviation and by ASTM D 4253-83 : A comparative study." ASTM Geotechnical Testing Journal, 15(2),180-189.

28. Mackey, R. D., and Kirk, D. P., (1967), "At Rest, Active and Passive Earth Pressures," Proceedings, South East Asian Conference on Soil Mechanics and Foundation Engineering, Bangkok, pp. 187-199.

29. Morgenstern, N. R., and Eisenstein, Z., (1970), "Methods of Estimating Lateral Loads and Deformations," Proceedings, ASCE Specialty Conference on Lateral Stresses in the Ground and the Design of Earth Retaining Structures, Cornell University, pp. 51-102.

30. Nakai, (1985), "Finite Element Computions for Active and Passive Earth Pressure Problems of Retaining Wall," Soils and Foundations, JSSMFE, Vol. 25,

No. 3, pp. 98-112.

31. NAVFAC DM-7.2, (1982)

32. PLAXIS BV. (2002): User's manual of PLAXIS, Published by A.A. Balkema Publishers.

33. Potts, D. M., and Fourie, A. B., (1986), "A Numerical Study of the Effects of Wall Deformation on Earth Pressures," Int. Numer. Anal. Methods Geometh., Vol. 10, pp. 383-405.

34. Rad, N.S., and Tumay, M. T. (1987). "Factors affecting sand specimen preparation by raining." ASTM Geotechnical Testing Journal, 10(1), 31-37.

35. Rowe, P. W., and Barden, L. (1964). "Importance of Free Ends in Triaxial Testing." Journal of the Soil Mechanics and Foundations Division, ASCE, 90(SM1), 1-77.

36. Sherif, M. A., Ishibashi, I., and Lee, C. D., (1981),"Dynamic Earth Pressure Against Retaining Structures," Soil Engineering Research Report, No. 21, January, Univ. Washington, American.

37. Sherif, M. A., Fang, Y. S., and Sherif, R. I., (1984), "Ka and Ko behind Rotating and Non-Yielding Walls," Journal of Geotechnical Engineering, ASCE, Vol. 110, No. 1, Jan., pp. 41-56.

38. Sowers, G. F. (1979), "Introductory Soil Mechanics and Foudations"

39. Spangler, M.C and Handy, R.L. (1984):Soil Engineering, Harper and Row, New York.

40. Take, W. A. and Valsangker, A. J. (2001)."Earth pressures on unyielding retaining walls of narrow backfill width." Canadian Geotechnical Journal, 38, 1220-1230.

41. Tatsuoka, F., and Haibara, O., (1985), "Shear Resistance between Sand and Smooth or Lubricated Surface," Soils and Foundations, JSSMFE, Vol. 25, No. 1, Mar., pp. 89-98.

42. Tatsuoka, F., Molenkamp, F., Torii, T., and Hino, T. (1984). "Behavior of

Lubrication Layers of Platens in Element Tests." *Soils and Foundations*, Japanese Society of Soil Mechanics and Foundation Engineering, 24(1), 113-128.

43. Tejchman, J., and Wu, W., (1995) "Experimental and Numerical Study of Sand-Steel Interfaces", International Journal for Numerical and Analytical Methods in Geotechanics, Vol. 19, No. 8, pp.513-536

44. Terzaghi, K., (1932), "Record Earth Pressure Testing Mechine," Engineering News-Record, Vol. 109, Sept., 29, pp. 365-369.

45. Terzaghi, K., (1941), "General Wedge Theory of Earth Pressure," ASCE Transaction, Vol. 106, pp. 68-80.

46. Terzaghi, K., and Peck, R. B.,(1967), Soil Mechanics in Engineering Practice,Wiley, New York.

47. Wang, F. J., (2005), "Effects of Ajacent Rock Face Inclination on Earth Pressure At-Rest," Master of Engineering Thesis, National Chiao Tung University, Hsinchu, Taiwan.

48. Wu, B. F., (1992), "Design and Construction of National Chiao Tung University Model Retaining Wall," Master of Engineering Thesis, National Chiao Tung University, Hsinchu, Taiwan.

49. Zheng, Y. C., (2008) "Active Earth Pressure on Retaining Walls with Intrusion of a Stiff Interface into Backfill," Master of Engineering Thesis, National Chiao Tung University, Hsinchu, Taiwan.

Table 2.1. Comparison of experimental and theoretical values
(after Mackey and Kirk, 1967)

Theories	Active Pressure Coefficient					
	Sand 1		Sand 2		Sand 3	
	Loose	Dense	Loose	Dense	Loose	Dense
Coulomb	0.25	0.13	0.22	0.14	0.19	0.13
Rankine	0.26	0.13	0.24	0.14	0.19	0.13
Krey(ϕ circle)	0.26	0.21	0.25	0.21	0.21	0.19
Ohde	0.26	0.21	0.25	0.21	0.21	0.19
Caquot and Kerisel	0.25	0.13	0.23	0.14	0.19	0.13
Janbu	0.27	0.12	0.22	0.13	0.18	0.13
Rowe	0.21	0.16	0.21	0.16	0.21	0.16
Experimental	**0.22**	**0.32**	**0.19**	**0.29**	**0.17**	**0.27**

Table 2.2. Wall displacements required to reach an active state

Investigator	Soil Type	Type of Wall Movement	Max. Wall Displacement Required
Mackey and Kirk (1967)	Loose Sand	T mode	0.00400 H
Bros (1972)	Sand	T mode	0.00060 H
Fang and Ishibashi (1986)	Loose Sand	T mode	0.00025 H
Fang et al. (1997)	Loose Sand	T mode	0.00150 H
This study (2009)	Loose Sand	T mode	0.00400 H

Note: T = Translation; and H = Wall height

Table 6.1 Earth pressure experiments for loose sand with different interface inclination angle β and spacing b

Spacing, b (mm)	Interface Inclination Angle, β	Test No.
b = 0	β = 0°	1215-3
		1229-3
	β = 50°	0820-1
		0820-3
	β = 60°	0818-1
		0818-2
	β = 70°	0817-2
		0817-5
	β = 80°	0819-1
		0819-2
b = 50	β = 50°	0126-1
		0126-2
	β = 60°	0223-1
		0223-3
	β = 70°	0302-3
		0302-5
	β = 80°	0308-4
		0309-1
	β = 90°	0511-2
		0512-1
b = 100	β = 50°	0401-1
		0401-3
	β = 60°	0406-3
		0414-2
	β = 70°	0421-1
		0421-3
	β = 80°	0427-1
		0429-4
	β = 90°	0504-1
		0504-2

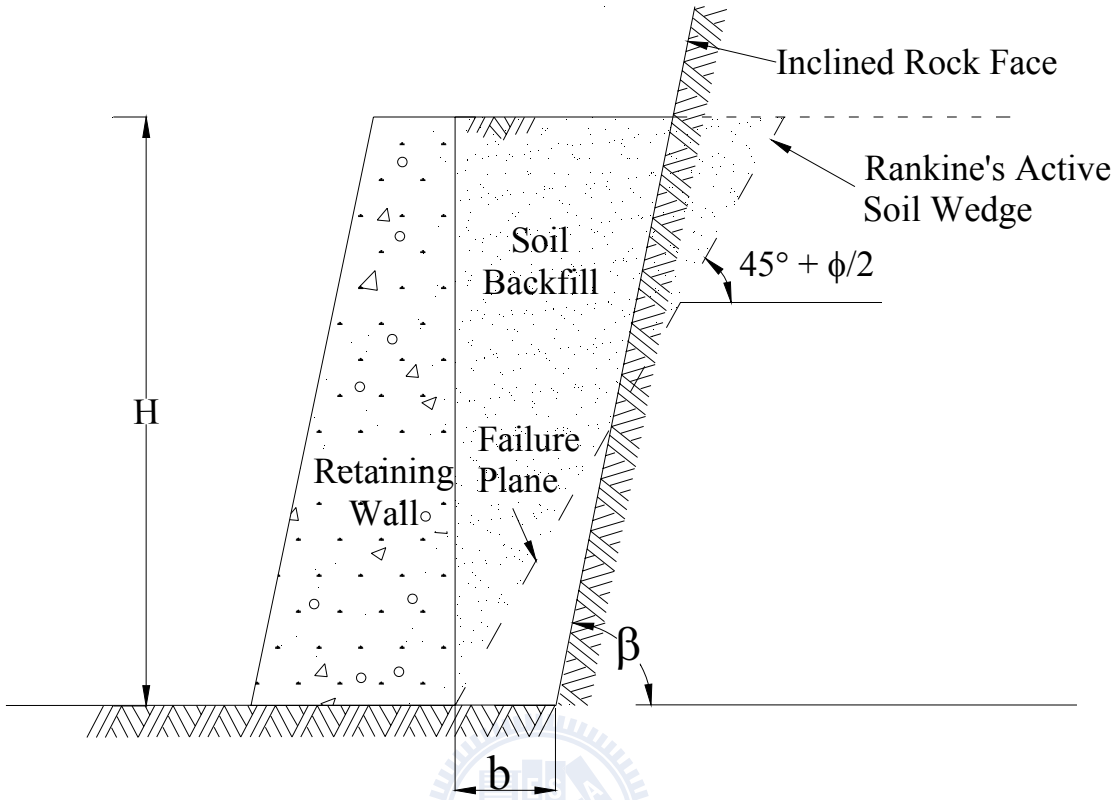

Fig. 1.1. Retaining walls with intrusion of a rock face into backfill

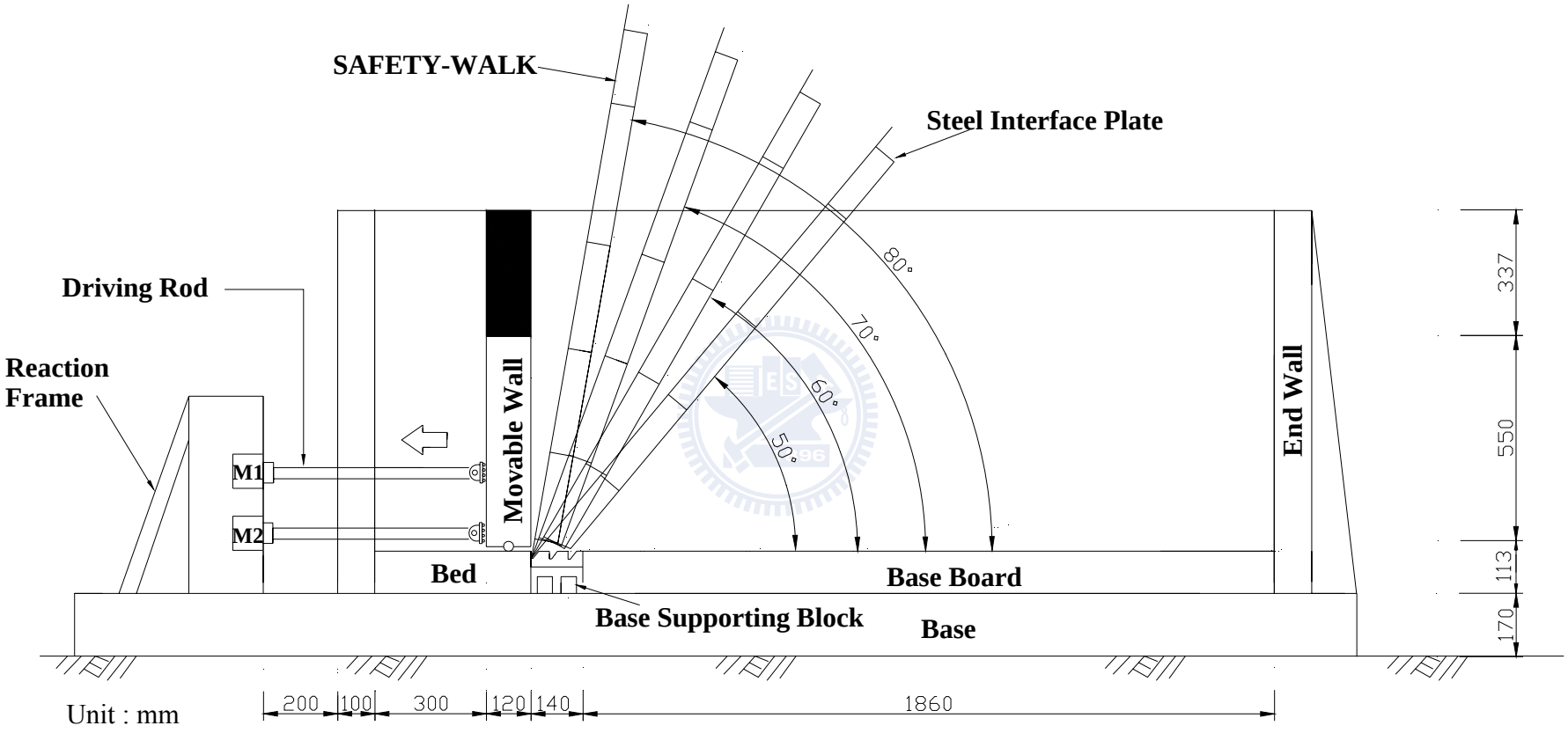

Fig. 1.2. Different interface inclinations for b = 0

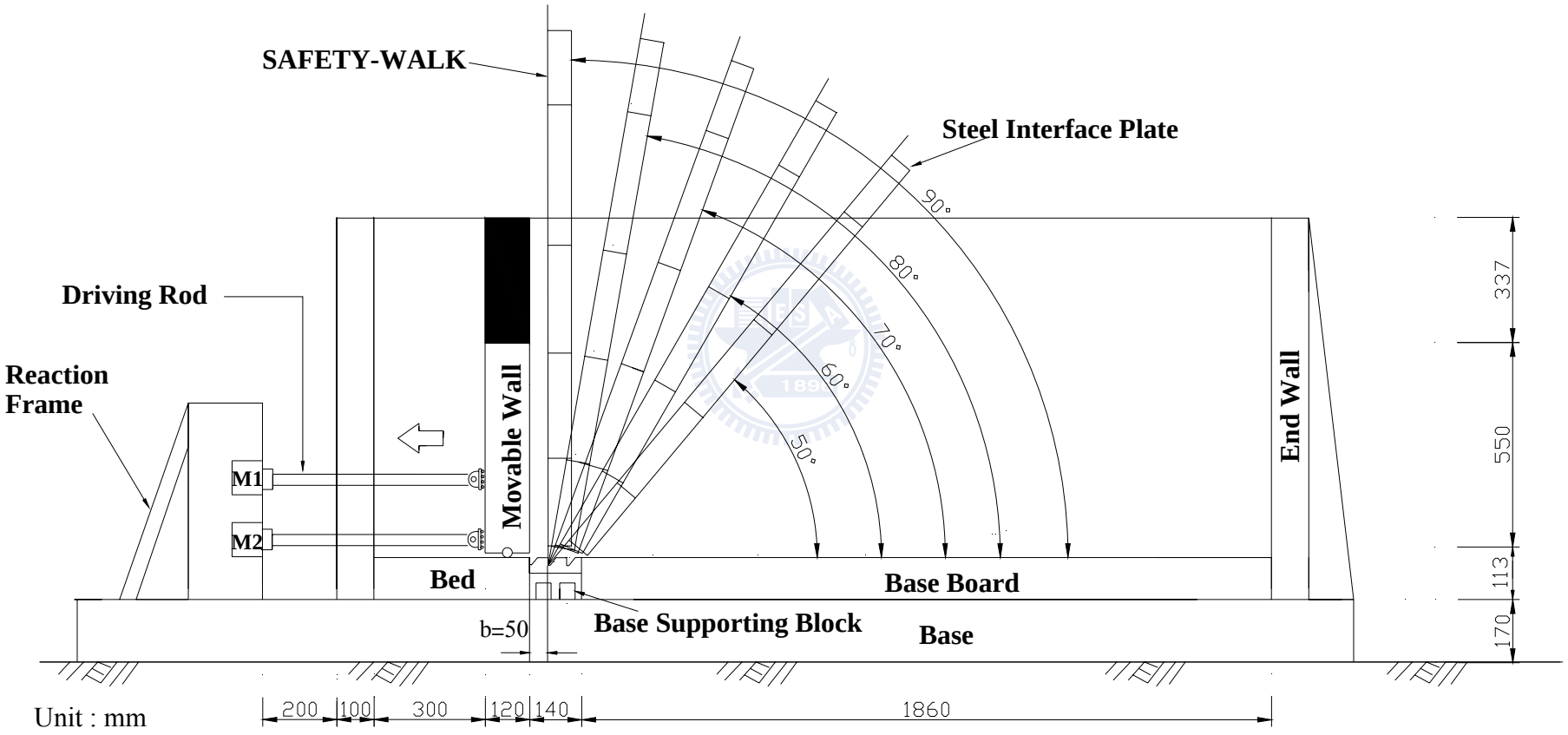

Fig. 1.3. Different interface inclinations for b = 50 mm

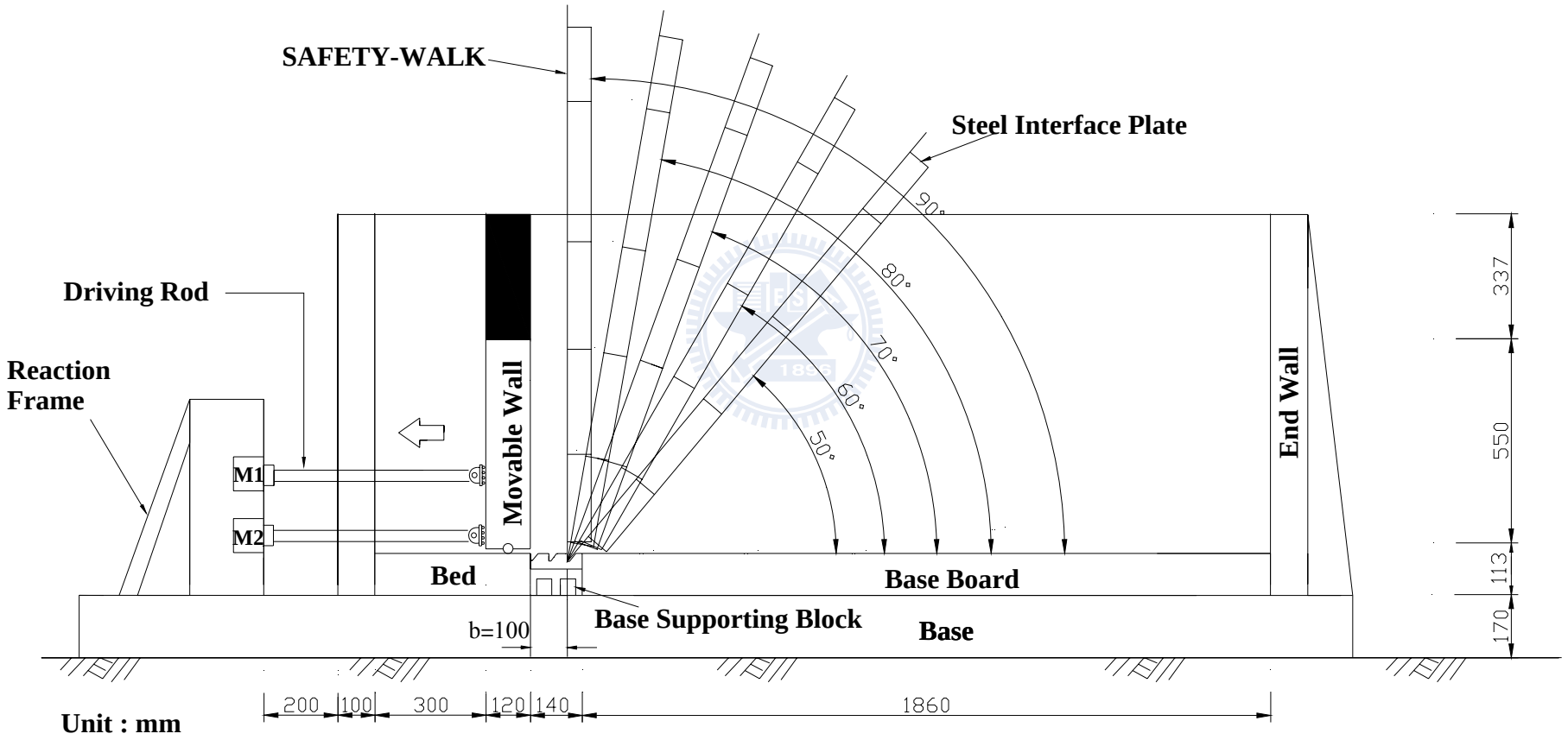

Fig. 1.4. Different interface inclinations for b = 100 mm

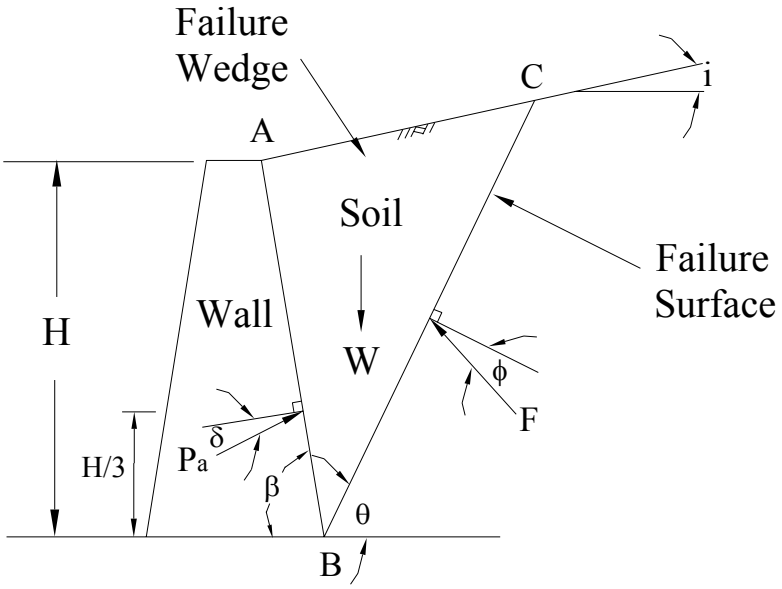

(a)

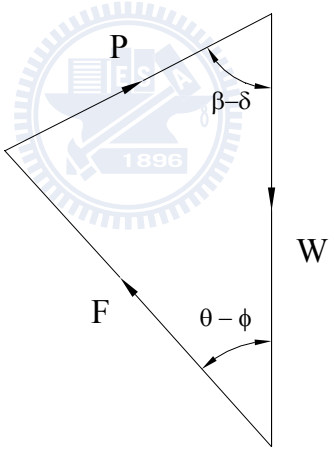

(b)

Fig. 2.1. Coulomb's theory of active earth pressure

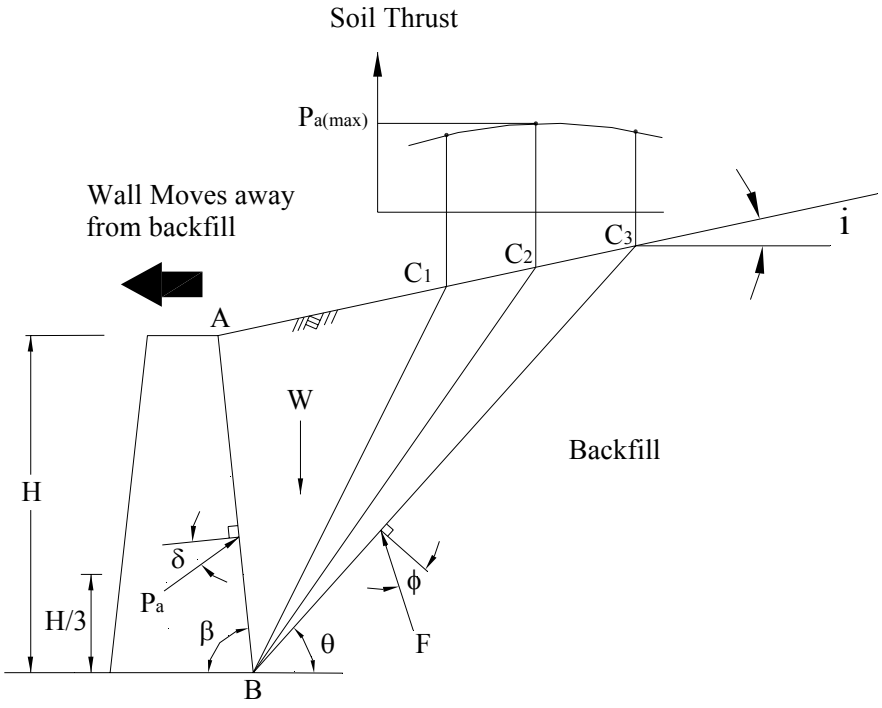

Fig. 2.2. Coulomb's active pressure determination

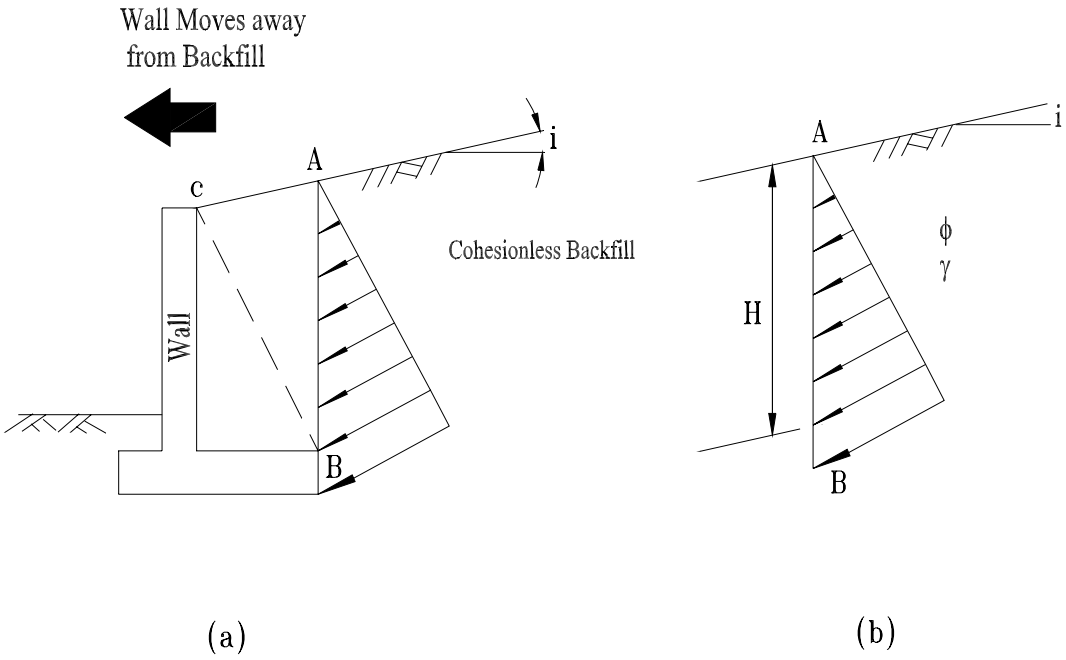

Fig. 2.3. Rankine's theory of active earth pressure

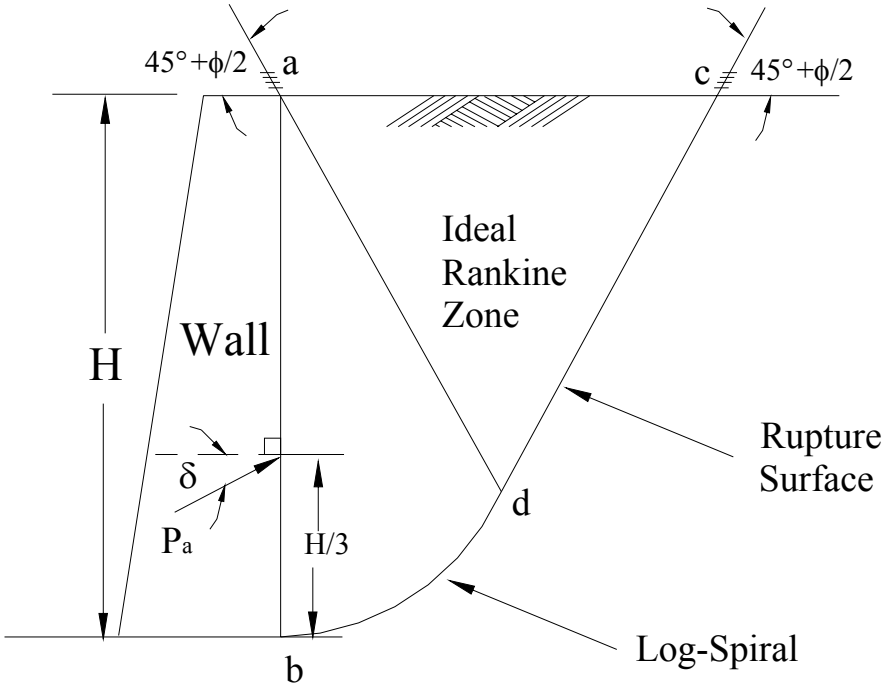

Fig. 2.4. Failure surface in soil by Terzaghi's log-spiral method

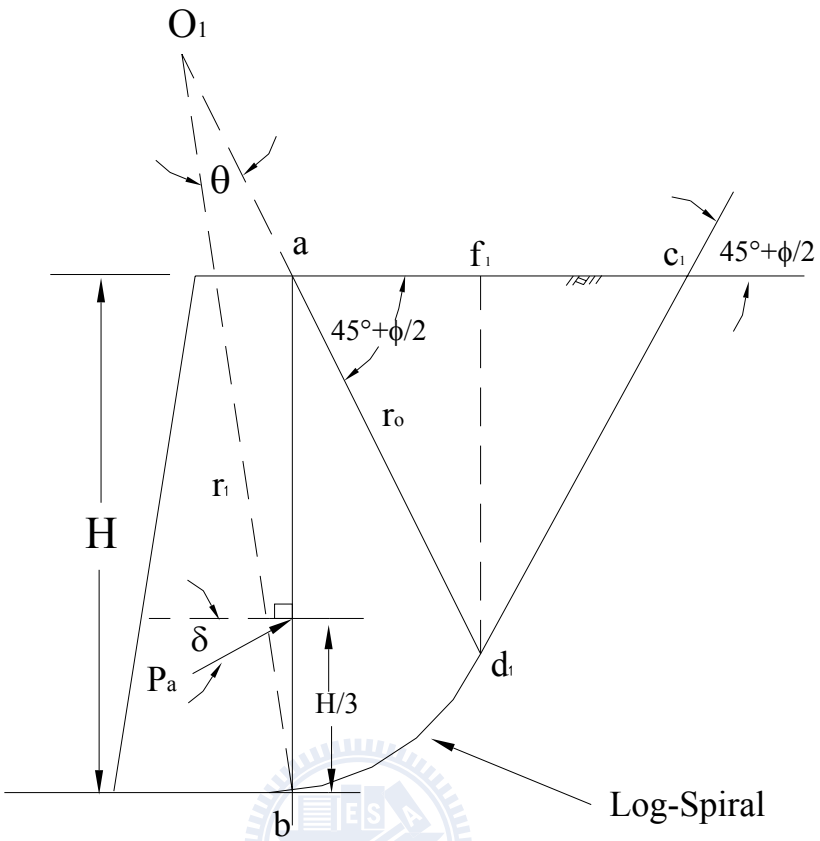

Fig. 2.5. Evaluation of active earth pressure by trial wedge method

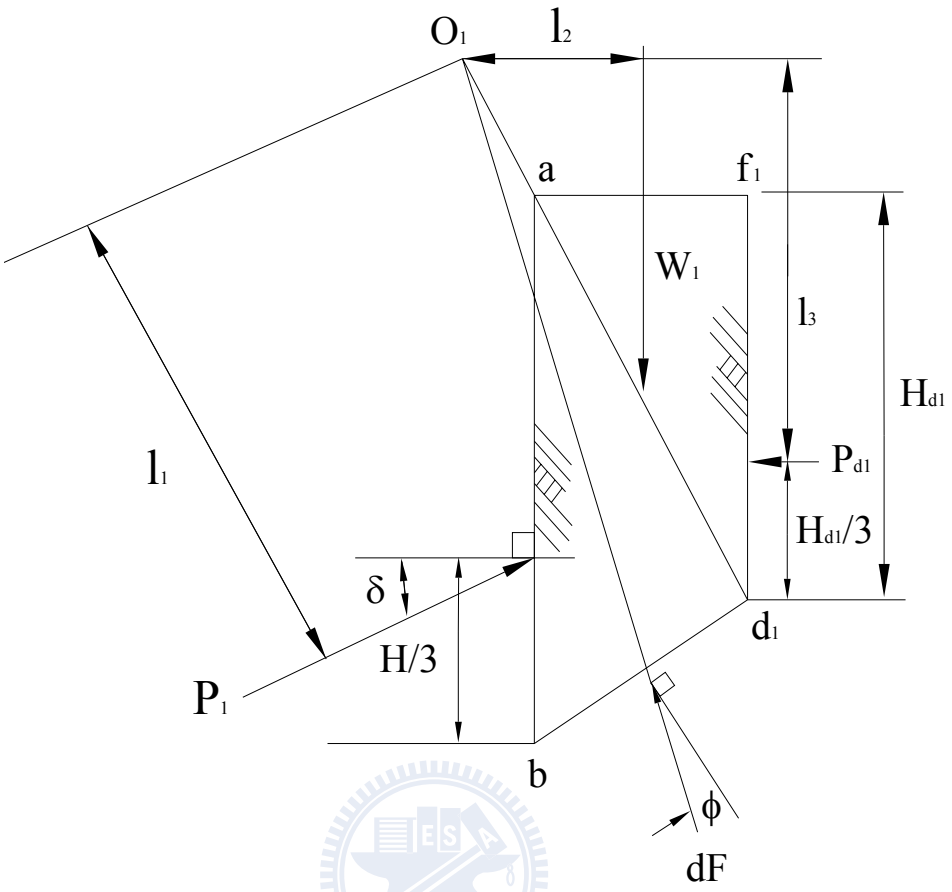

Fig. 2.6 Stability of soil mass abd_1f_1

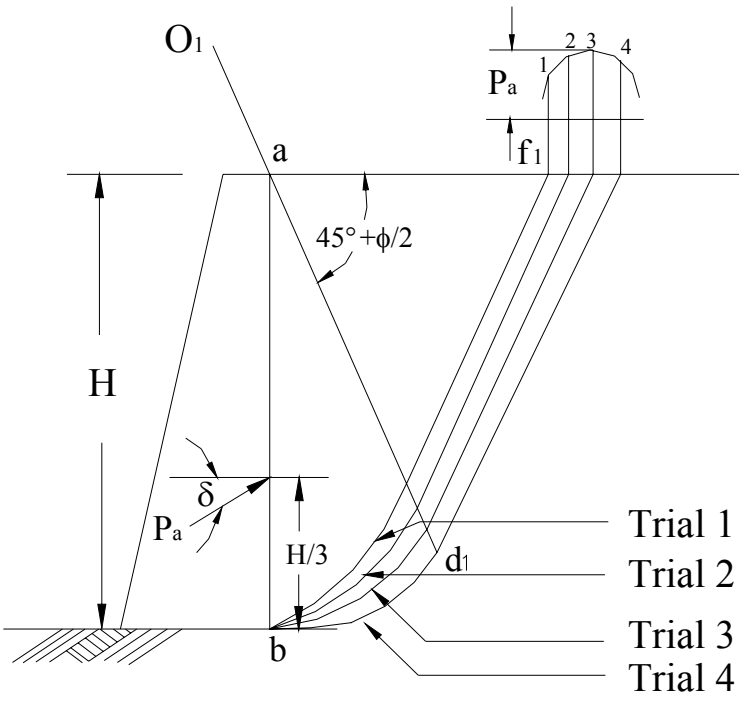

Fig. 2.7. Active earth pressure determination with Terzaghi's log-sprial failure surfaces

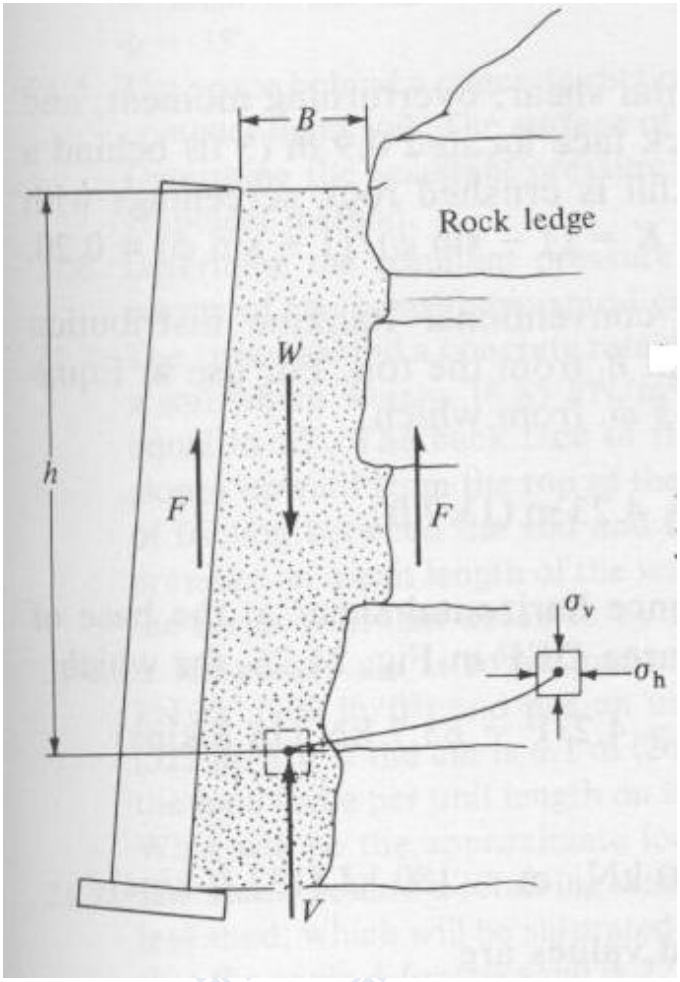

Fig. 2.8. Fascia retaining wall of backfill width B and wall friction F (after Spangler and Handy, 1984)

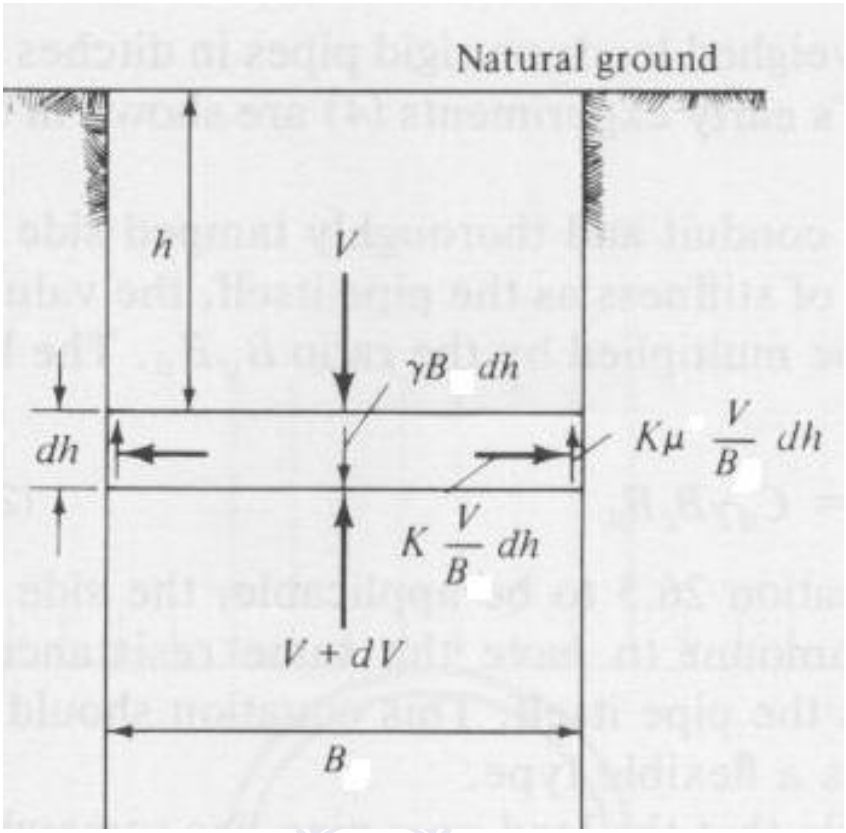

Fig. 2.9. Horizontal element of backfill material
(after Spangler and Handy, 1984)

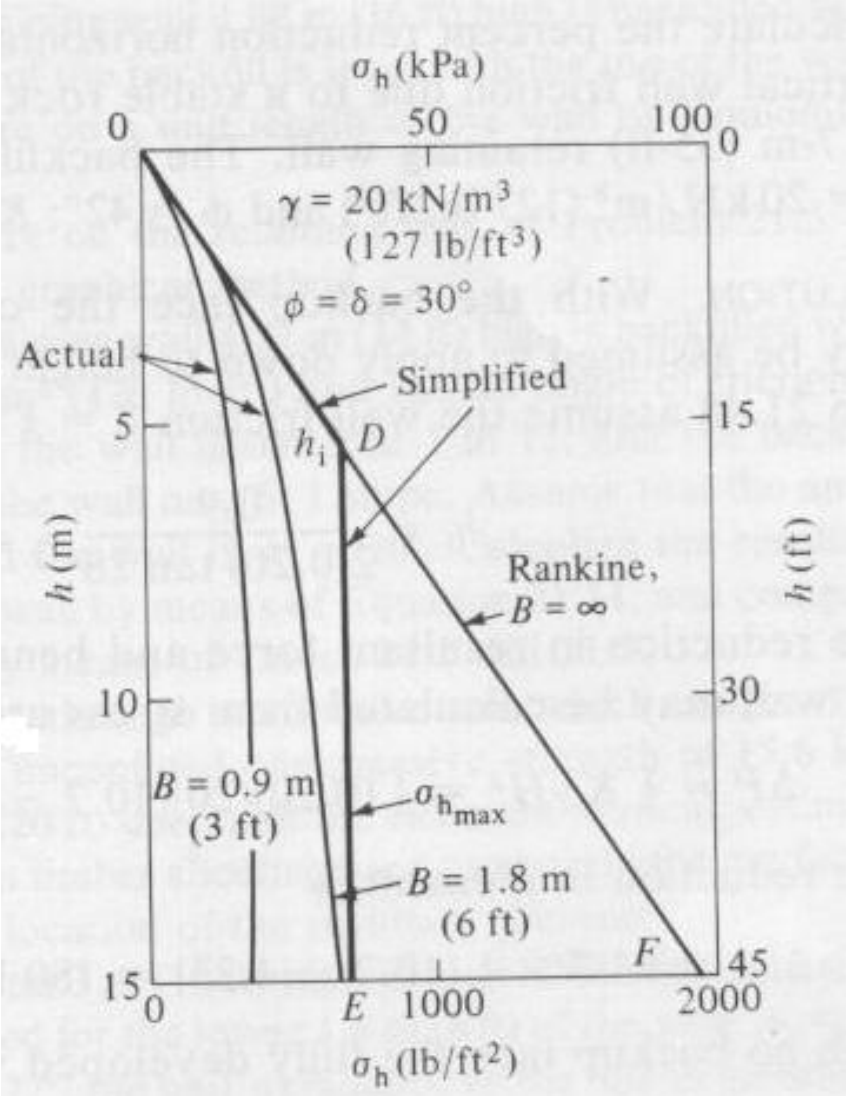

Fig. 2.10. Distribution of soil pressure against fascia walls due to partial support from wall friction F (after Spangler and Handy, 1984)

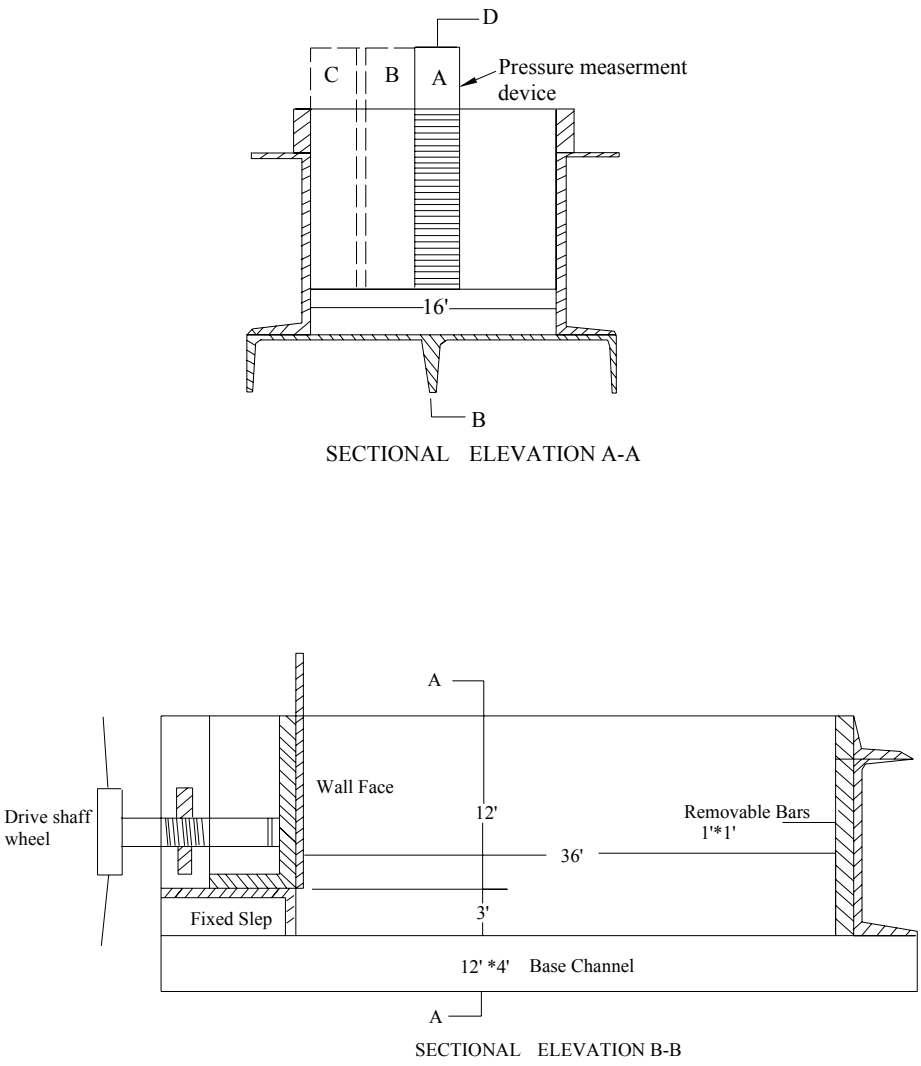

Fig. 2.11. University of Manchester model retaining wall
(after Mackey and Kirk, 1967)

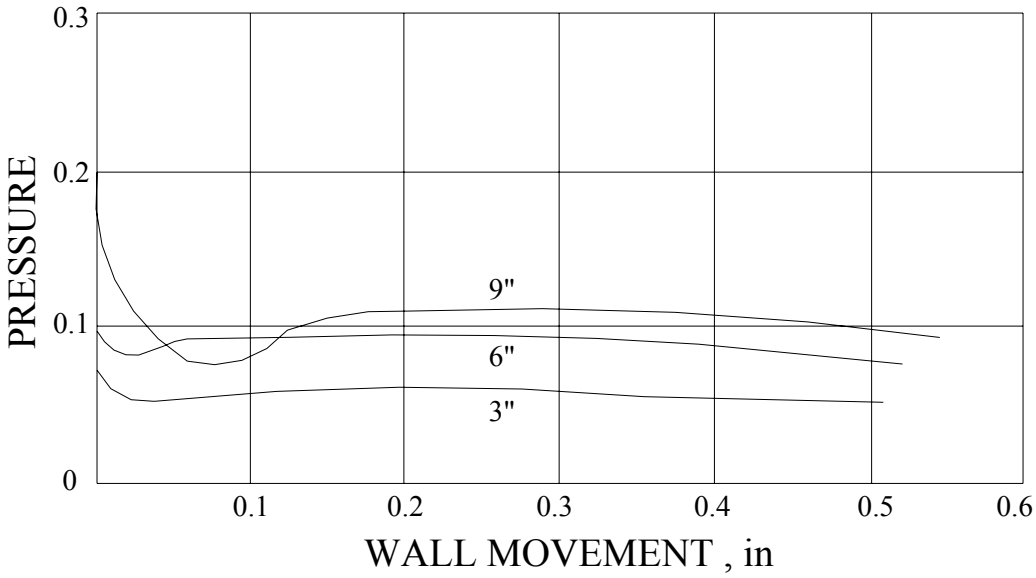

Fig. 2.12. Earth pressure with wall movement (after Mackey and Kirk, 1967)

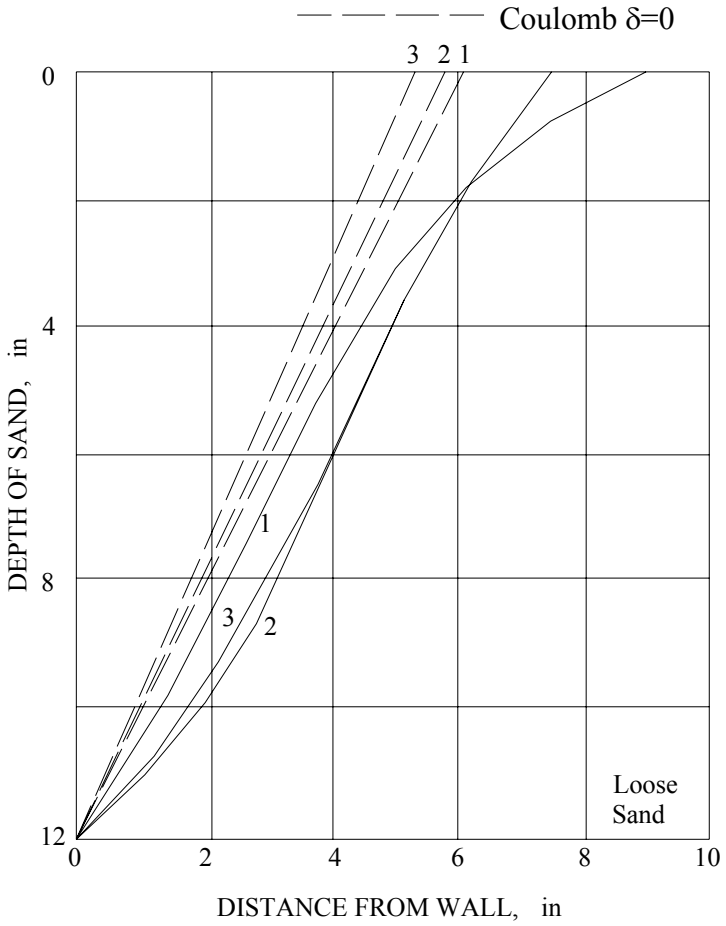

Sand 1: A uniformly graded fine sand
Sand 2: A medium graded sand
Sand 3: A uniformly graded coarse sand

Fig. 2.13. Failure surfaces (after Mackey and Kirk, 1967)

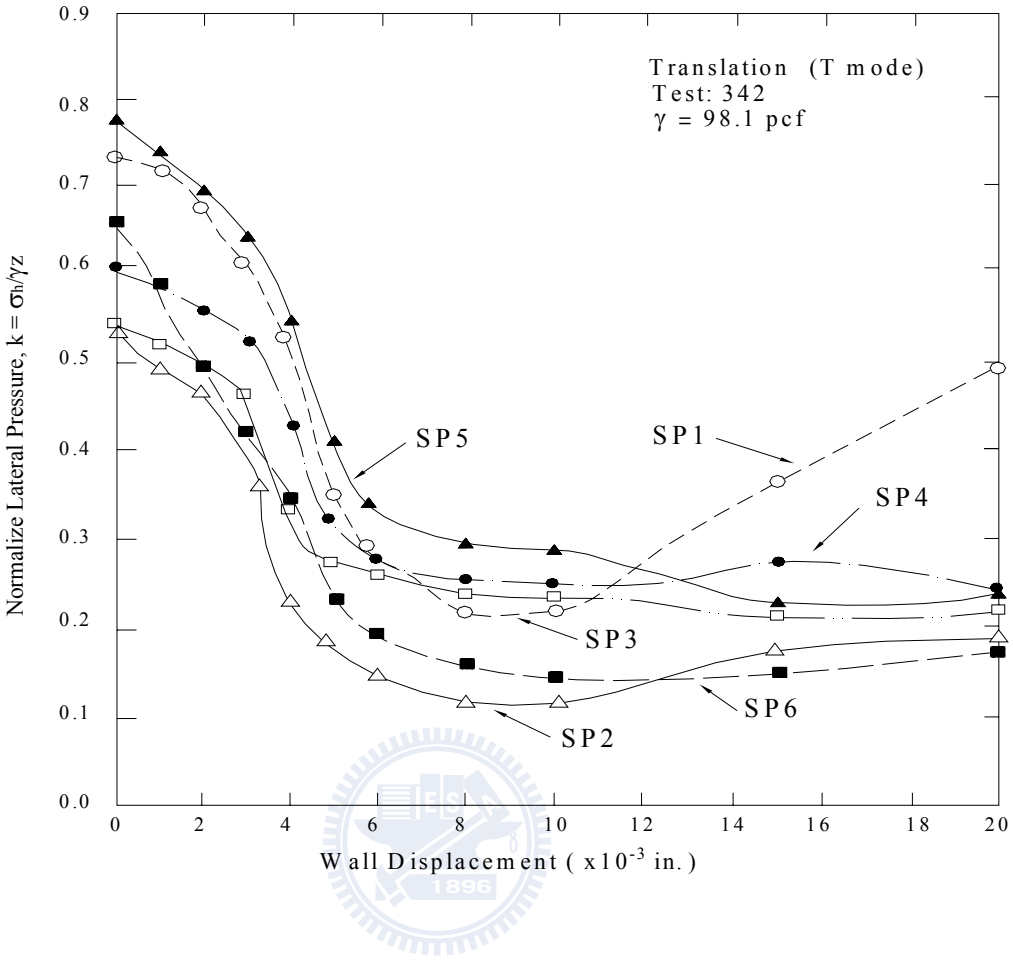

Fig. 2.14. Change of normalized lateral pressure with translation wall displacement (after Fang and Ishibashi, 1986)

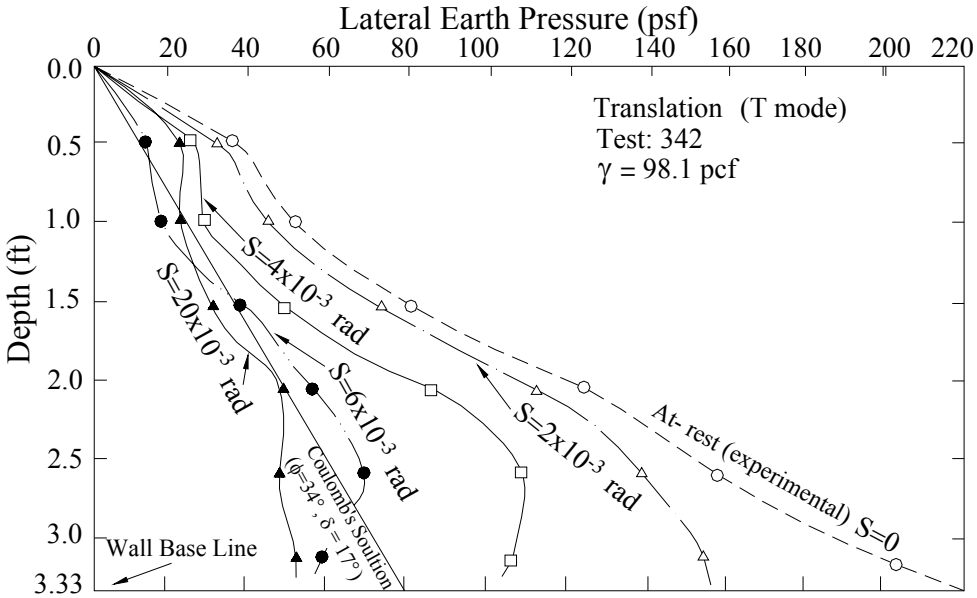

Fig. 2.15. Distributions of horizontal earth pressure at different wall displacement (after Fang and Ishibashi, 1986)

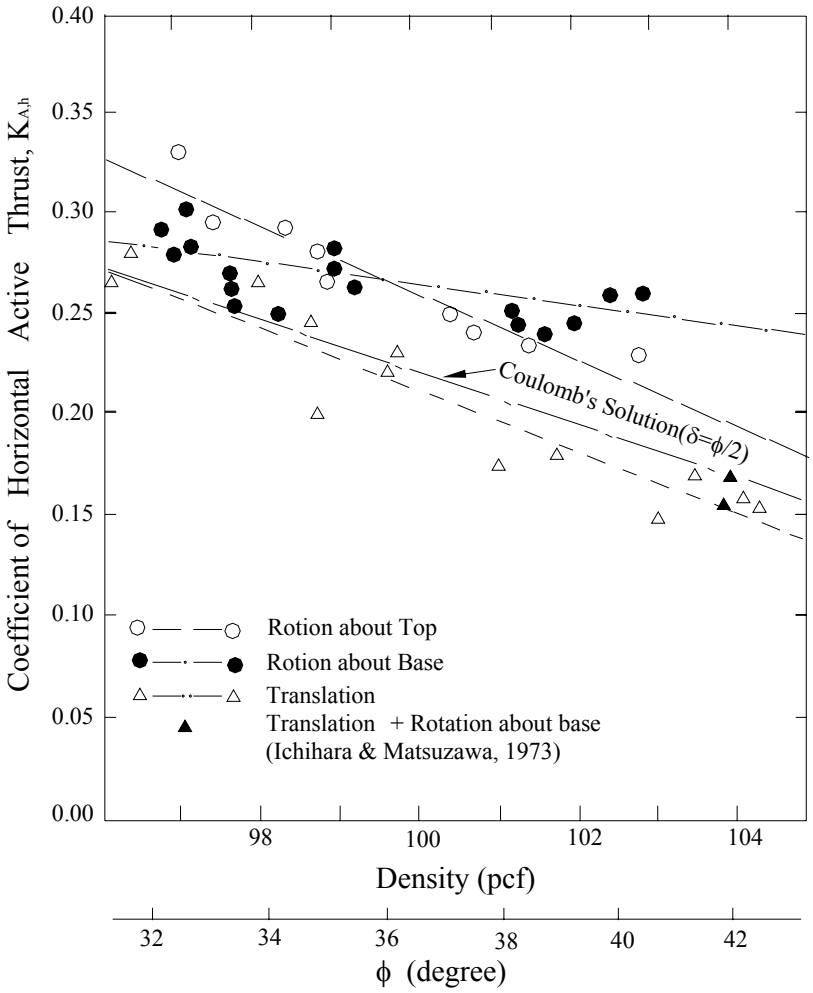

Fig. 2.16. Coefficient of horizontal active thrust as a function of soil density (after Fang and Ishibashi, 1986)

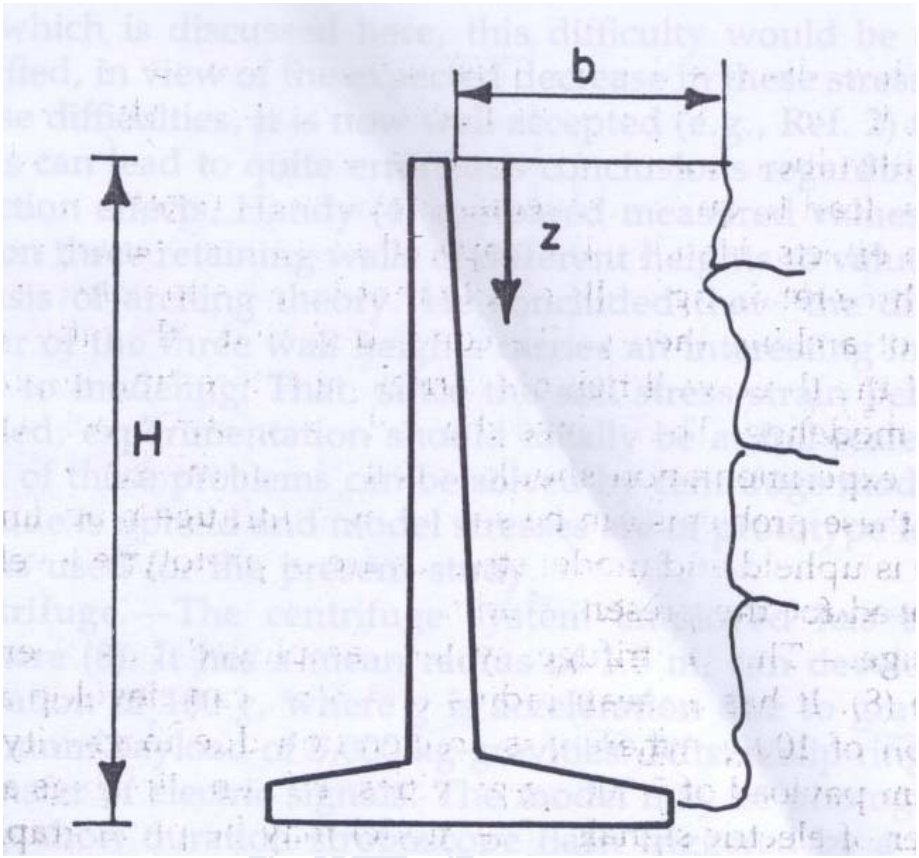

Fig. 2.17 Schematic representation of retaining wall near rock face
(after Frydman and Keissar, 1987)

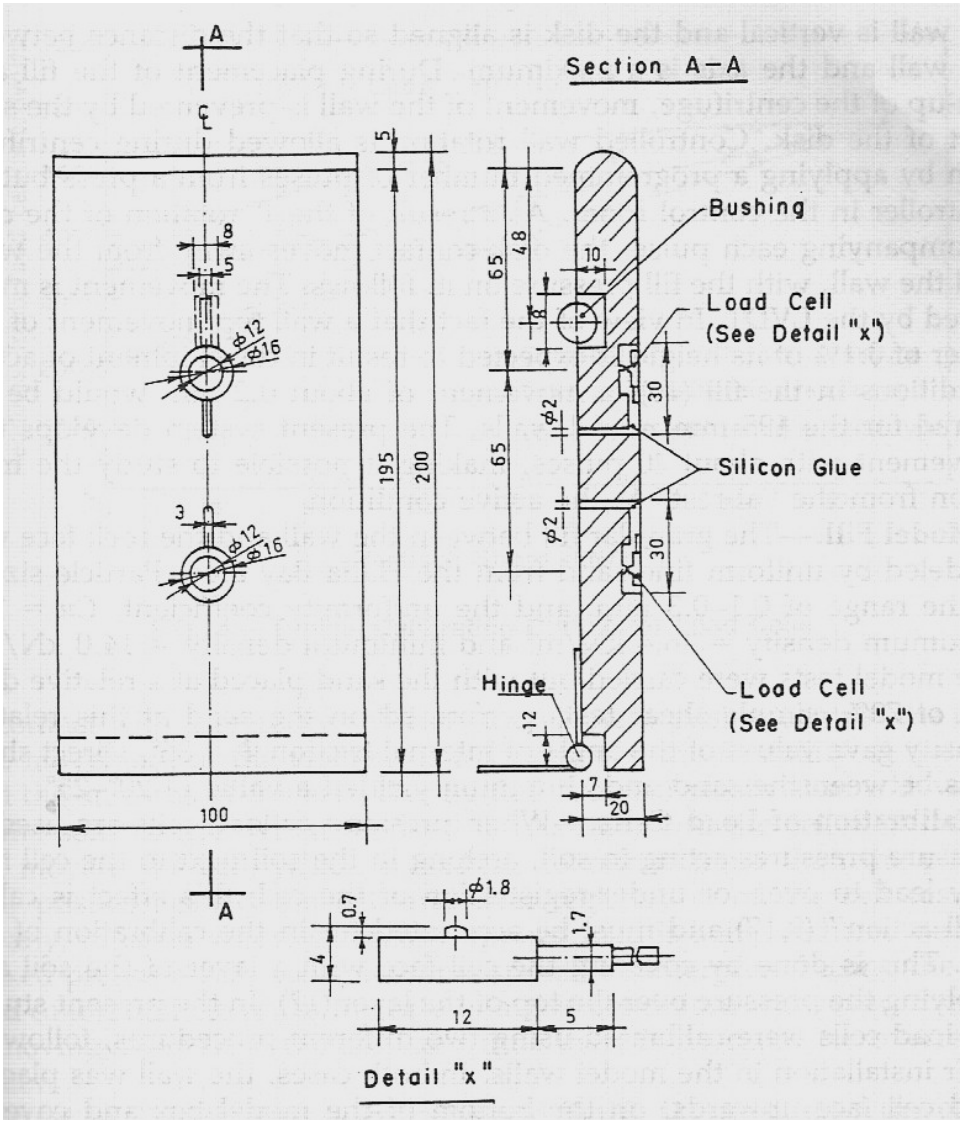

Fig. 2.18. Model retaining wall (after Frydman and Keissar, 1987)

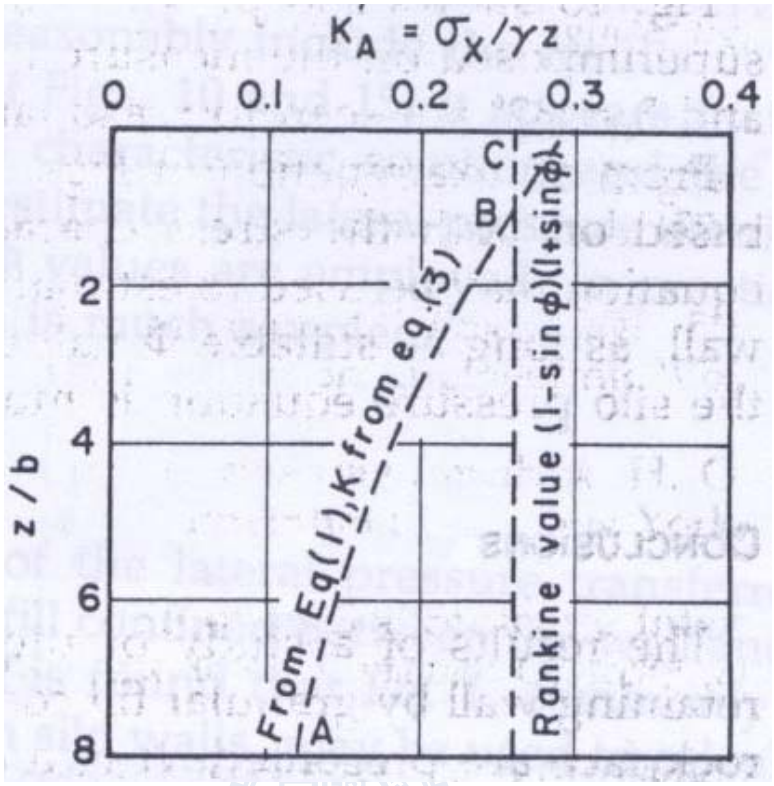

Fig. 2.19. Distribution of K'_a with z/b from silo pressure equation (after Frydman and Keissar, 1987)

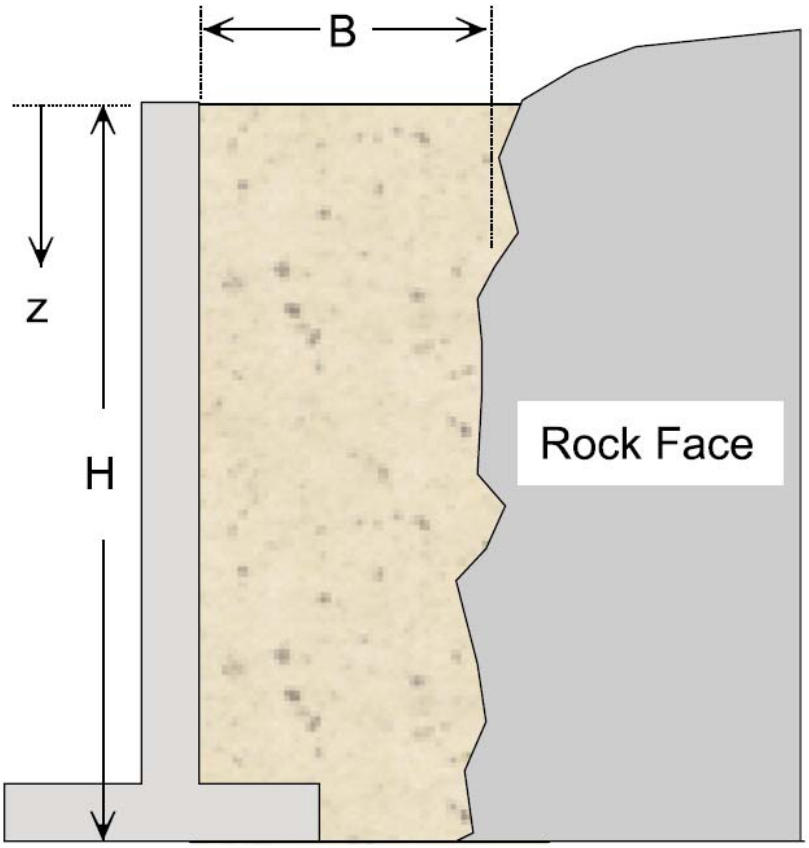

Fig. 2.20. Fascia retaining wall of backfill width, B, and height, H.
(after Take and Valsangkar, 2001)

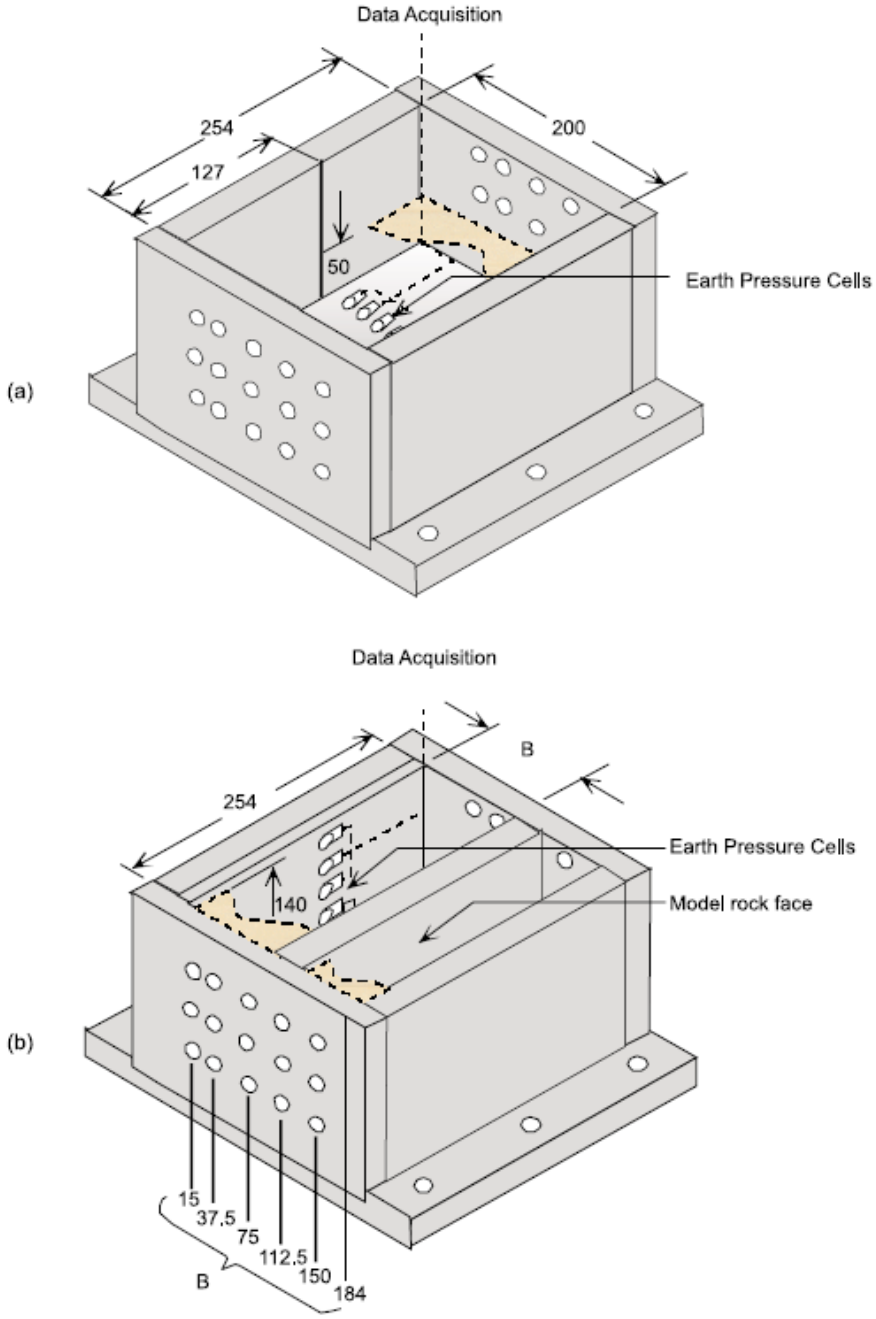

Fig. 2.21. Orientation of earth pressure cells during (a) calibration and (b) fascia wall experiments (after Take and Valsangkar, 2001)

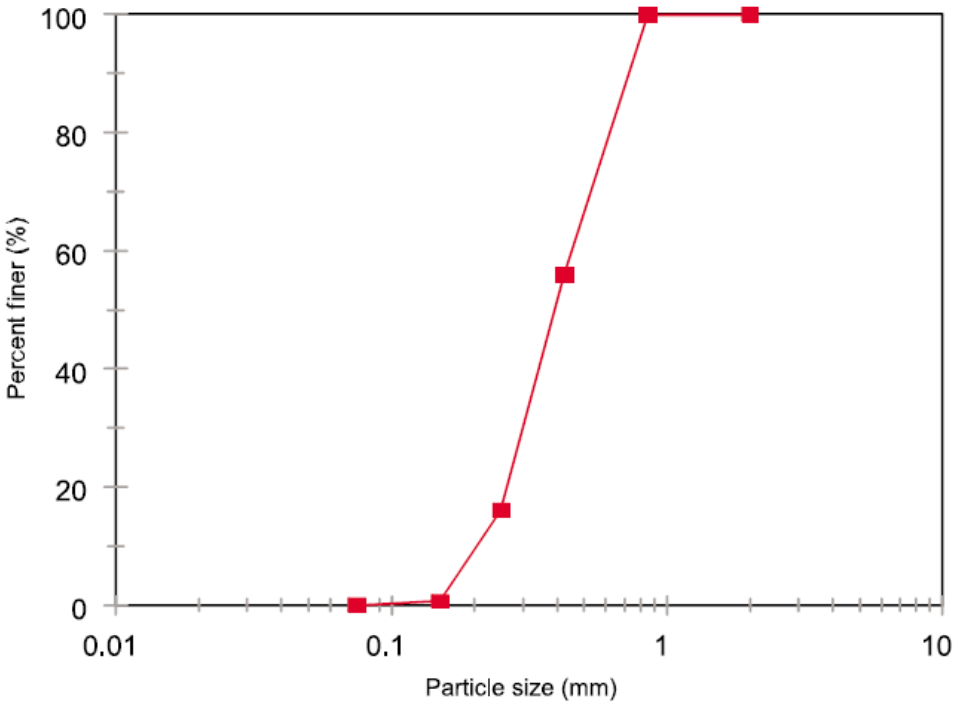

Fig. 2.22. Particle-size distribution of model backfill material (after Take and Valsangkar, 2001)

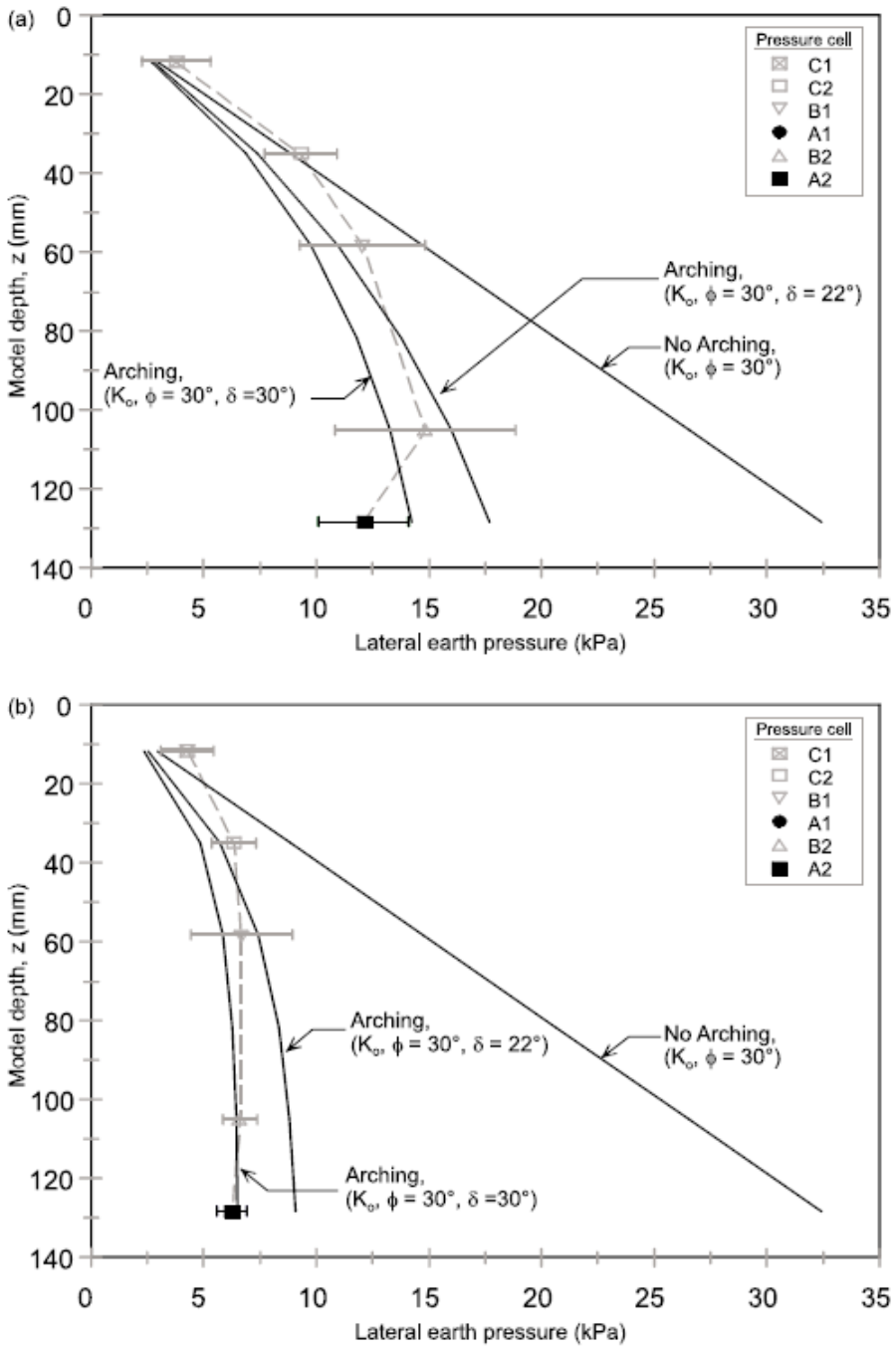

Fig. 2.23. Mean measured earth pressures on model retaining wall backfilled with loose sand to widths of (a) 38 mm (b) 15 mm (after Take and Valsangkar, 2001)

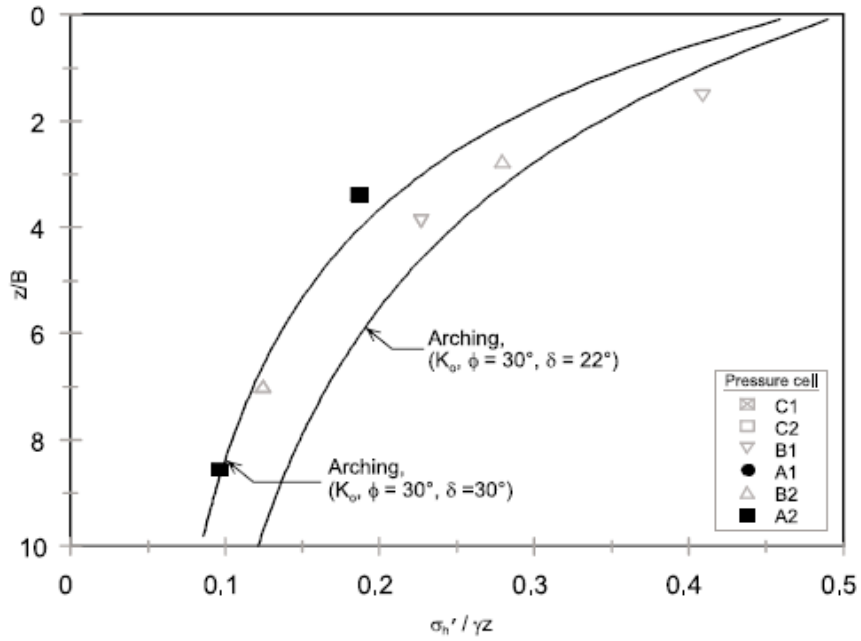

Fig. 2.24. Observed reduction in lateral earth pressure with ratio z/B (loose backfill) (after Take and Valsangkar, 2001)

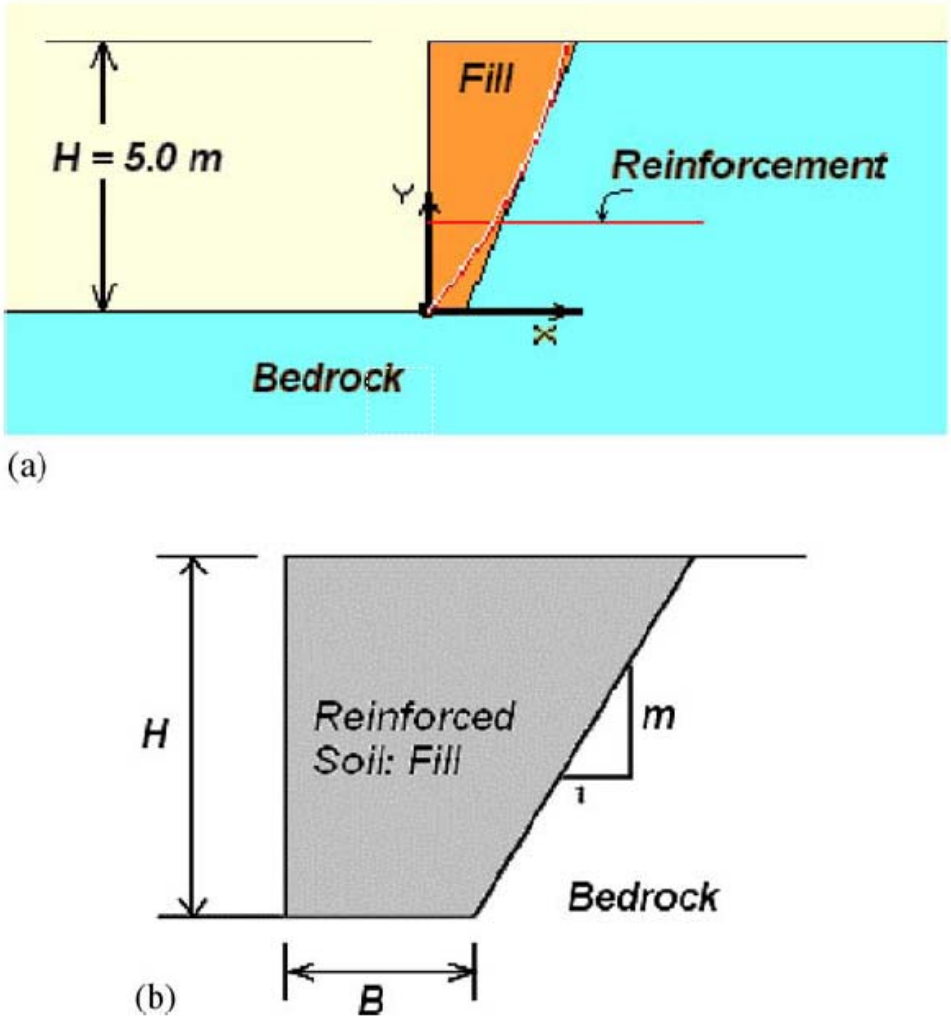

Fig. 2.25. Typical geometry: (a) analyzed (b) notation
(after Leshchinsky, et al. 2004)

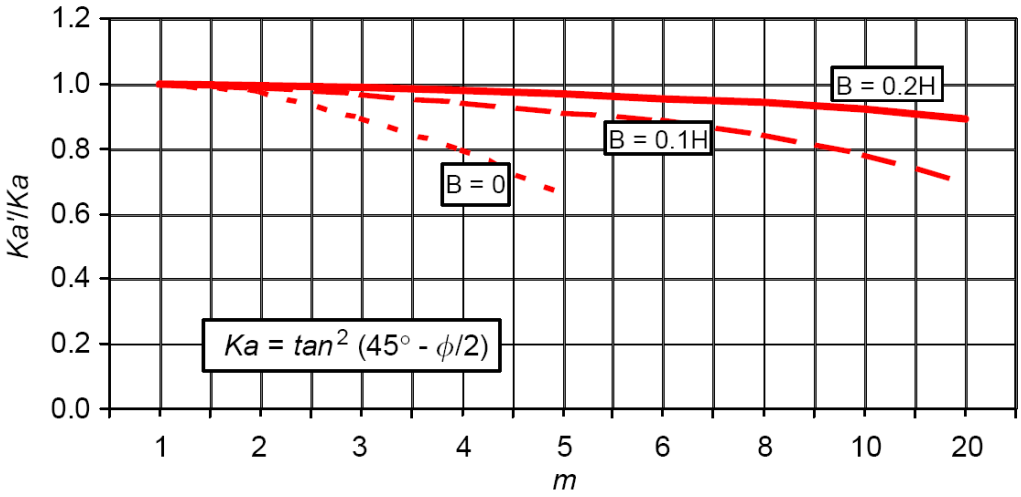

Fig. 2.26. Analysis results (after Leshchinsky, et al. 2004)

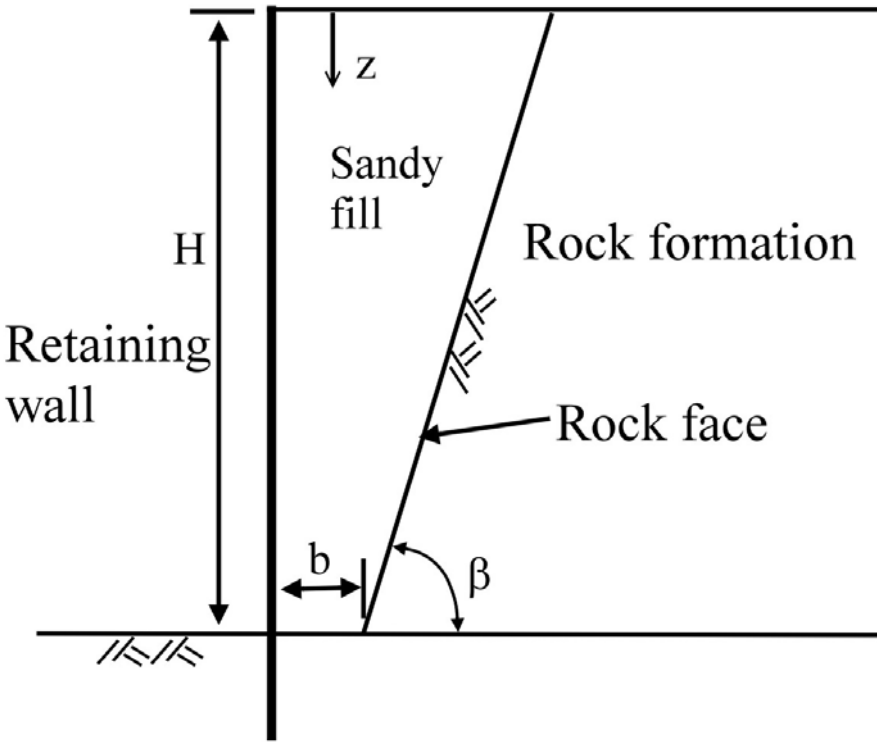

Fig. 2.27. Typical geometry of backfill zone behind a retaining wall used in this study (after Fan and Fang, 2009)

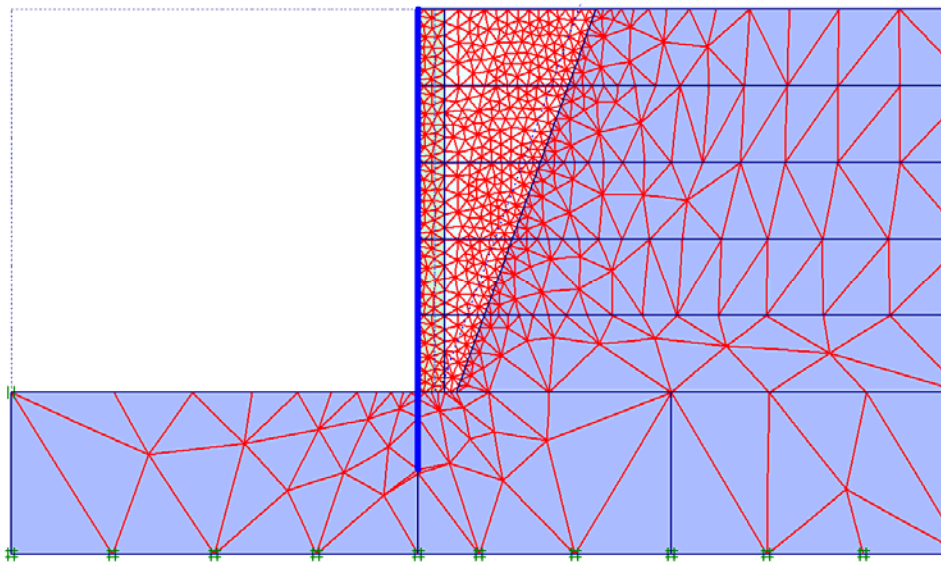

Fig. 2.28. The finite element mesh for a retaining wall with limited backfill space (β=70° and b=0.5m)(after Fan and Fang, 2009)

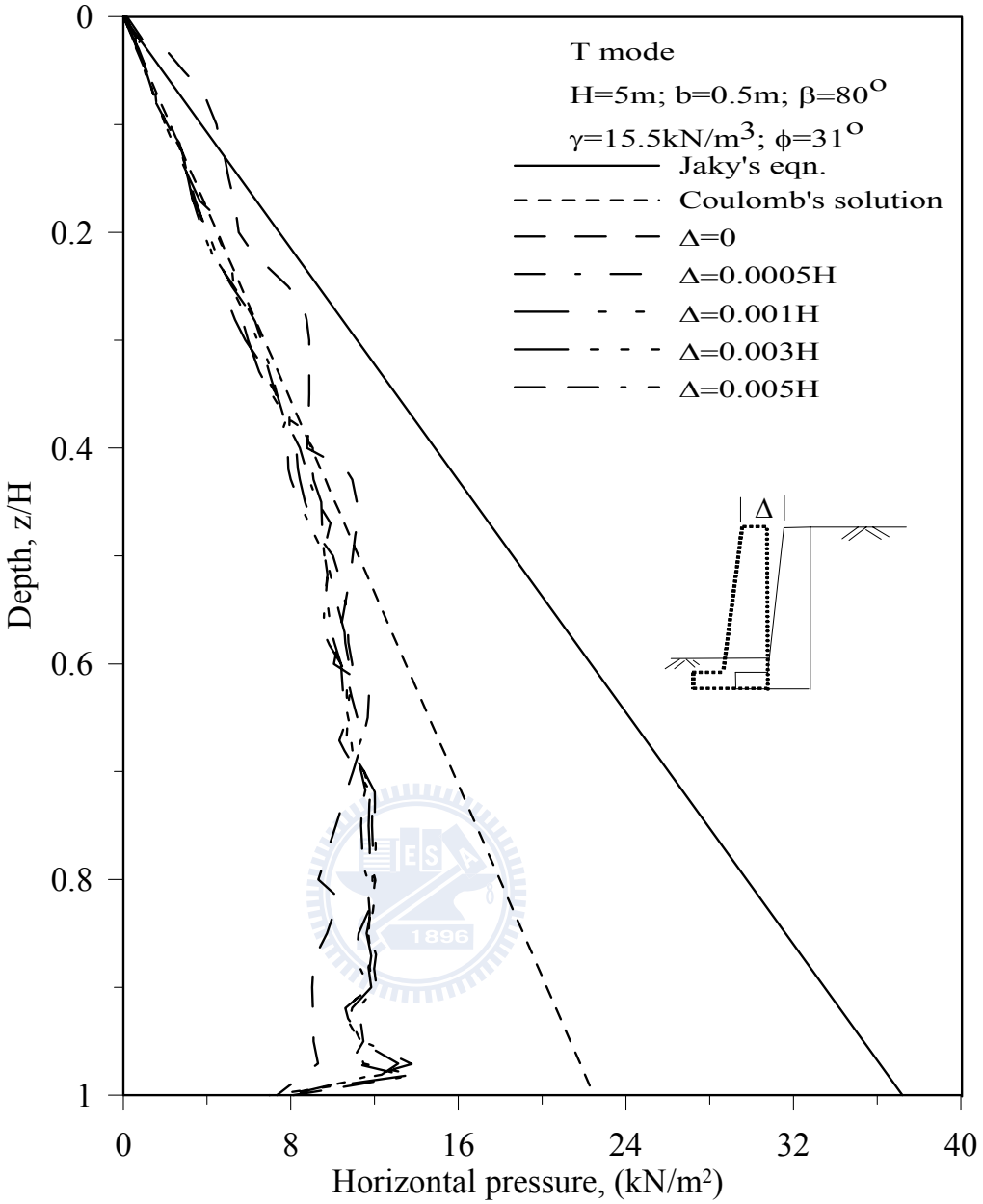

Fig. 2.29. Distribution of earth pressures with the depth at various wall displacements for walls in translation (T mode) (after Fan and Fang, 2009)

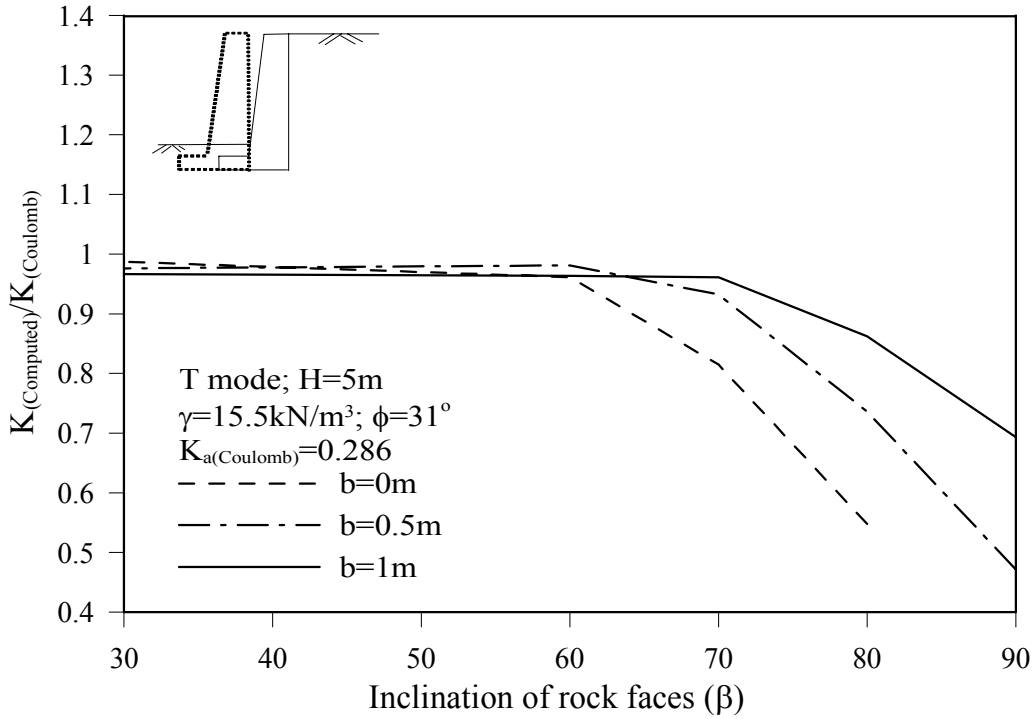

Fig. 2.30. Variation of the coefficient of active earth pressures ($K_{a(Computed)}/K_{a(Coulomb)}$) with the inclination of rock faces at various fill widths (b) for walls undergoing translation (after Fan and Fang, 2009)

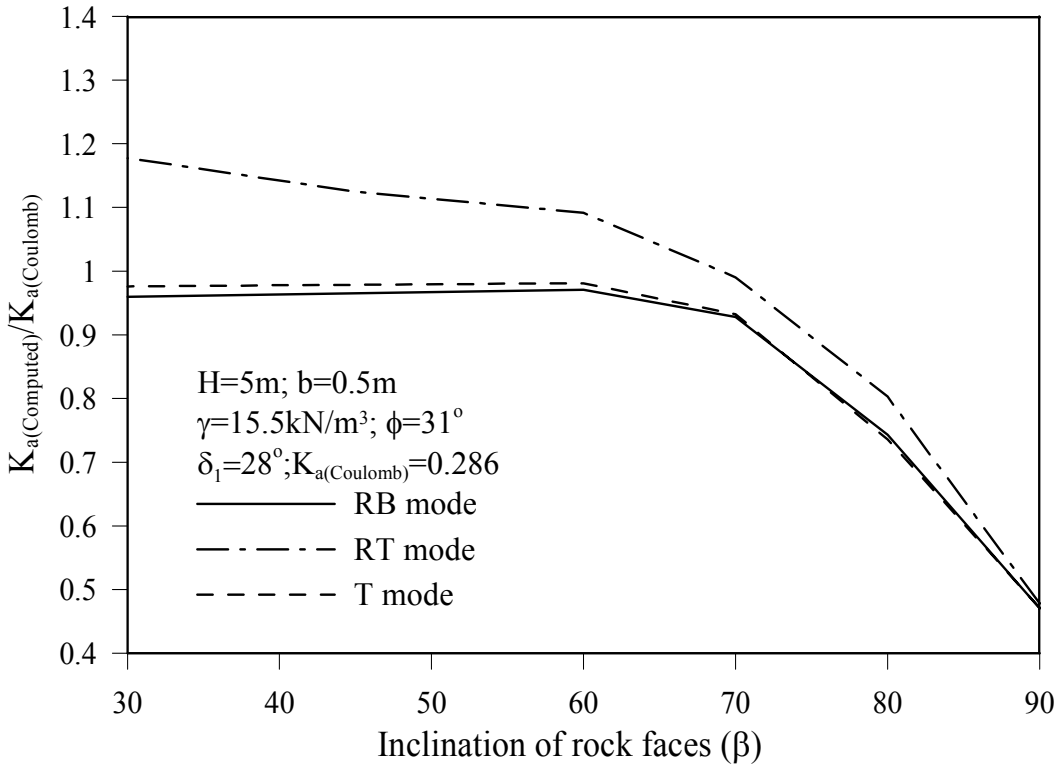

Fig. 2.31. Influence of types of wall movement on the coefficient of active earth pressures ($K_{a(Computed)}/K_{a(Coulomb)}$) for various inclinations of rock faces at a fill width (b) of 0.5 m (after Fan and Fang, 2009)

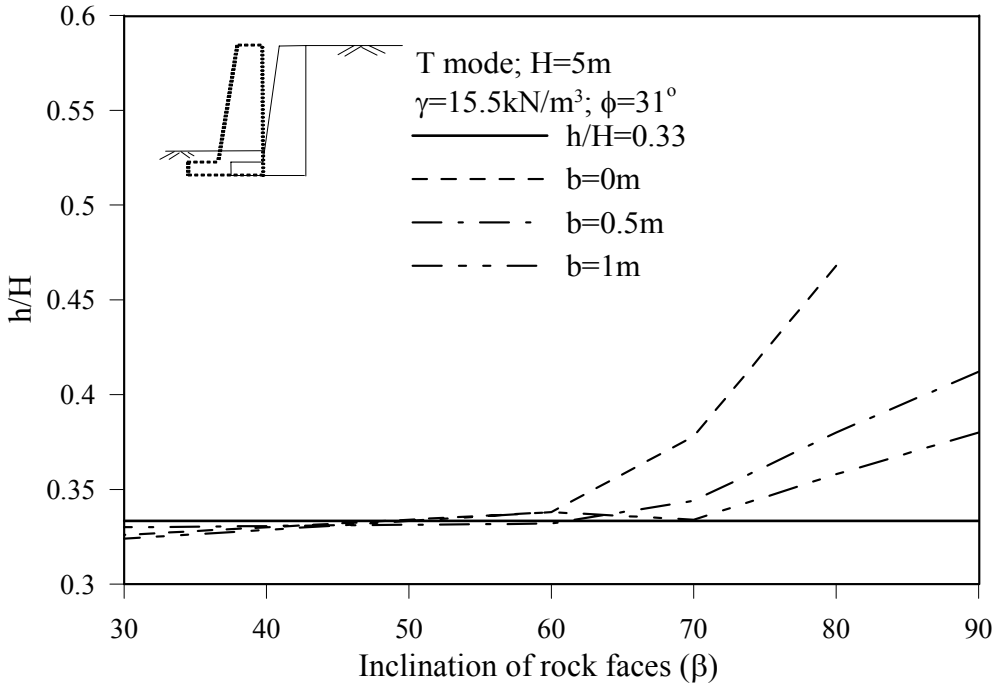

Fig. 2.32. Variation of the location of resultant (h/H) of active earth pressures with the inclination of rock faces at various fill widths (b) for walls undergoing translation (T mode). (after Fan and Fang, 2009)

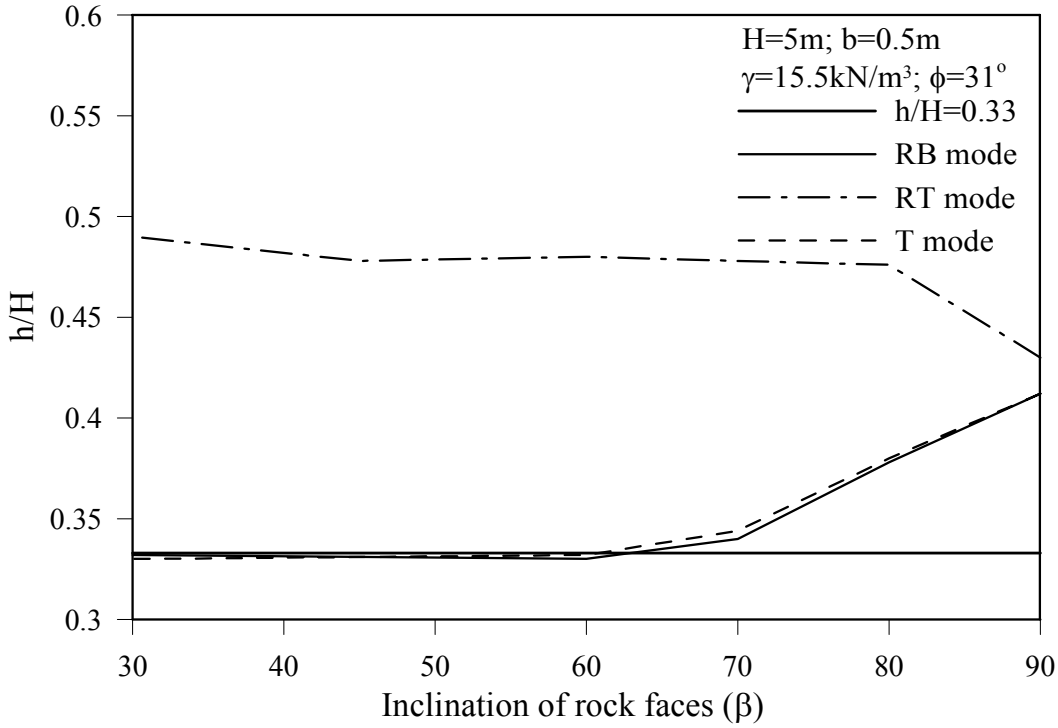

Fig. 2.33. Influence of types of wall movement on the location of resultant of active earth pressures for various inclinations of rock faces at a fill width (b) of 0.5 m (after Fan and Fang, 2009)

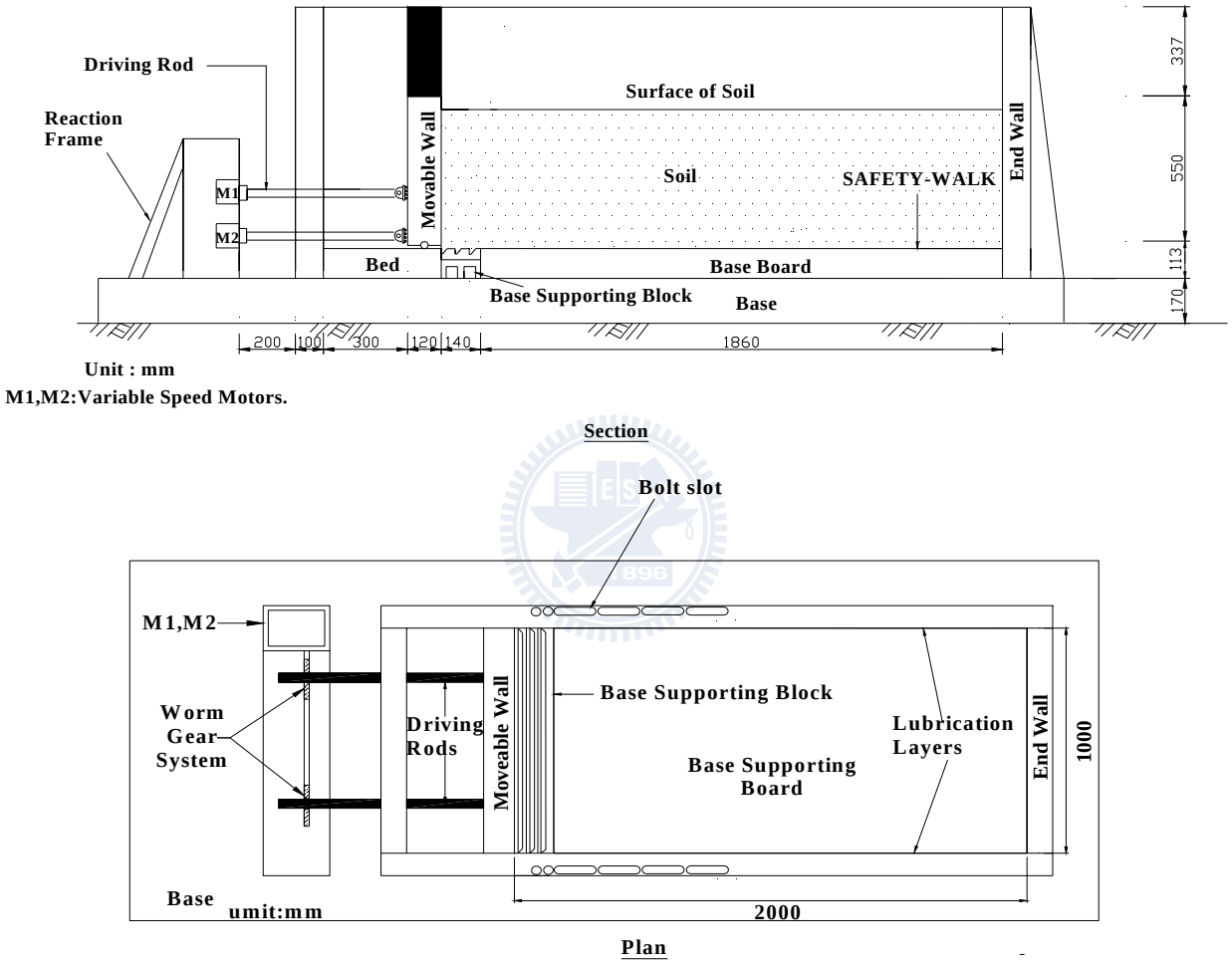

Unit: mm

Fig.3.1. NCTU Model Retaining-Wall Facility

Fig.3.2.Picture of NCTU model retaining wall

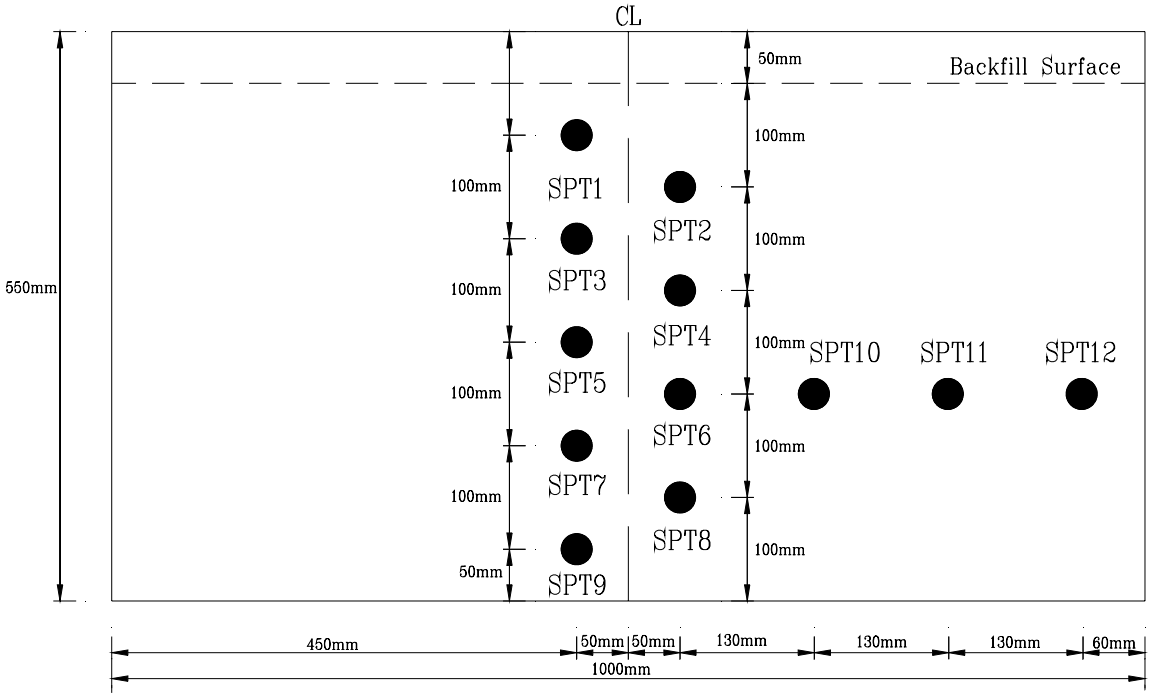

Front-view

Unit : mm

Fig. 3.3. Locations of pressure transducers on NCTU model wall

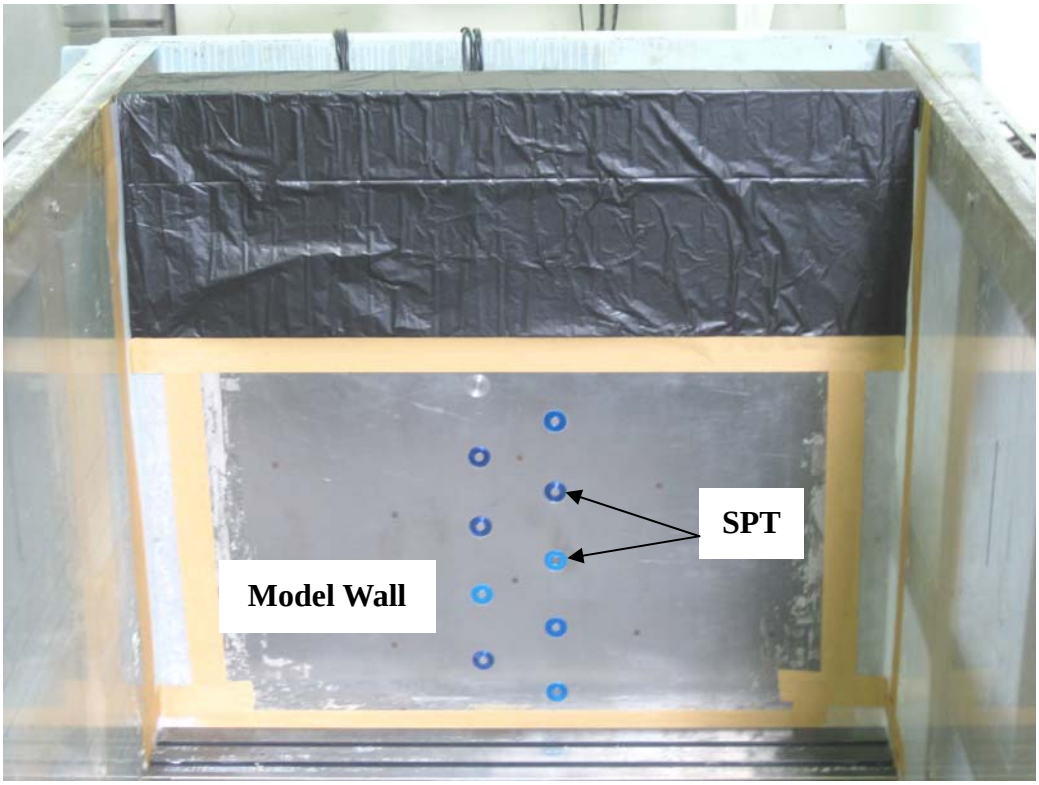

Fig.3.4. Picture of locations of pressure transducers on NCTU model wall

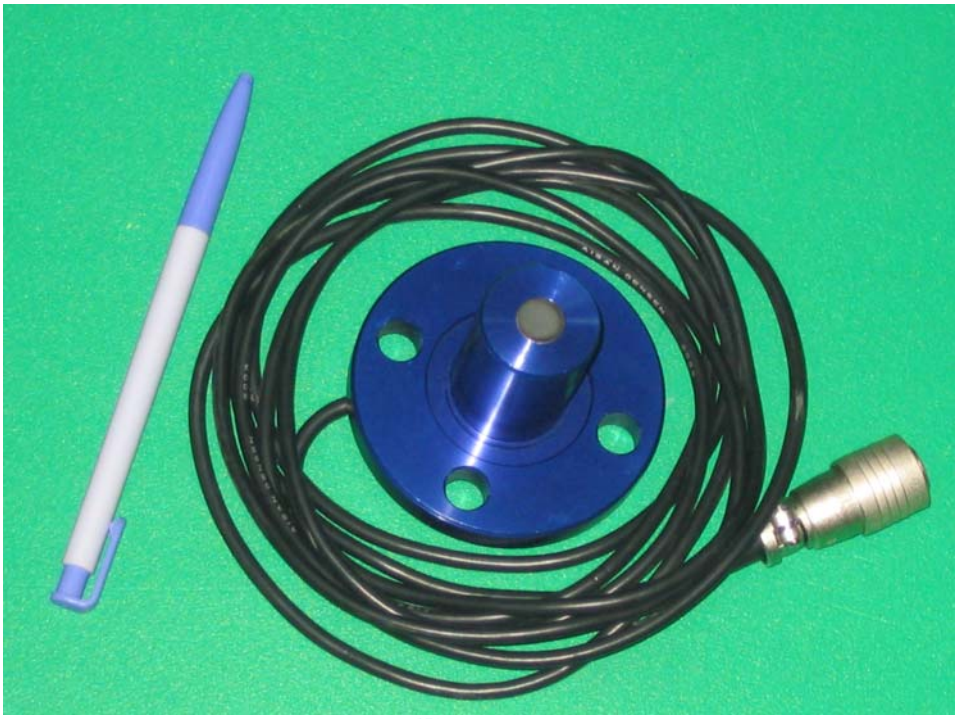

Fig. 3.5. Soil pressure transducer (Kyowa PGM-0.2KG)

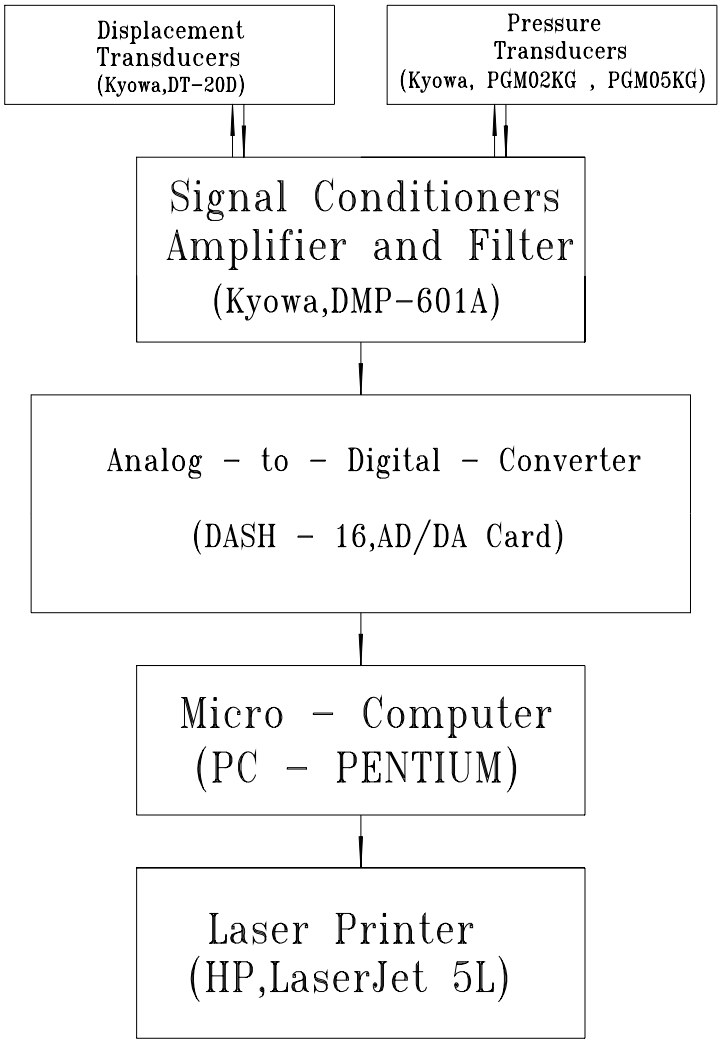

Fig. 3.6 Data Acquisition System

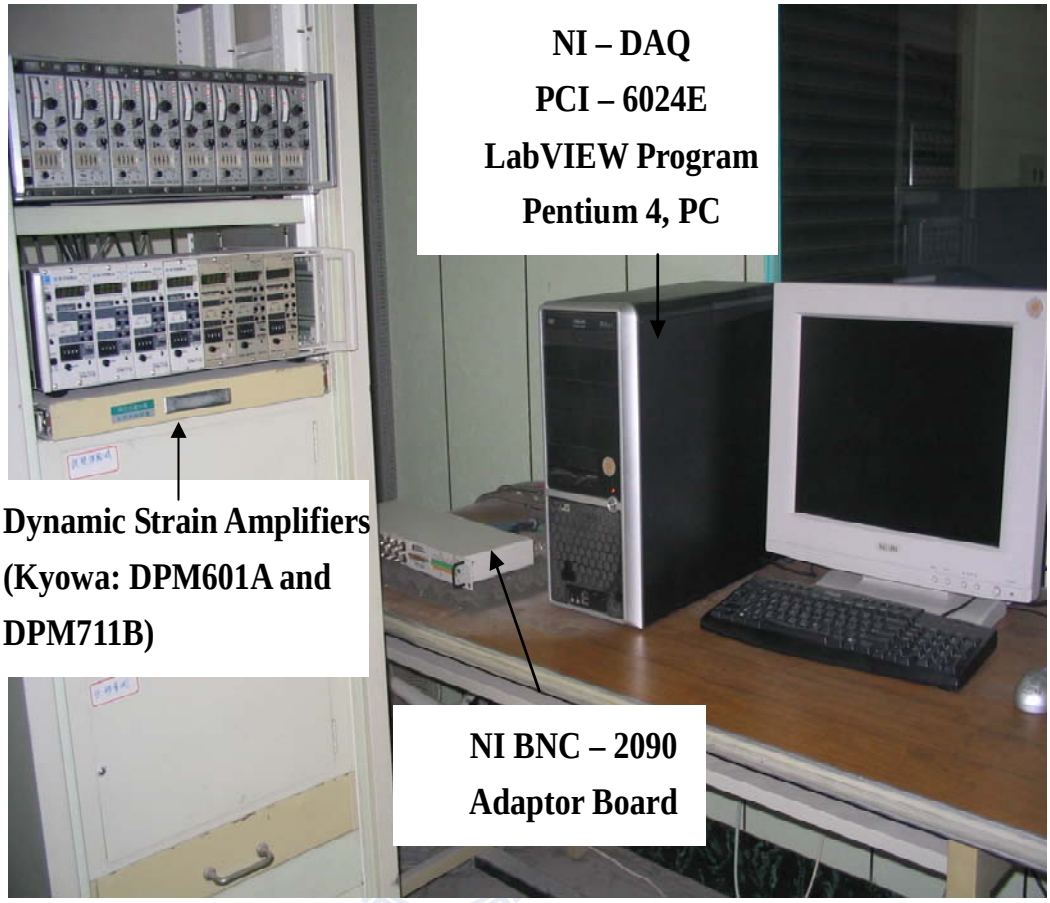

Fig. 3.7. Picture of Data acquisition system

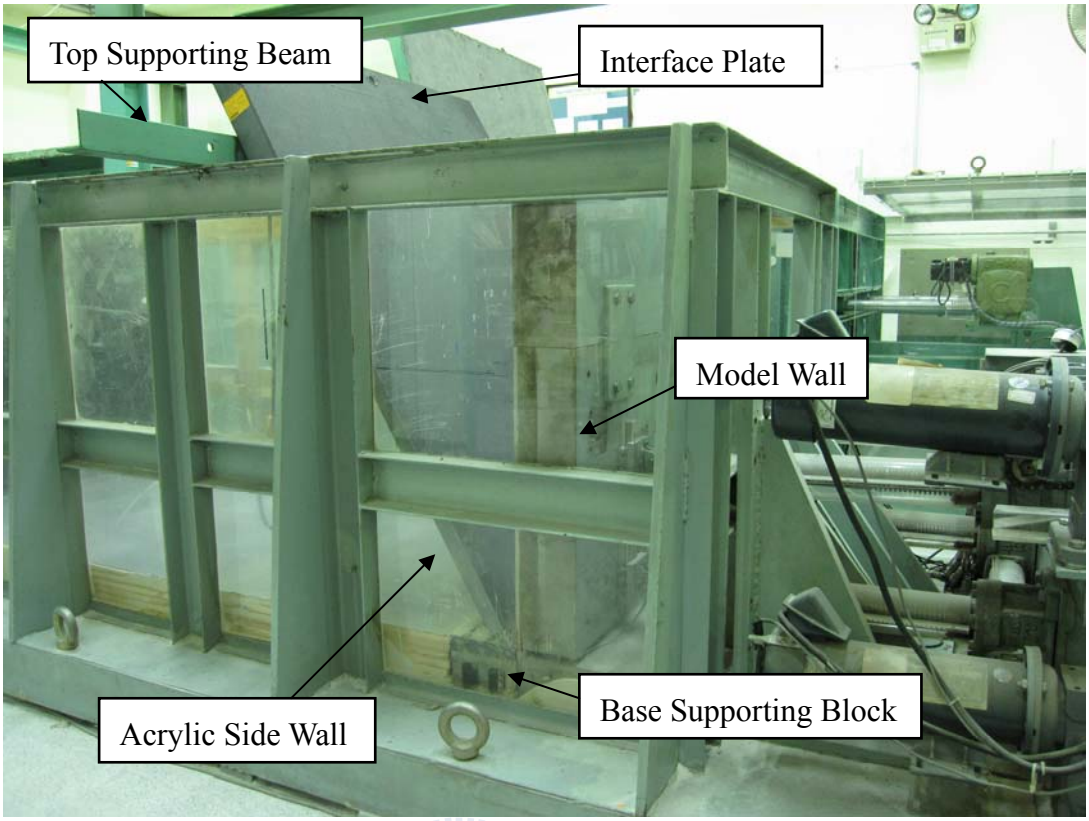

Fig. 4.1. NCTU model retaining wall with inclined interface plate

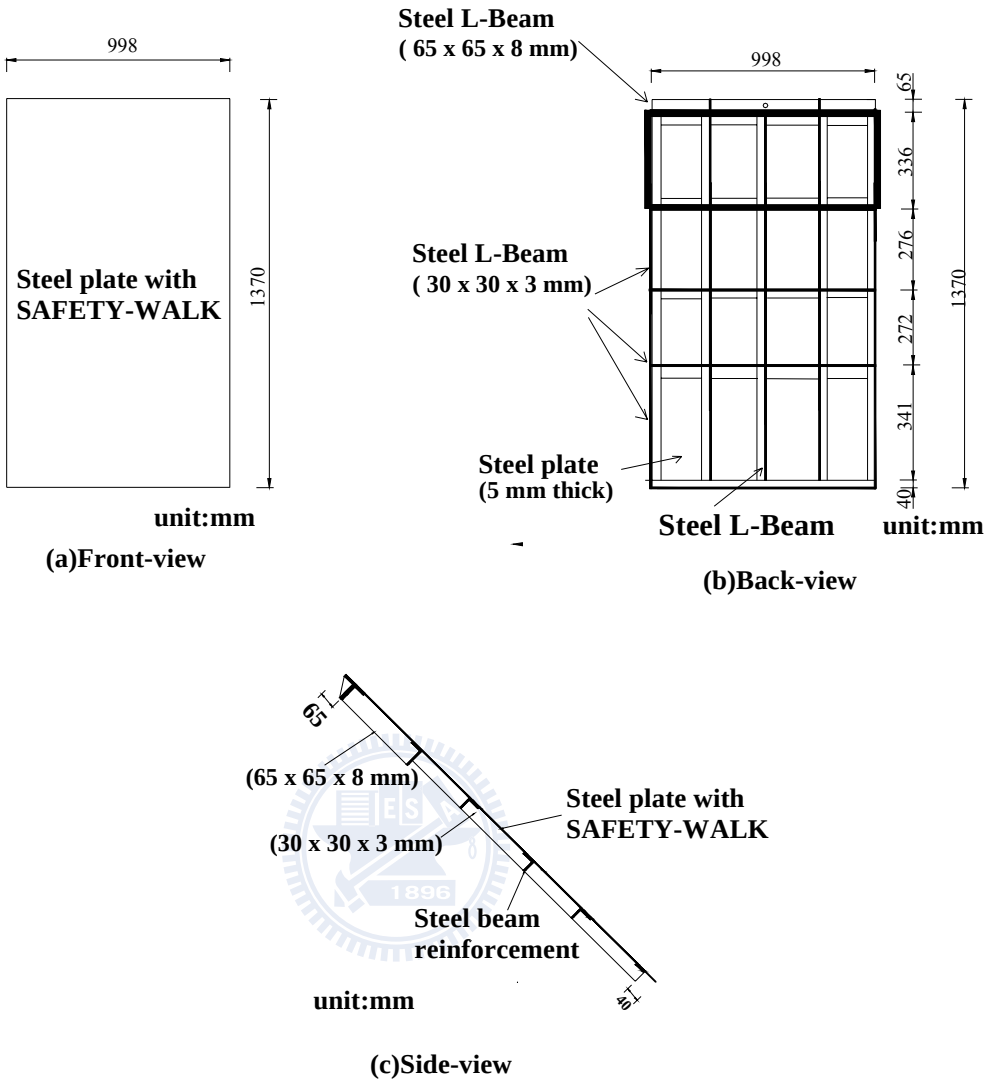

Fig. 4.2. Steel interface plate (after Zheng,2008)

(a) Front-view

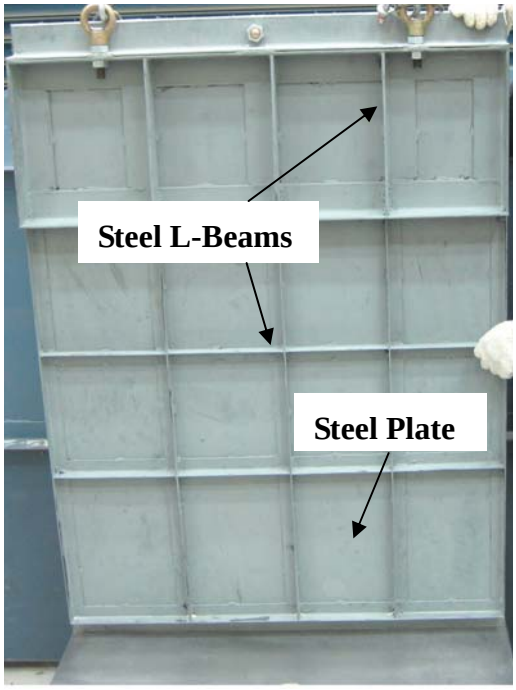

(b) Back-view

Fig. 4.3. Steel interface plate (after Zheng,2008)

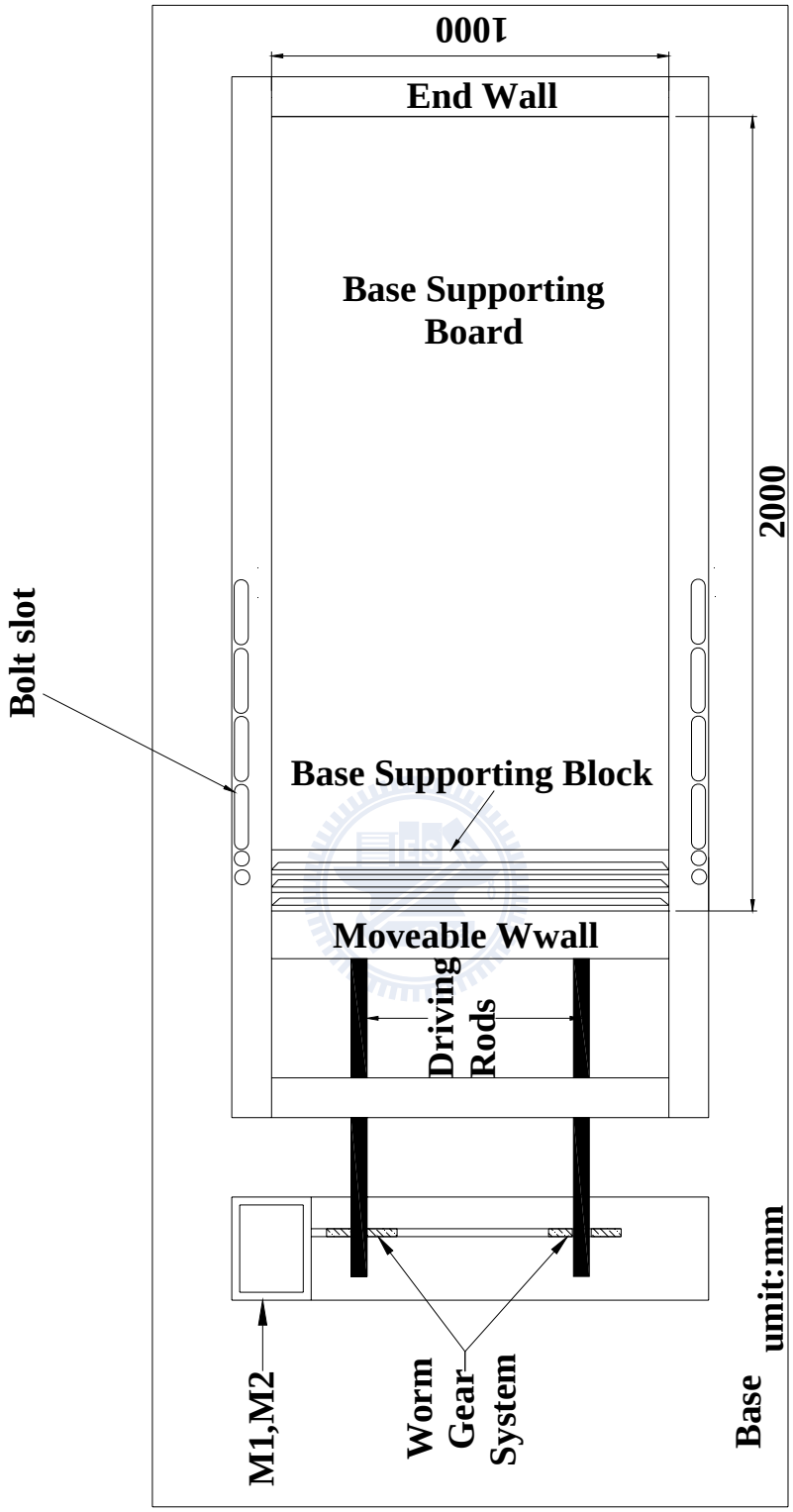

Fig. 4.4 Top-view of model wall

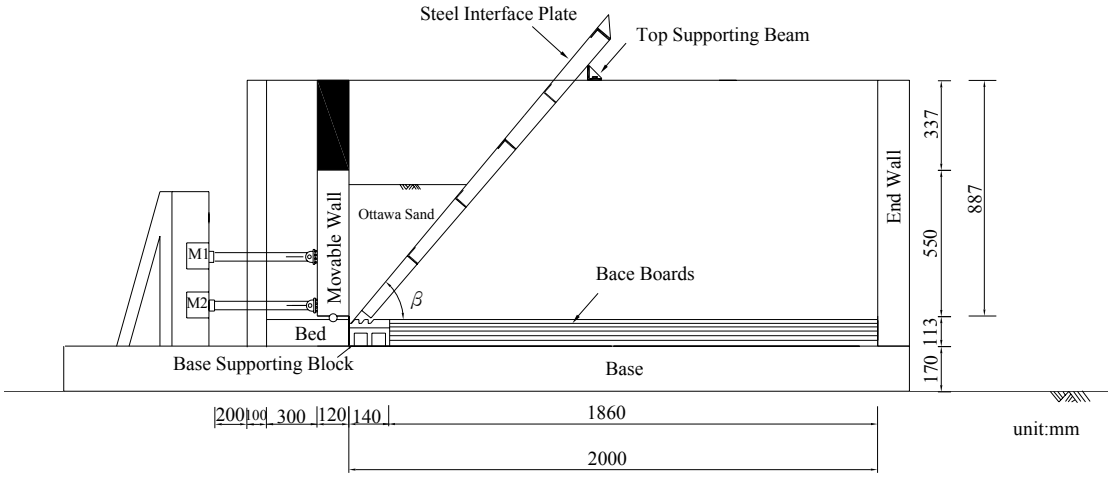

Fig. 4.5. NCTU model retaining wall with interface plate supports

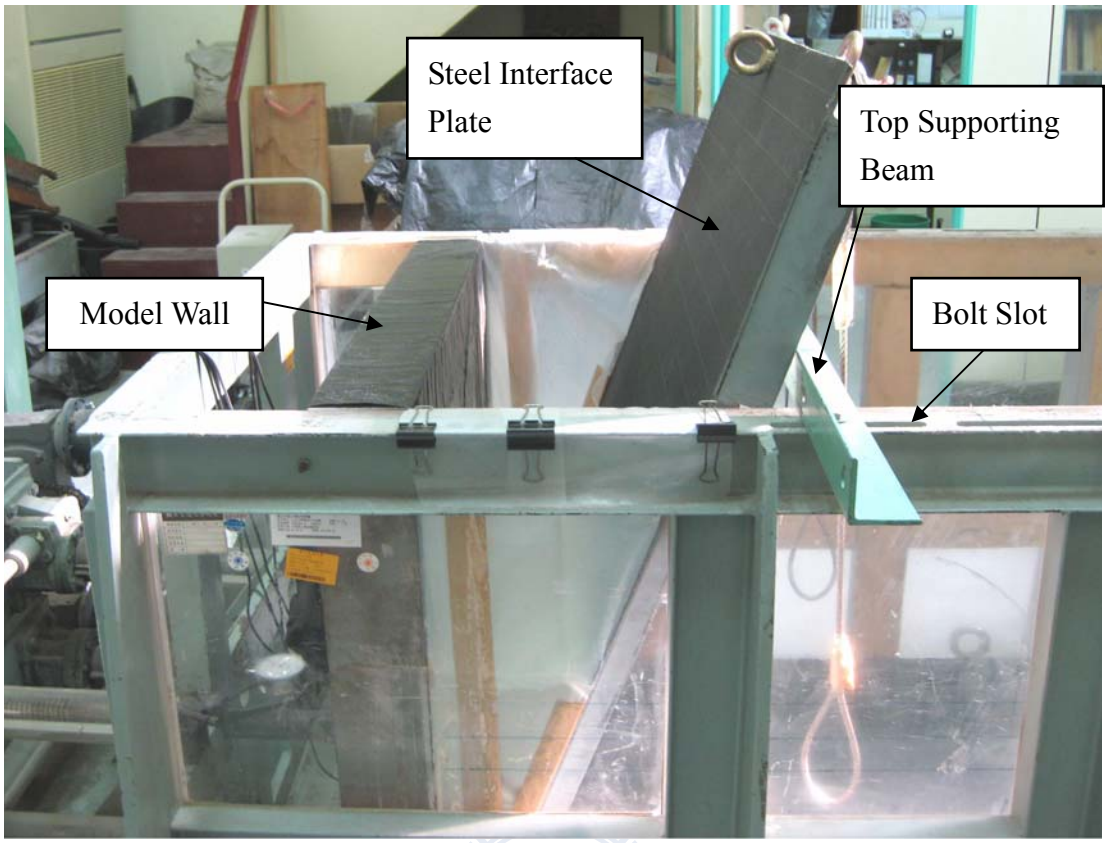

Fig. 4.6. Steel interface plate and top supporting beam

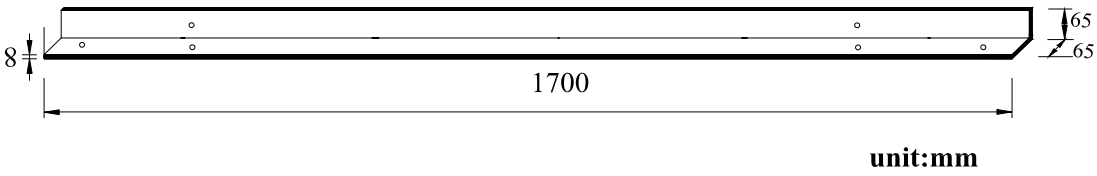

(a)

(b)

Fig. 4.7. Top supporting beam (after Zheng,2008)

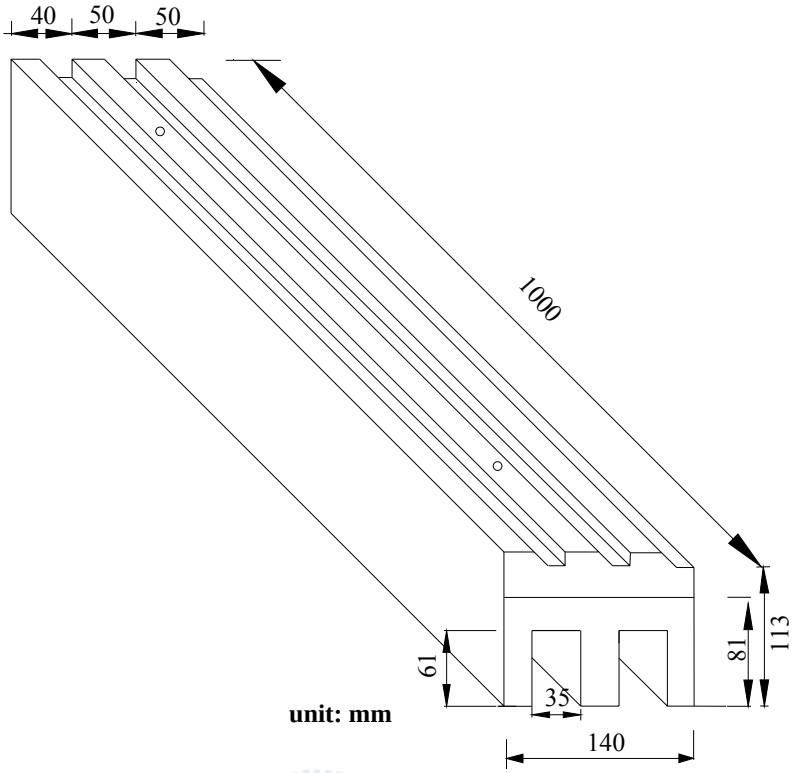

(a)

(b)

Fig. 4.8. Base supporting block (after Zheng,2008)

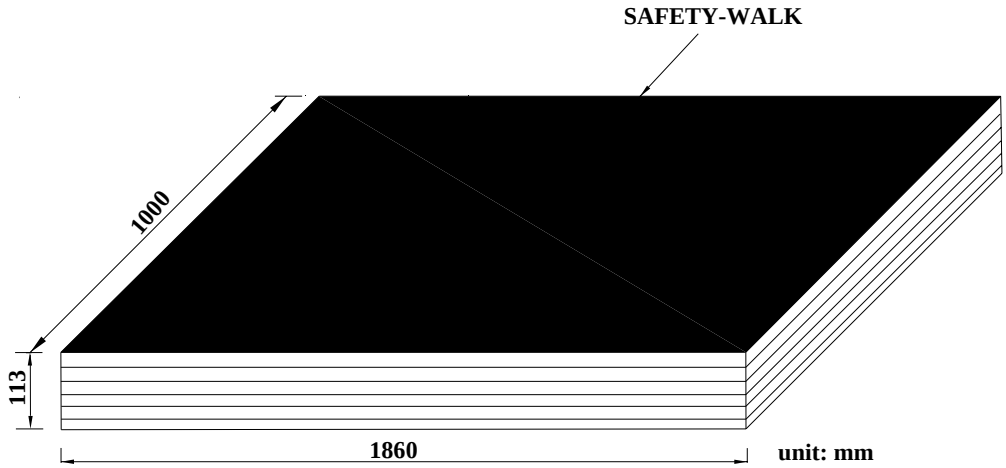

(a)

(b)

Fig. 4.9. Base supporting boards (after Zheng,2008)

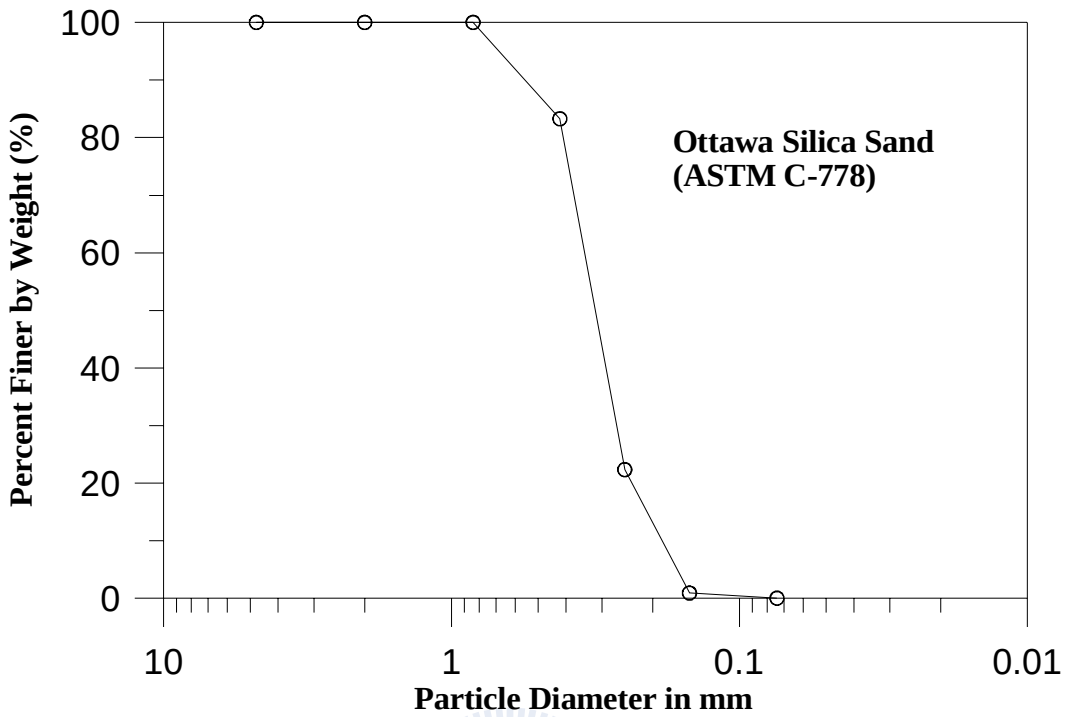

Fig. 5.1. Grain size distribution of Ottawa sand (after Hou, 2006)

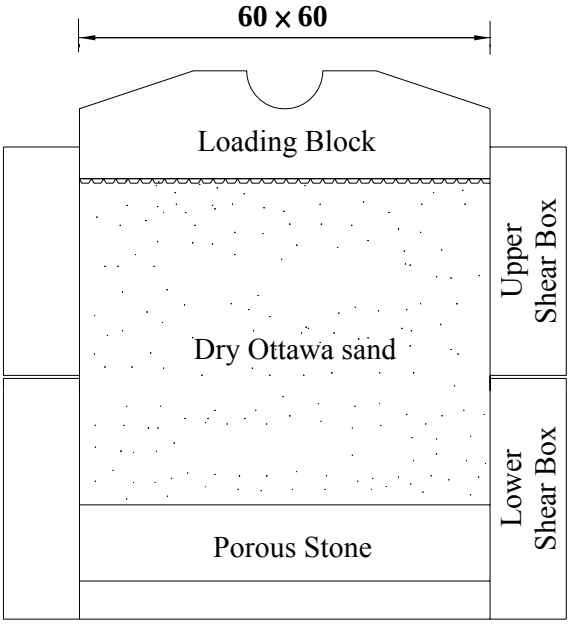

unit : mm

Fig. 5.2. Shear box of direct shear test device (after Wu, 1992)

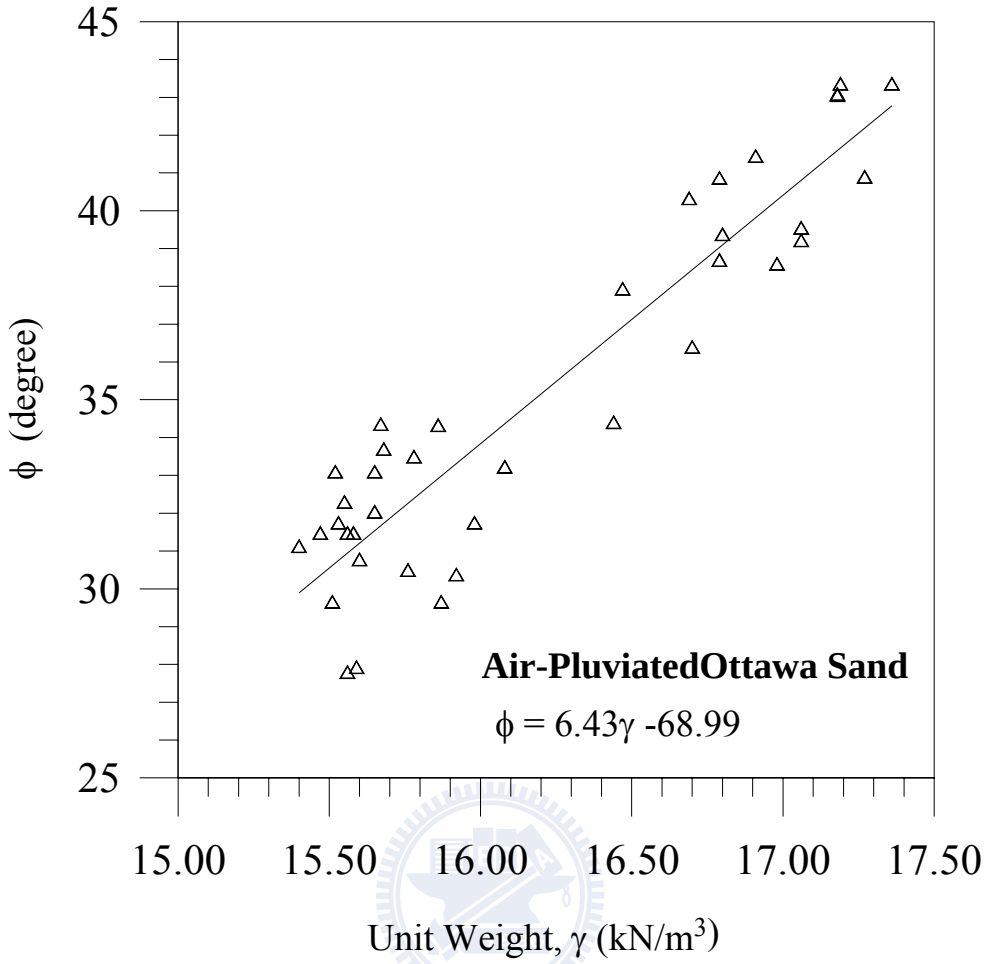

Fig. 5.3. Relationship between unit weight γ and internal friction angle ϕ (after Chang, 2000)

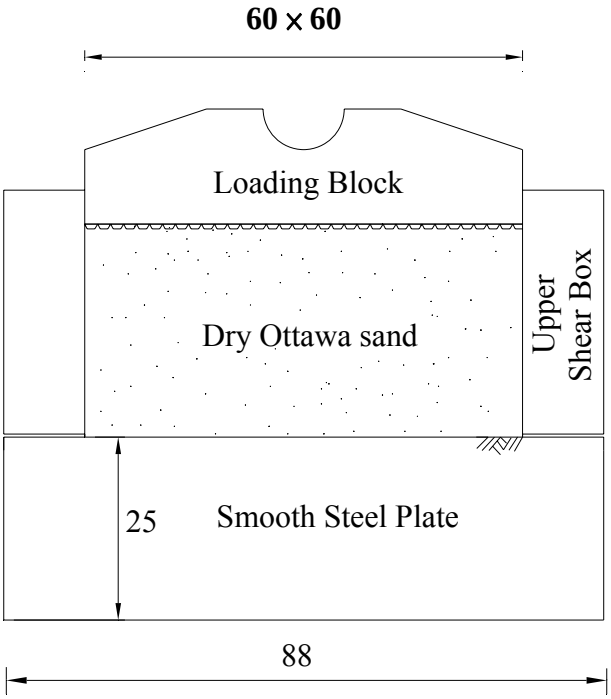

unit : mm

Fig. 5.4. Direct shear test arrangement to determinate wall friction (after Chang, 2000)

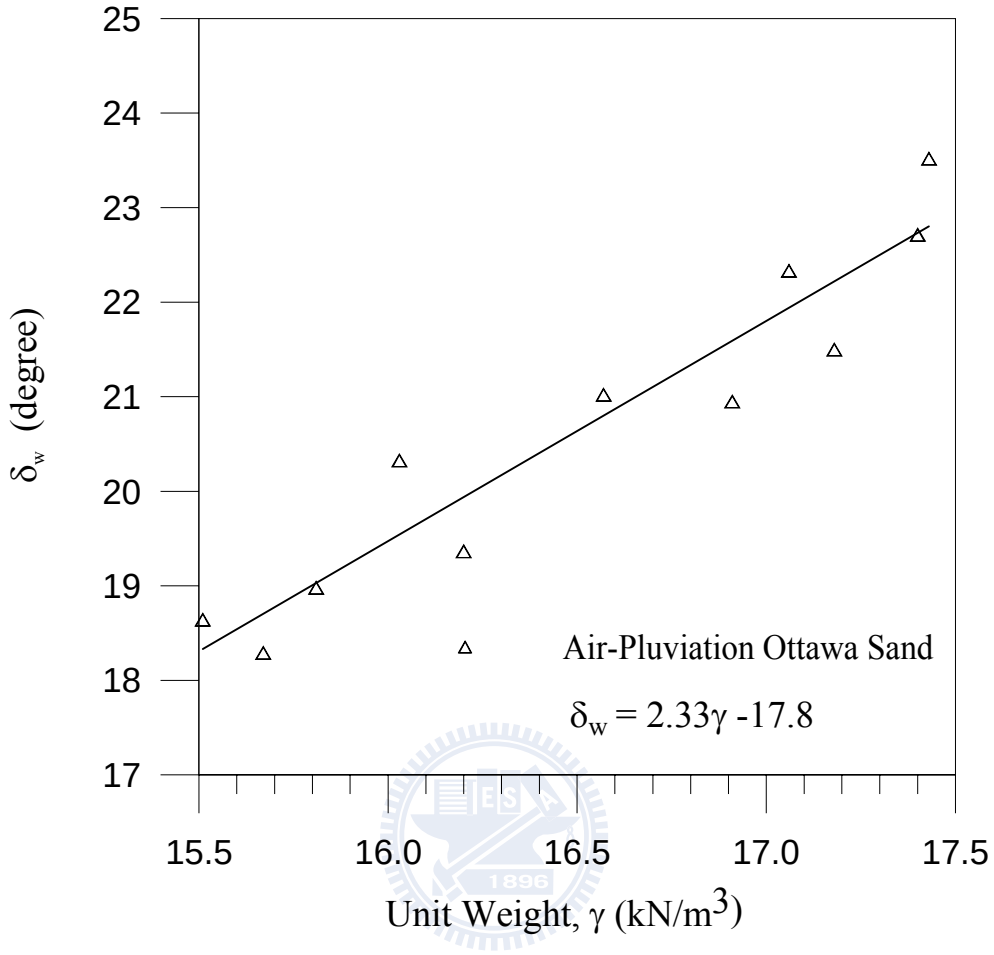

Fig.5.5. Relationship between unit weight γ and wall friction angle δ_w (after Chang, 2000)

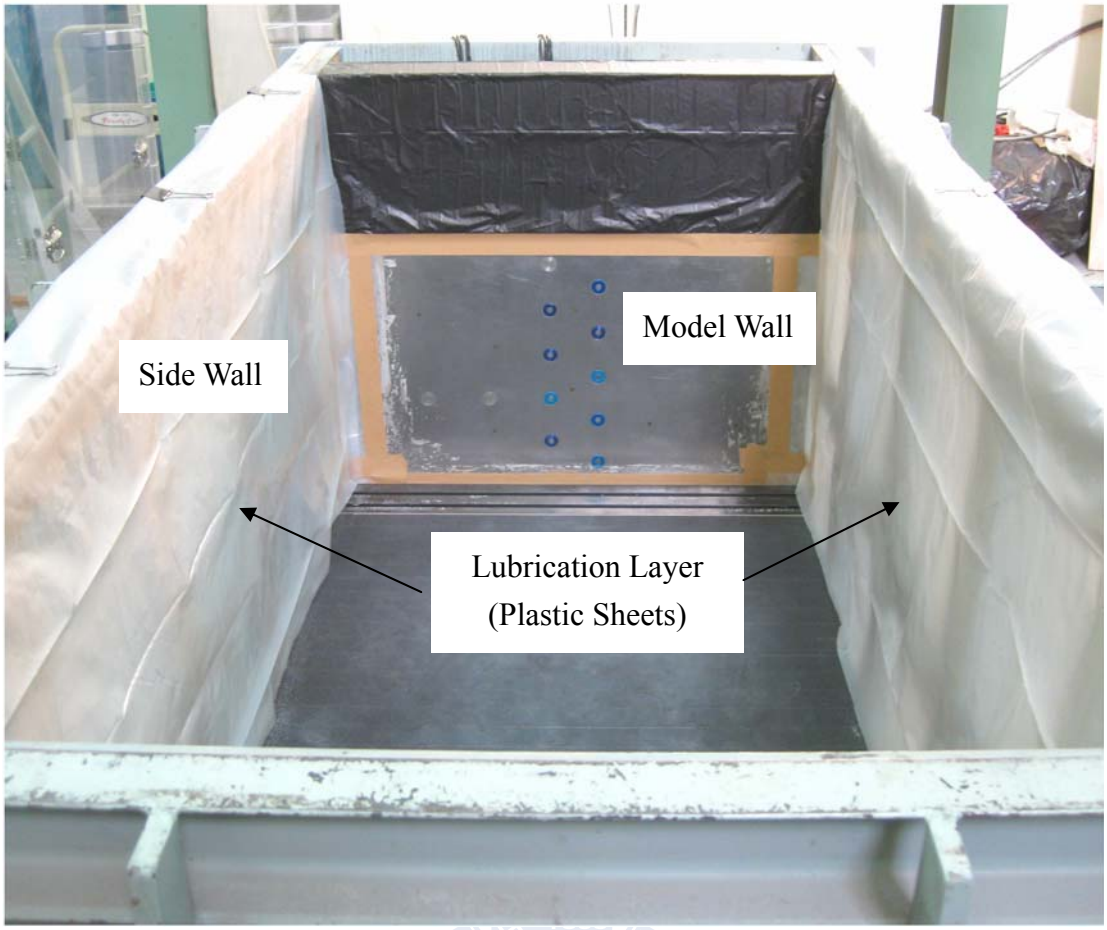

Fig. 5.6. Lubrication layers on side walls

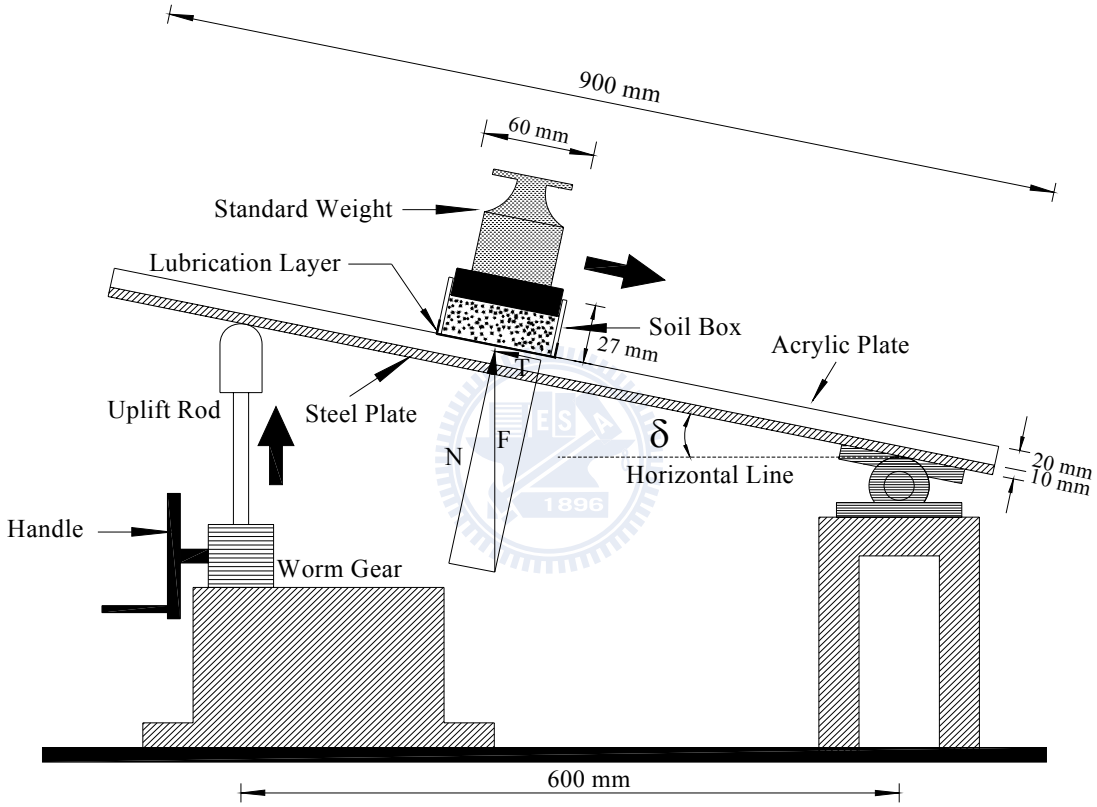

Fig. 5.7. Schematic diagram of sliding block test (after Fang et al., 2004)

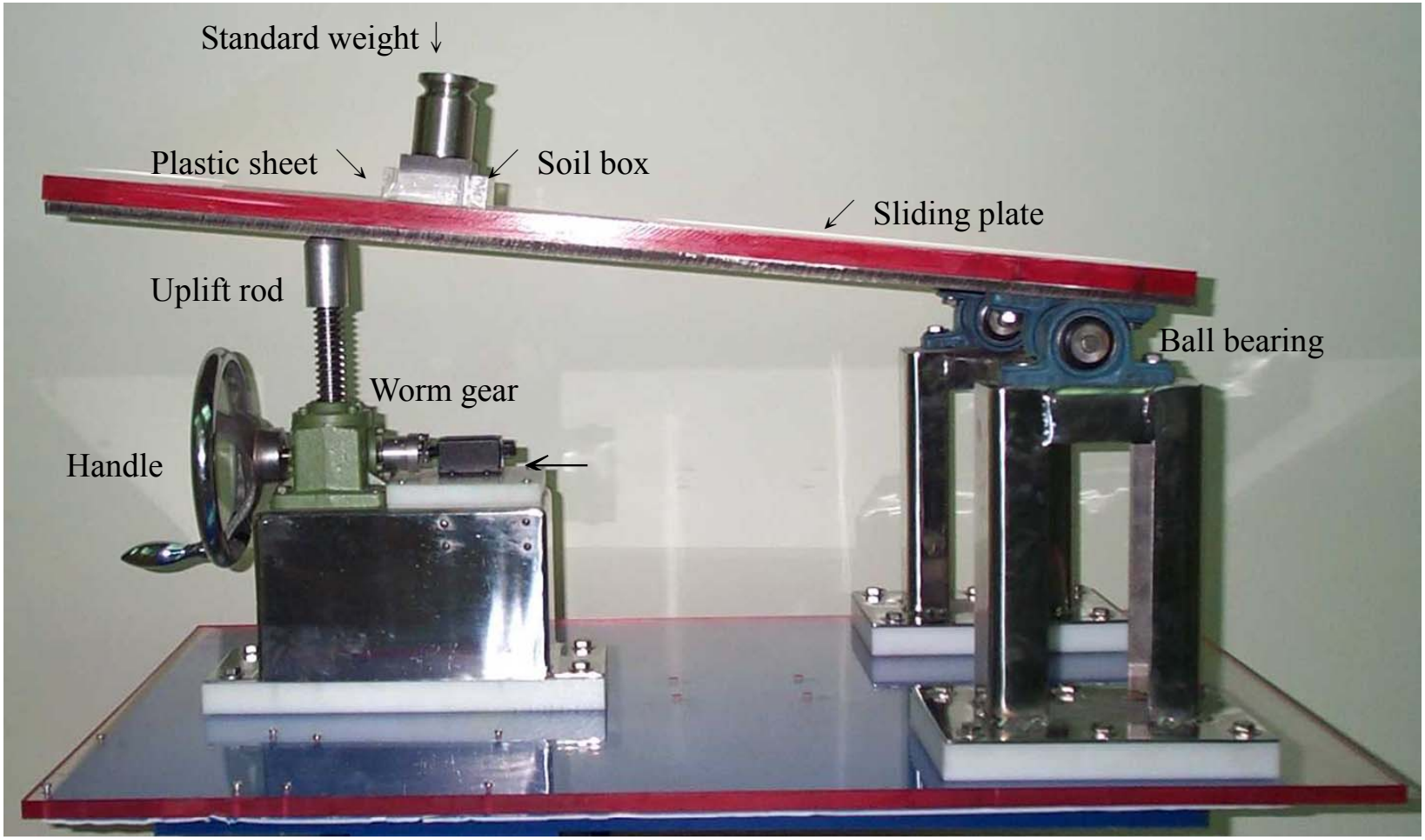

Fig.5.8 Sliding block test apparatus (after Fang et al., 2004)

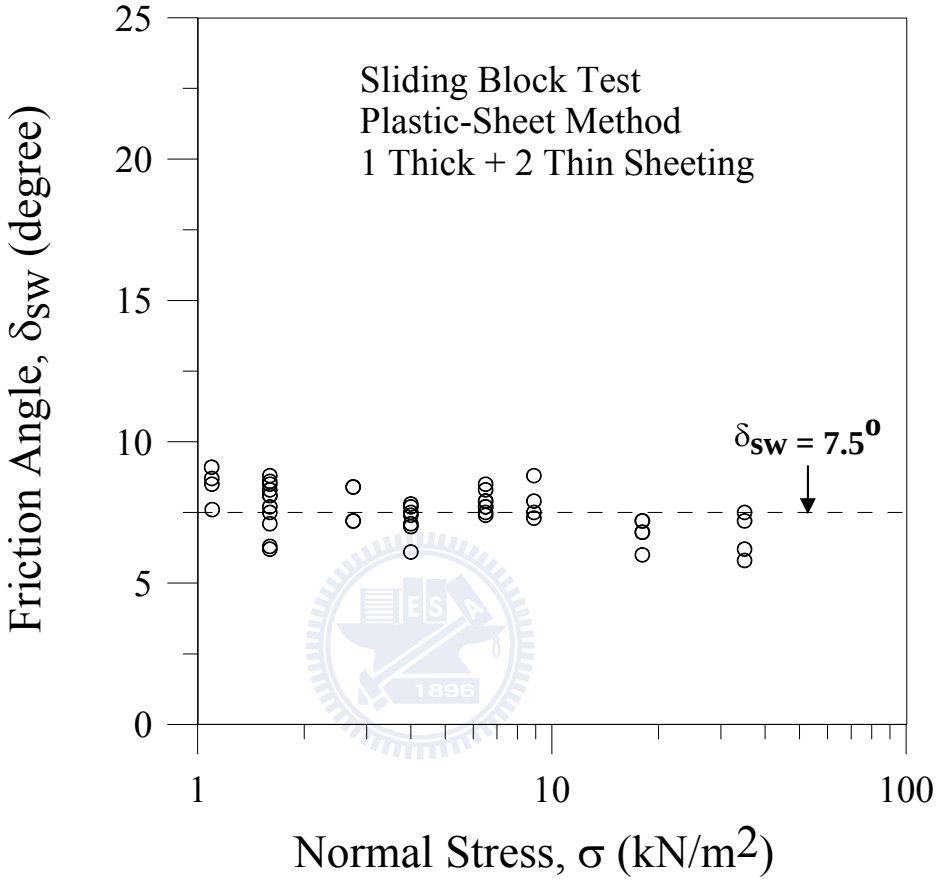

Fig. 5.9 Variation of side-wall friction angle with normal stress

(after Fang et al., 2004)

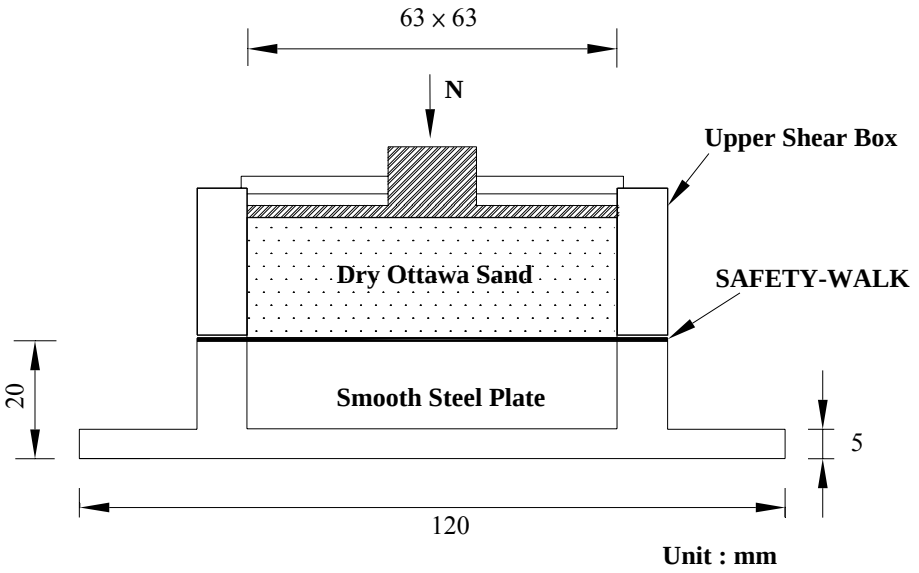

(a)

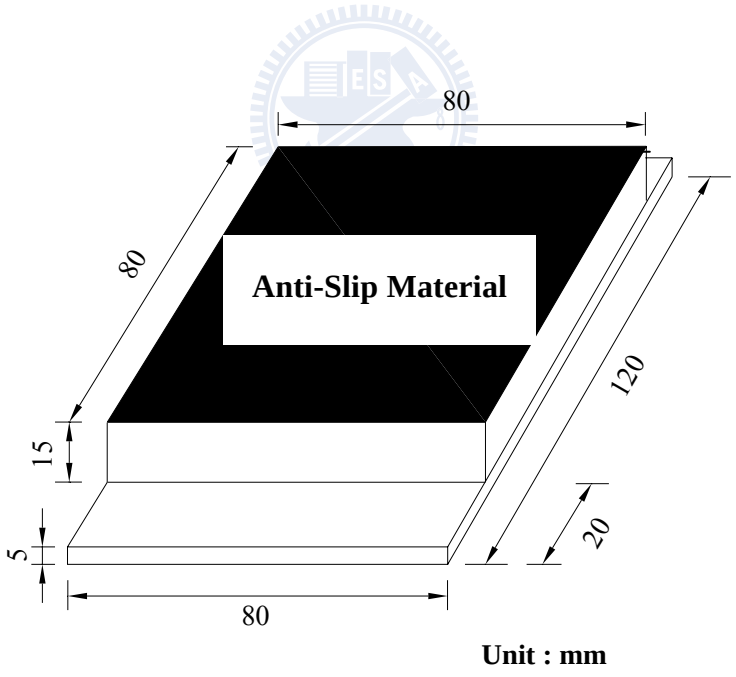

(b)

Fig. 5.10. Direct shear test arrangement to determine interface friction angle

(after Wang, 2006)

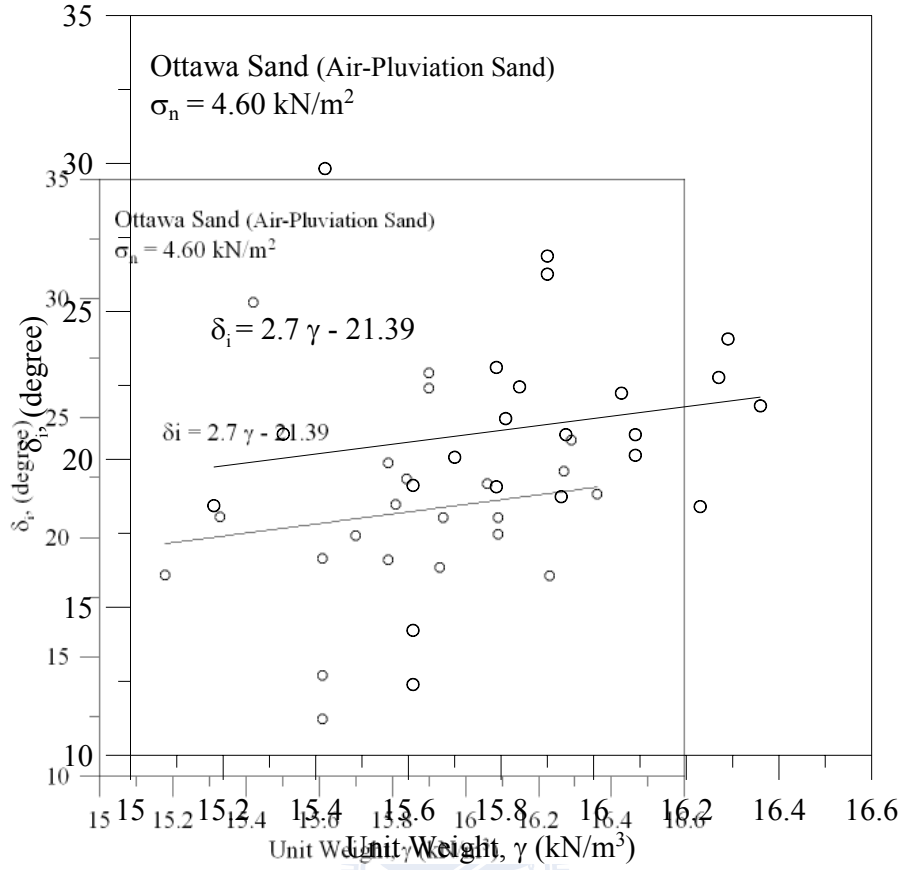

Fig. 5.11. Relationship between unit weight γ and interface plate friction angle δ_i (after Wang, 2005)

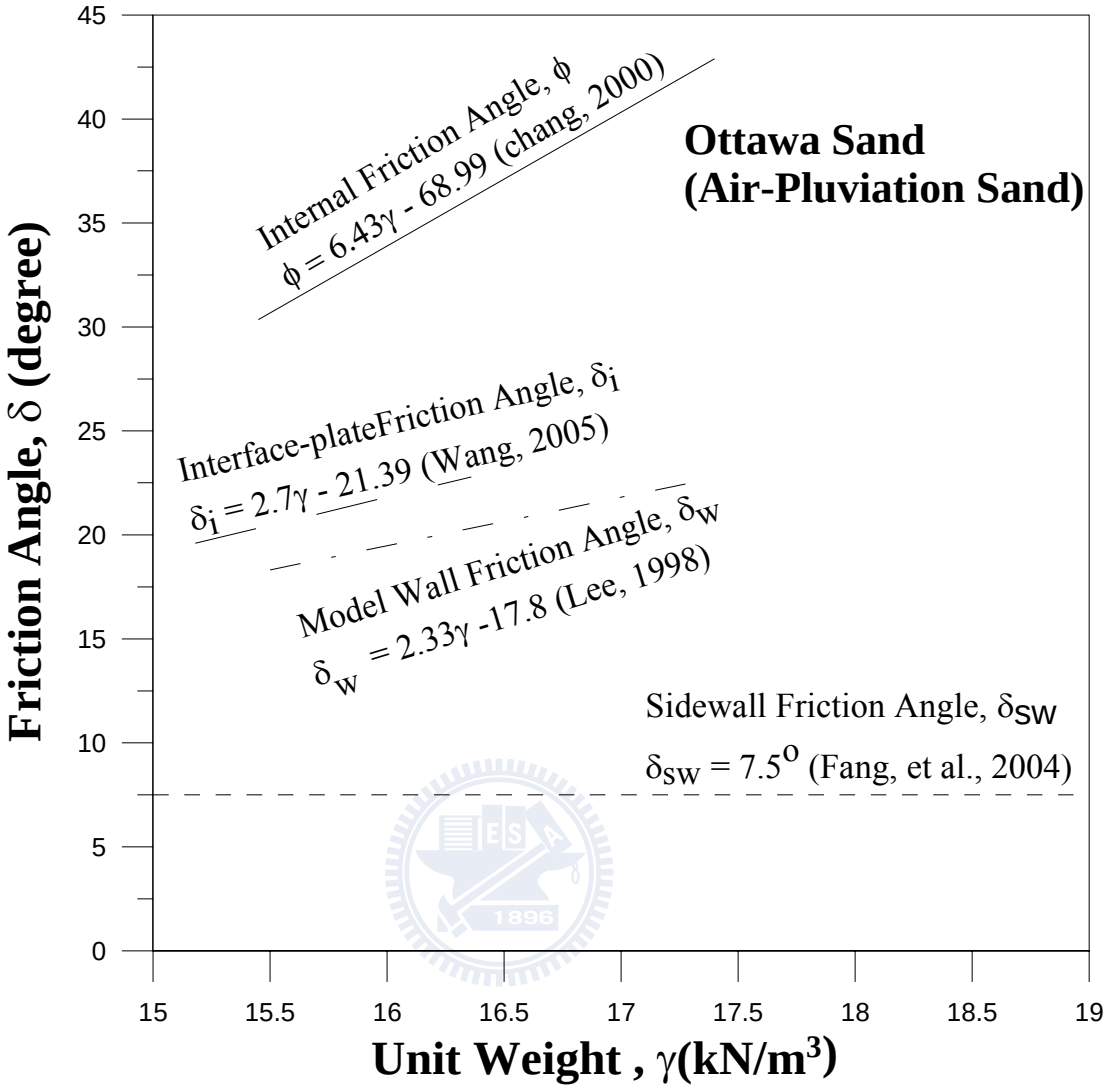

Fig. 5.12. Relationship friction angle δ and soil unit weight γ (after Fang et al.)

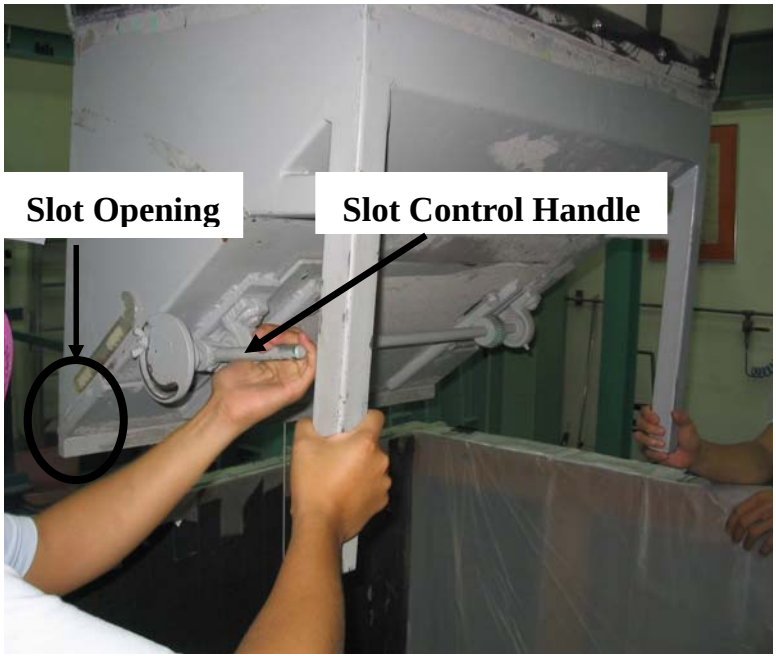

(a)

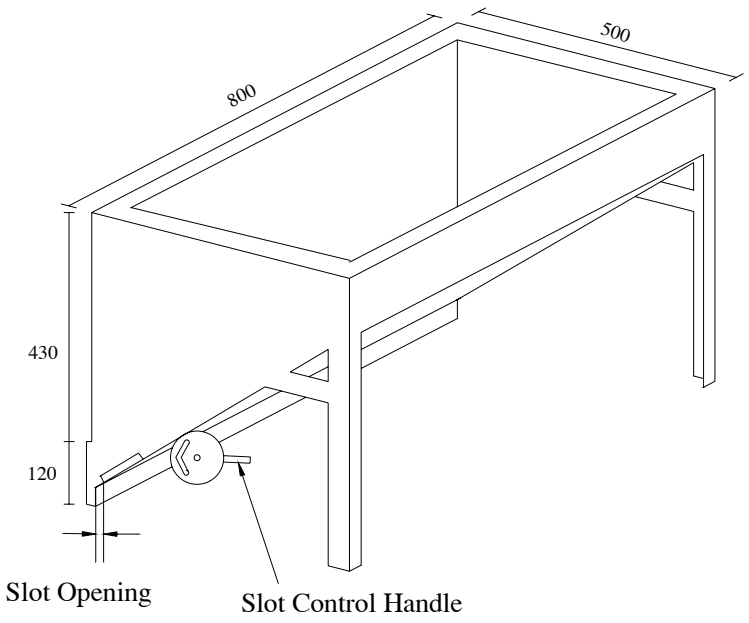

Unit:mm

(b)

Fig. 5.13. Soil hopper (after Chang, 2000)

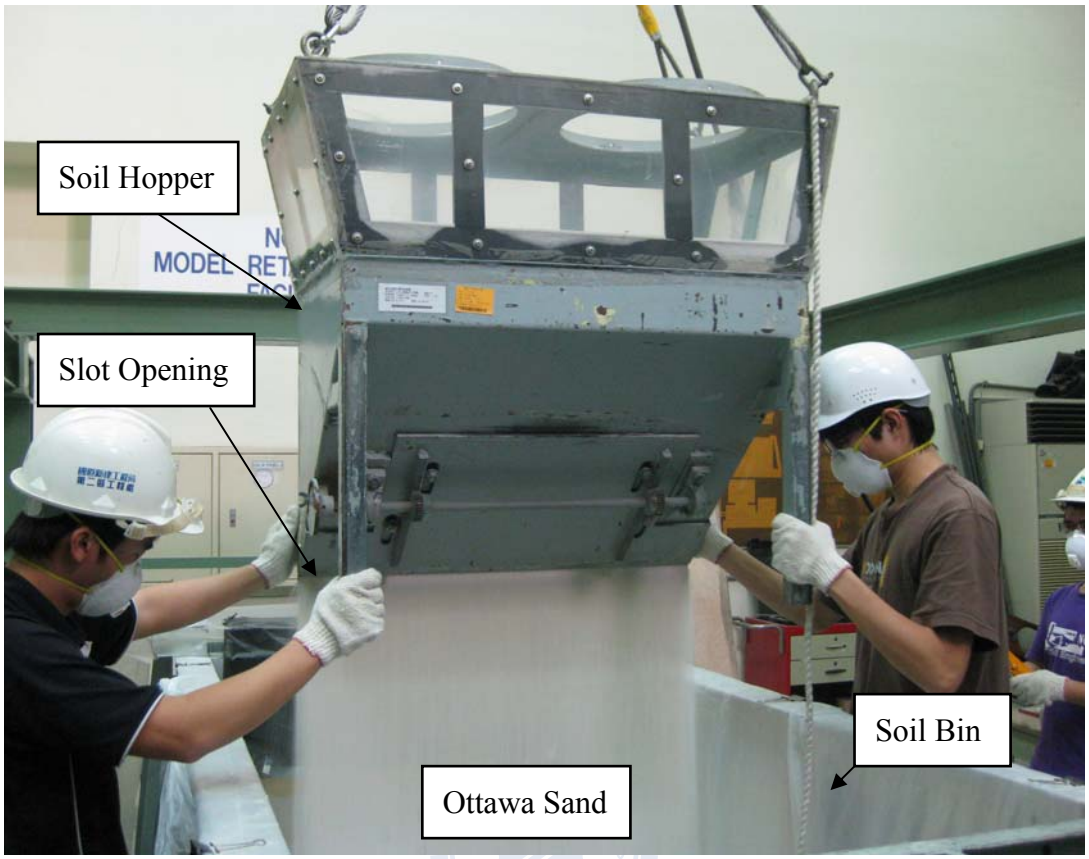

Fig. 5.14. Pluviation of Ottawa sand into soil bin

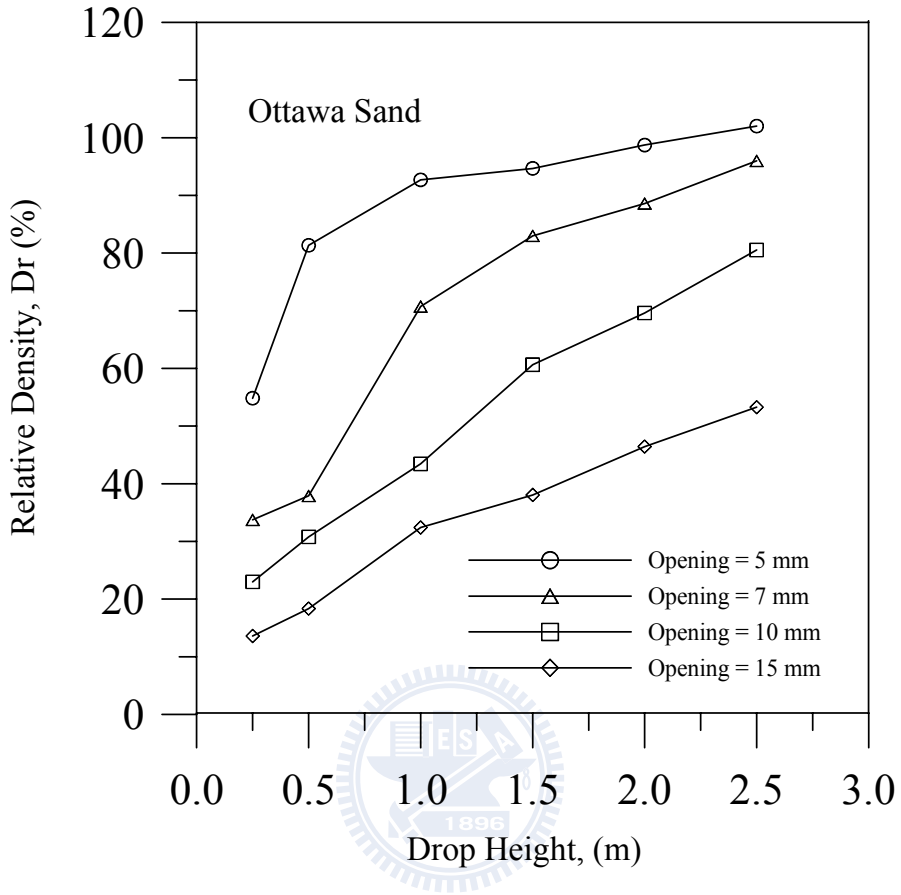

Fig. 5.15. Relationship between relation density and drop height (after Ho, 1999)

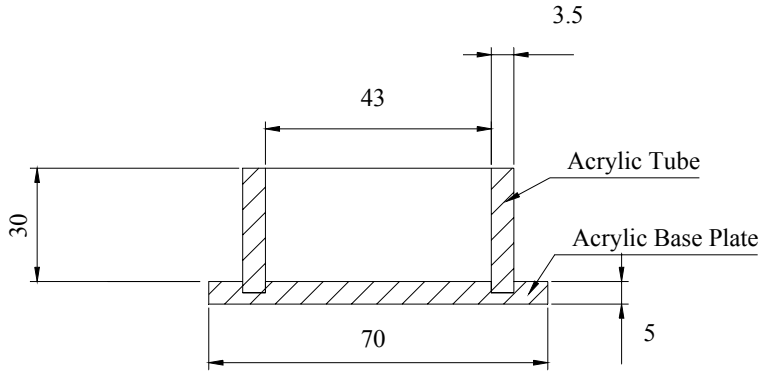

Side-view

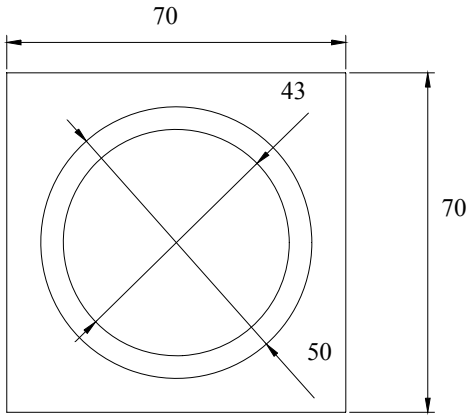

Top-view

unit : mm

Fig. 5.16. Soil-density control cup

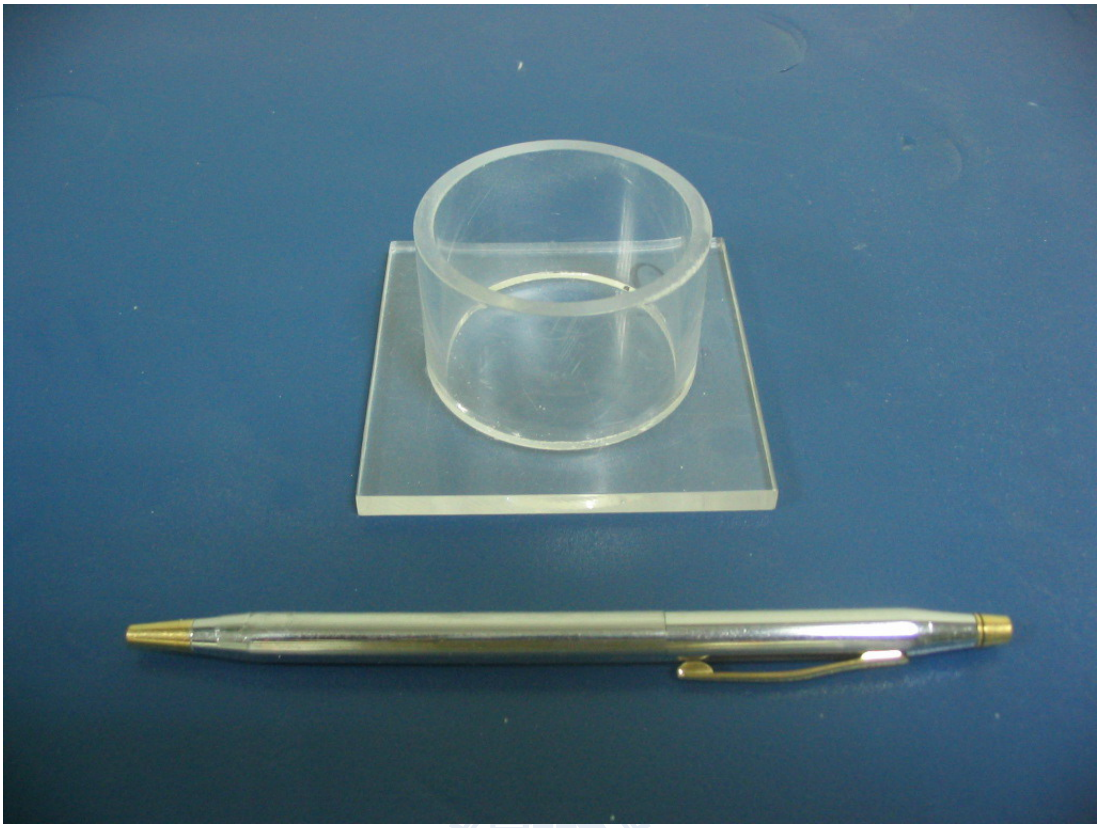

Fig. 5.17. Soil-density cup (after Chien, 2007)

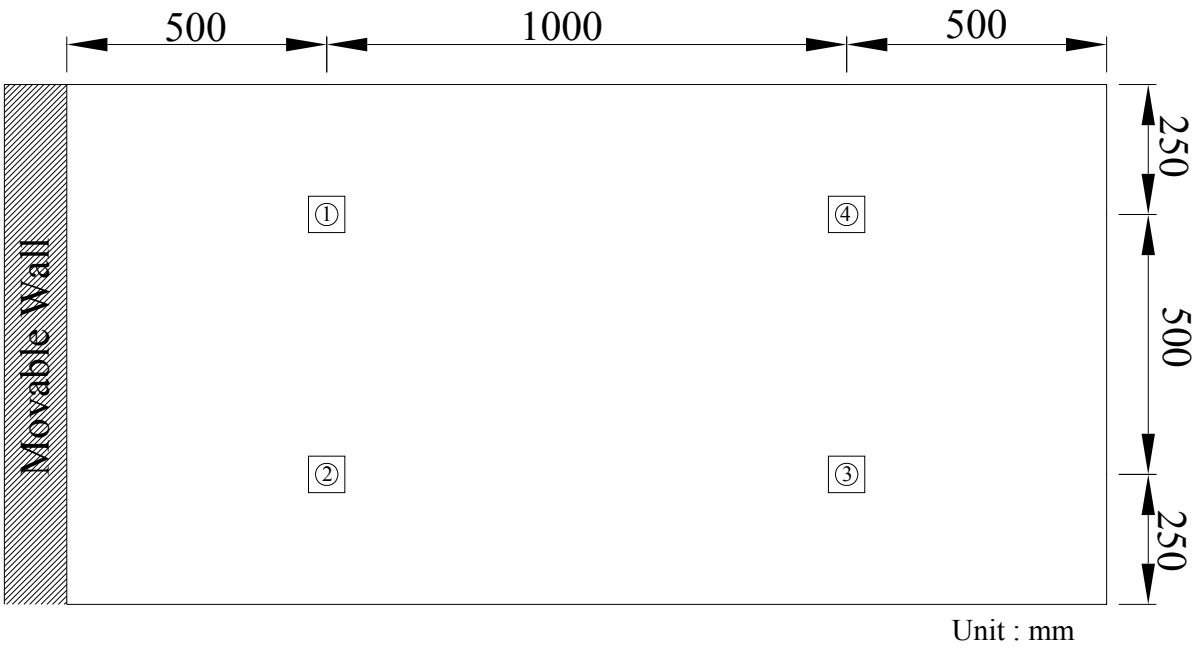

Fig. 5.18. Soil density cups at the same elevation (top-view)

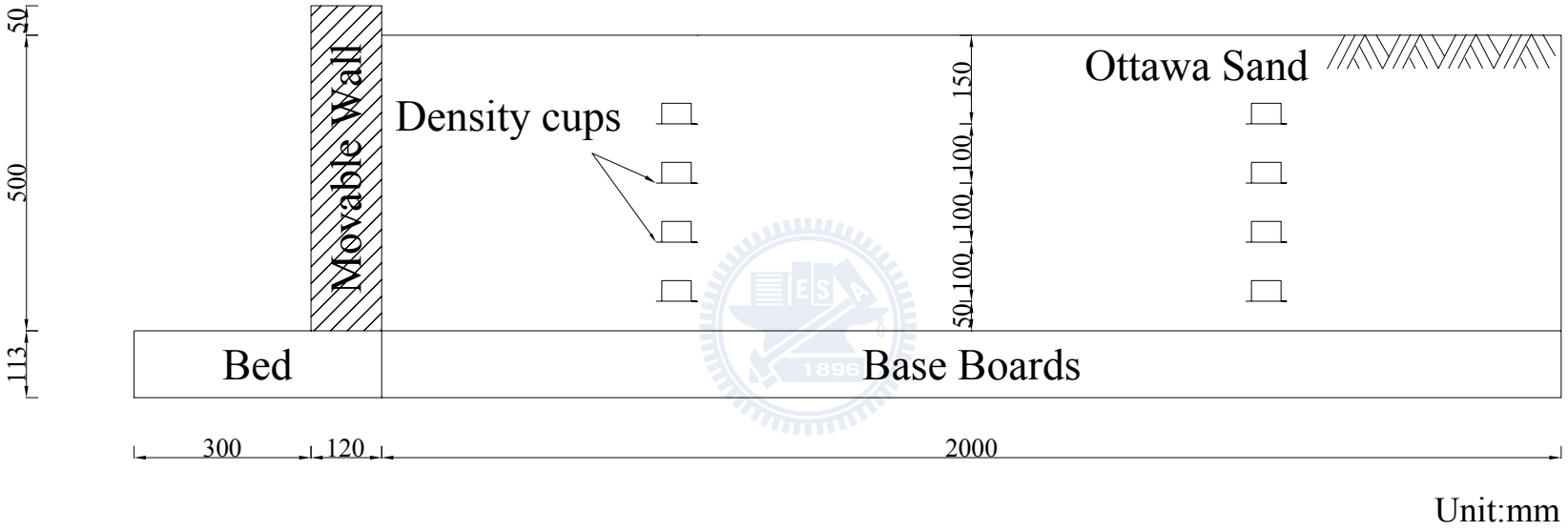

Side – View

Fig. 5.19. Density control cups at different elevation (side-view)

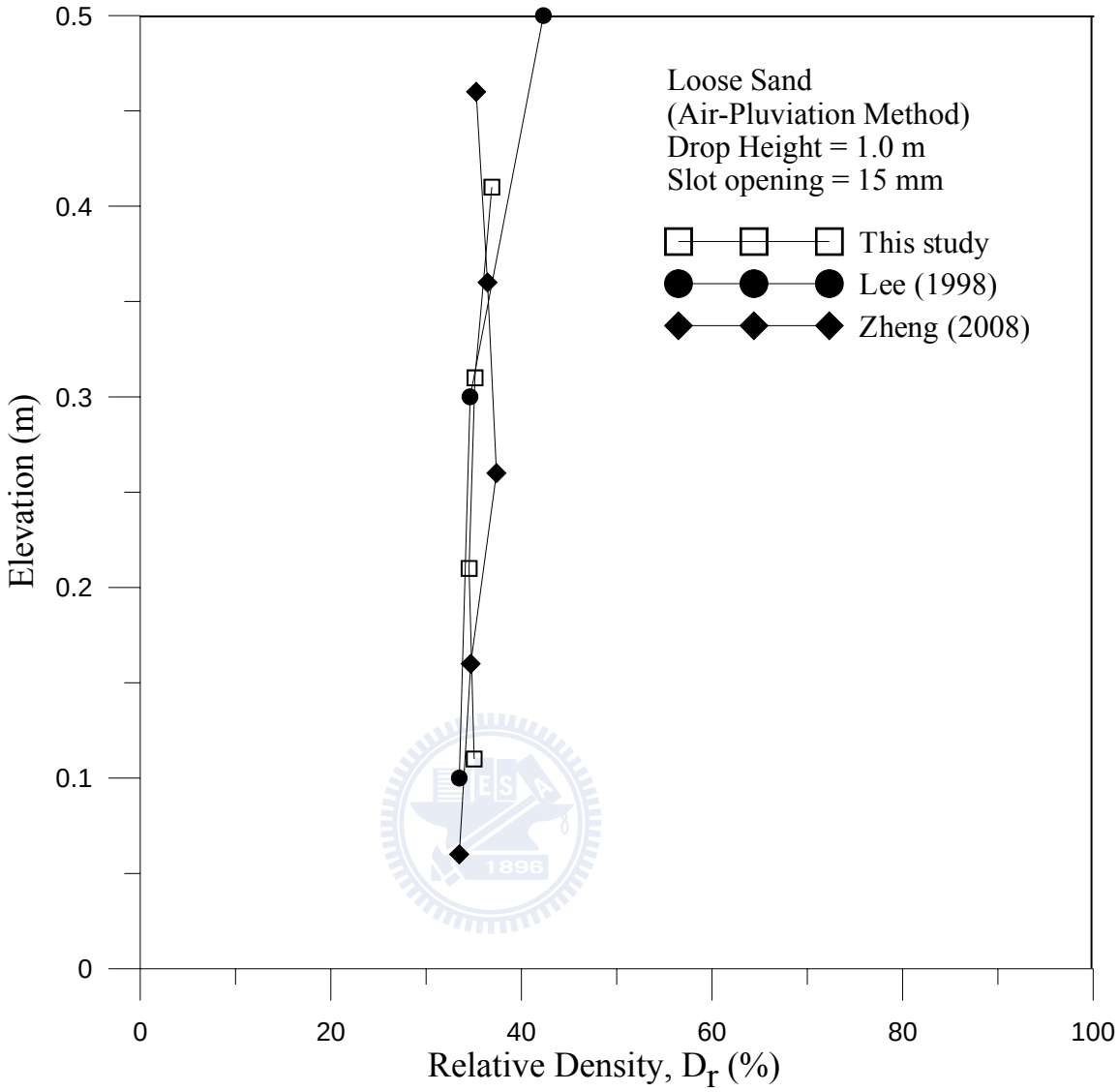

Fig. 5.20. Distribution of soil relative density with depth

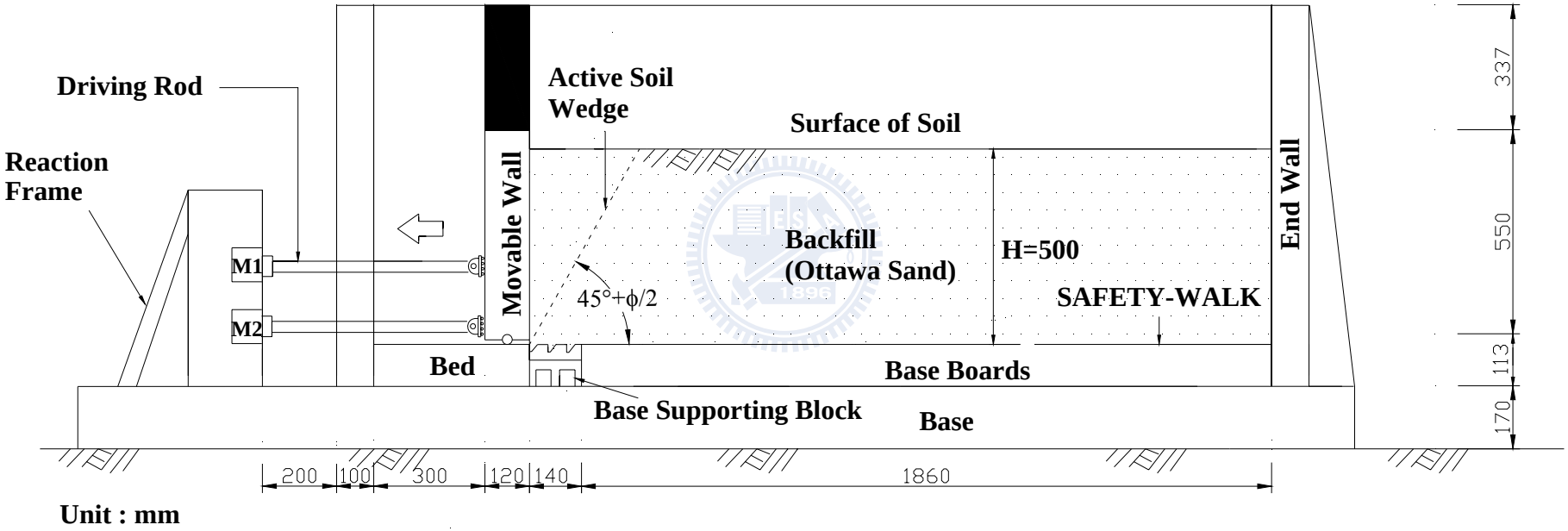

(a)

Fig. 6.1. Model wall test without interface inclination (β = 0°)

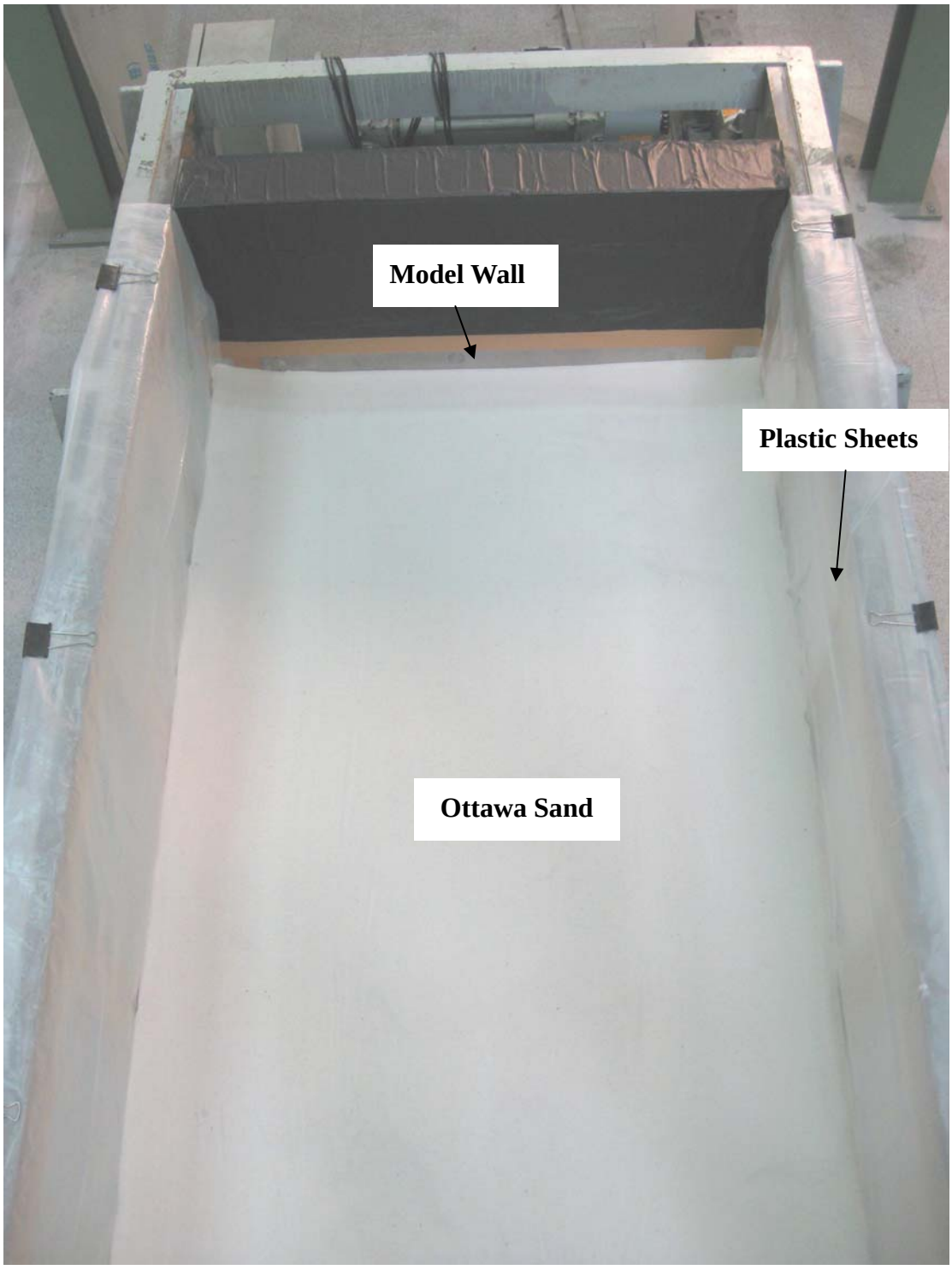

(b)

Fig. 6.1. Model wall test without interface inclination ($\beta = 0°$)

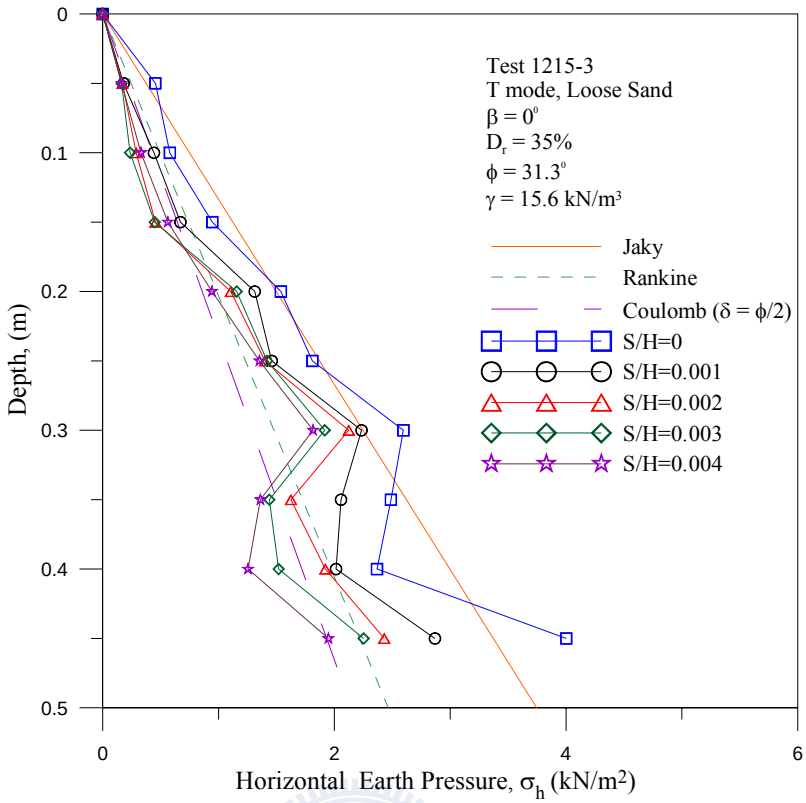

Fig. 6.2. Distribution of horizontal earth pressure for β = 0° (Test 1215-3)

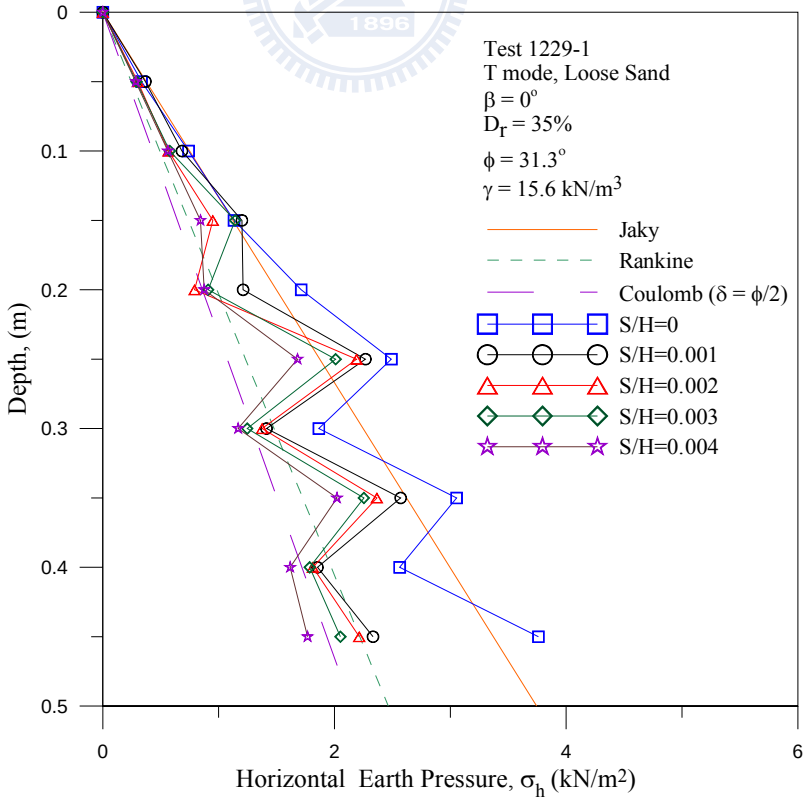

Fig. 6.3. Distribution of horizontal earth pressure for β = 0° (Test 1229-1)

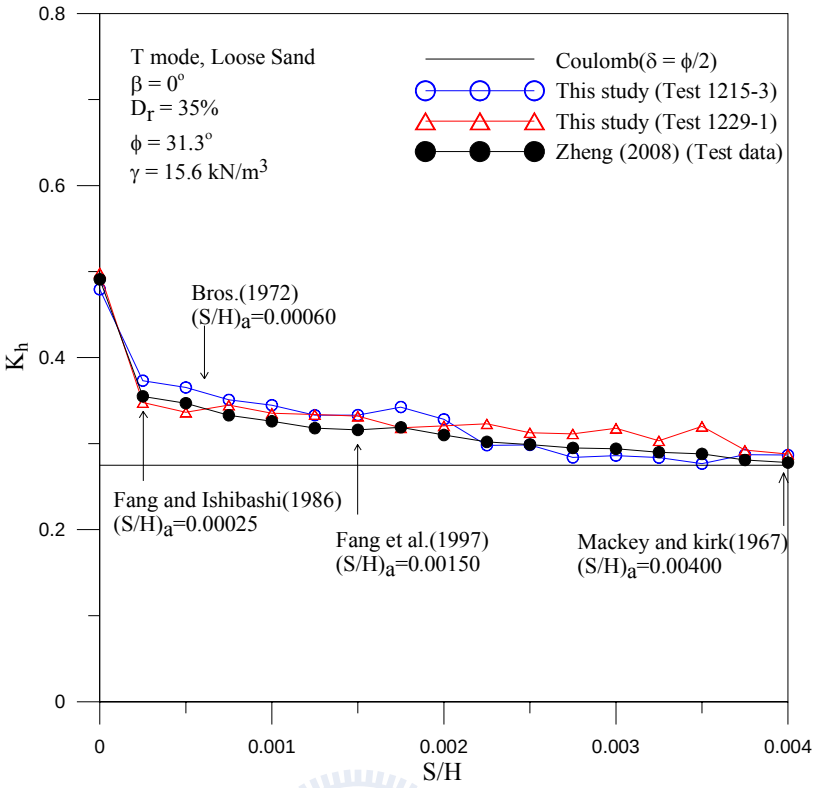

Fig. 6.4. Earth pressure coefficient K_h versus wall movement for β = 0°

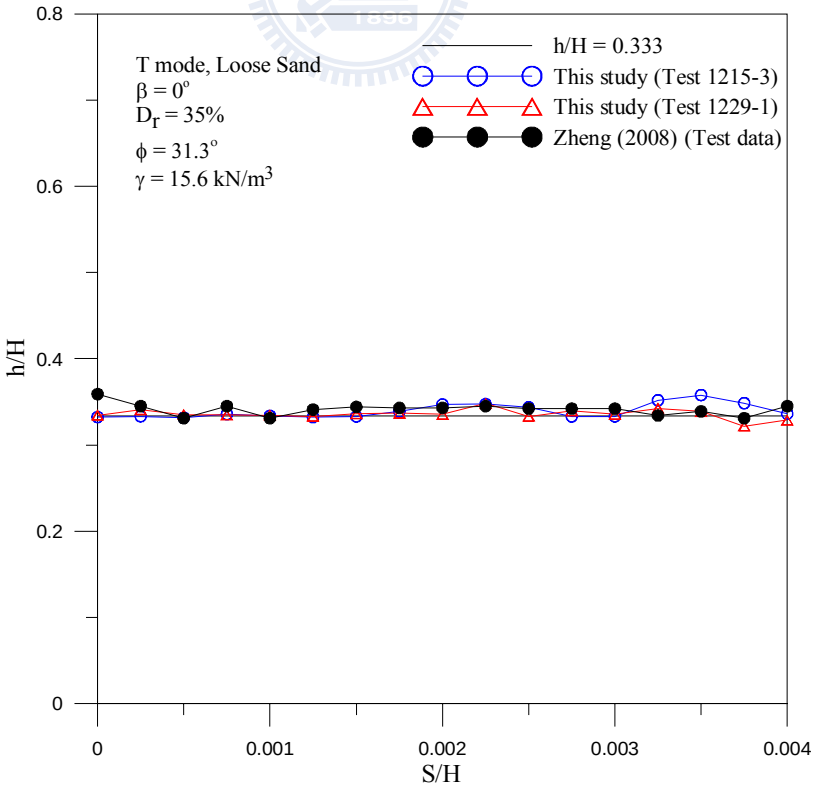

Fig. 6.5. Location of total thrust application for β = 0°

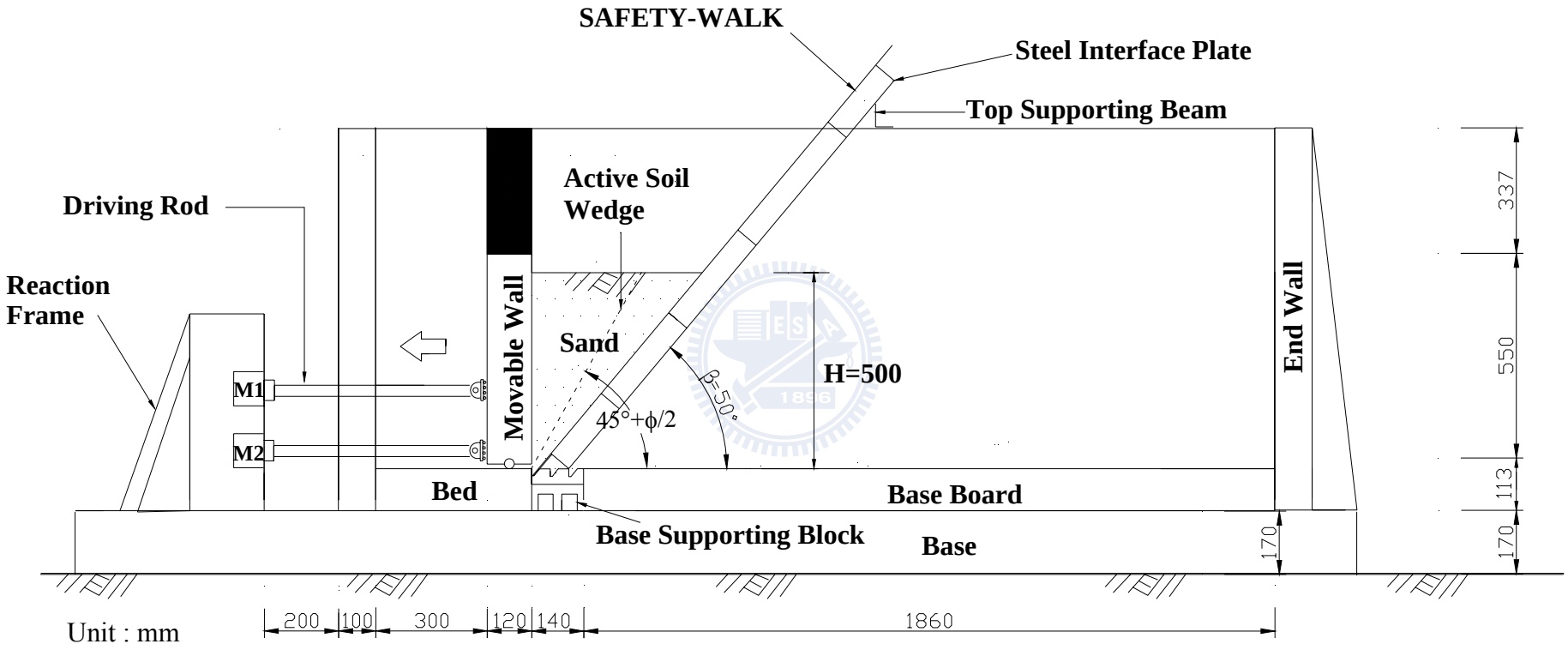

(a)

Fig. 6.6. Model wall test with interface inclination $\beta = 50^0$ and b = 0

(b)

Fig. 6.6. Model wall test with interface inclination $\beta = 50^0$ and b = 0

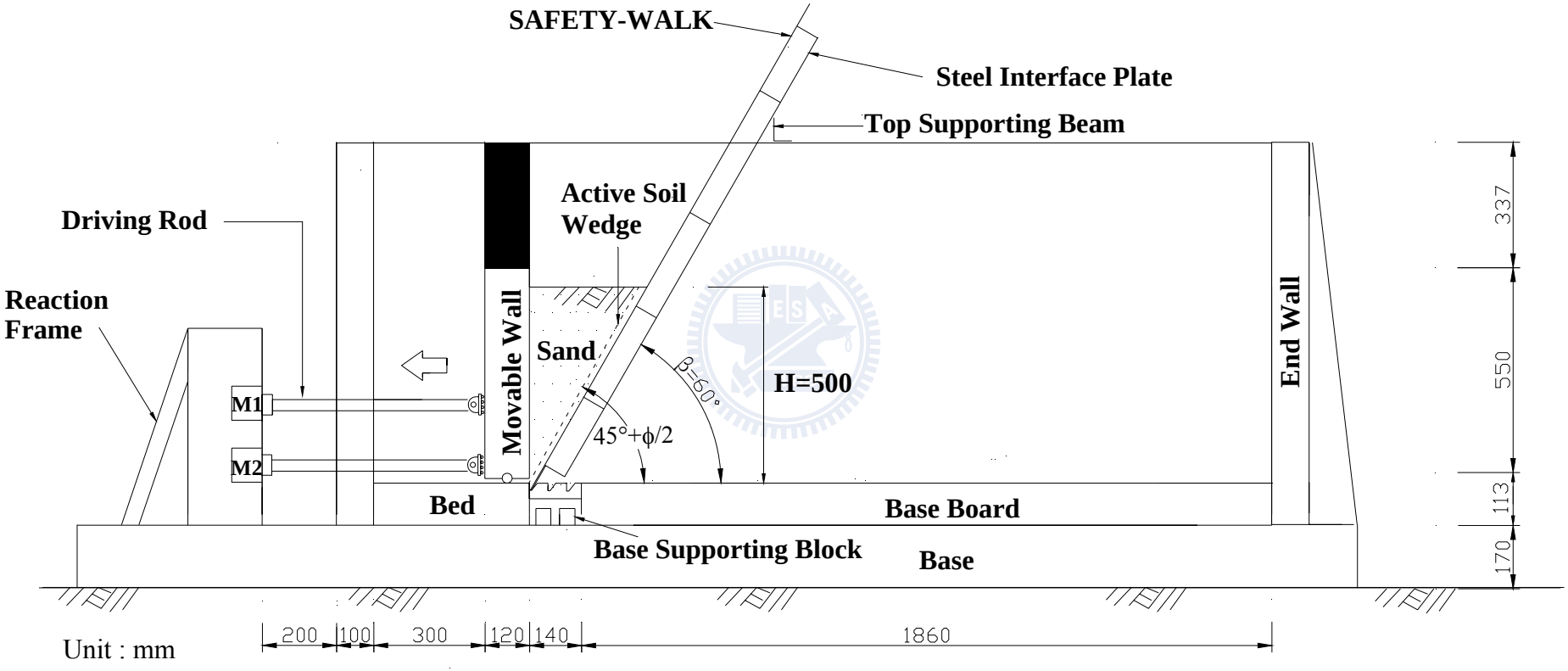

(a)

Fig. 6.7. Model wall test with interface inclination $\beta = 60^0$ and b = 0

(b)

Fig. 6.7. Model wall test with interface inclination $\beta = 60^0$ and b = 0

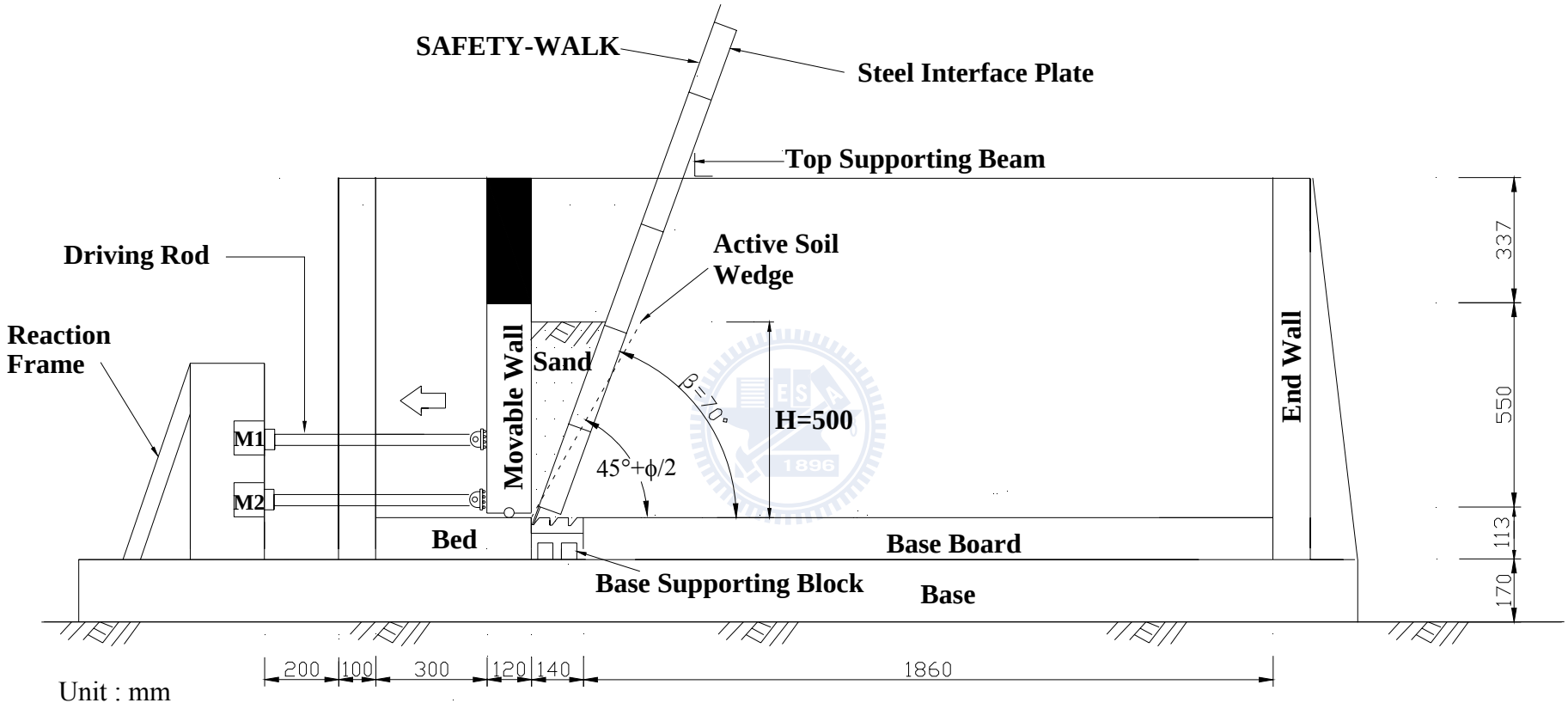

(a)

Fig. 6.8. Model wall test with interface inclination $\beta = 70^0$ and b = 0

(b)

Fig. 6.8. Model wall test with interface inclination $\beta = 70^0$ and b = 0

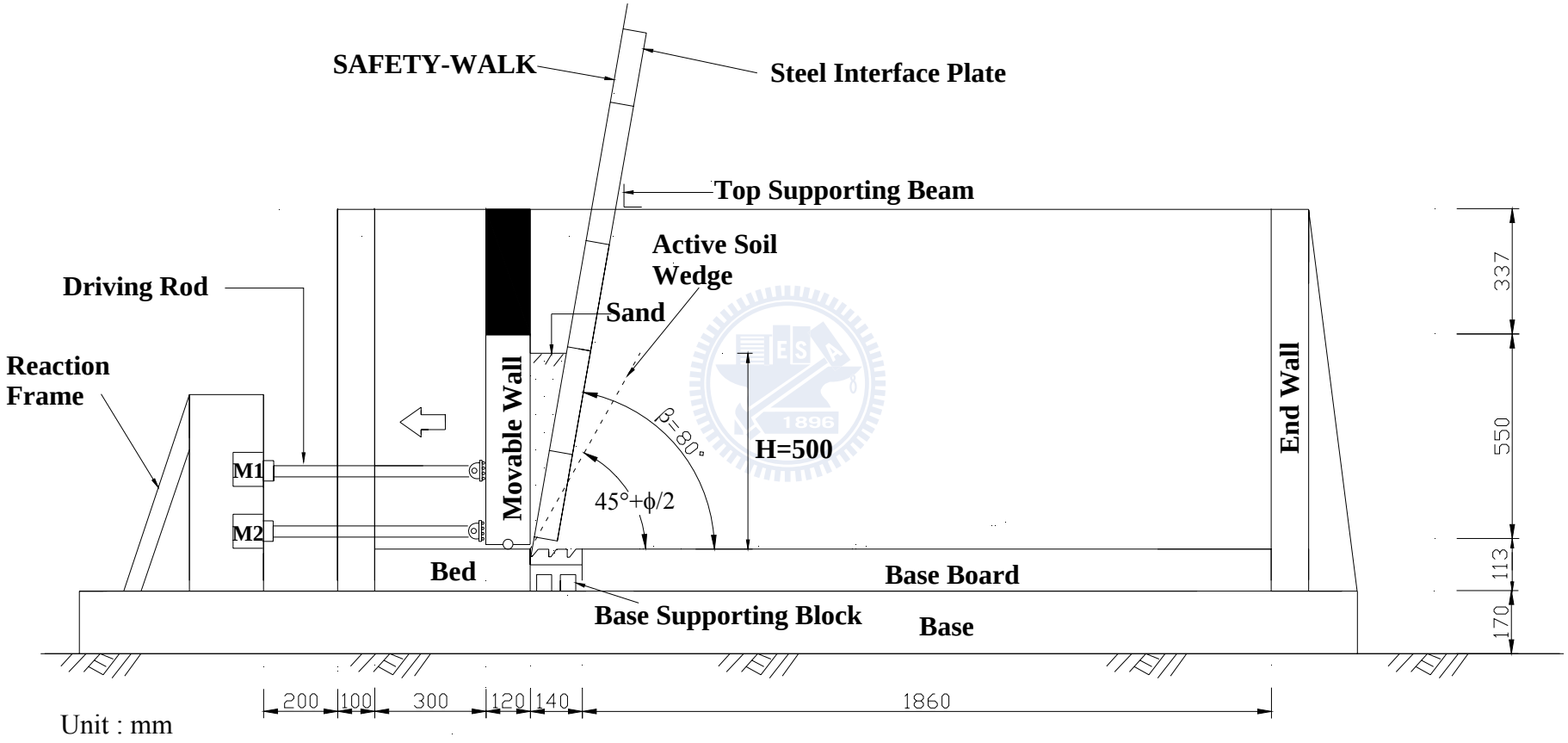

(a)

Fig. 6.9. Model wall test with interface inclination β = $80^0$and b= 0

(b)

Fig. 6.9. Model wall test with interface inclination $\beta = 80^0$ and b = 0

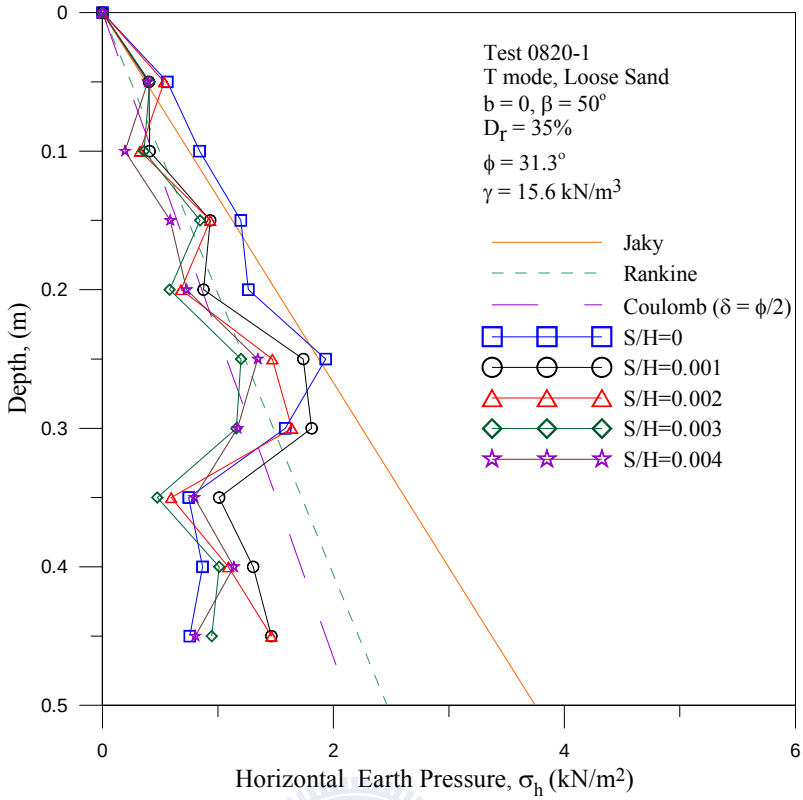

Fig. 6.10. Distribution of horizontal earth pressure for β = 50° (Test 0820-1)

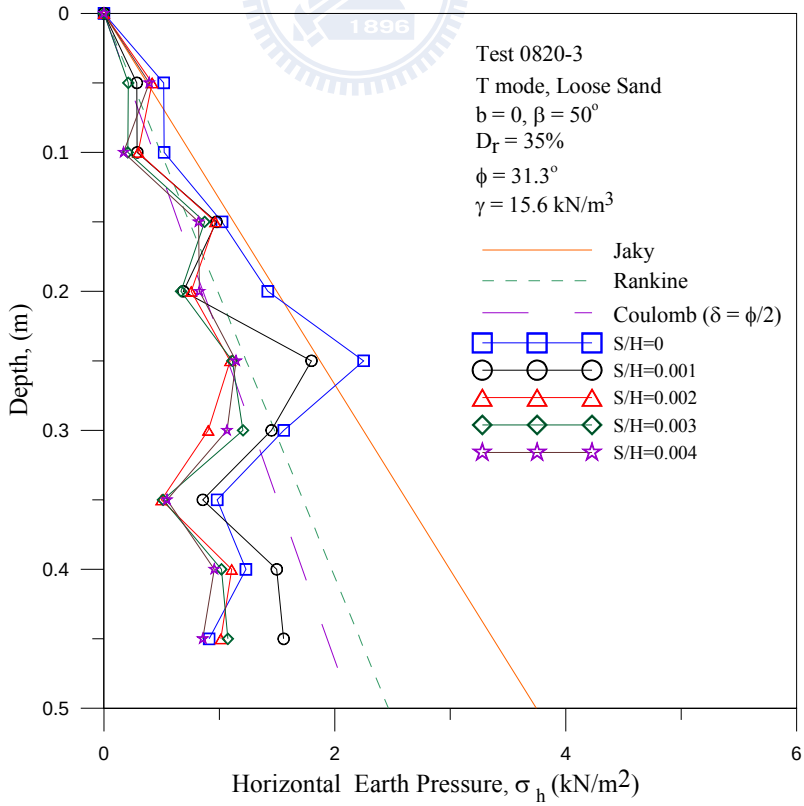

Fig. 6.11. Distribution of horizontal earth pressure for β = 50° (Test 0820-3)

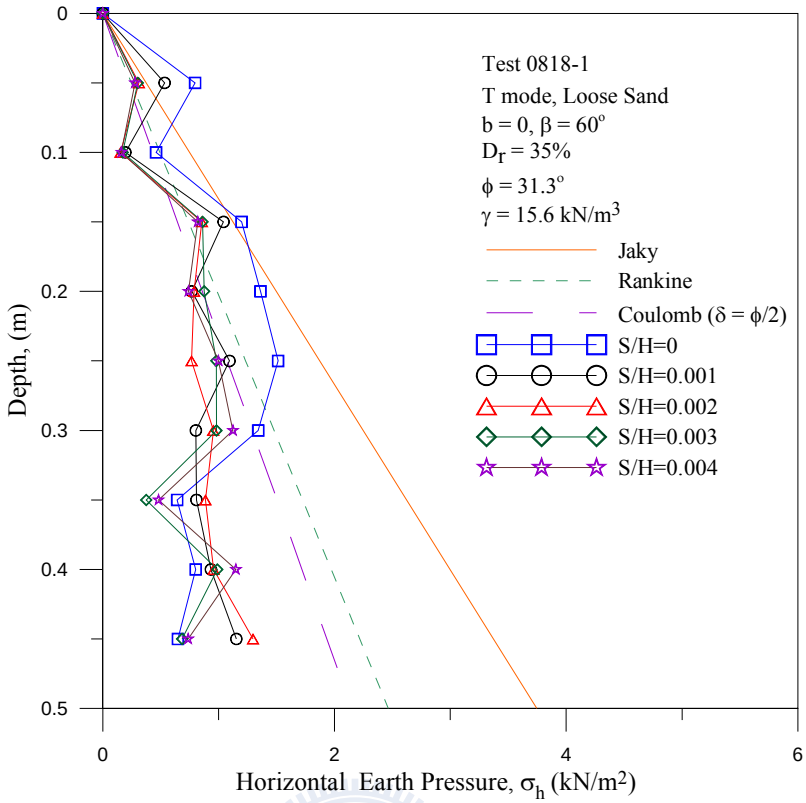

Fig. 6.12. Distribution of horizontal earth pressure for β = 60° (Test 0818-1)

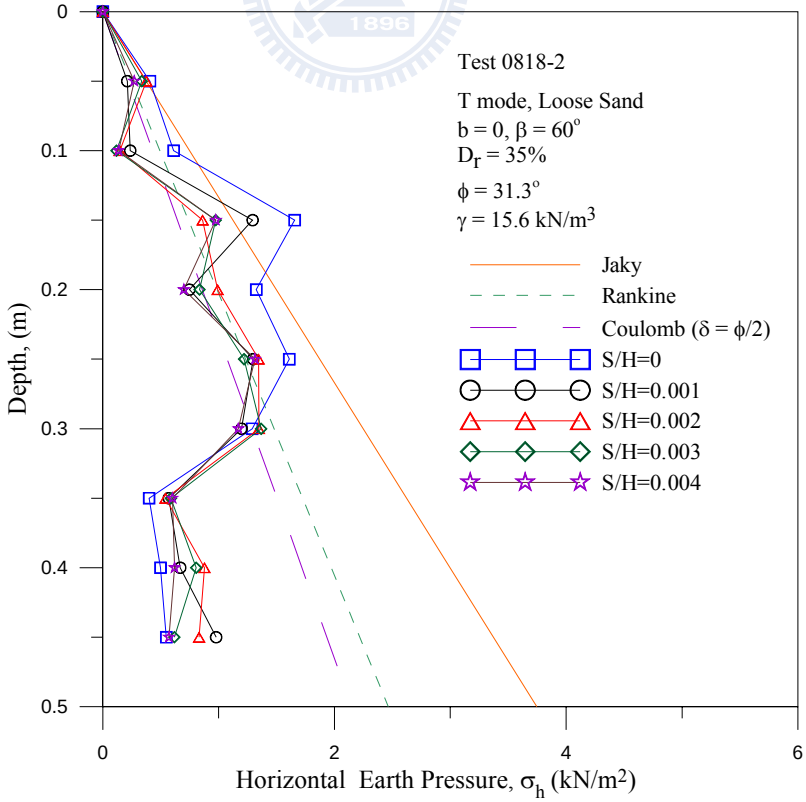

Fig. 6.13. Distribution of horizontal earth pressure for β = 60° (Test 0818-2)

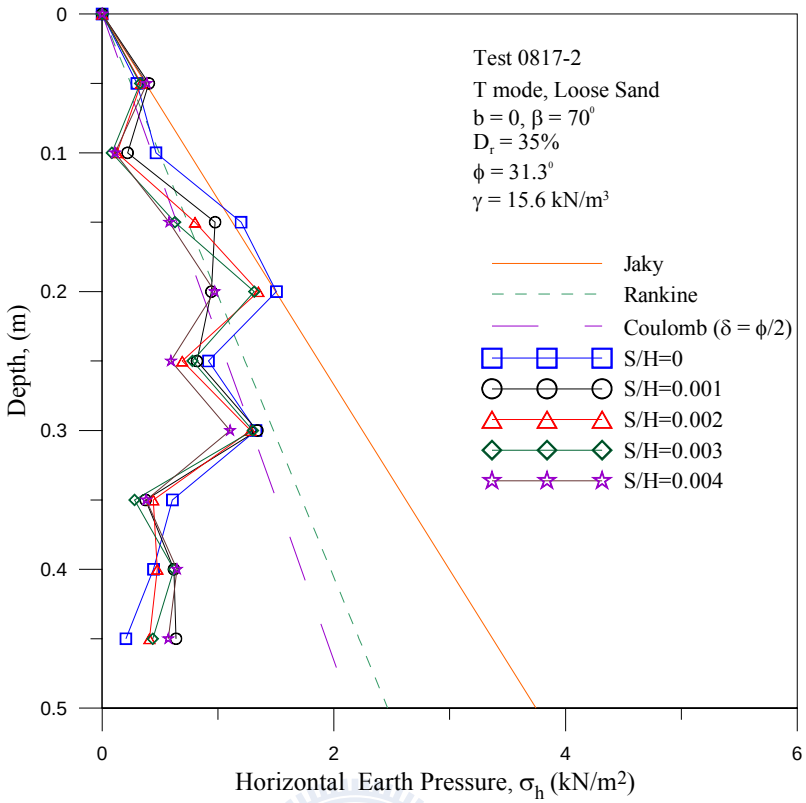

Fig. 6.14. Distribution of horizontal earth pressure for β = 70° (Test 0817-2)

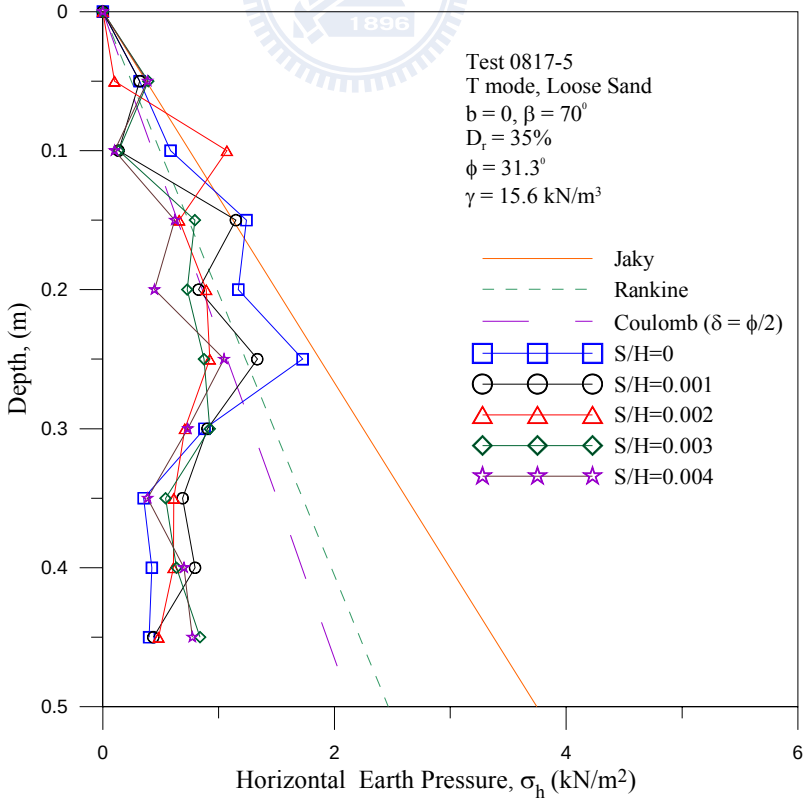

Fig. 6.15. Distribution of horizontal earth pressure for β = 70° (Test 0817-5)

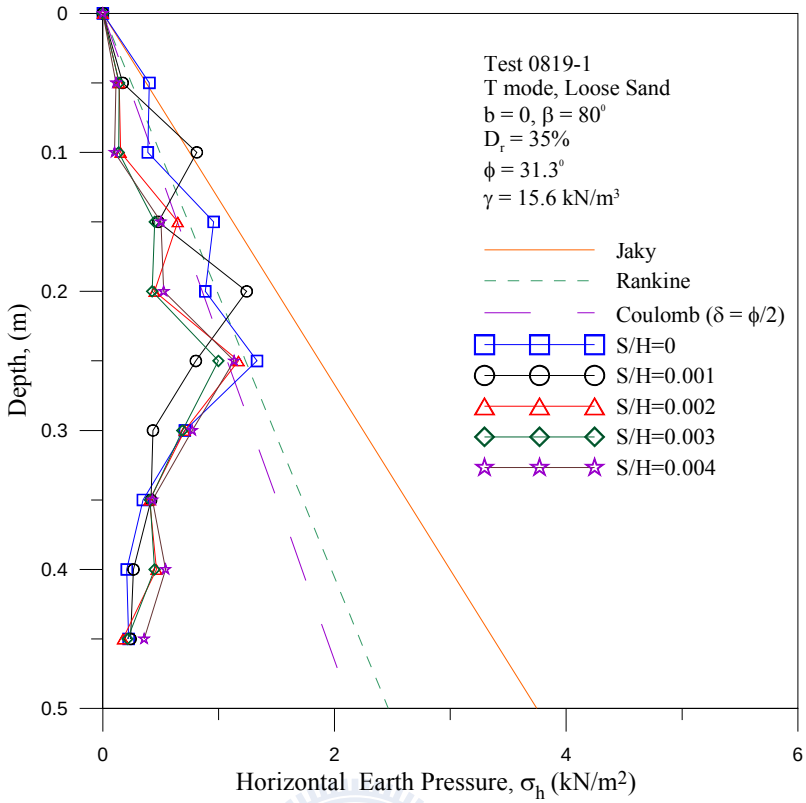

Fig. 6.16. Distribution of horizontal earth pressure for β = 80° (Test 0819-1)

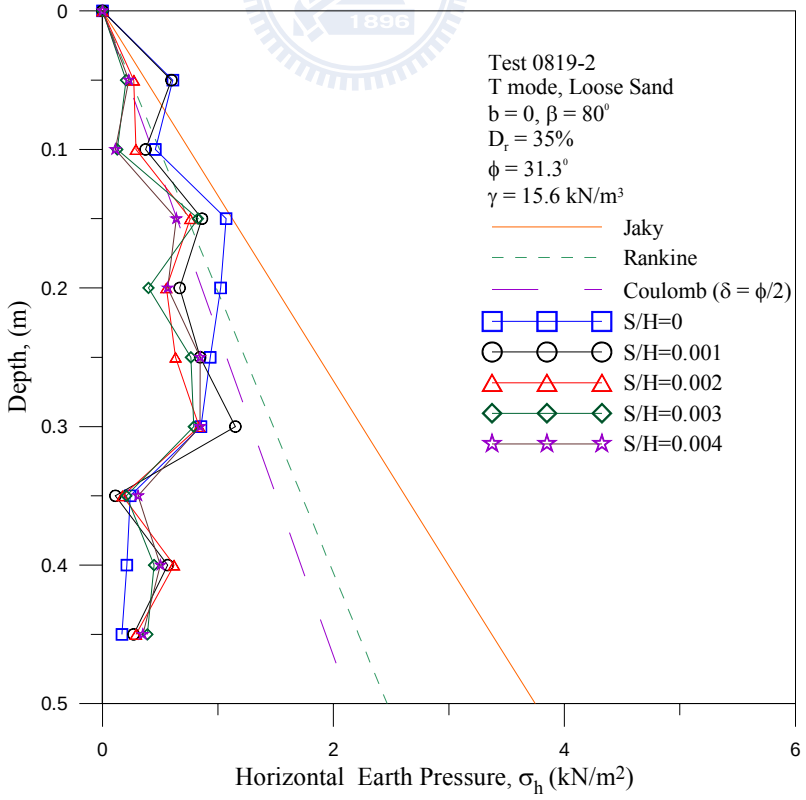

Fig. 6.17. Distribution of horizontal earth pressure for β = 80° (Test 0819-2)

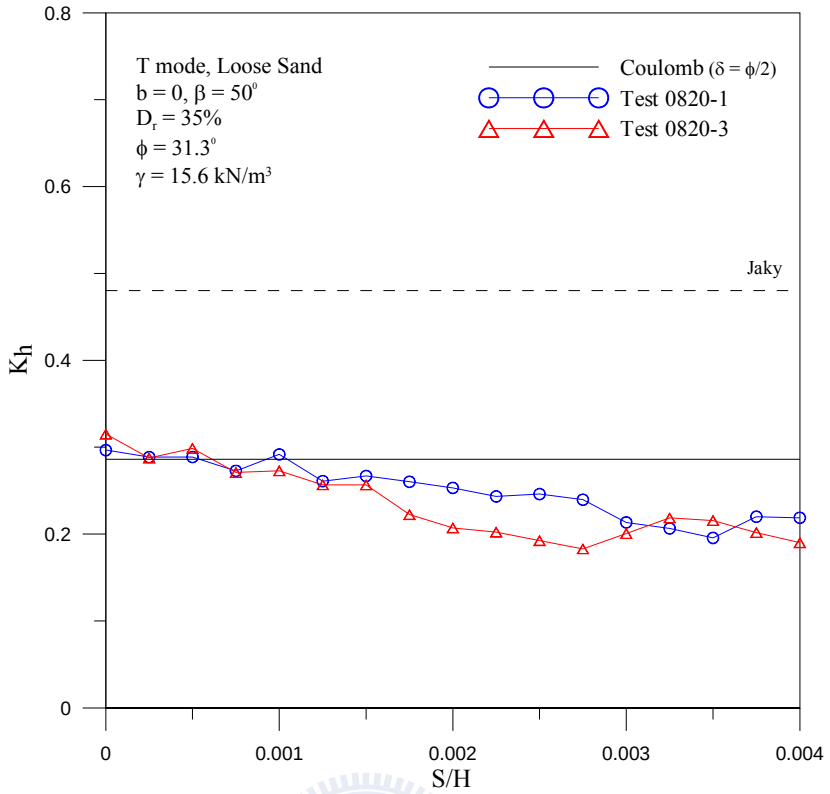

Fig. 6.18. Earth pressure coefficient K_h versus wall movement for β = 50°

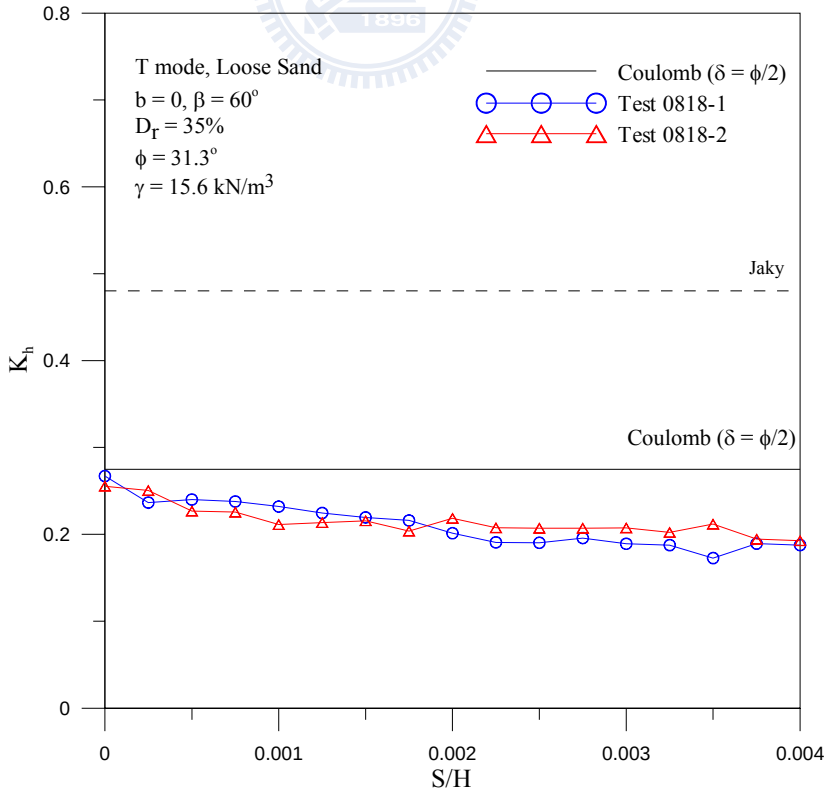

Fig. 6.19. Earth pressure coefficient K_h versus wall movement for β = 60°

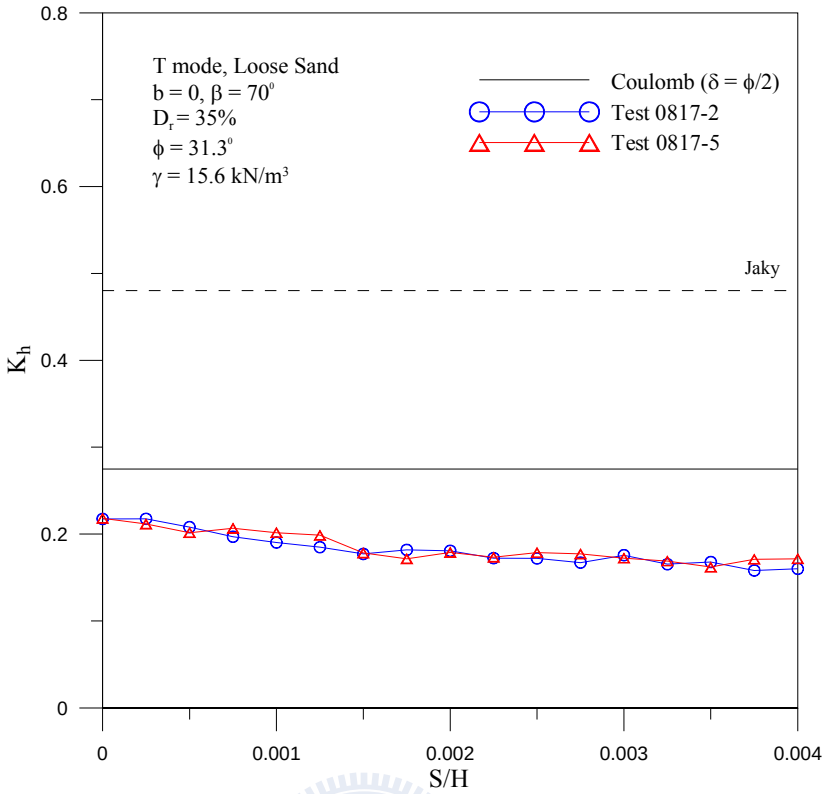

Fig. 6.20. Earth pressure coefficient K_h versus wall movement for β = 70°

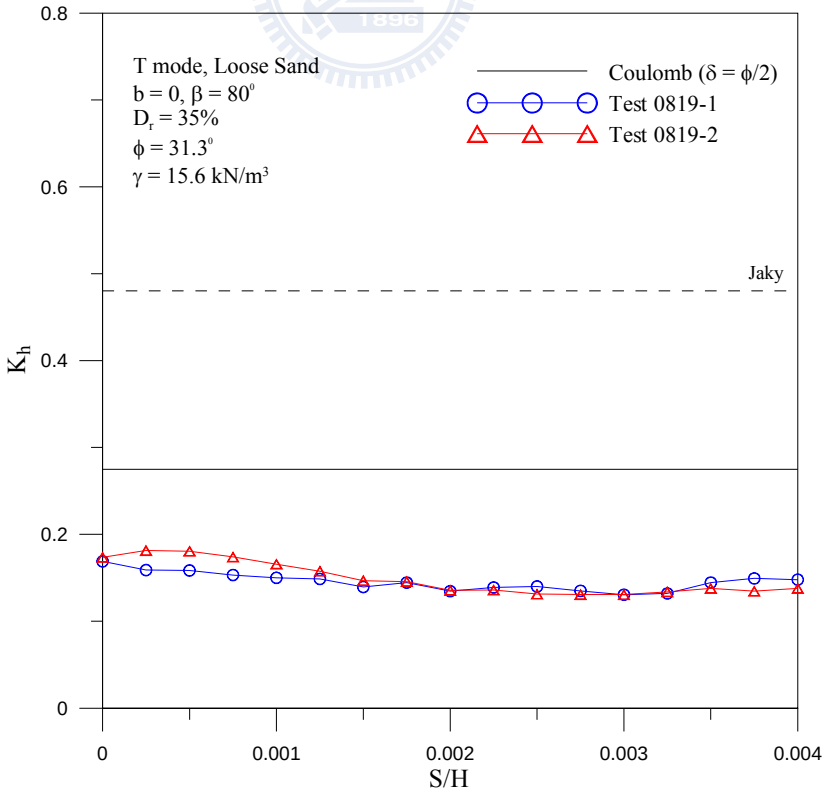

Fig. 6.21. Earth pressure coefficient K_h versus wall movement for β = 80°

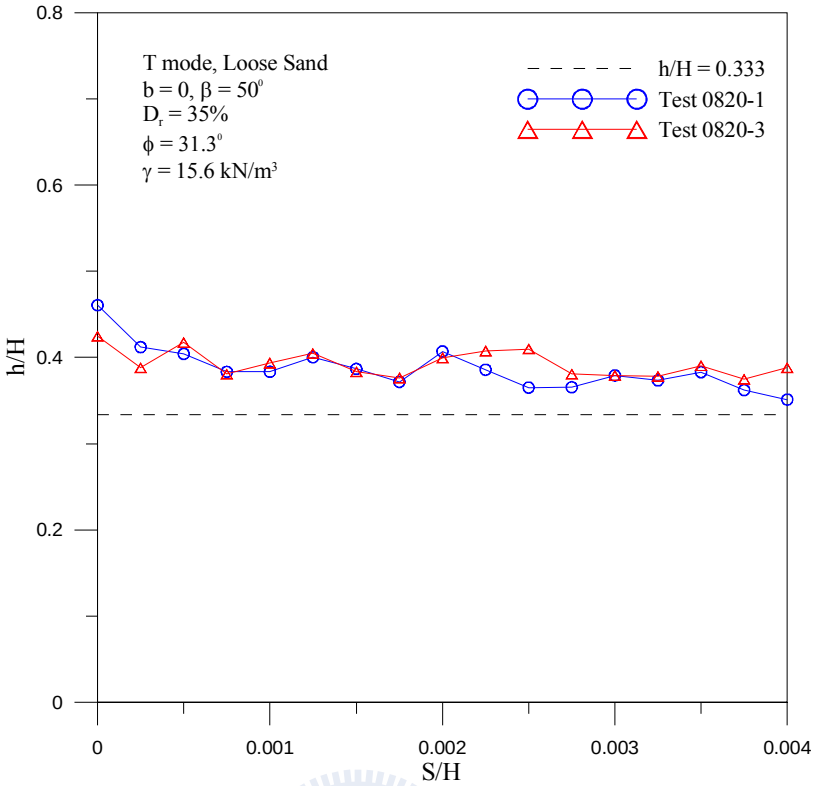

Fig. 6.22. Location of total thrust application for β = 50°

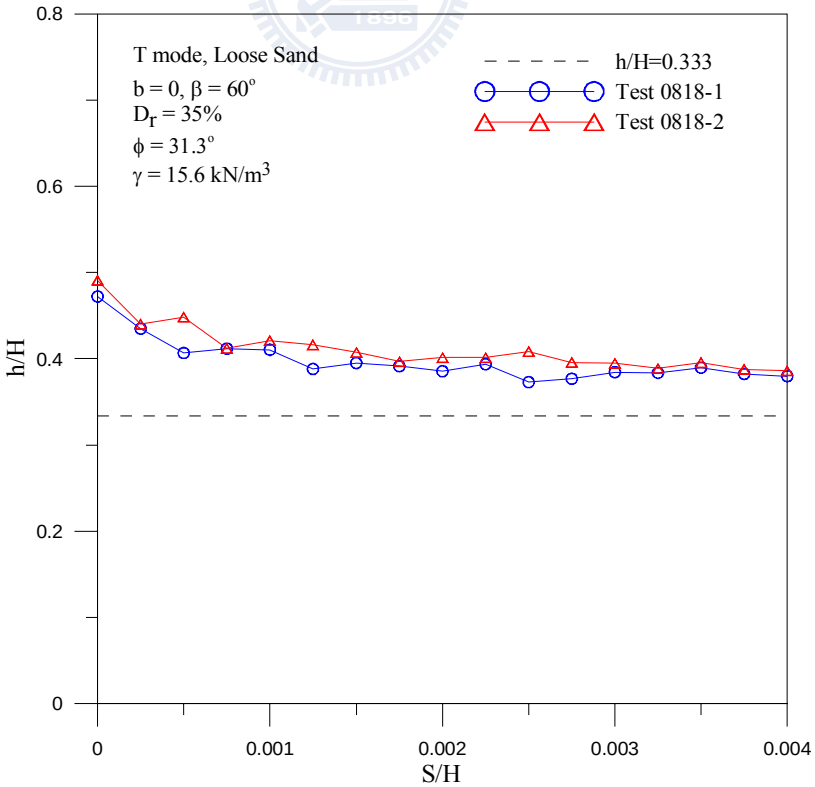

Fig. 6.23. Location of total thrust application for β = 60°

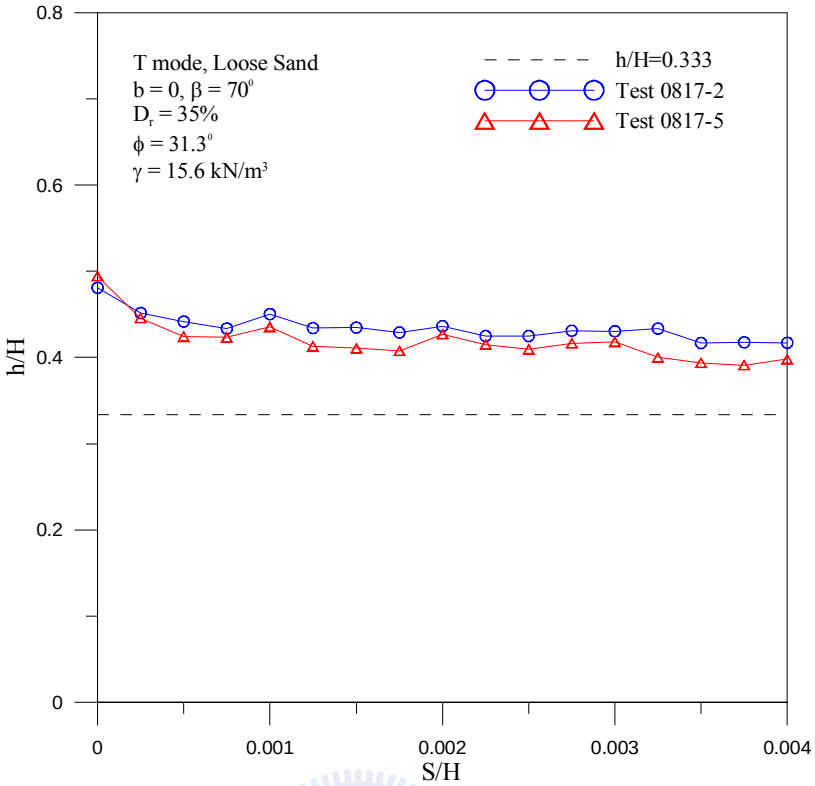

Fig. 6.24. Location of total thrust application for β = 70°

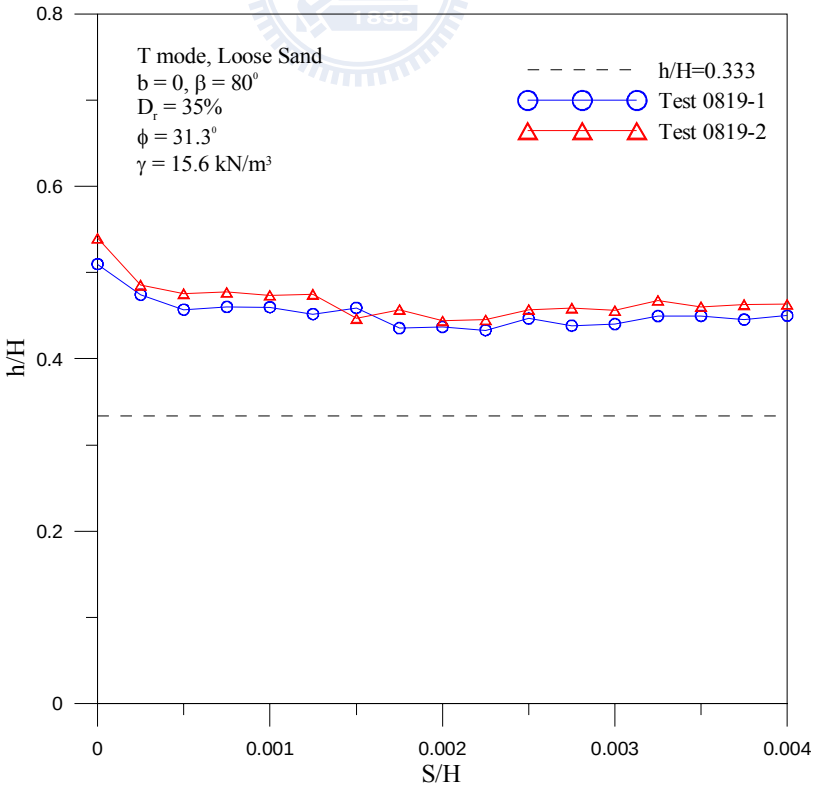

Fig. 6.25. Location of total thrust application for β = 80°

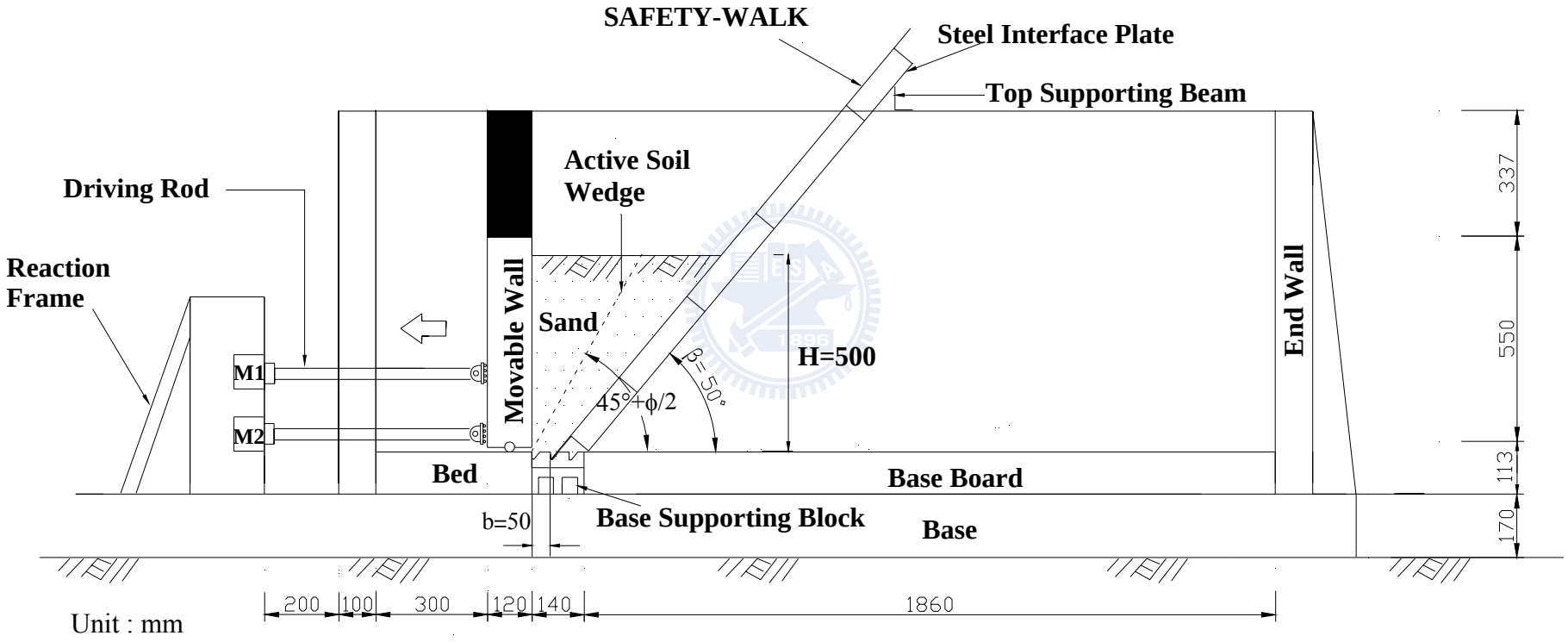

(a)

Fig. 6.26. Model wall test with interface inclination $\beta = 50^0$and b = 50 mm

(b)

Fig. 6.26. Model wall test with interface inclination $\beta = 50^0$ and b = 50 mm

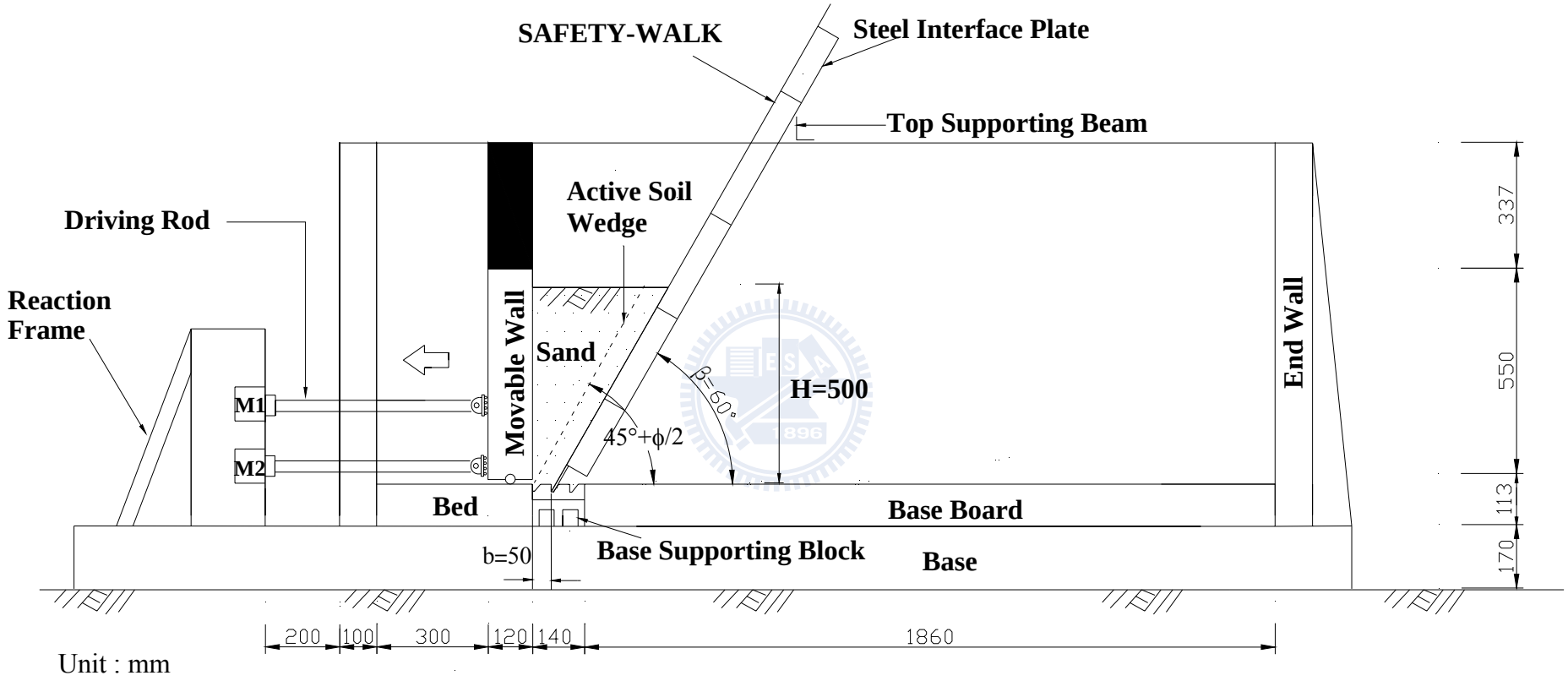

(a)

Fig. 6.27. Model wall test with interface inclination $\beta = 60^0$ and b = 50 mm

(b)

Fig. 6.27. Model wall test with interface inclination $\beta = 60^0$and b = 50 mm

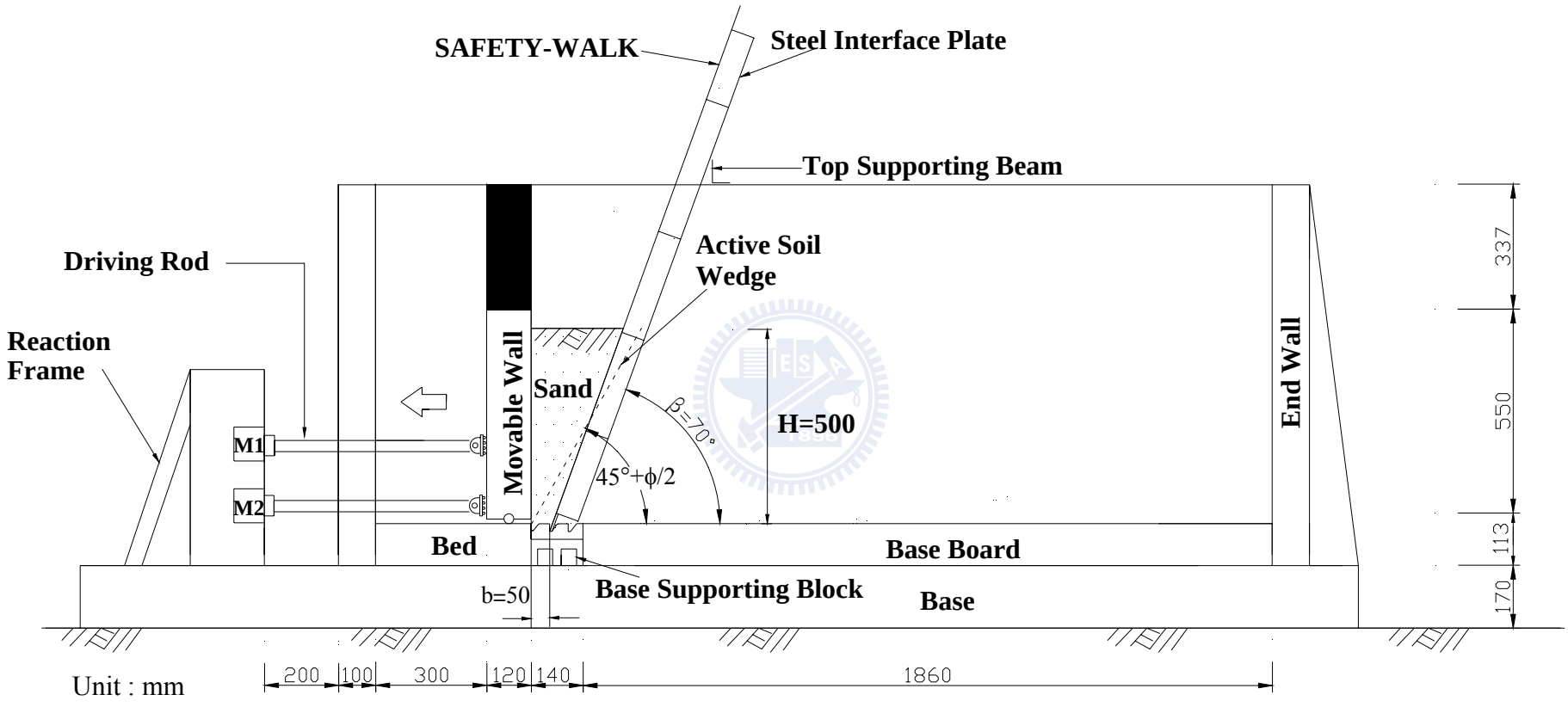

(a)

Fig. 6.28. Model wall test with interface inclination $\beta = 70^0$ and b = 50 mm

(b)

Fig. 6.28. Model wall test with interface inclination $\beta = 70^0$ and b = 50 mm

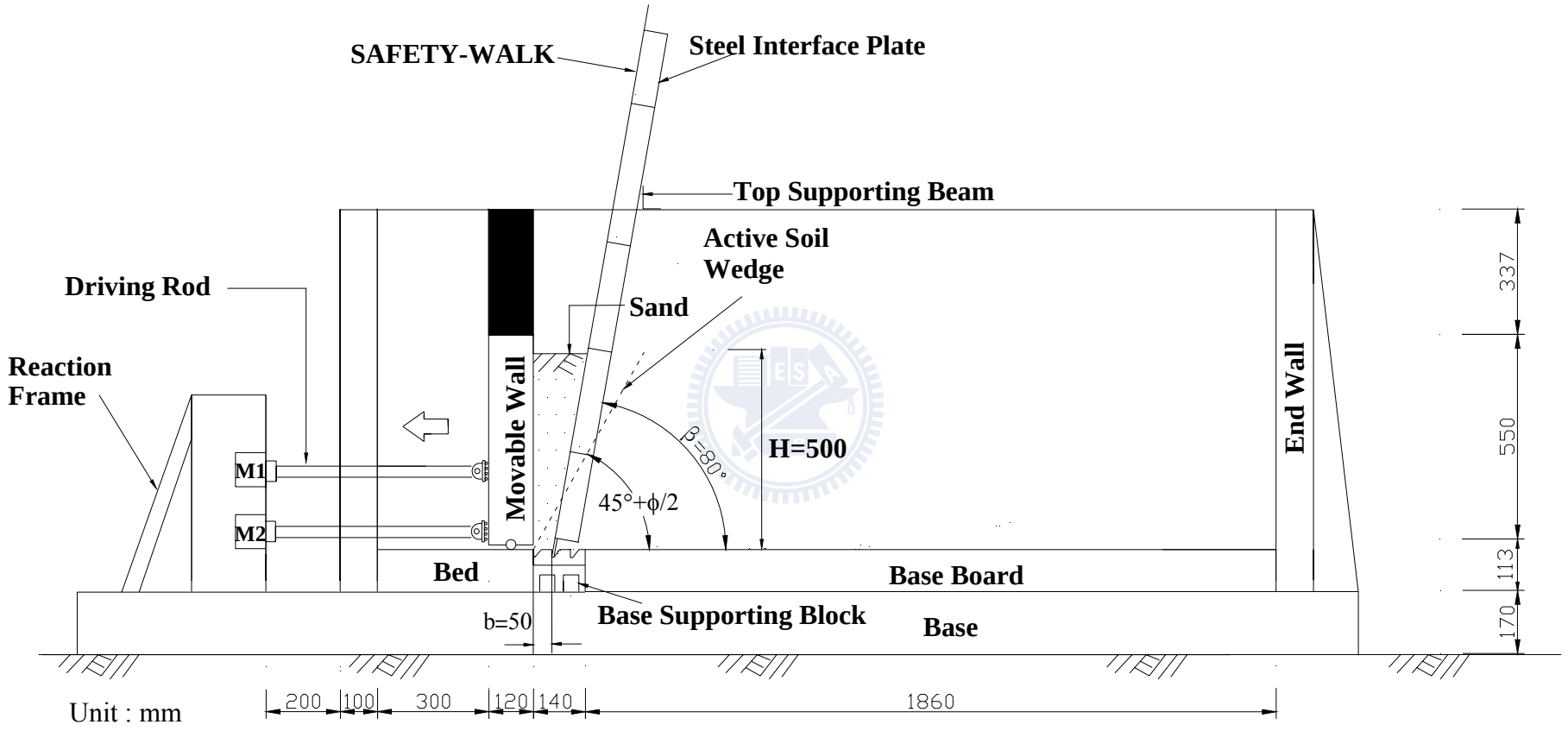

(a)

Fig. 6.29. Model wall test with interface inclination $\beta = 80^0$and b = 50 mm

(b)

Fig. 6.29. Model wall test with interface inclination $\beta = 80^0$ and b = 50 mm

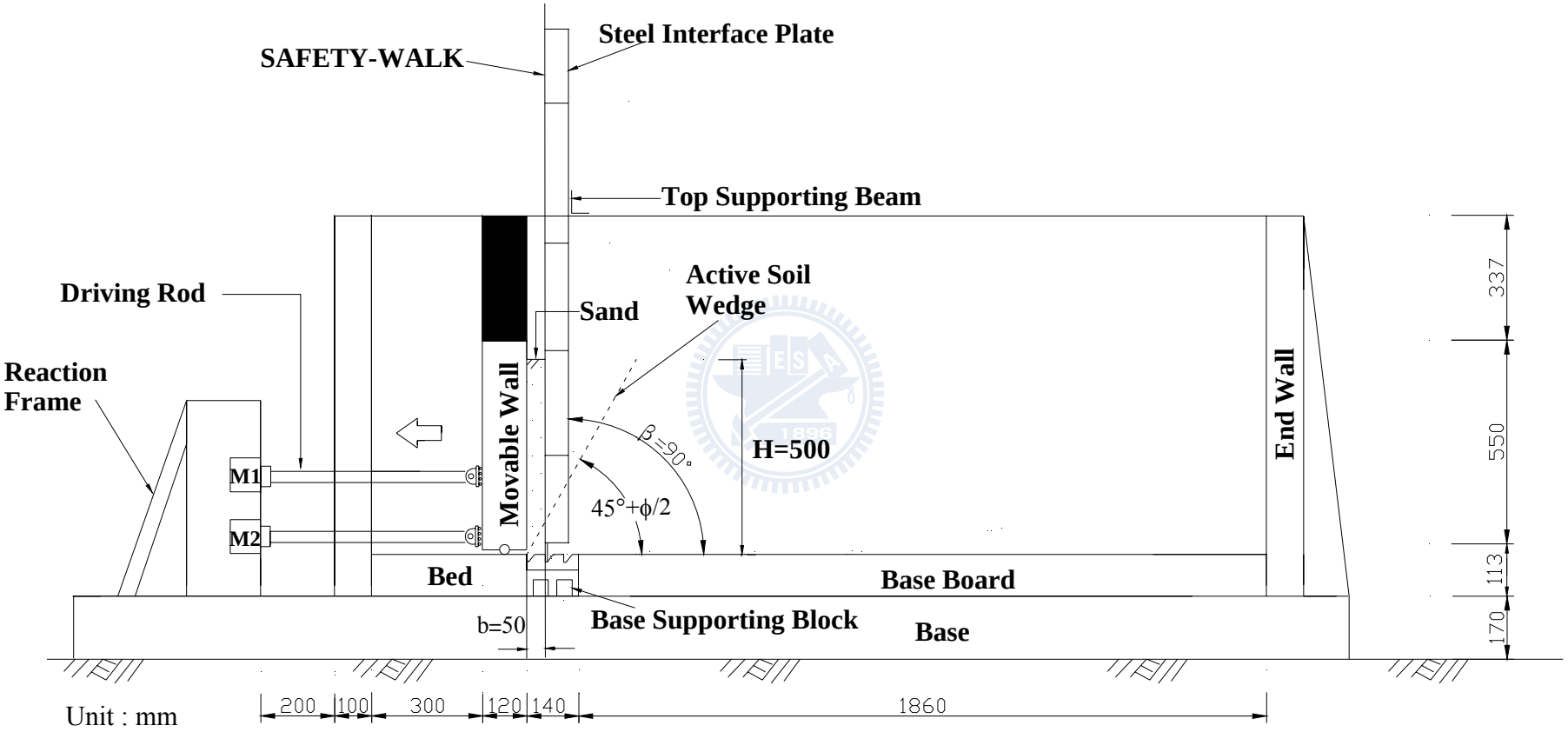

(a)

Fig. 6.30. Model wall test with interface inclination $\beta = 90^0$ and b = 50 mm

(b)

Fig. 6.30. Model wall test with interface inclination $\beta = 90^0$ and b = 50 mm

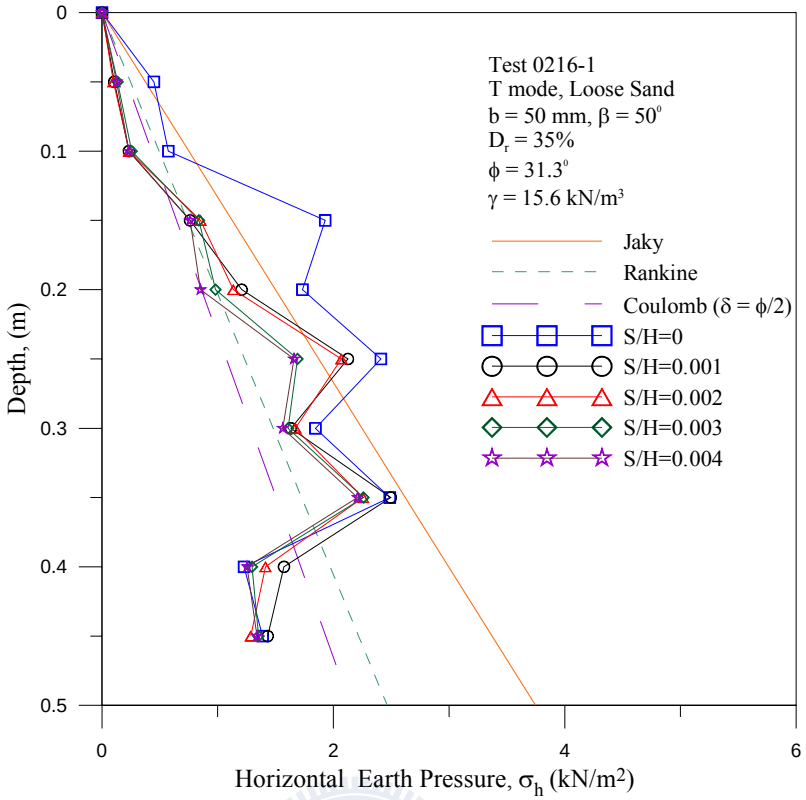

Fig. 6.31. Distribution of horizontal earth pressure for β = 50° and b = 50 mm (Test0216-1)

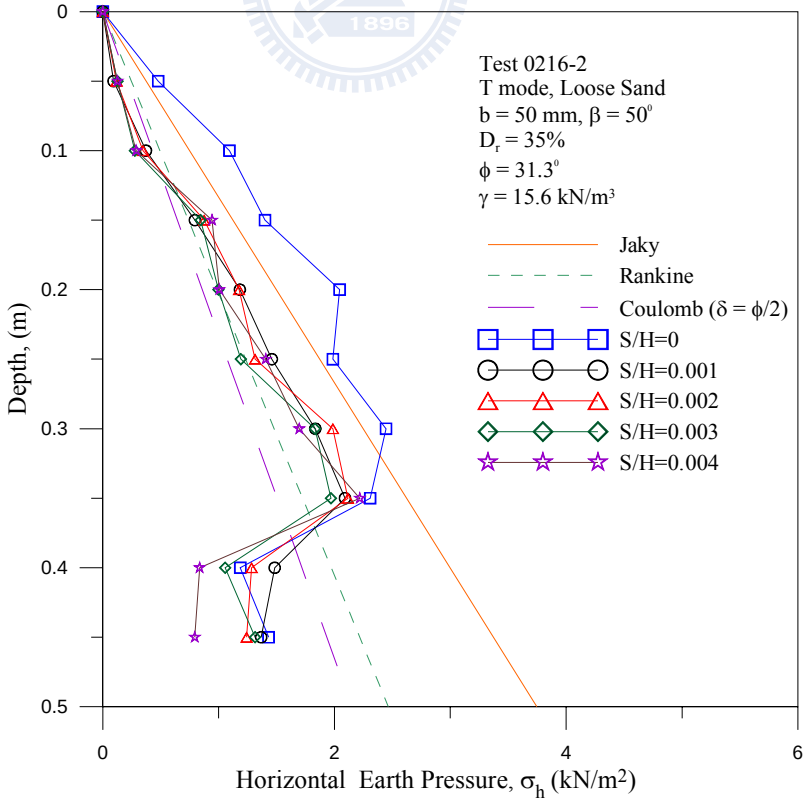

Fig. 6.32. Distribution of horizontal earth pressure for β = 50° and b= 50 mm (Test 0216-2)

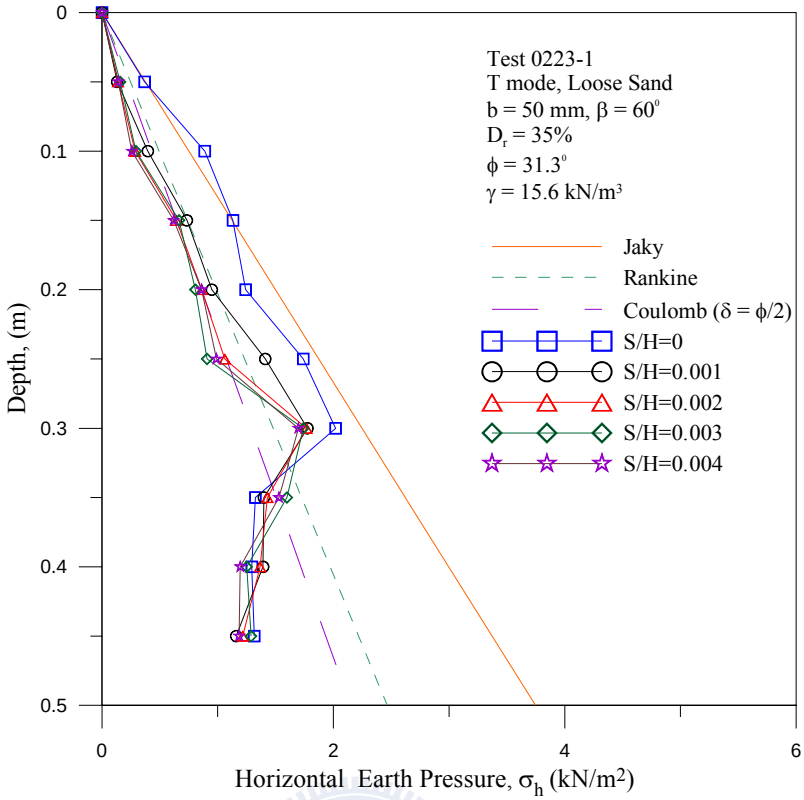

Fig. 6.33. Distribution of horizontal earth pressure for β = 60° and b = 50 mm (Test 0223-1)

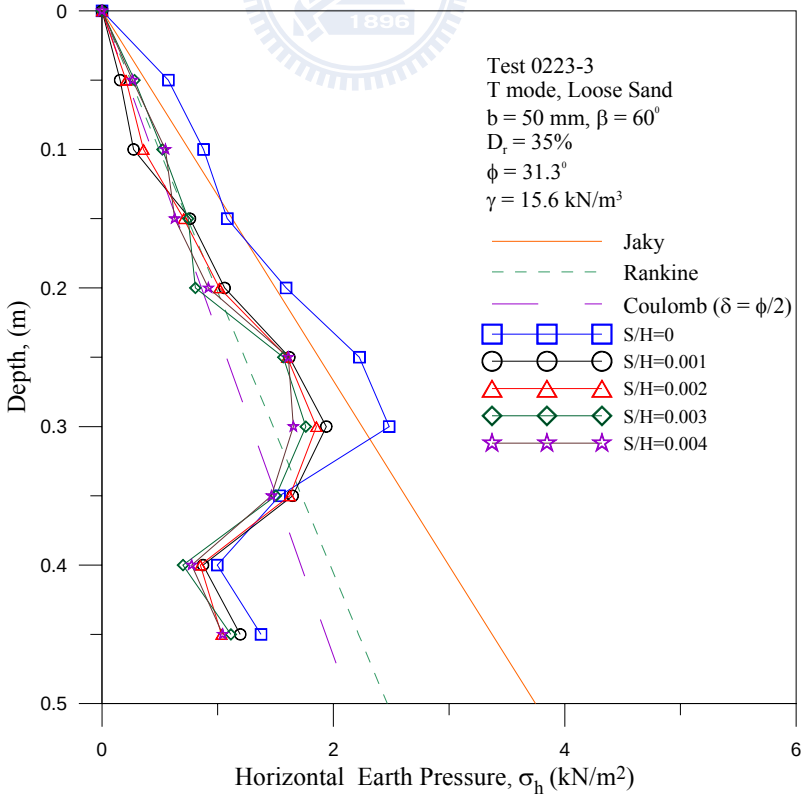

Fig. 6.34. Distribution of horizontal earth pressure for β = 60° and b= 50 mm (Test 0223-1)

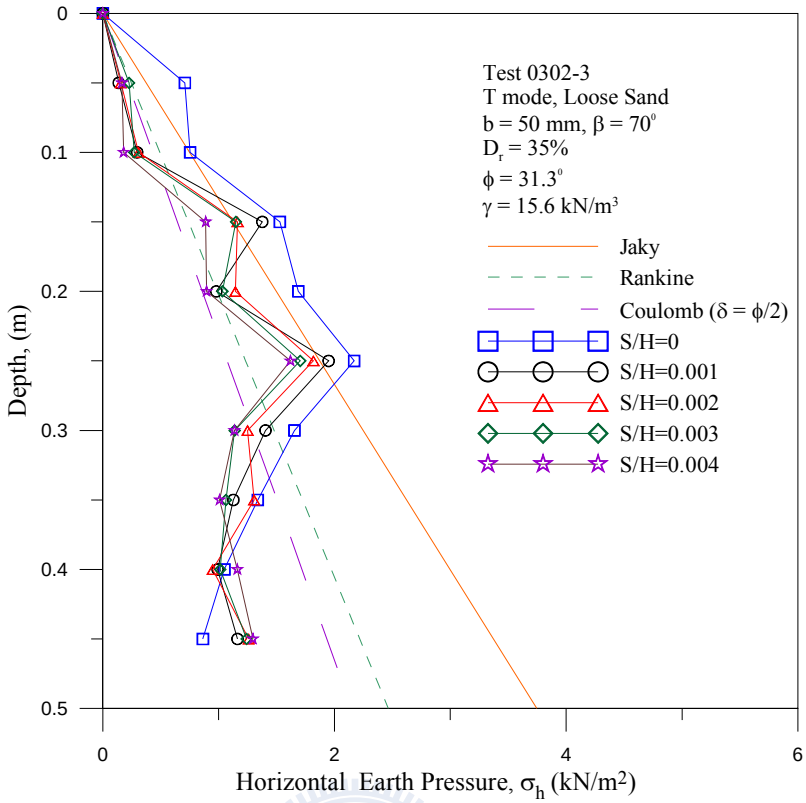

Fig. 6.35. Distribution of horizontal earth pressure for β = 70° and b = 50 mm (Test 0302-3)

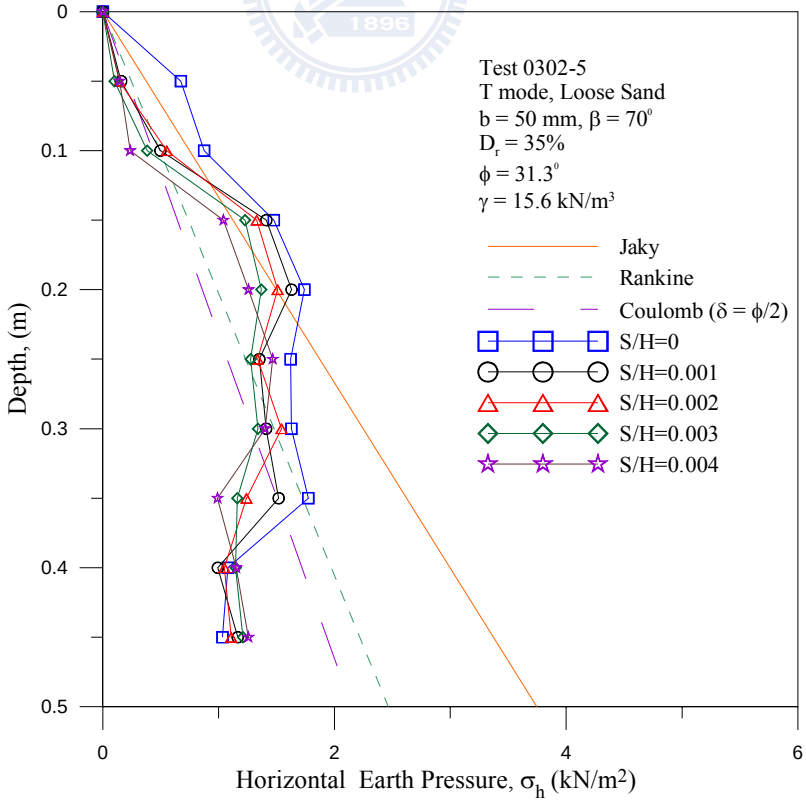

Fig. 6.36. Distribution of horizontal earth pressure for β = 70° and b= 50 mm (Test 0302-5)

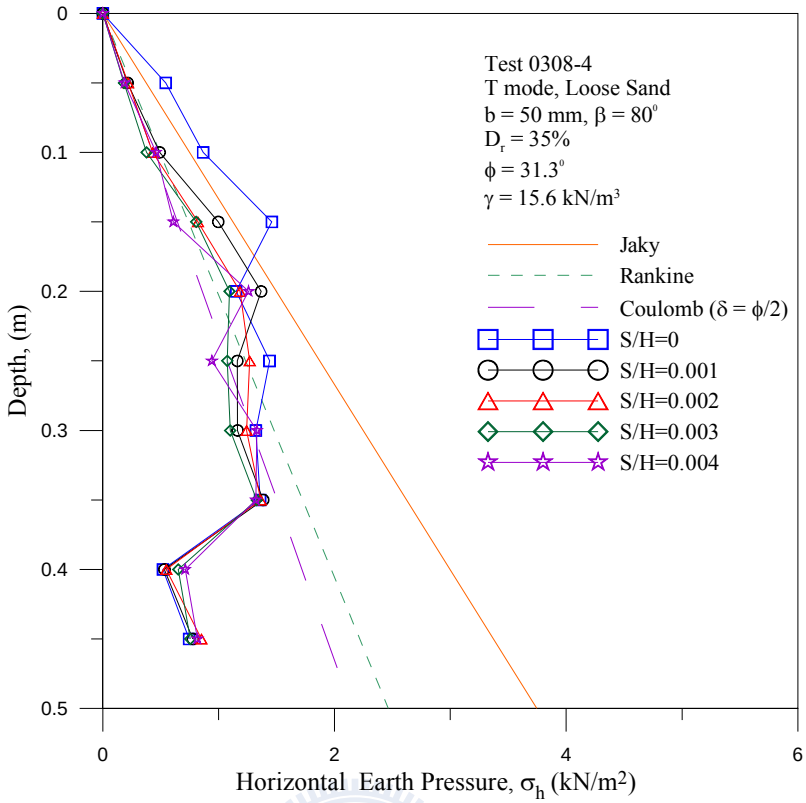

Fig. 6.37. Distribution of horizontal earth pressure for β = 80° and b = 50 mm (Test 0308-4)

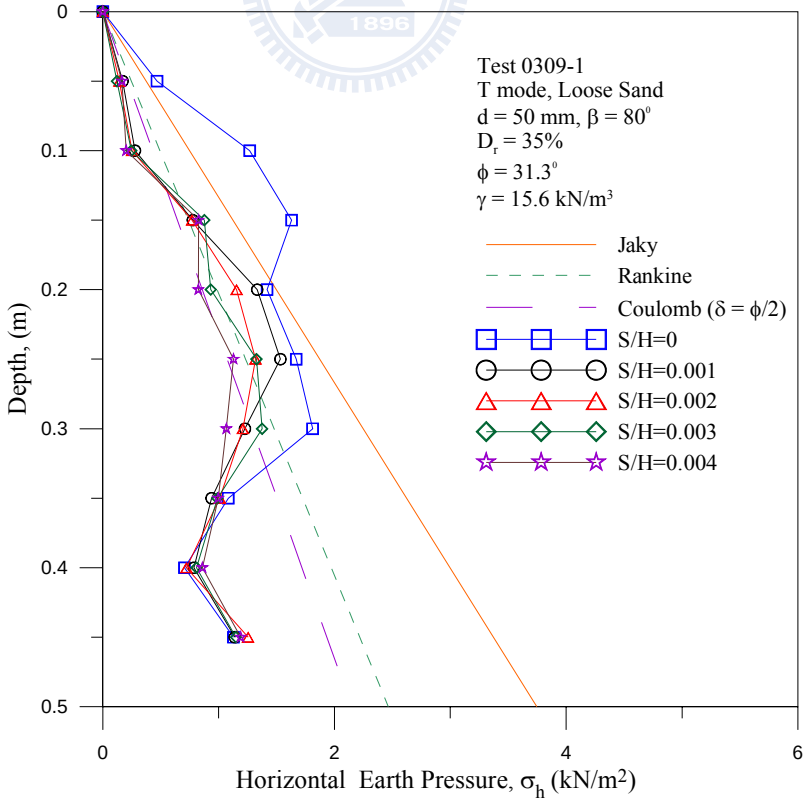

Fig. 6.38. Distribution of horizontal earth pressure for β = 80° and b= 50 mm (Test 0309-1)

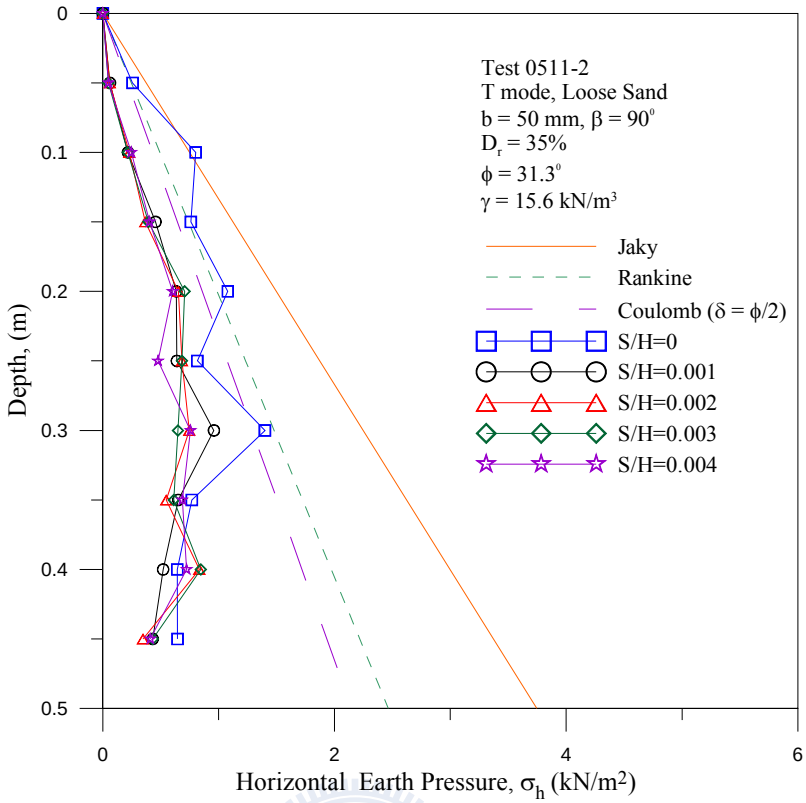

Fig. 6.39. Distribution of horizontal earth pressure for β = 90° and b = 50 mm (Test 0511-2)

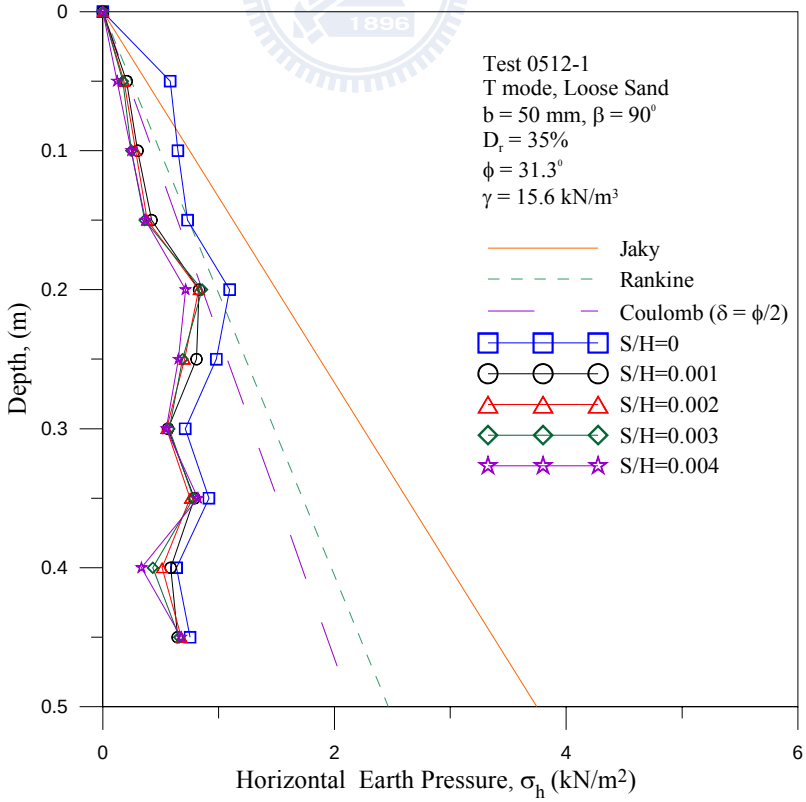

Fig. 6.40. Distribution of horizontal earth pressure for β = 90° and b= 50 mm (Test 0512-1)

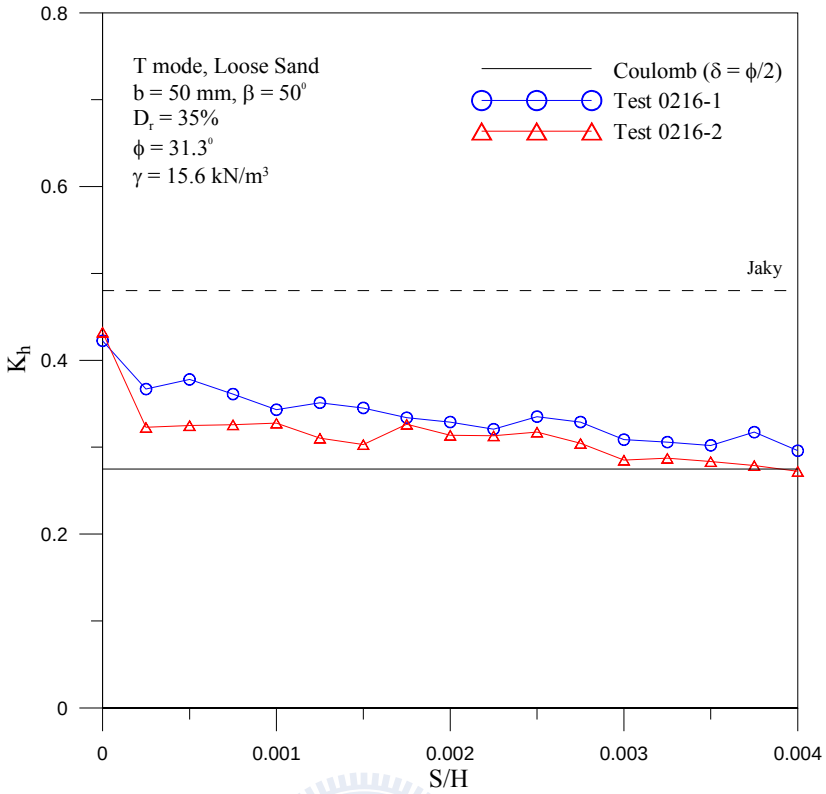

Fig. 6.41. Earth pressure coefficient K_h versus wall movement for β = 50°and b = 50 mm

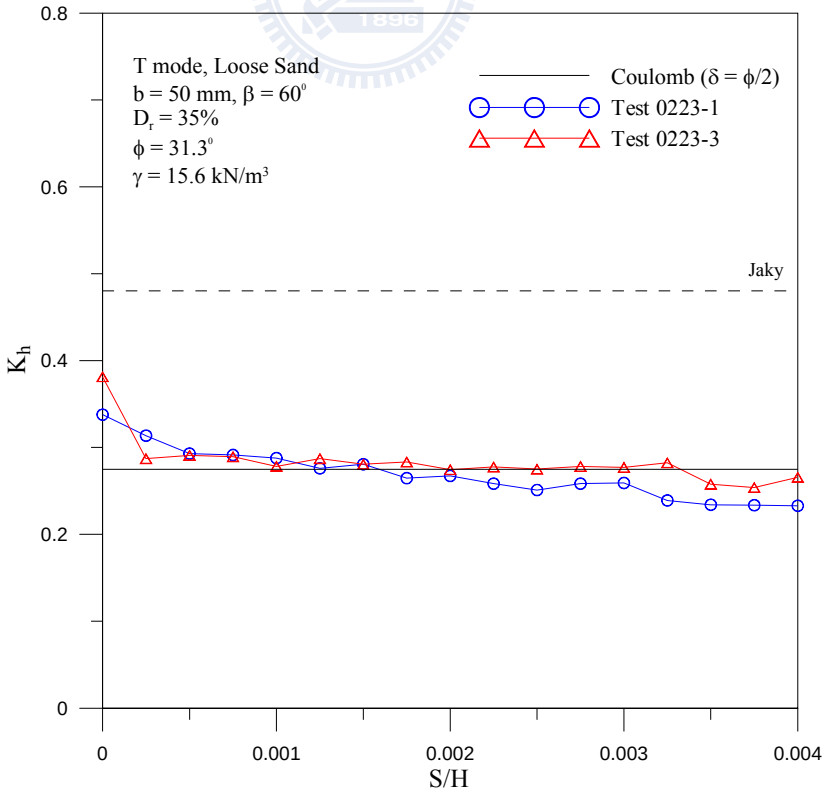

Fig. 6.42. Earth pressure coefficient K_h versus wall movement for β = 60° and b= 50 mm

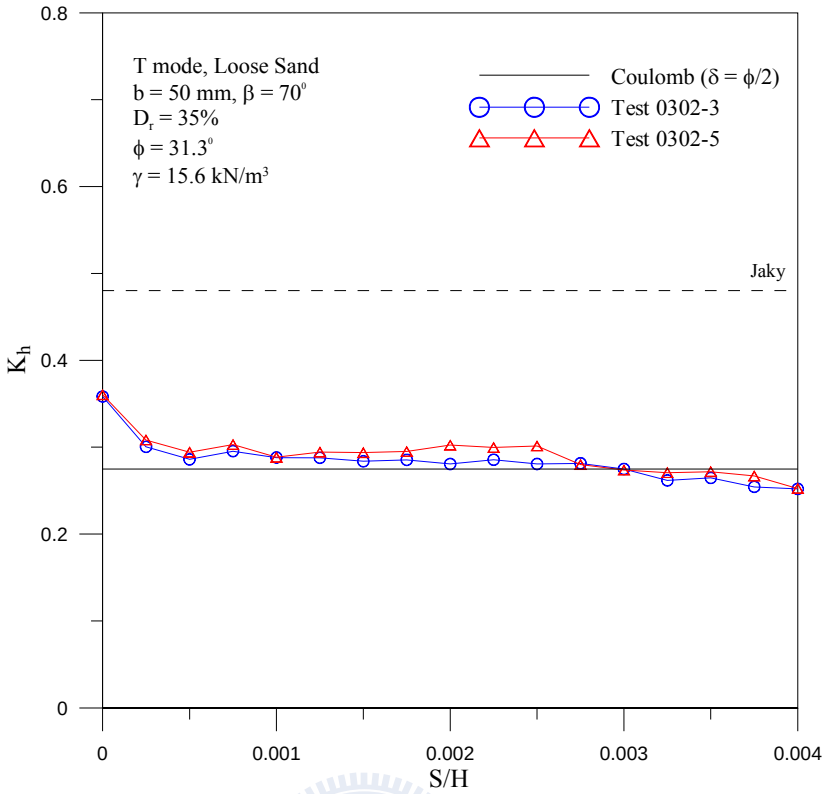

Fig. 6.43. Earth pressure coefficient K_h versus wall movement for β = 70° and b = 50 mm

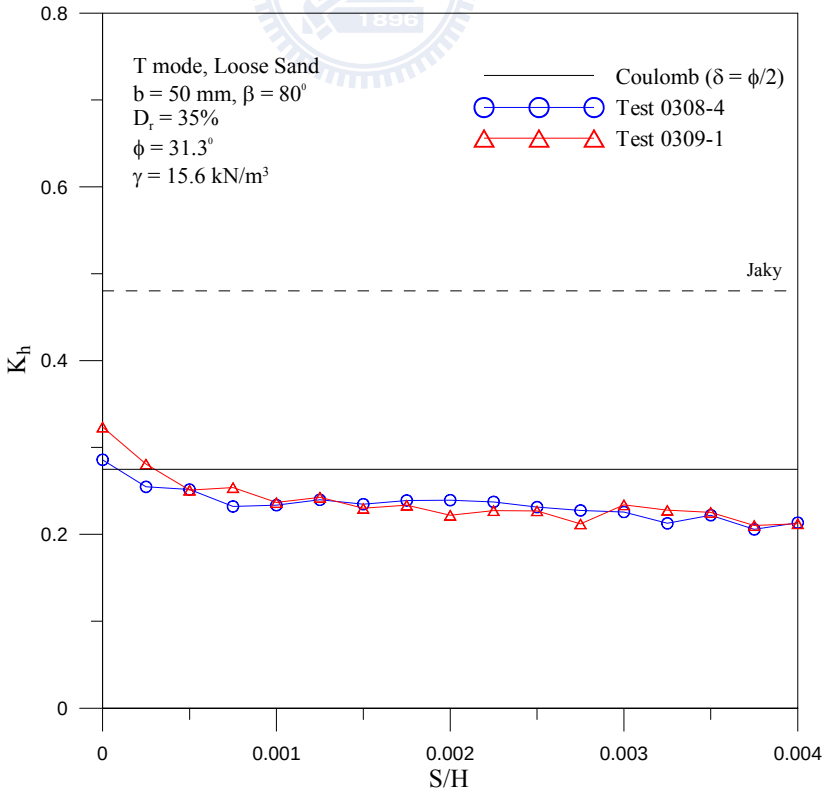

Fig. 6.44. Earth pressure coefficient K_h versus wall movement for β = 80° and b= 50 mm

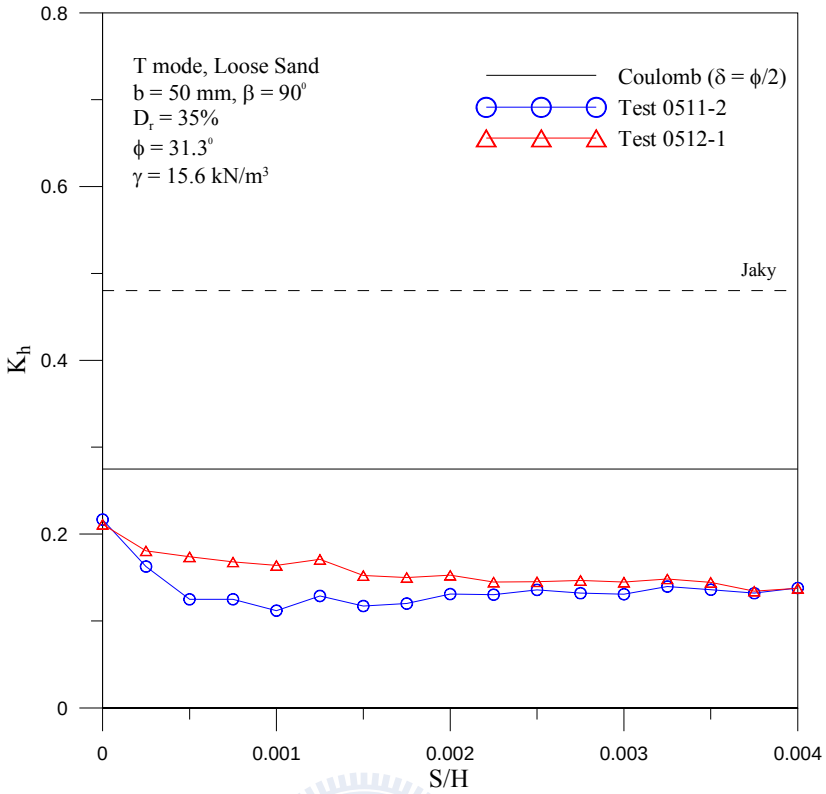

Fig. 6.45. Earth pressure coefficient K_h versus wall movement for β = 90° and b = 50 mm

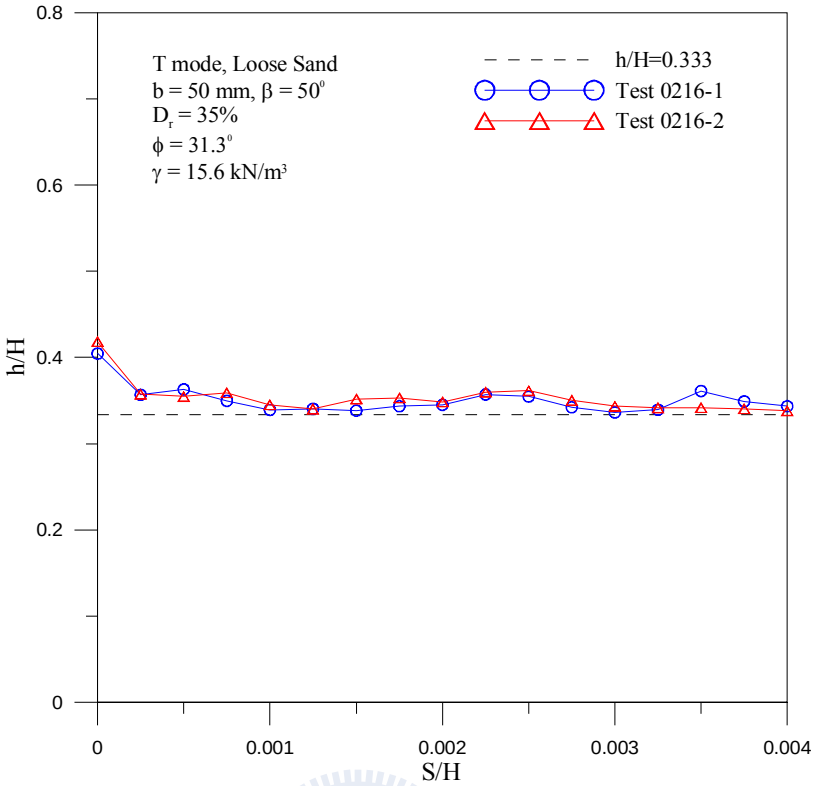

Fig. 6.46. Location of total thrust application for β = 50° and b = 50 mm

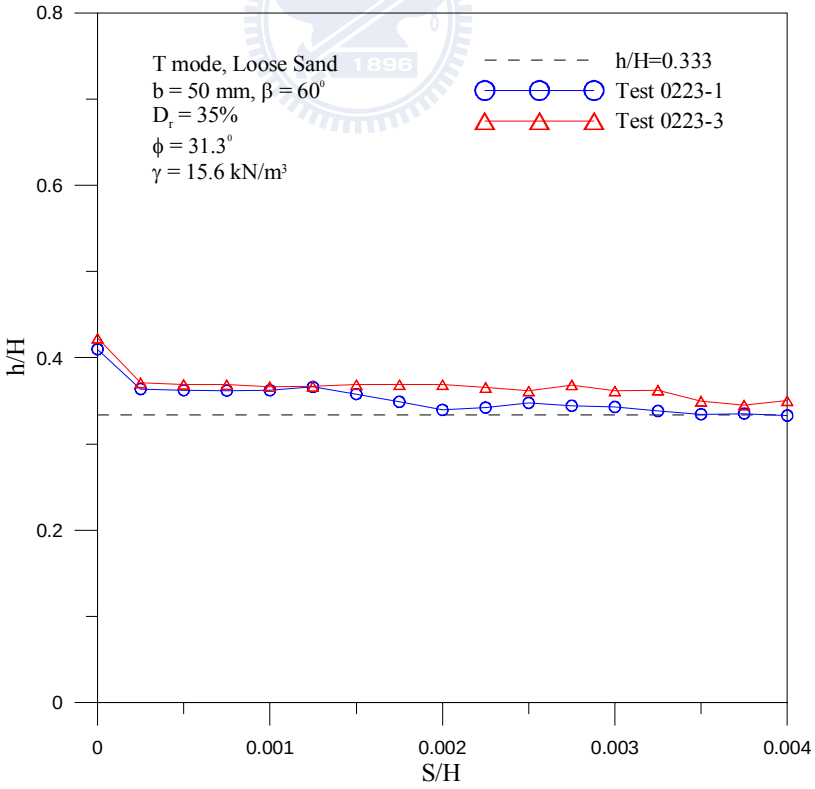

Fig. 6.47. Location of total thrust application for β = 60° and b = 50 mm

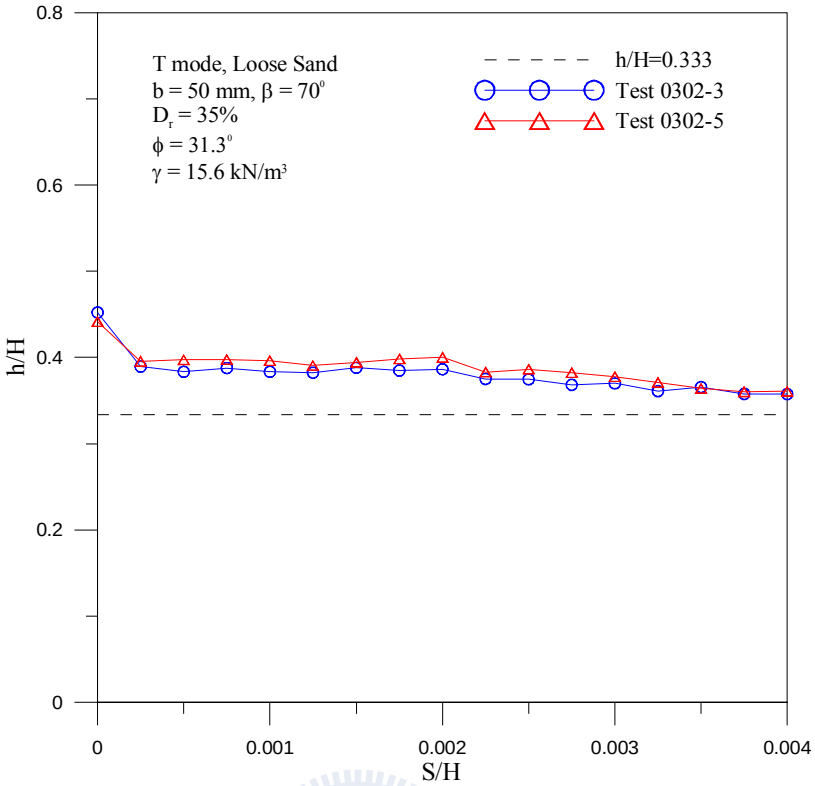

Fig. 6.48. Location of total thrust application for β = 70° and b = 50 mm

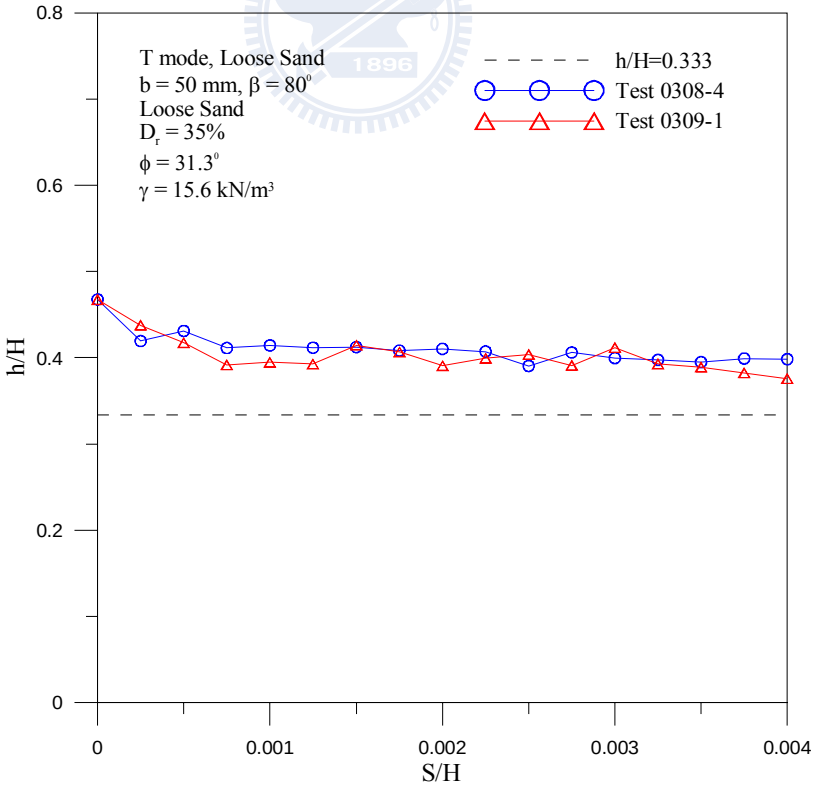

Fig. 6.49. Location of total thrust application for β = 80° and b = 50 mm

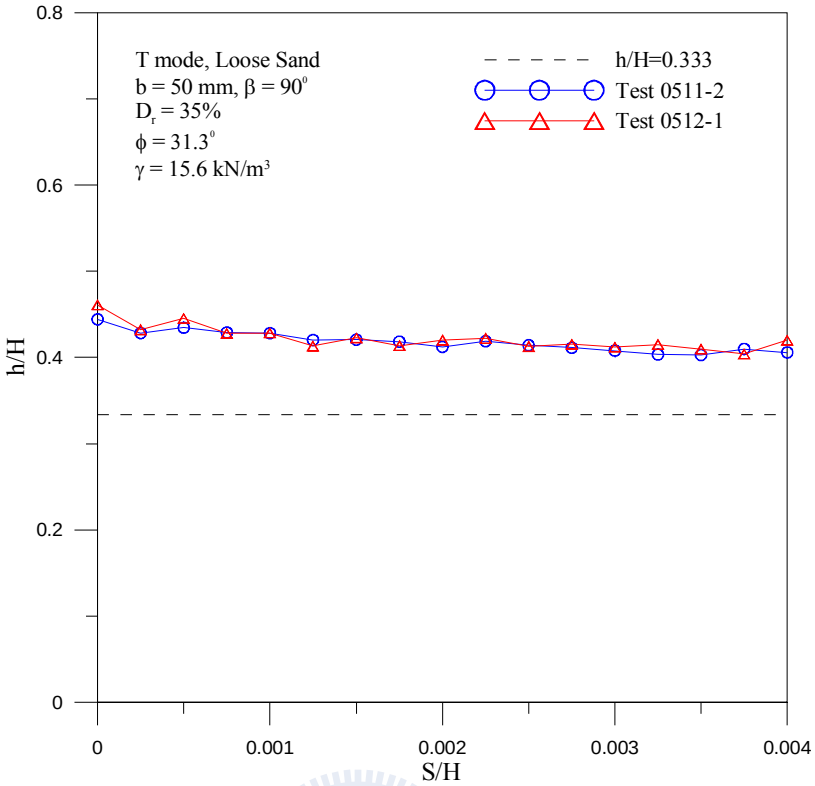

Fig. 6.50. Location of total thrust application for β = 90° and b = 50 mm

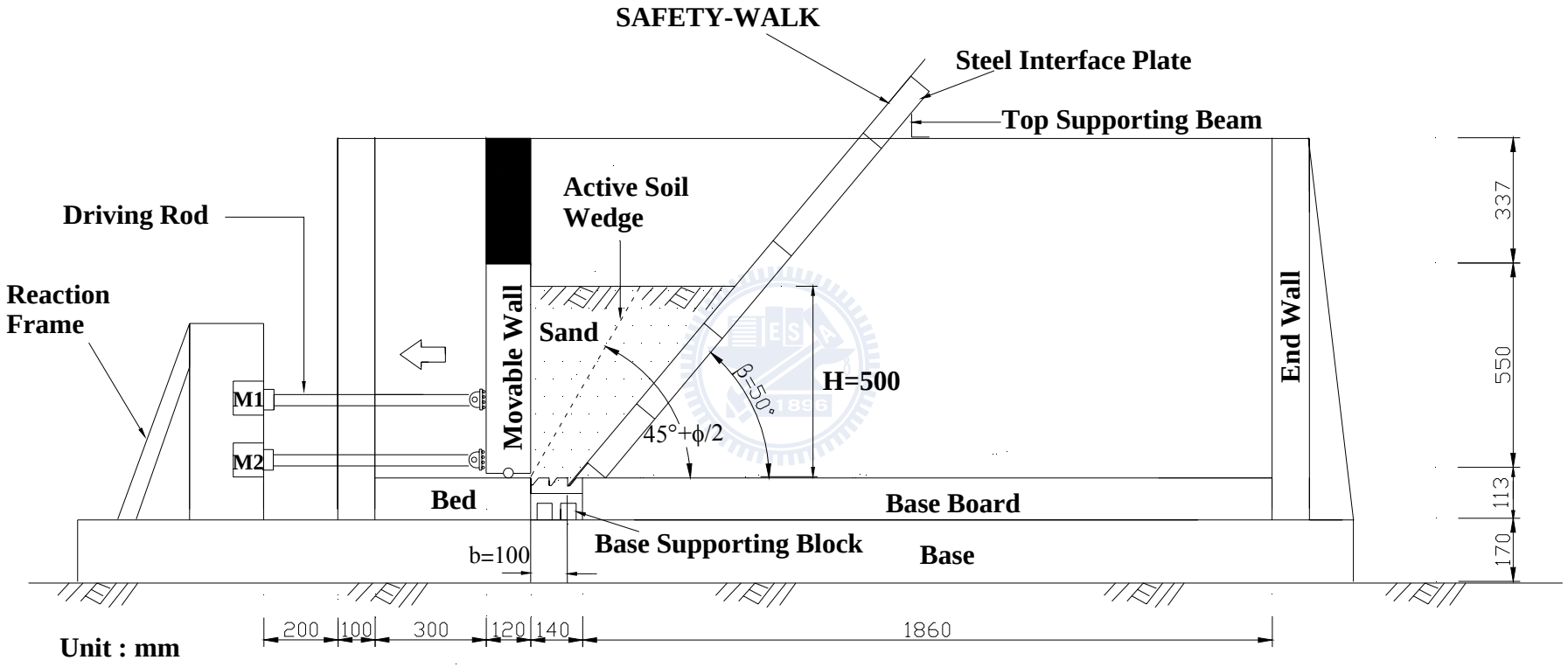

(a)

Fig. 6.51. Model wall test with interface inclination $\beta = 50^0$ and b = 100 mm

(b)

Fig. 6.51. Model wall test with interface inclination $\beta = 50^0$ and b = 100 mm

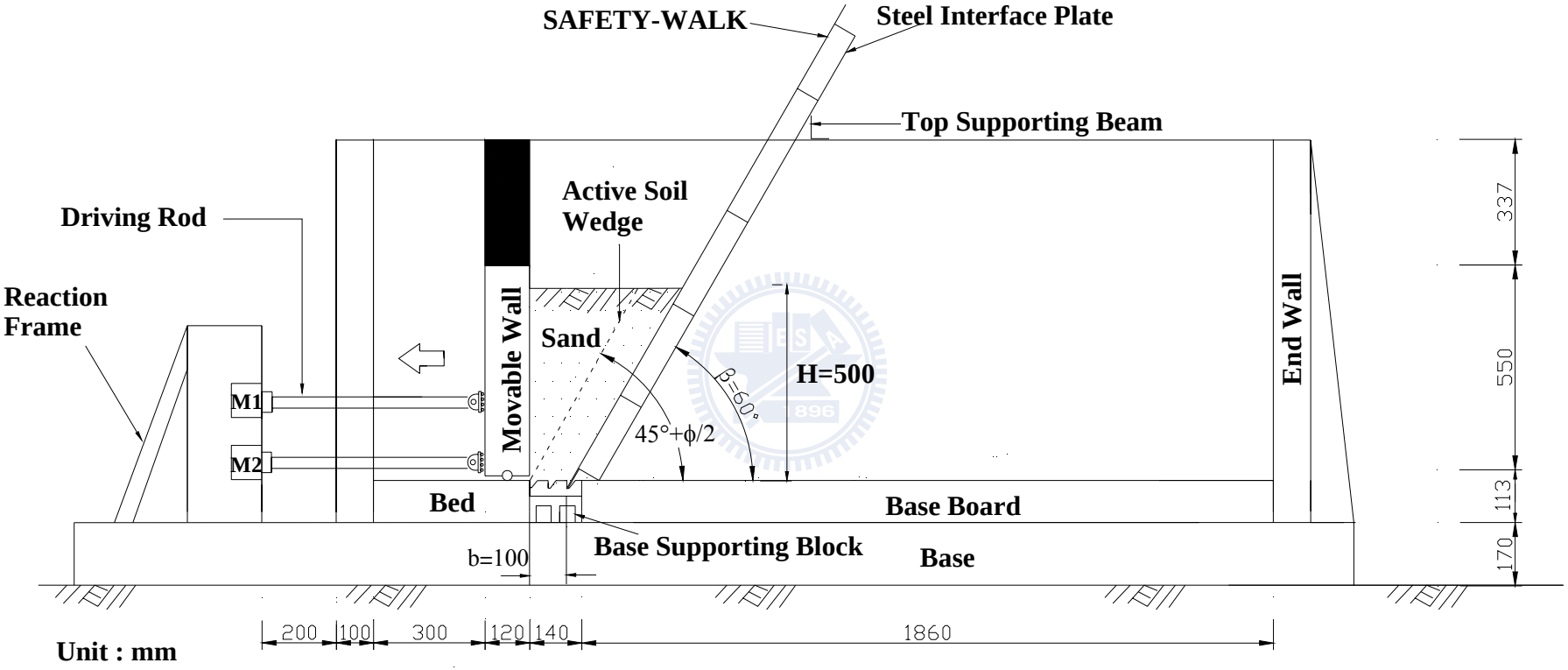

(a)

Fig. 6.52. Model wall test with interface inclination $\beta = 60^0$ and b = 100 mm

(b)

Fig. 6.52. Model wall test with interface inclination $\beta = 60^0$ and b = 100 mm

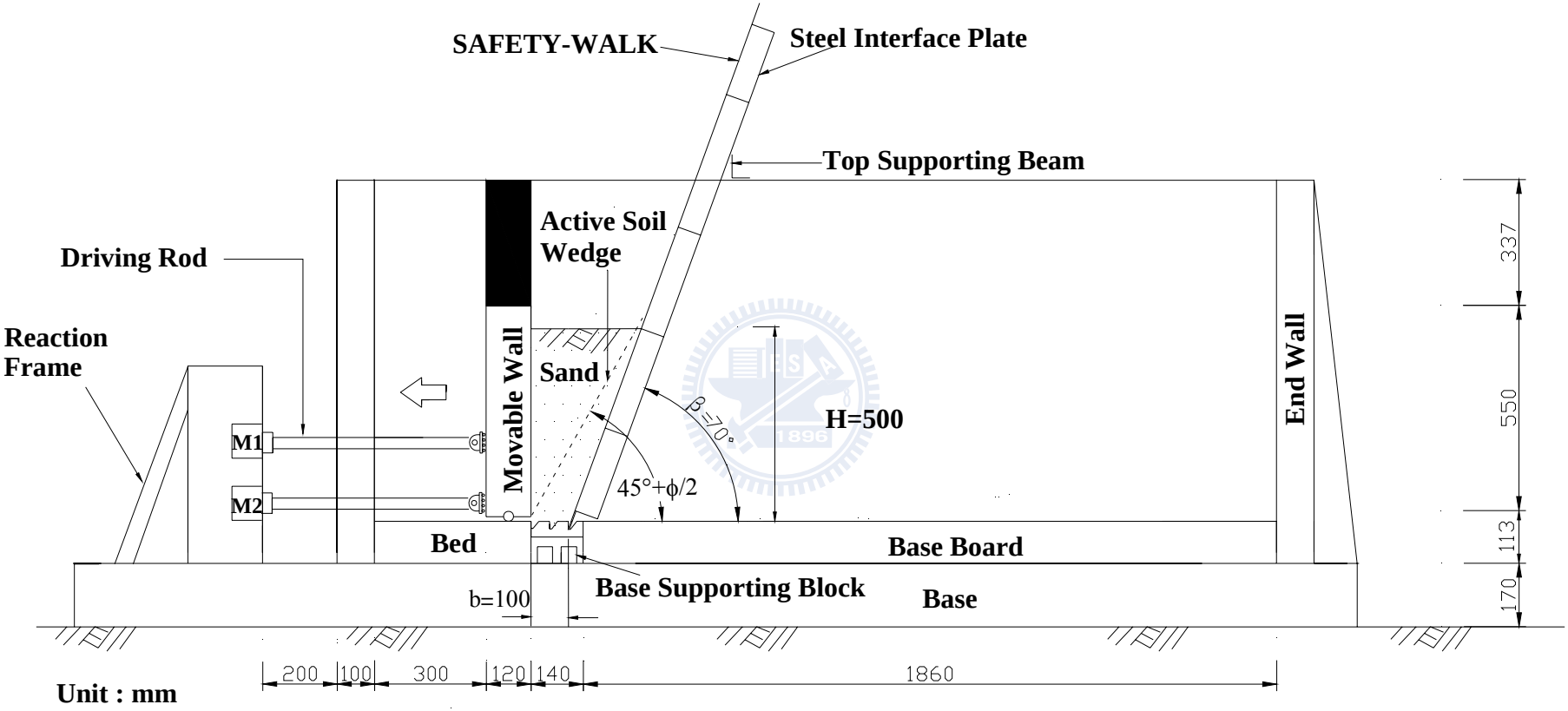

(a)

Fig. 6.53. Model wall test with interface inclination $\beta = 70^0$ and b = 100 mm

(b)

Fig. 6.53. Model wall test with interface inclination $\beta = 70^0$ and b = 100 mm

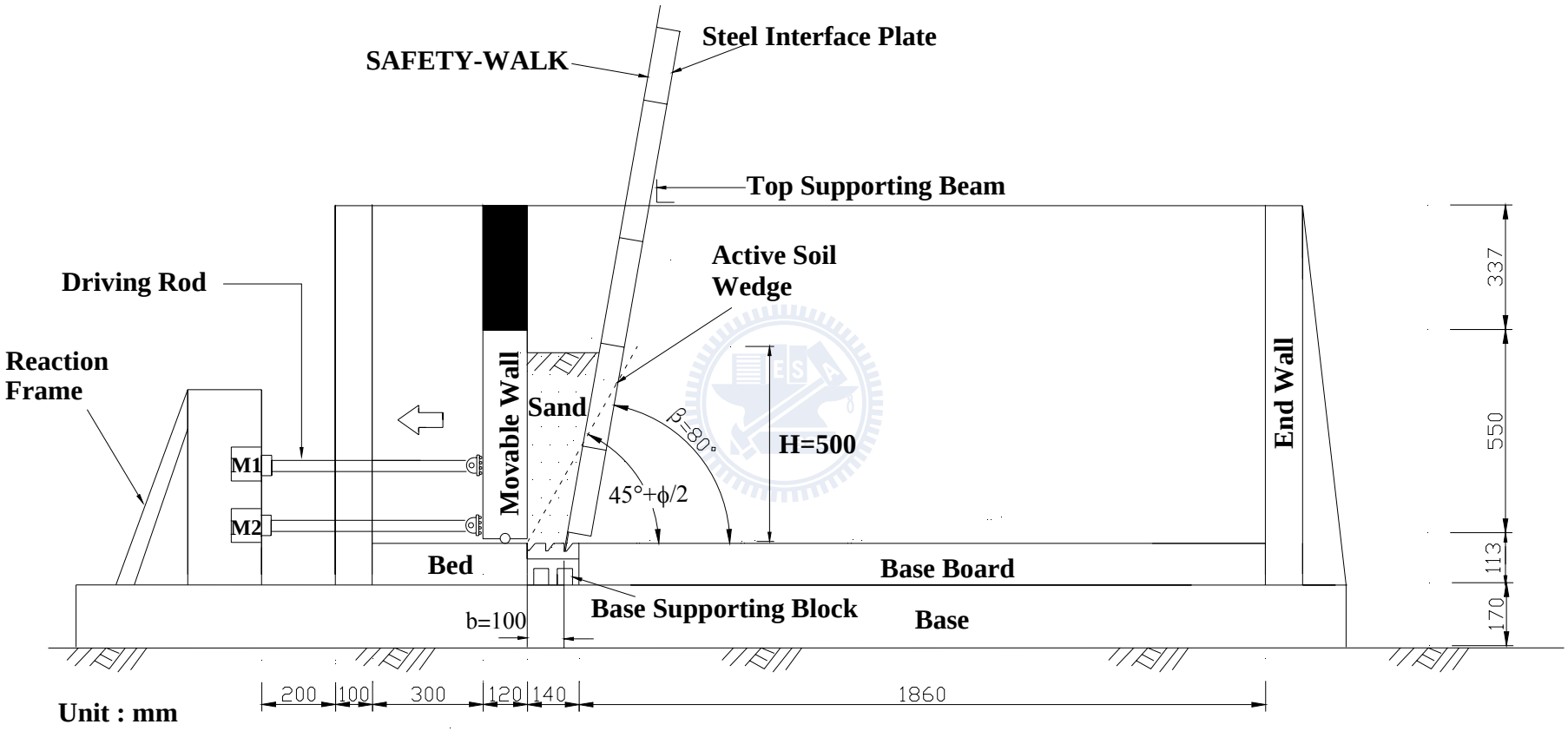

(a)

Fig. 6.54. Model wall test with interface inclination $\beta = 80^0$ and b = 100 mm

(b)

Fig. 6.54. Model wall test with interface inclination $\beta = 80^0$ and b = 100 mm

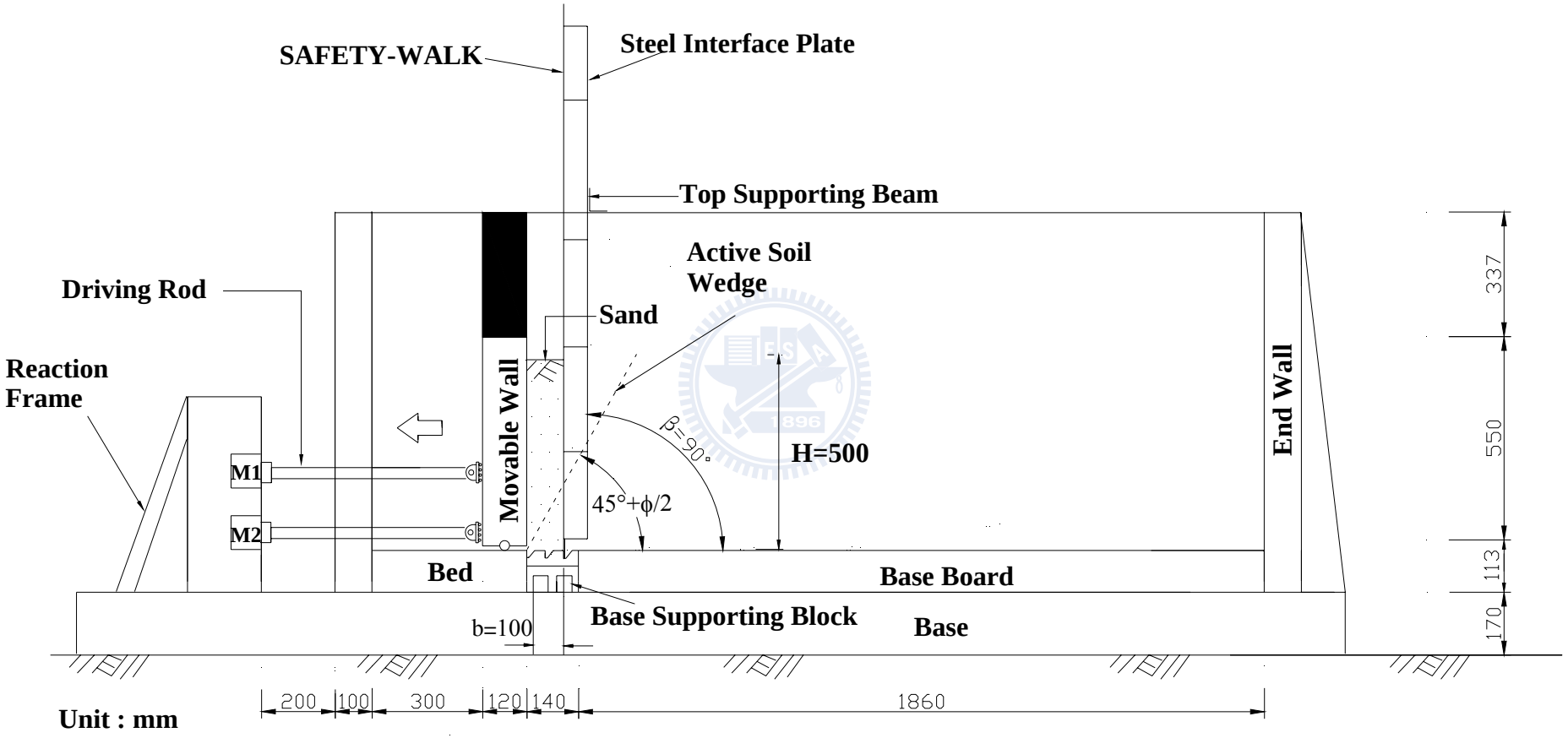

(a)

Fig. 6.55. Model wall test with interface inclination β = $90^0$and b = 100 mm

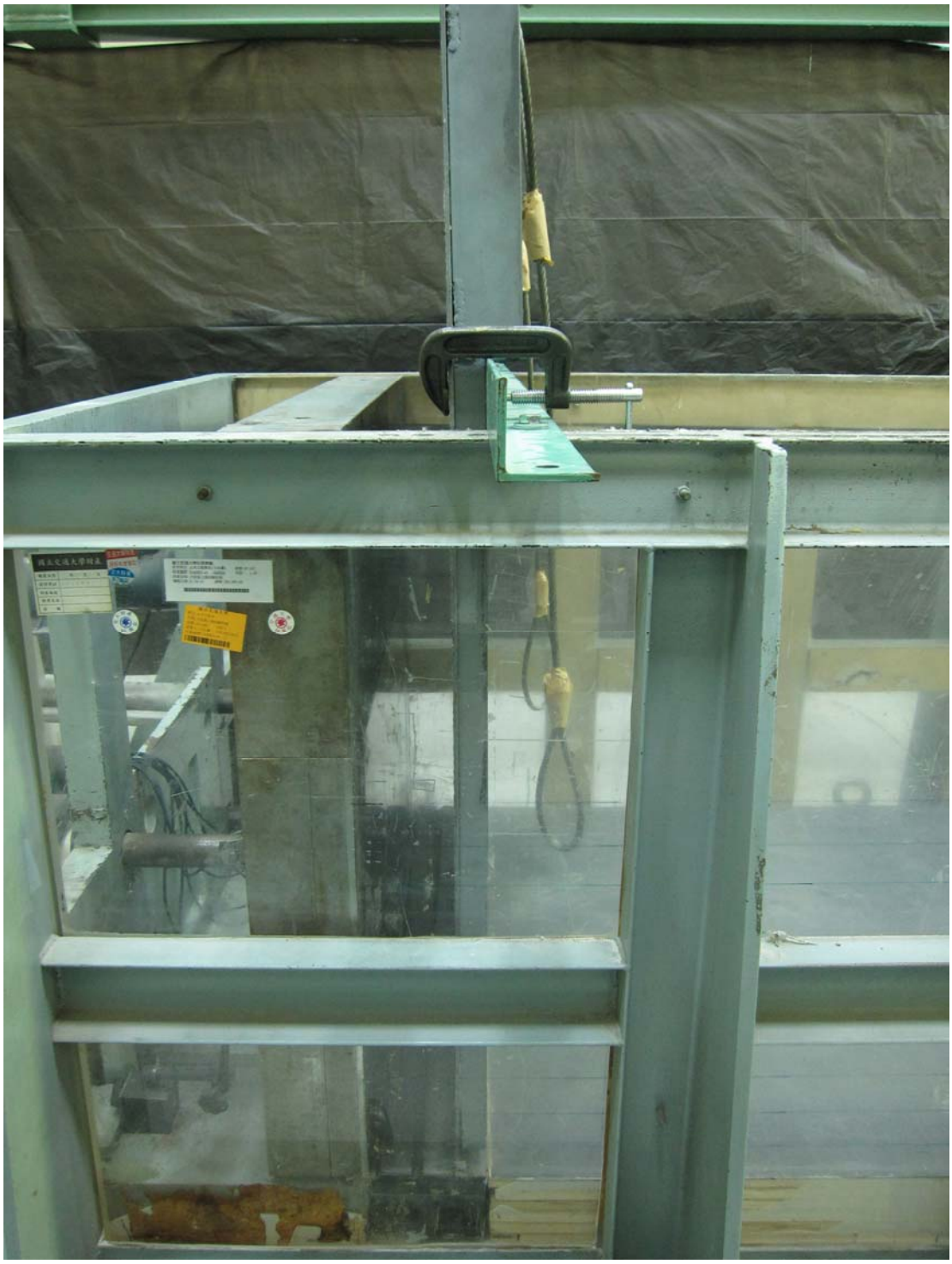

(b)

Fig. 6.55. Model wall test with interface inclination $\beta = 90^0$ and b = 100 mm

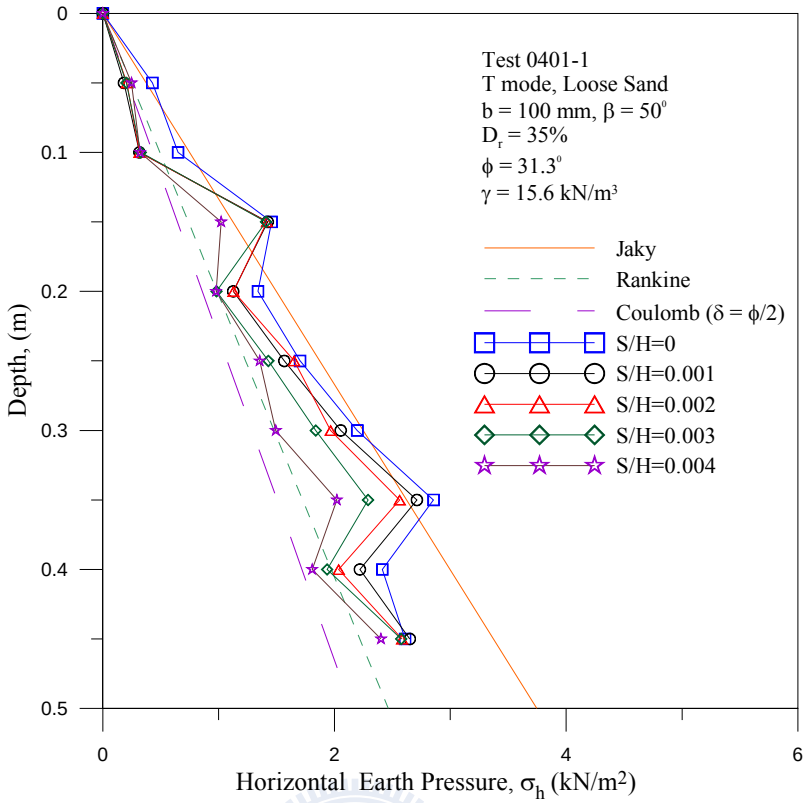

Fig. 6.56. Distribution of horizontal earth pressure for β = 50° and b = 100 mm (Test 0401-1)

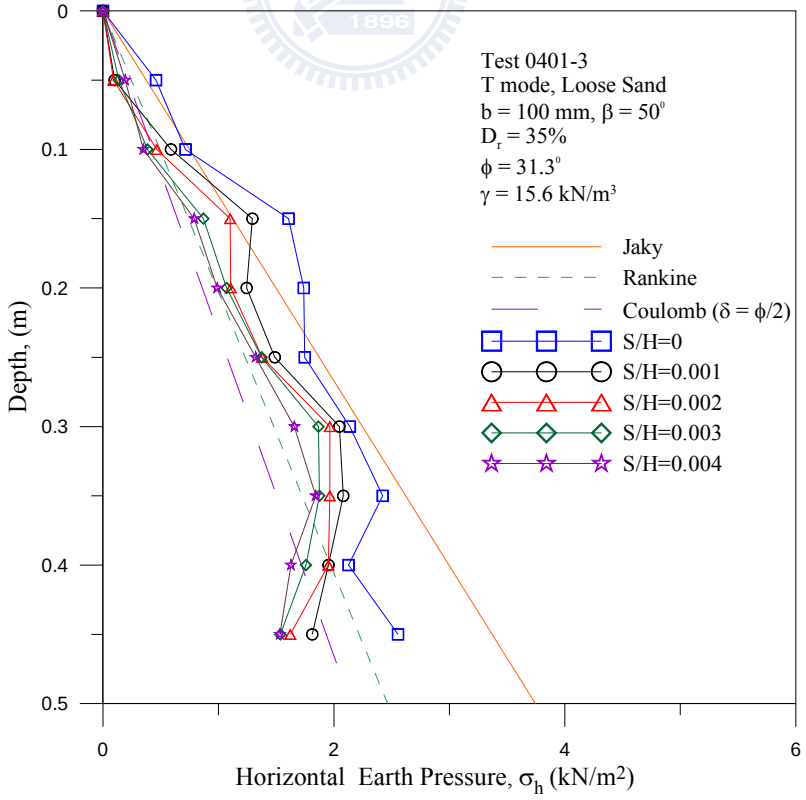

Fig. 6.57. Distribution of horizontal earth pressure for β = 50° and b = 100 mm (Test 0401-3)

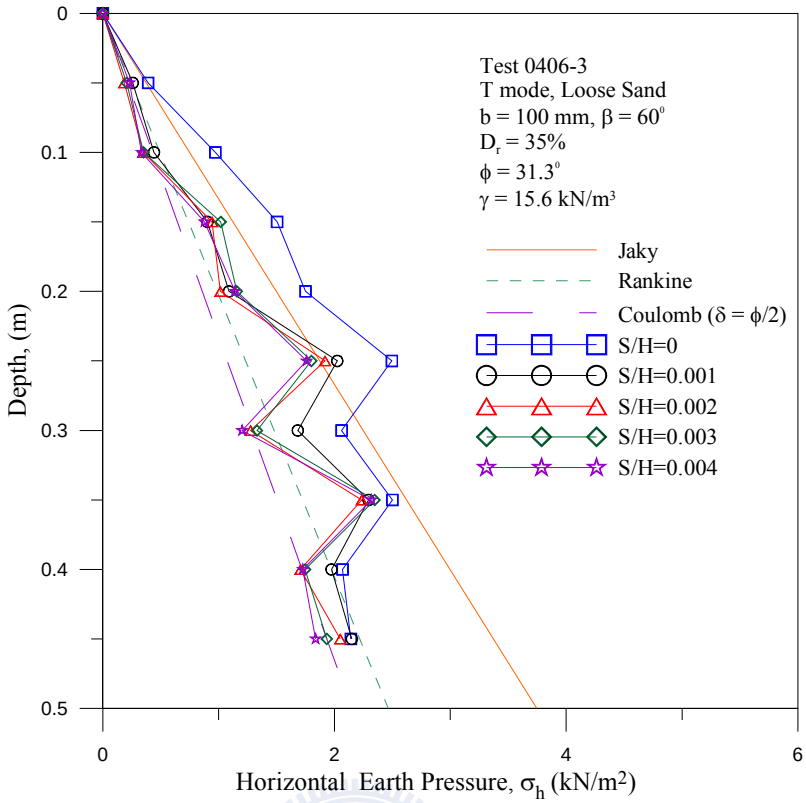

Fig. 6.58. Distribution of horizontal earth pressure for β = 60° and b = 100 mm (Test 0406-3)

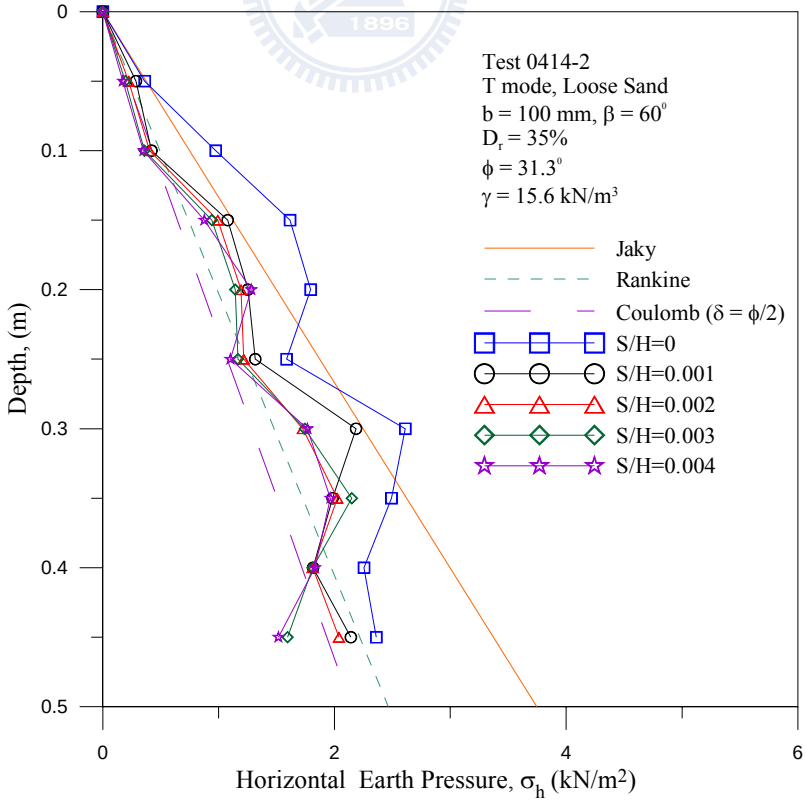

Fig. 6.59. Distribution of horizontal earth pressure for β = 60° and b = 100 mm (Test 0414-2)

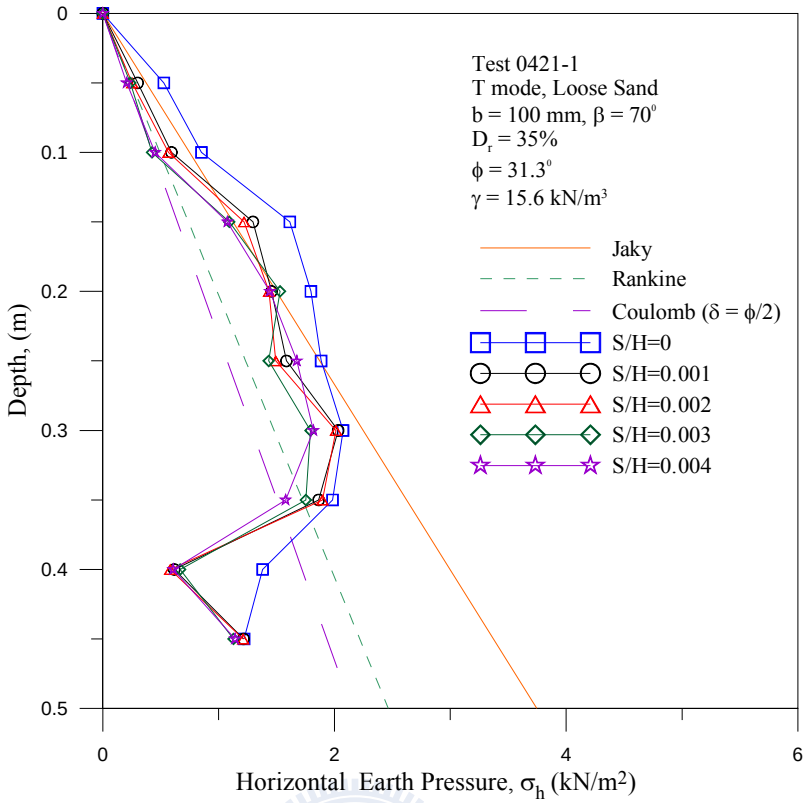

Fig. 6.60. Distribution of horizontal earth pressure for β = 70° and b = 100 mm (Test 0421-1)

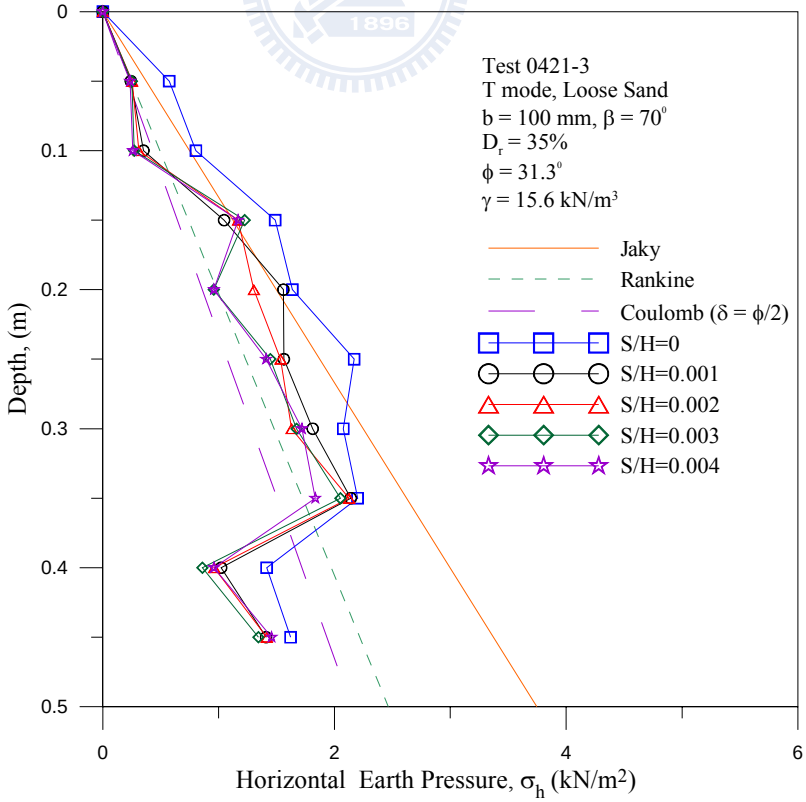

Fig. 6.61. Distribution of horizontal earth pressure for β = 70° and b = 100 mm (Test 0421-3)

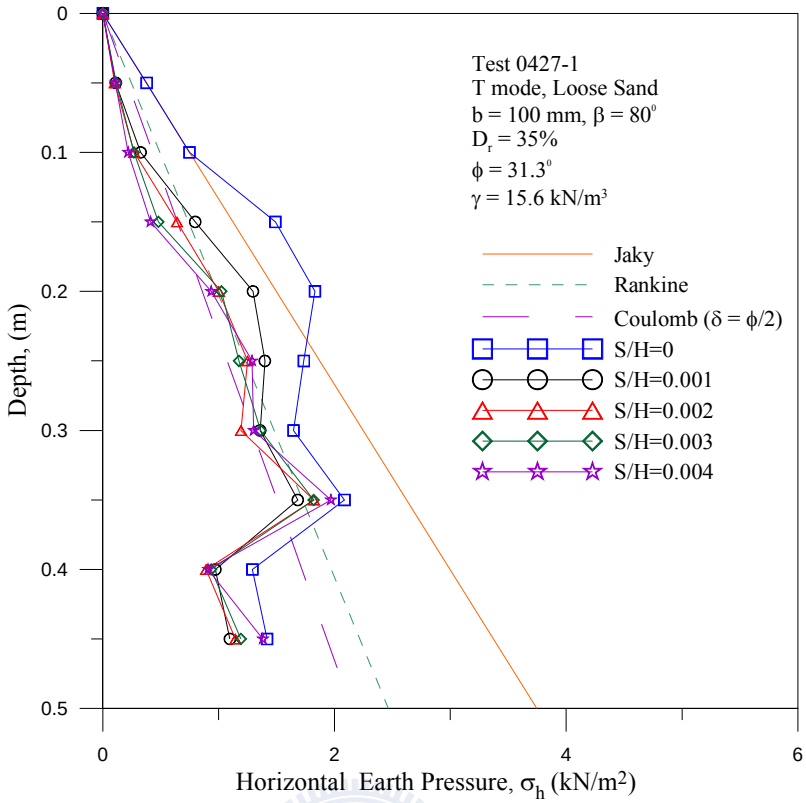

Fig. 6.62. Distribution of horizontal earth pressure for β = 80° and b = 100 mm (Test 0427-1)

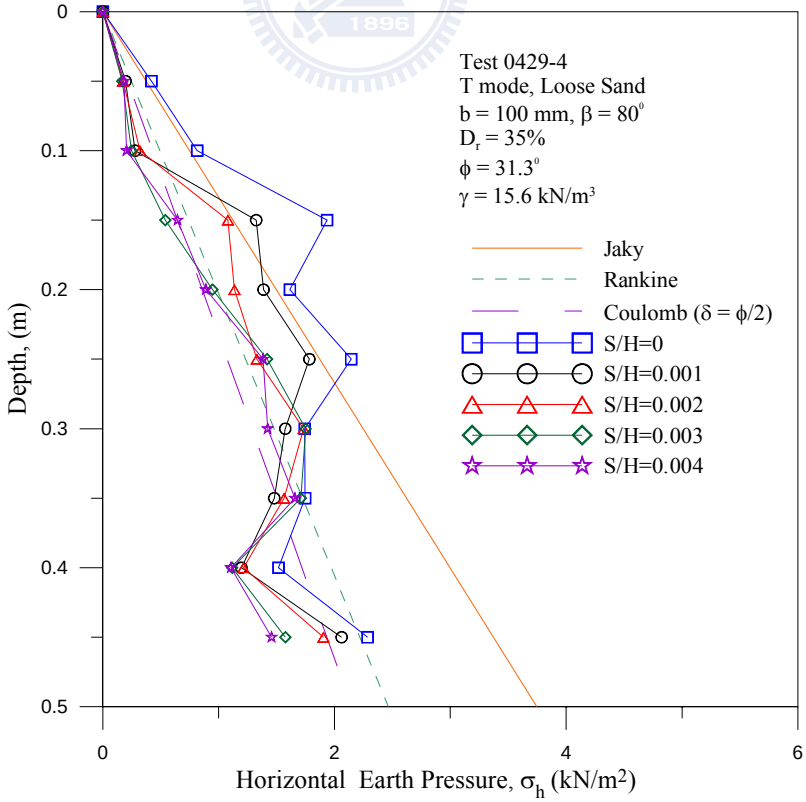

Fig. 6.63. Distribution of horizontal earth pressure for β = 80° and b = 100 mm (Test 0429-4)

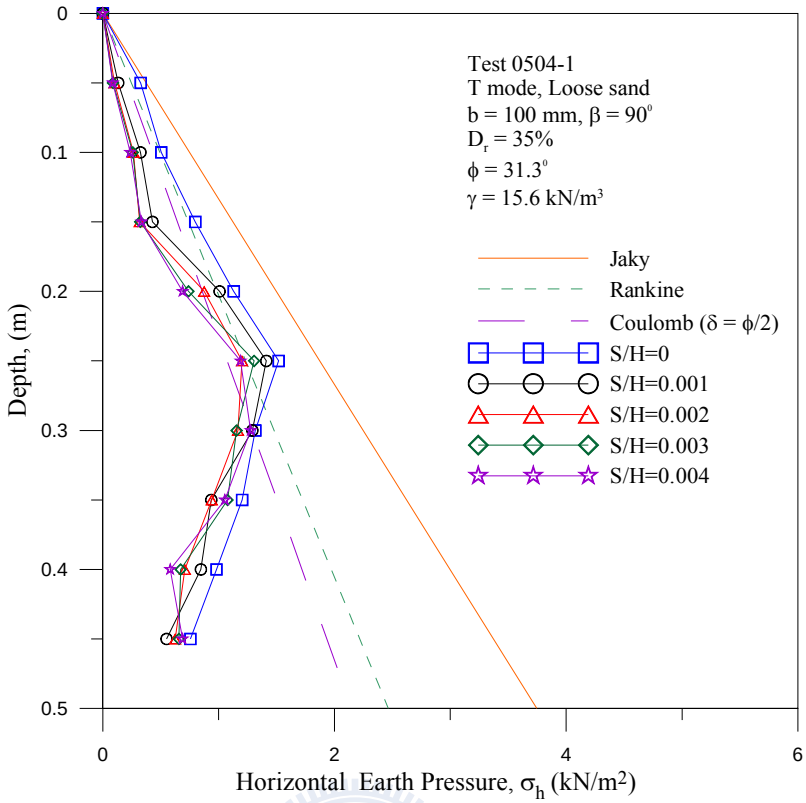

Fig. 6.64. Distribution of horizontal earth pressure for β = 90° and b = 100 mm (Test 0504-1)

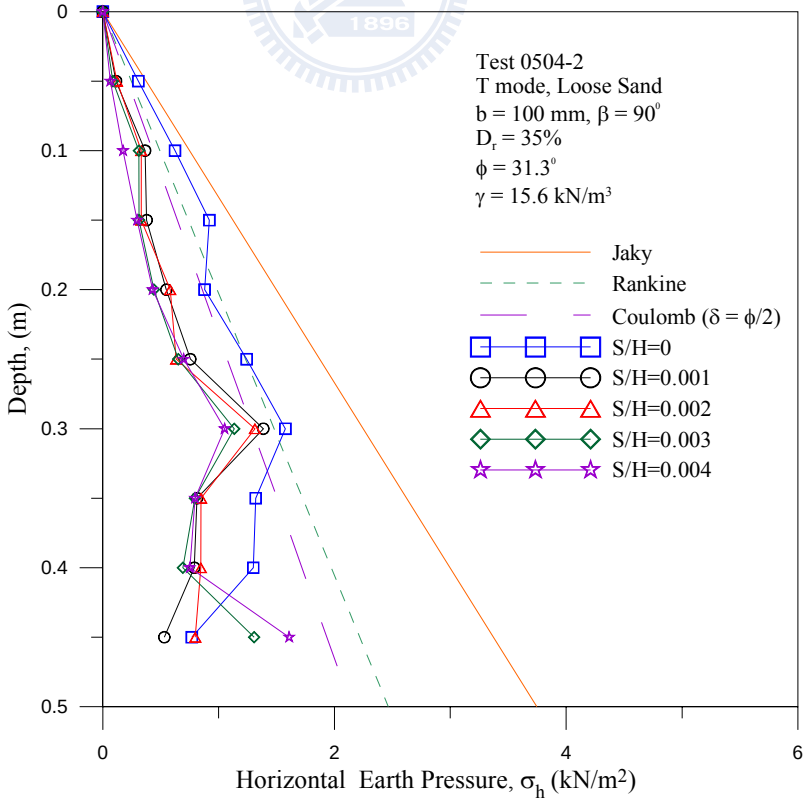

Fig. 6.65. Distribution of horizontal earth pressure for β = 90° and b = 100 mm (Test 0504-2)

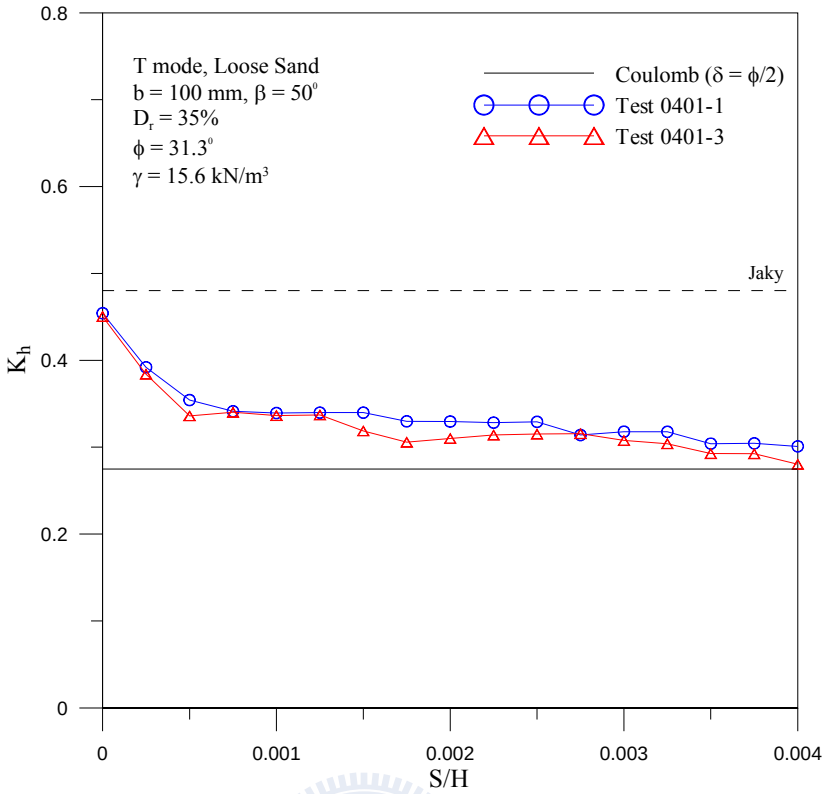

Fig. 6.66. Earth pressure coefficient K_h versus wall movement for β = 50° and b = 100 mm

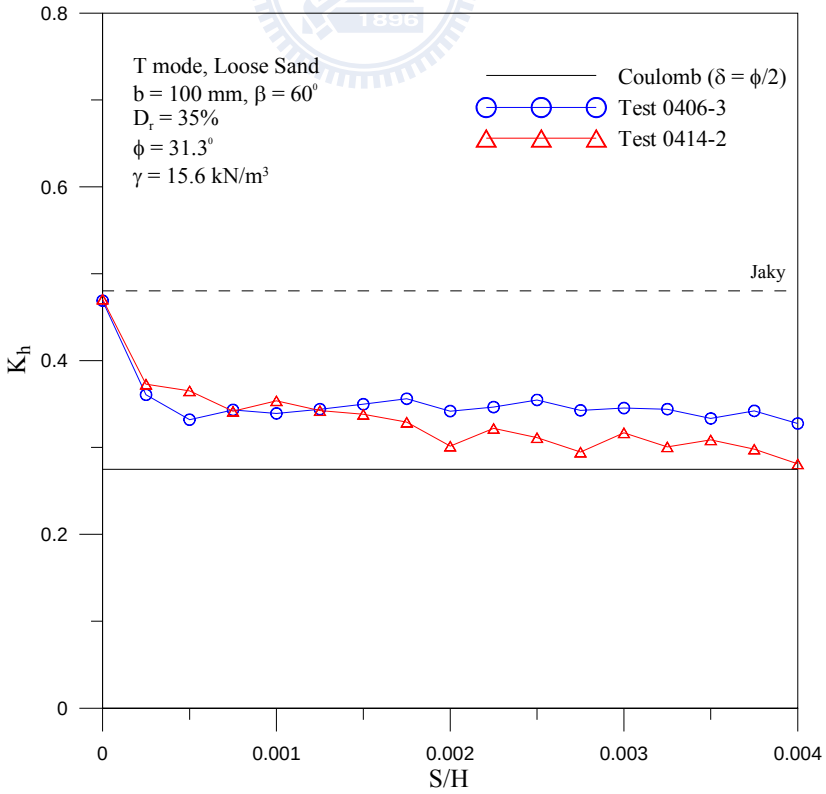

Fig. 6.67. Earth pressure coefficient K_h versus wall movement for β = 60° and b = 100 mm

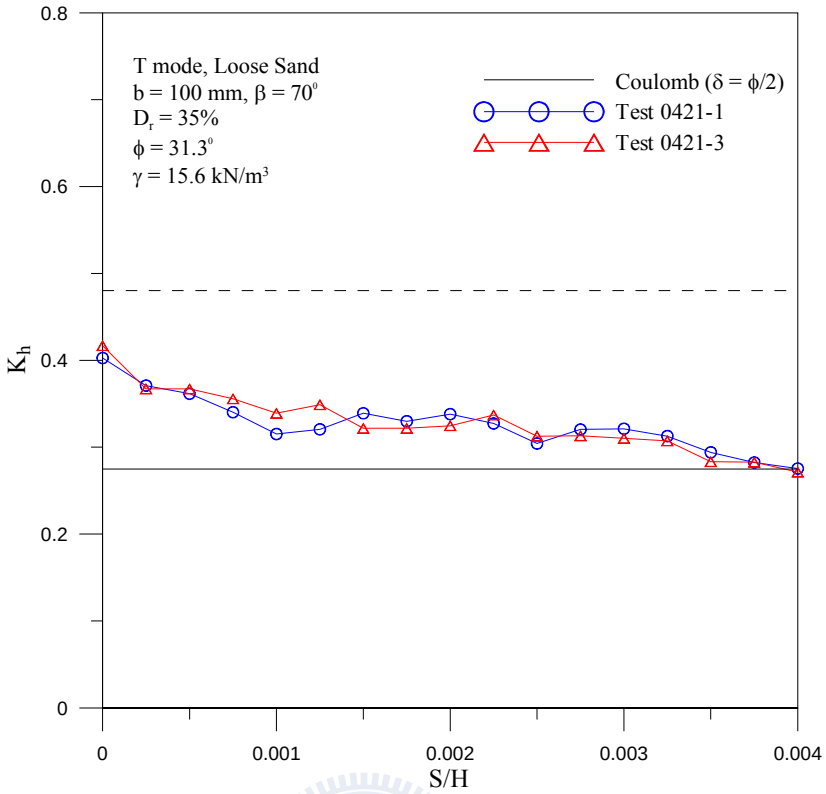

Fig. 6.68. Earth pressure coefficient K_h versus wall movement for β = 70° and b = 100 mm

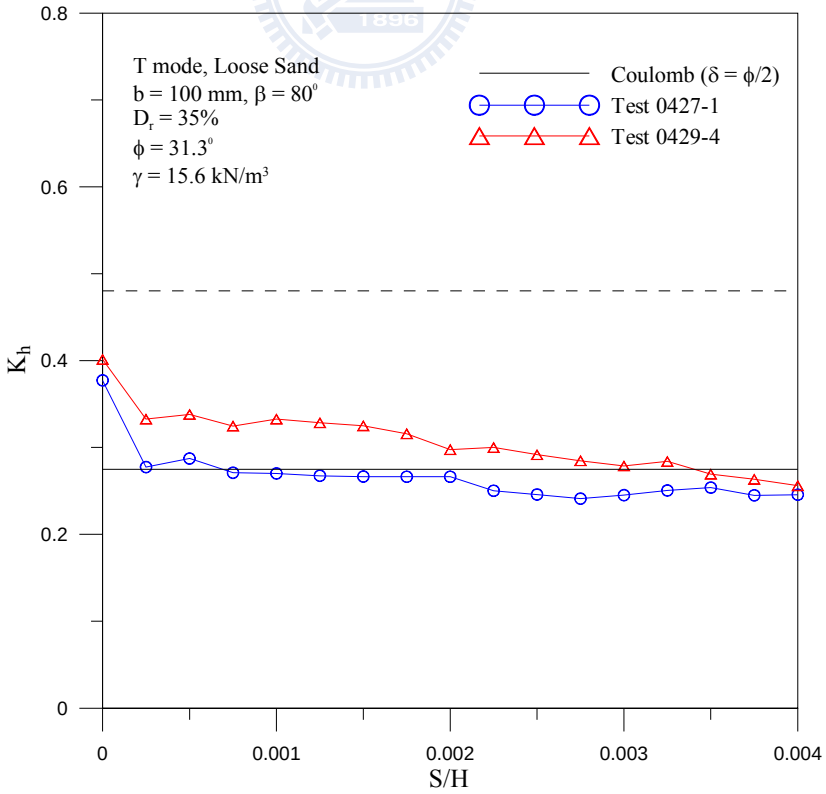

Fig. 6.69. Earth pressure coefficient K_h versus wall movement for β = 80° and b = 100 mm

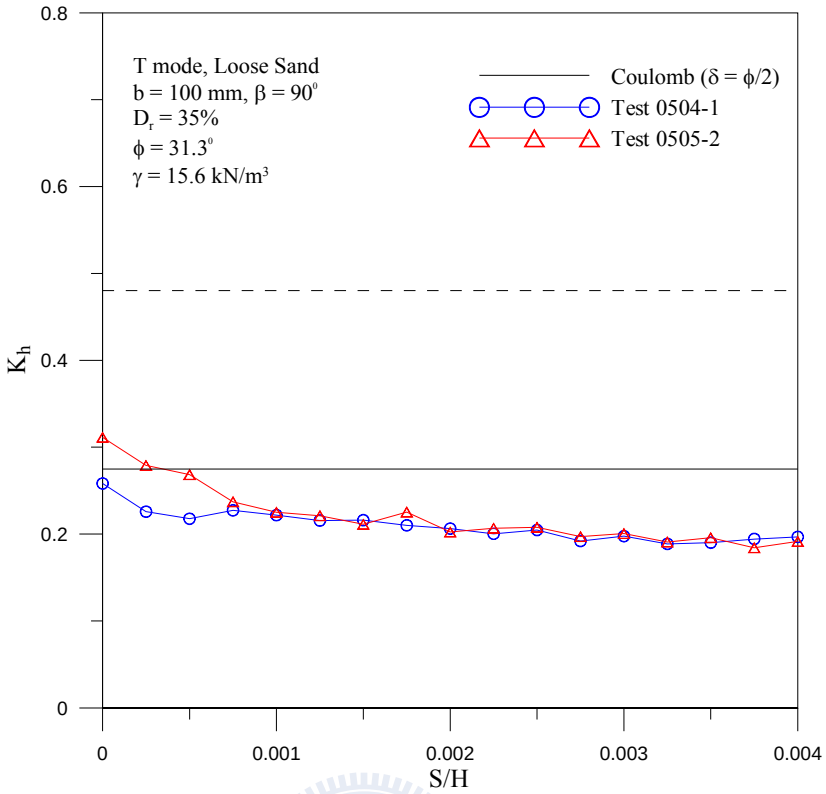

Fig. 6.70. Earth pressure coefficient K_h versus wall movement for β = 90° and b = 100 mm

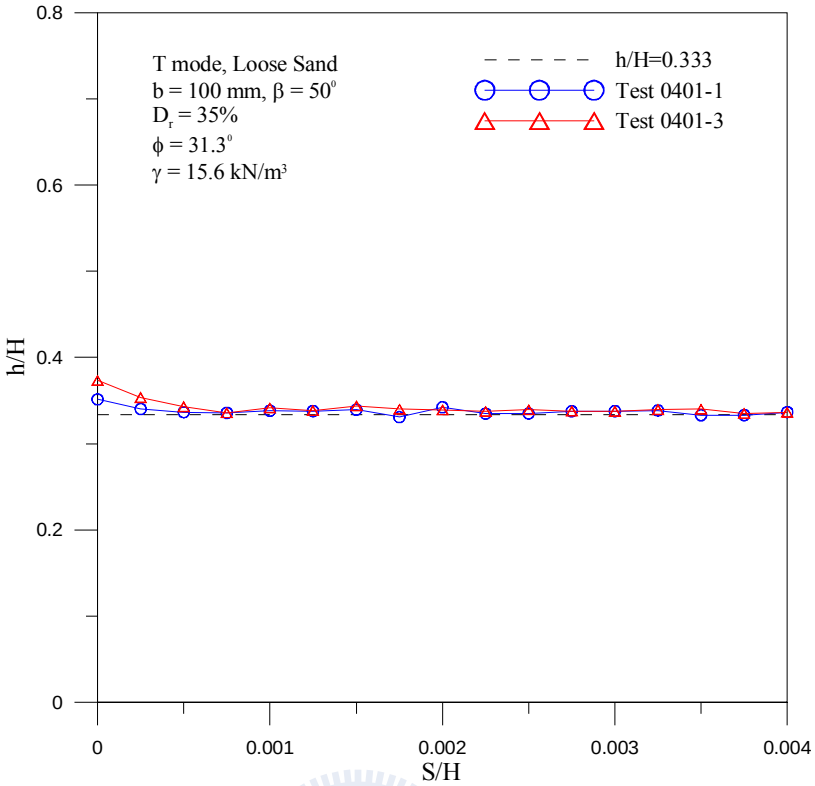

Fig. 6.71. Location of total thrust application for β = 50° and b = 100 mm

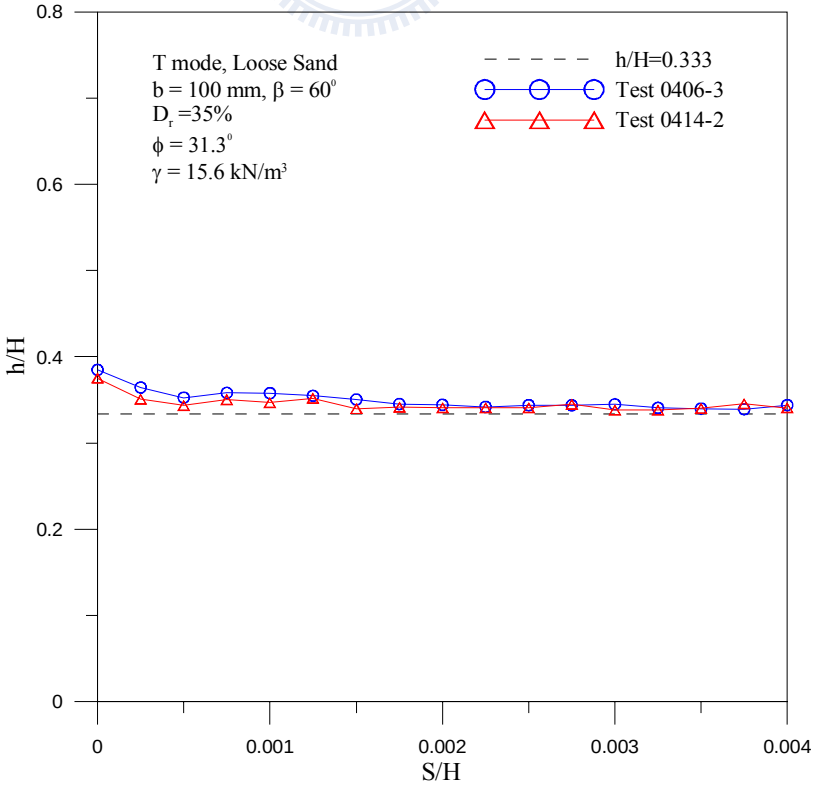

Fig. 6.72. Location of total thrust application for β = 60° and b = 100 mm

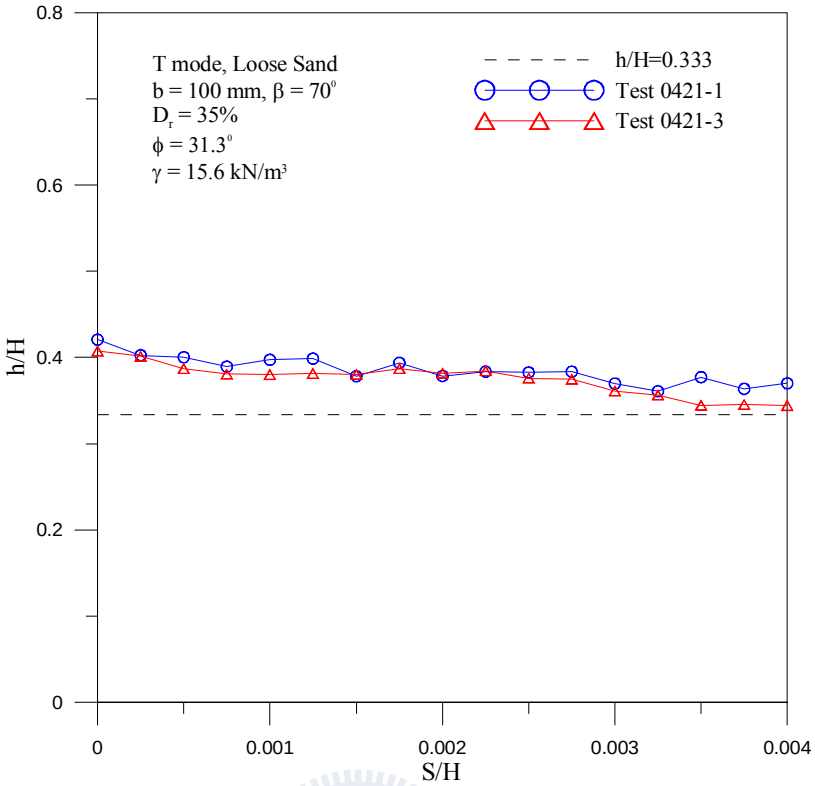

Fig. 6.73. Location of total thrust application for β = 70° and b = 100 mm

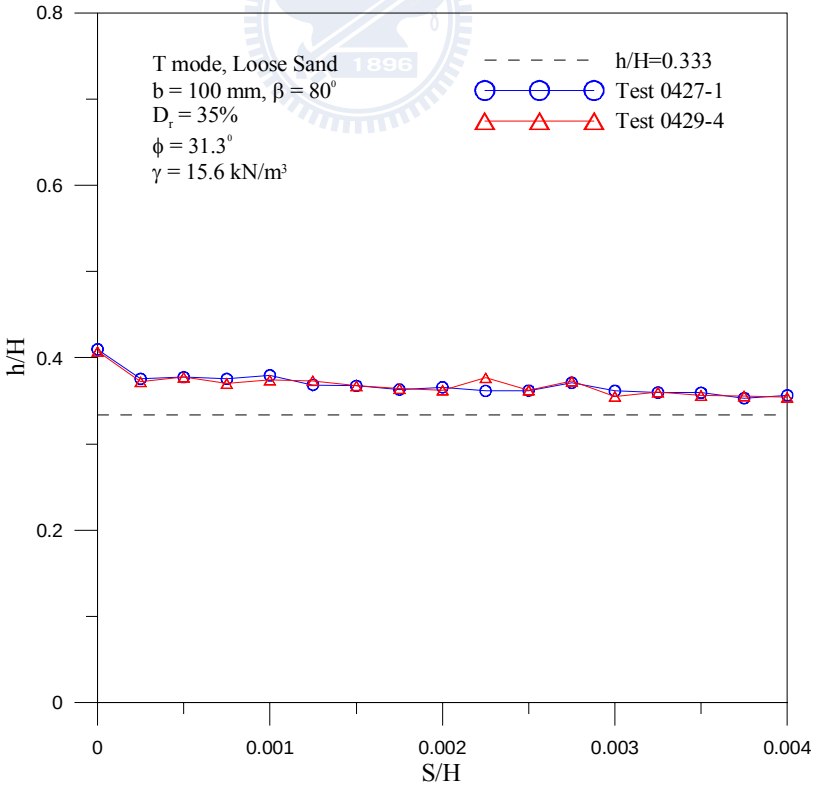

Fig. 6.74. Location of total thrust application for β = 80° and b = 100 mm

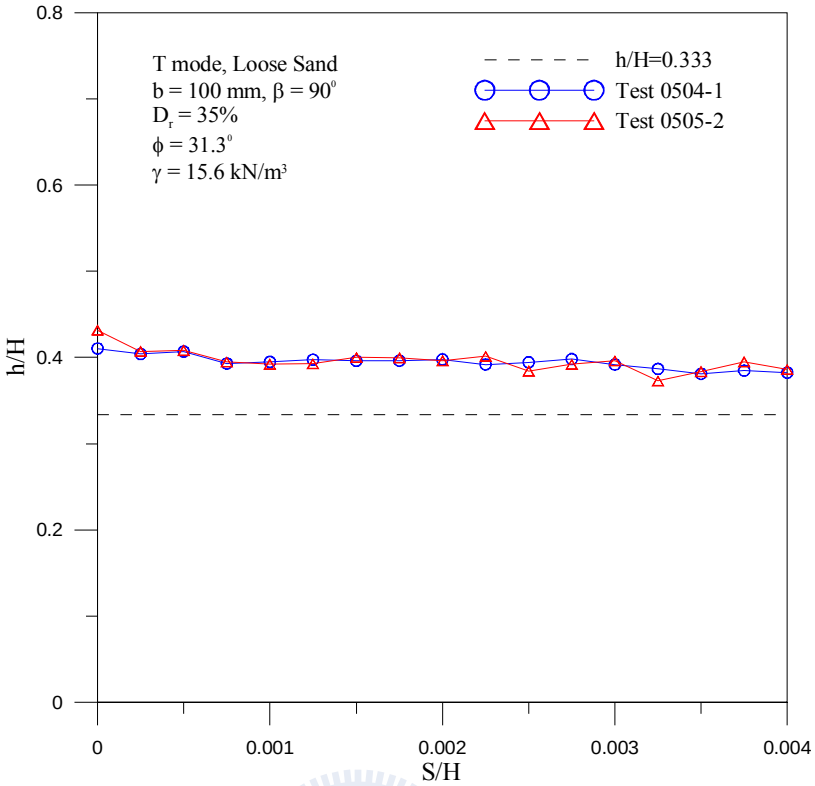

Fig. 6.75. Location of total thrust application for β = 90° and b = 100 mm

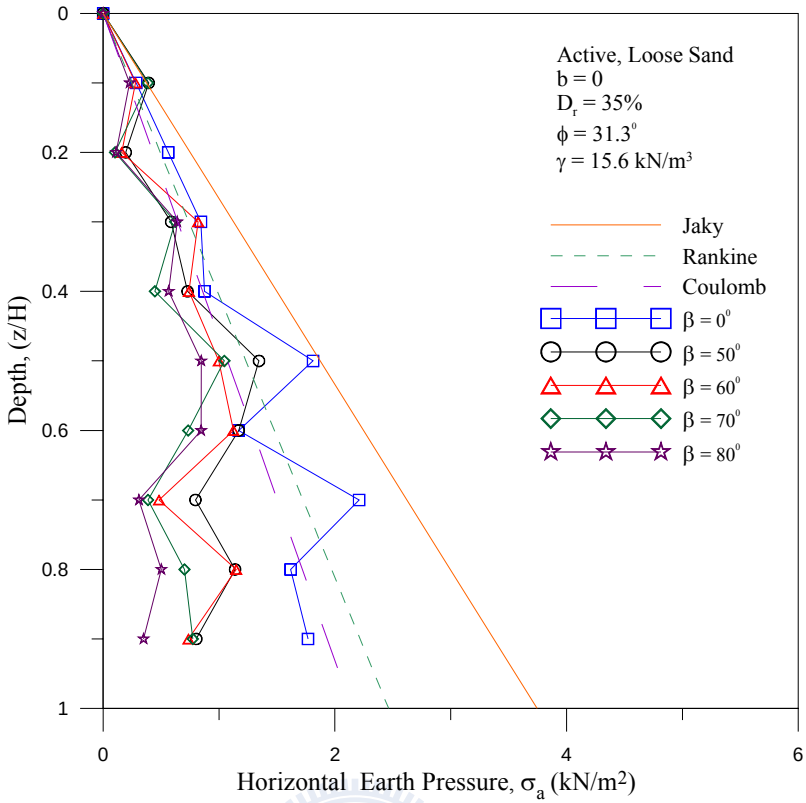

Fig. 6.76. Distribution of active earth pressure at different interface inclination angle for b = 0

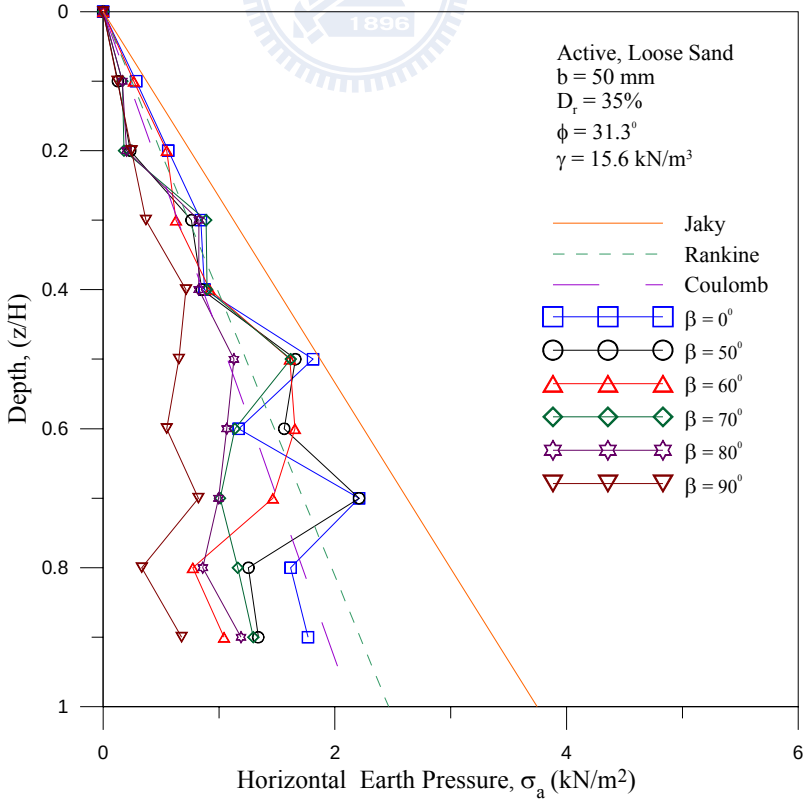

Fig. 6.77. Distribution of active earth pressure at different interface inclination angle for b = 50 mm

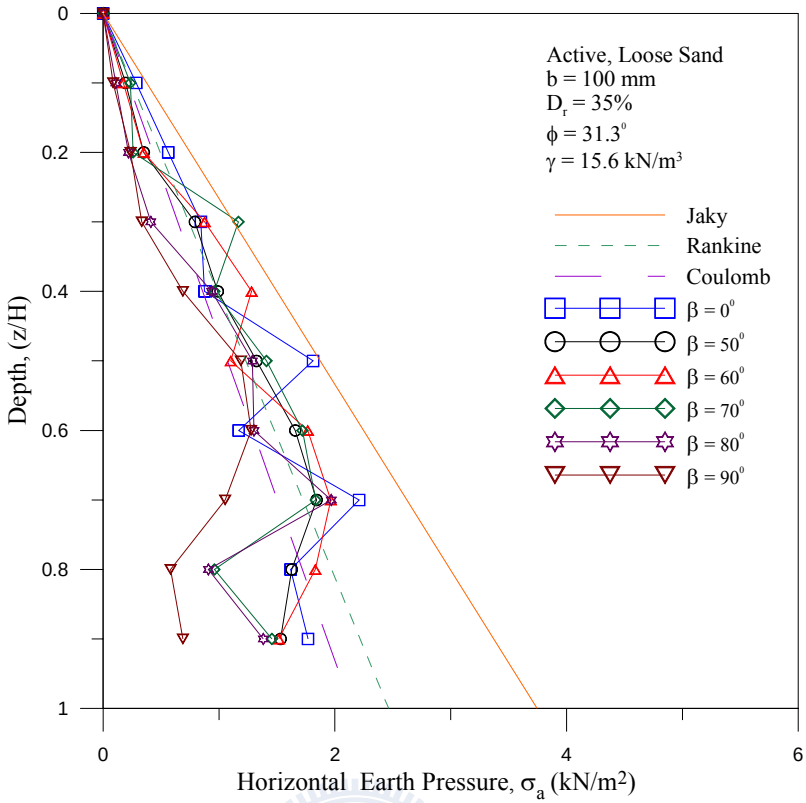

Fig. 6.78. Distribution of active earth pressure at different interface inclination angle for b = 100 mm

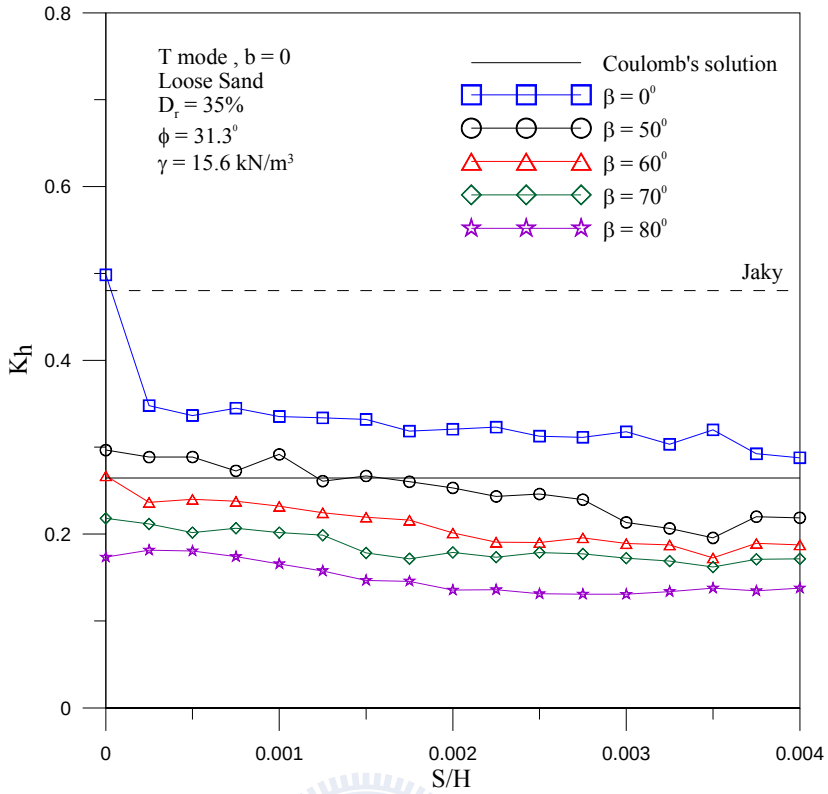

Fig. 6.79. Variation of earth pressure coefficient K_h with increasing wall movement for b = 0

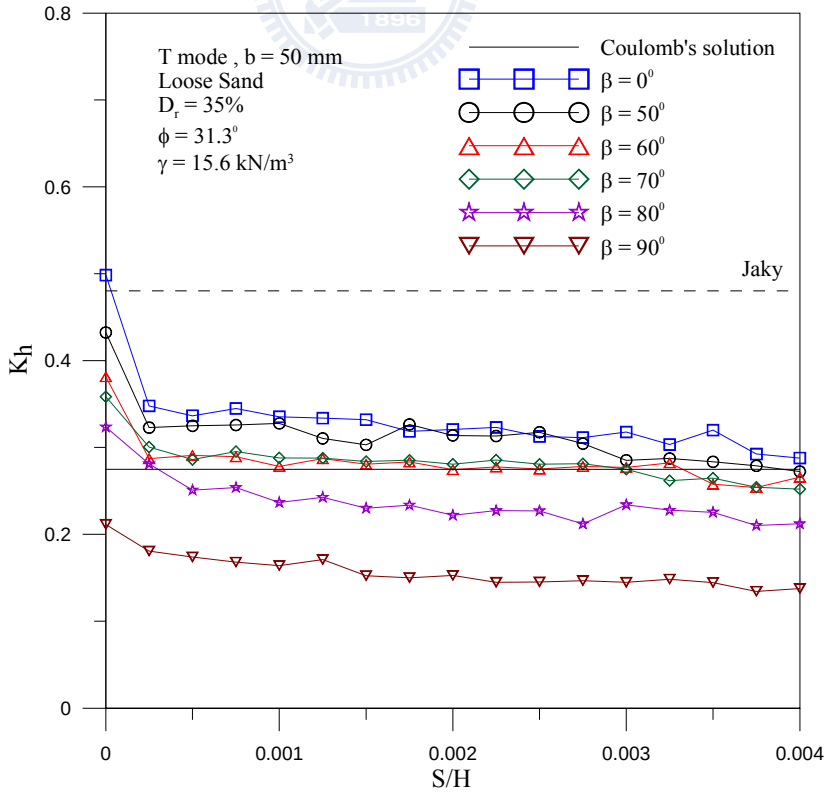

Fig. 6.80. Variation of earth pressure coefficient K_h with increasing wall movement for b = 50 mm

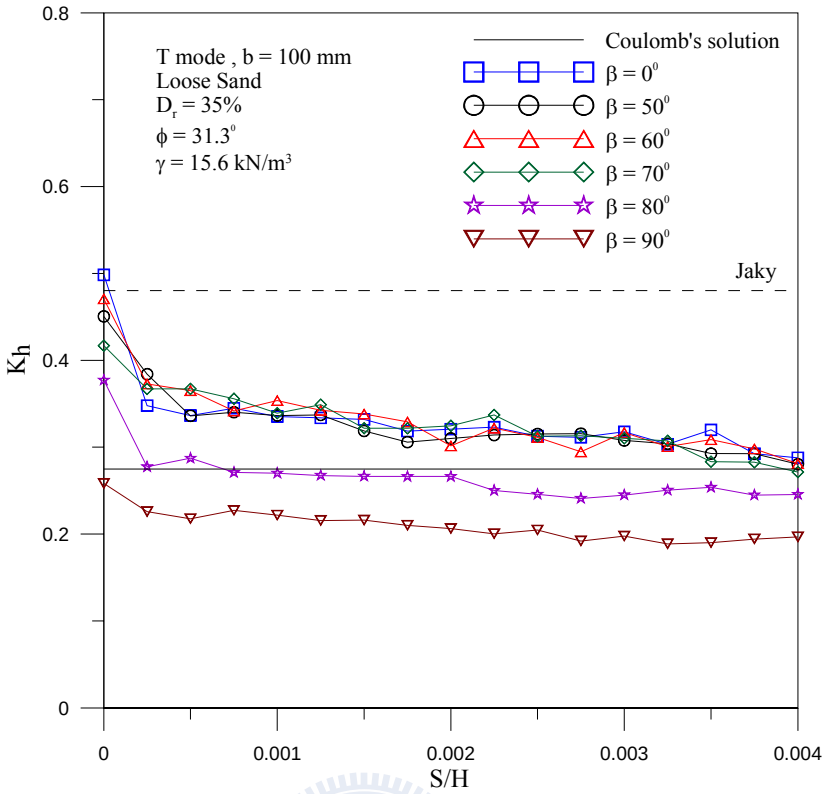

Fig. 6.81. Variation of earth pressure coefficient $K_{a,h}$ with increasing wall movement for b = 100 mm

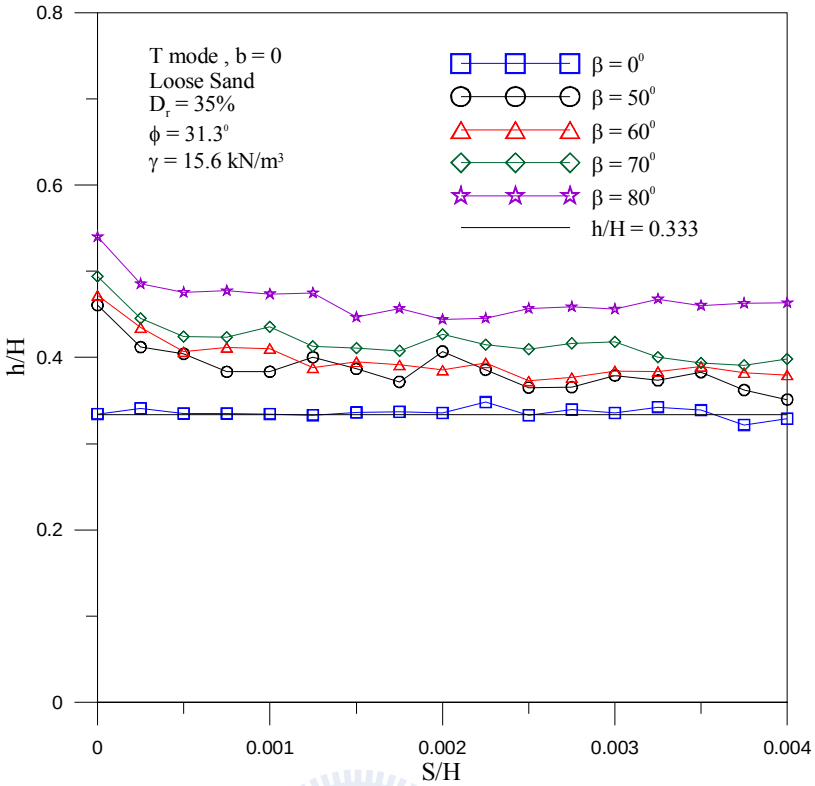

Fig. 6.82. Variation of total thrust location with increasing wall movement for b = 0

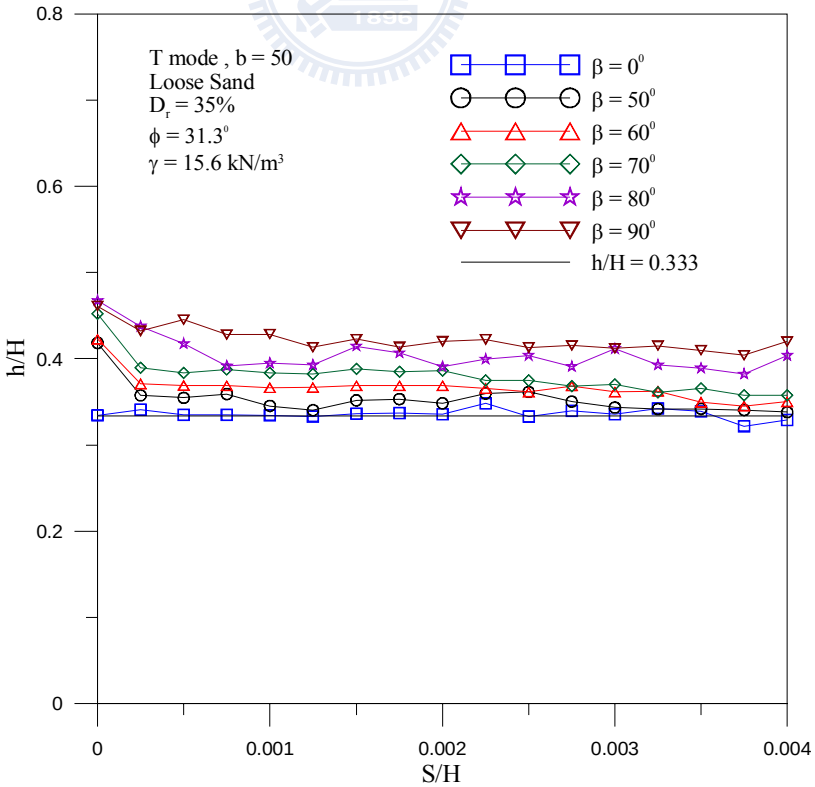

Fig. 6.83. Variation of total thrust location with increasing wall movement for b = 50 mm

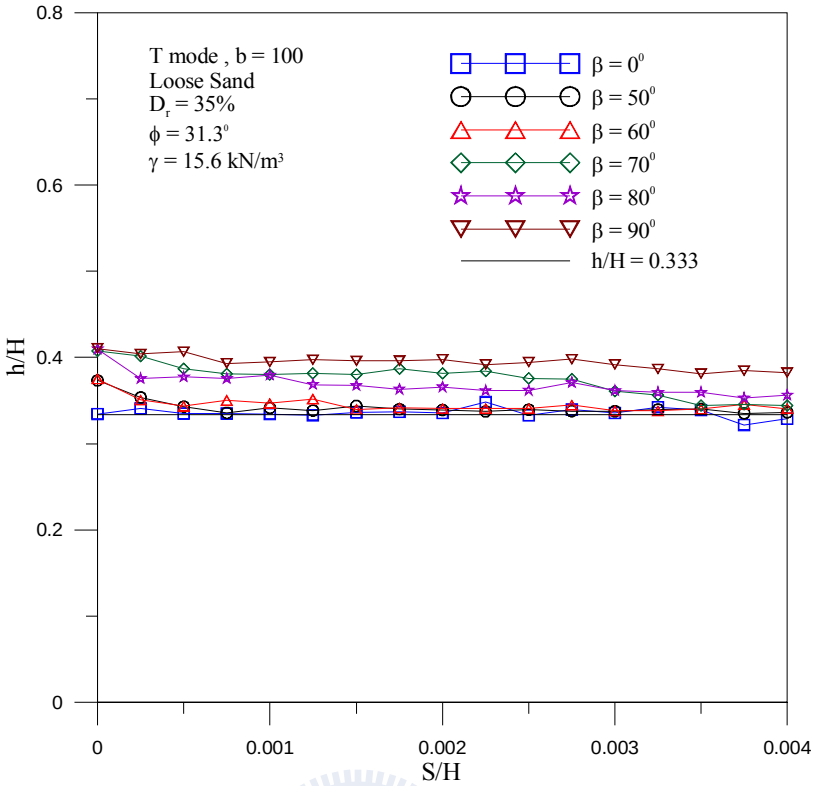

Fig. 6.84. Variation of total thrust location with increasing wall movement for b = 100 mm

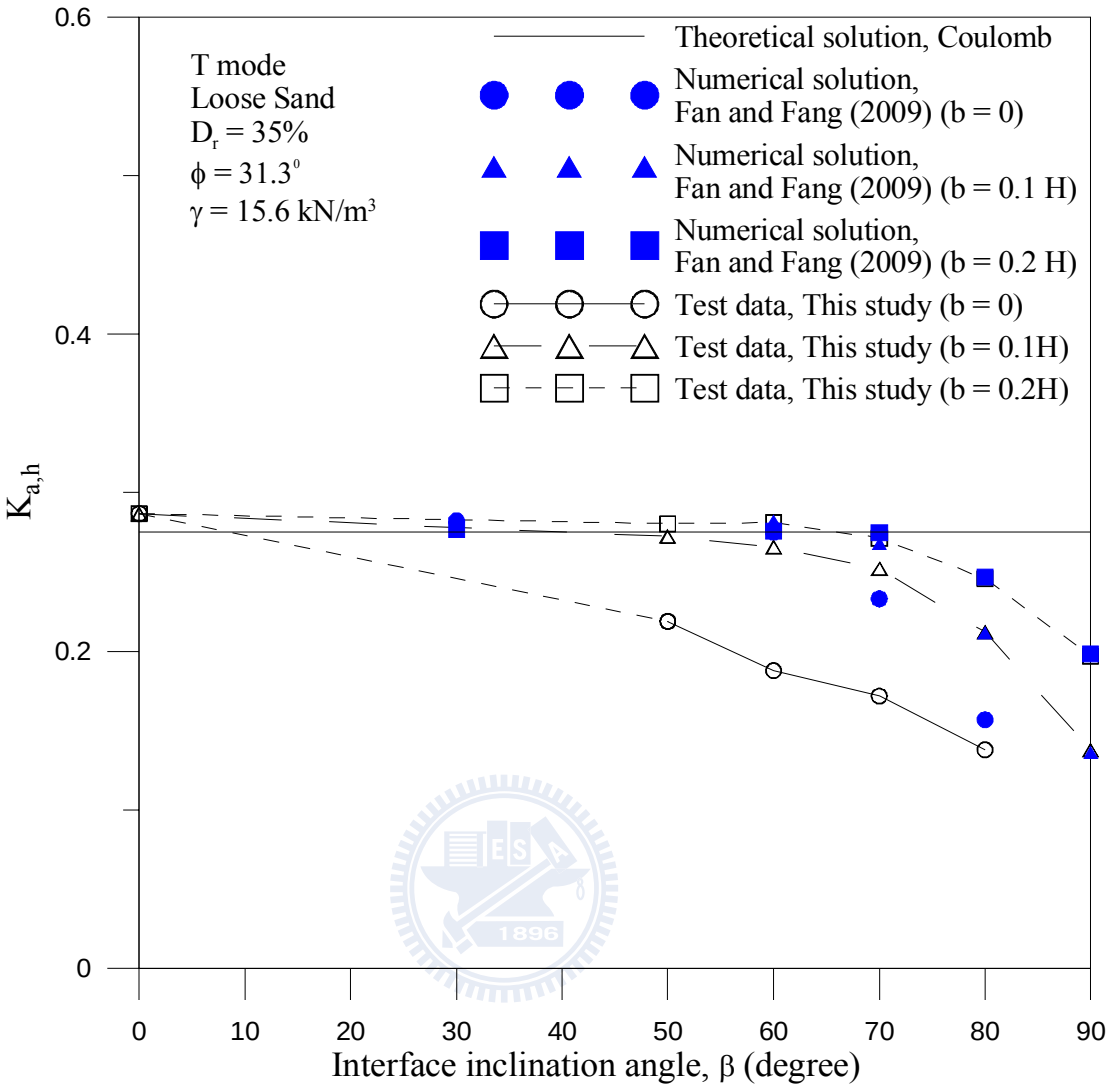

Fig. 6.85. Active earth pressure coefficient $K_{a,h}$ versus interface inclination angle

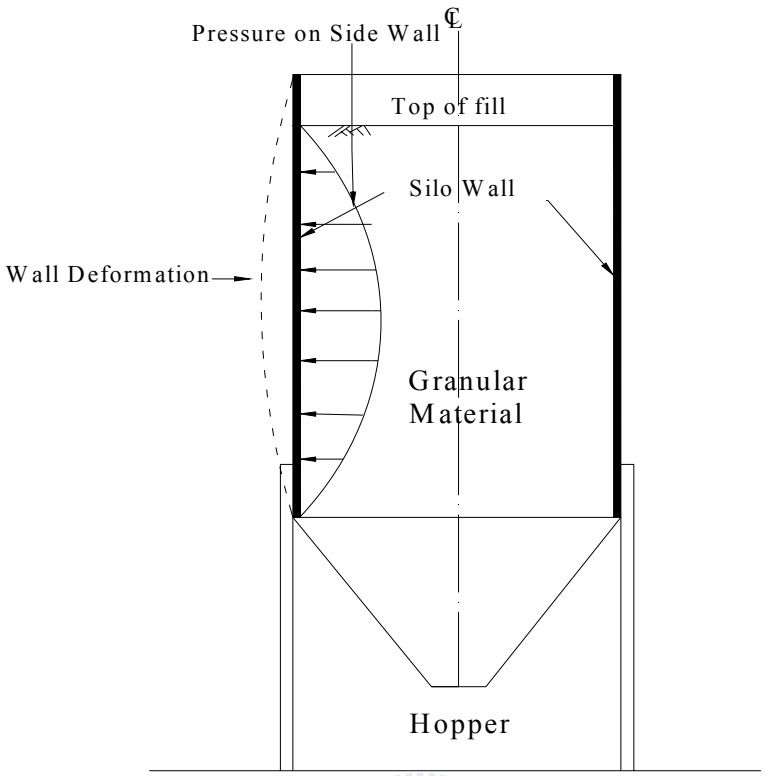

(a)

(b)

Fig. 6.86. Circular silo filled with granular material

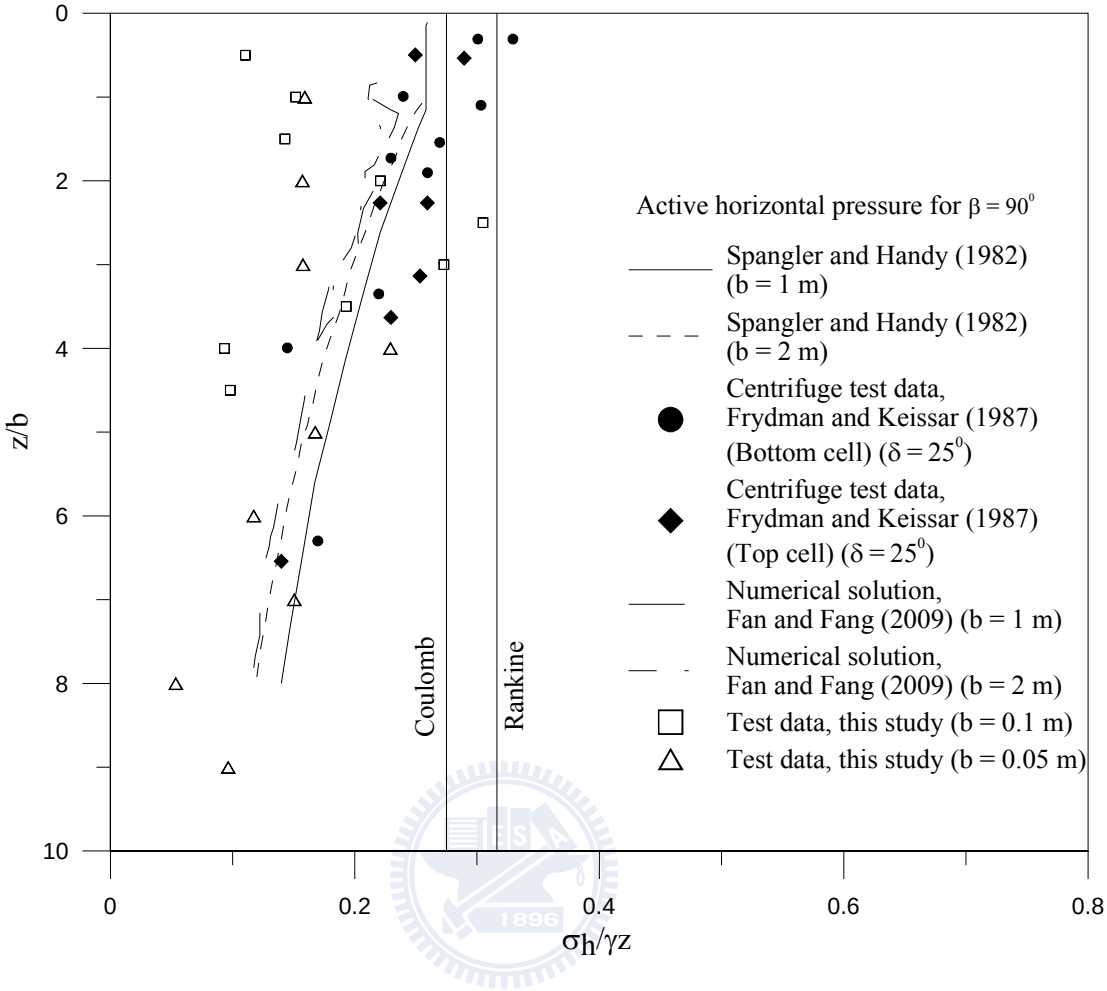

Fig. 6.87. Comparison of the distribution of active earth pressures

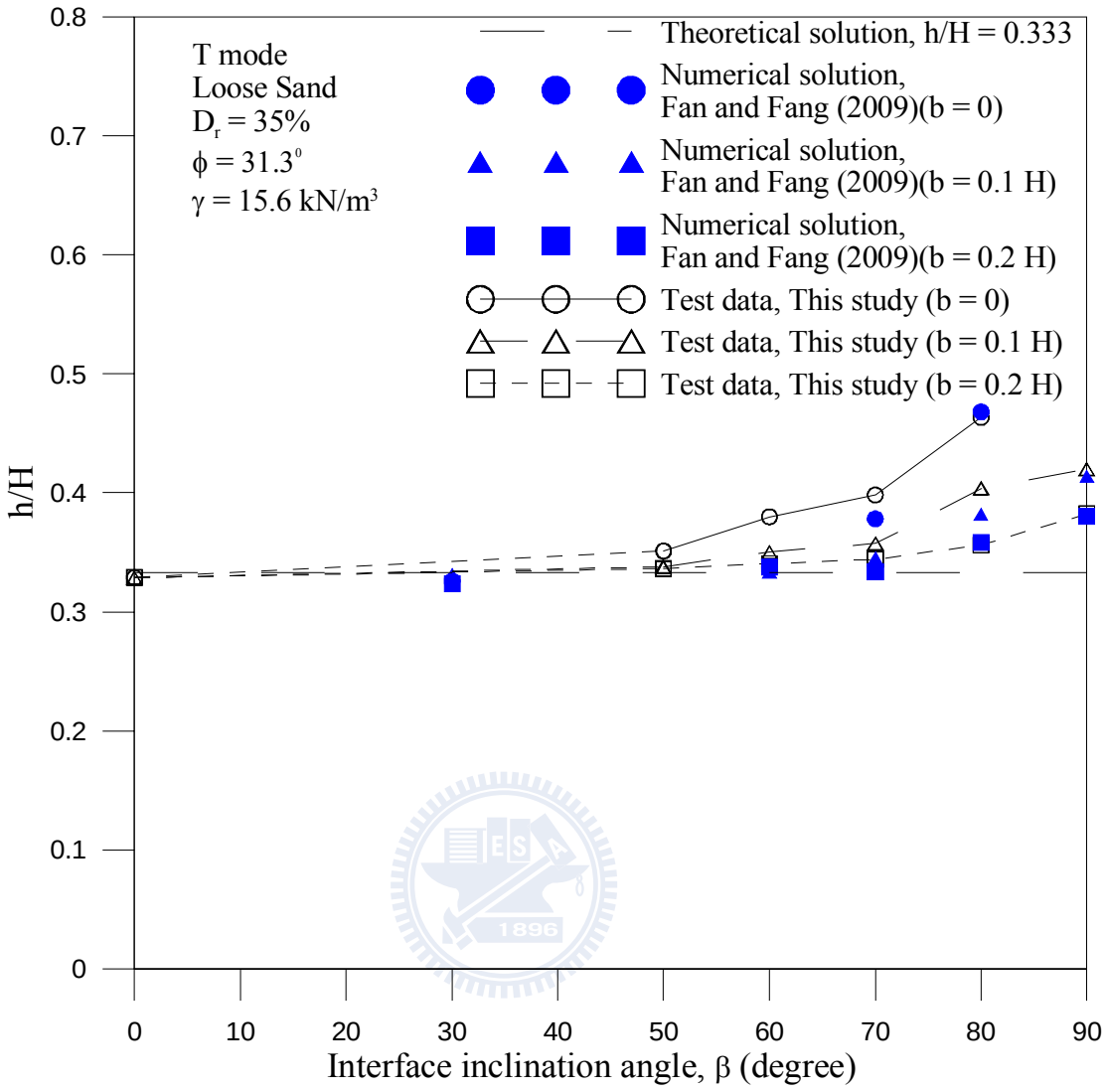

Fig. 6.88. Point of application of active soil thrust versus interface inclination angle β

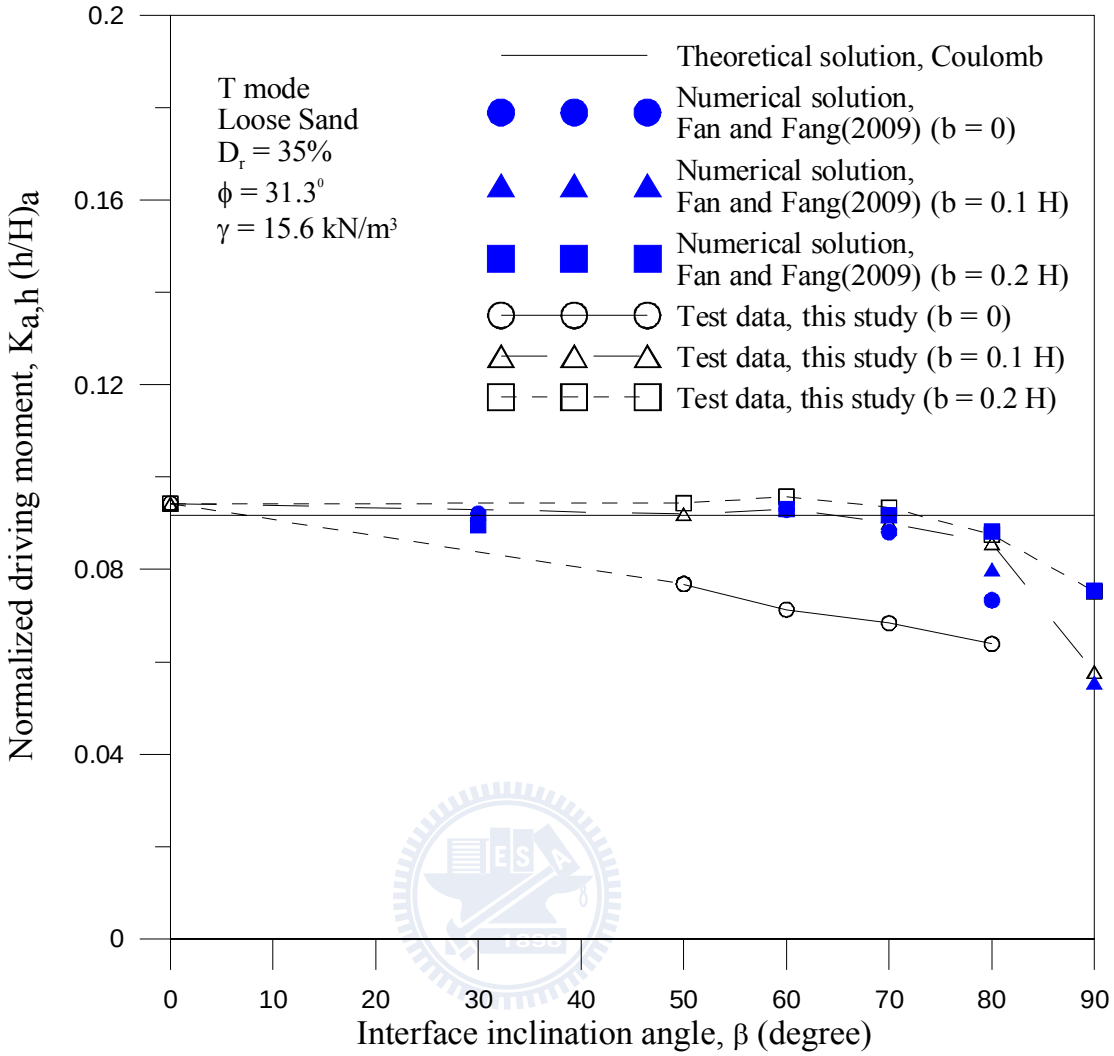

Fig. 6.89. Normalized driving moment versus interface inclination angle

Appendix A:

Calibration of Soil Pressure transducers

To investigate the lateral earth pressure acting on the model retaining wall, ten strain-gage type soil pressure transducers (SPT) were used. The transducers PGM-02KG manufactured by KYOWA are installed on the surface of model retaining wall to measure the lateral earth pressure against the retaining wall. The pressure acts between soil particles and the transducer is quite different from the pressure that acts between liquid and transducer. It is necessary to calibrate the soil pressure transducer in an environment similar to that of the actual testing condition. A special system was designed for the calibration of the strain-gage type soil-pressure transducers. The system consists of the calibration device, the controlled air-pressure system, signal conditioner, and the sensor data acquisition system, as indicated in Fig. A1 and Fig. A2.

The calibration device is a shallow cylindrical chamber with an inner diameter of 400 mm and a height of 30 mm. The chamber is made of a solid steel plate, which is the same material as the model retaining wall. The soil-pressure transducer was inserted through the bottom of the chamber. It is important that the surface of the sensor was installed flush with the upper face of the chamber. To simulate the interface between the sand particle and soil pressure transducer, 10 mm-thick sand layer was poured into the calibration device over the transducer. Then a 0.2

mm-thick rubber membrane was placed over the sandy layer, as shown in Fig. A.1. A uniformly distributed air-pressure was applied on the membrane, over the soil particles, and transmitted to the transducer. The output voltage of the transducer was found to increase linearly with the increase of applied pressure, as shown in Fig. A.3 to Fig. A.7.

A rubber O-ring was arranged to prevent air leakage between the chamber and the cap. It should be noted that the air pressure applied for the calibration of transducer should be consistent with the operating pressure range for model wall experiments. For this study, the transducers were calibrated for the pressure range of 0 to 9.81 kPa. To reduce the effect of sidewall friction, the thickness of sand layer in the chamber should be limited, so that the side-friction between the sand the sidewall of the chamber could be minimized. Fig. A.3 to Fig. A.7 shows the test results of the soil pressure transducers calibrated without the compressible layer. Table A.1 is a summary of the calibration factors of each soil pressure transducer.

Table A.1. Soil Pressure Transducer Calibration Factors

Transducer No.	Dynamic Strain Amplifier			Capacity(kN/m^2)	Calibration Factor[(kN/m^2)/volt]
	No.	Range Selector (*100 $\mu\xi$)	Calibration Setter($\mu\xi$)		
EZ0660017	9	5	2014	19.62	3.5535
EX3720002	10	5	2014	19.62	3.4857
EZ0660029	11	5	2090	19.62	3.5333
FG6900006	12	5	1815	19.62	3.978
FL8550010	13	5	1880	19.62	3.9342
FL8550011	14	5	2047	19.62	3.8622
EX3270001	15	5	2198	19.62	3.0667
EE2450023	16	5	1984	19.62	3.2621
FL8550012	17	5	1794	19.62	3.8417

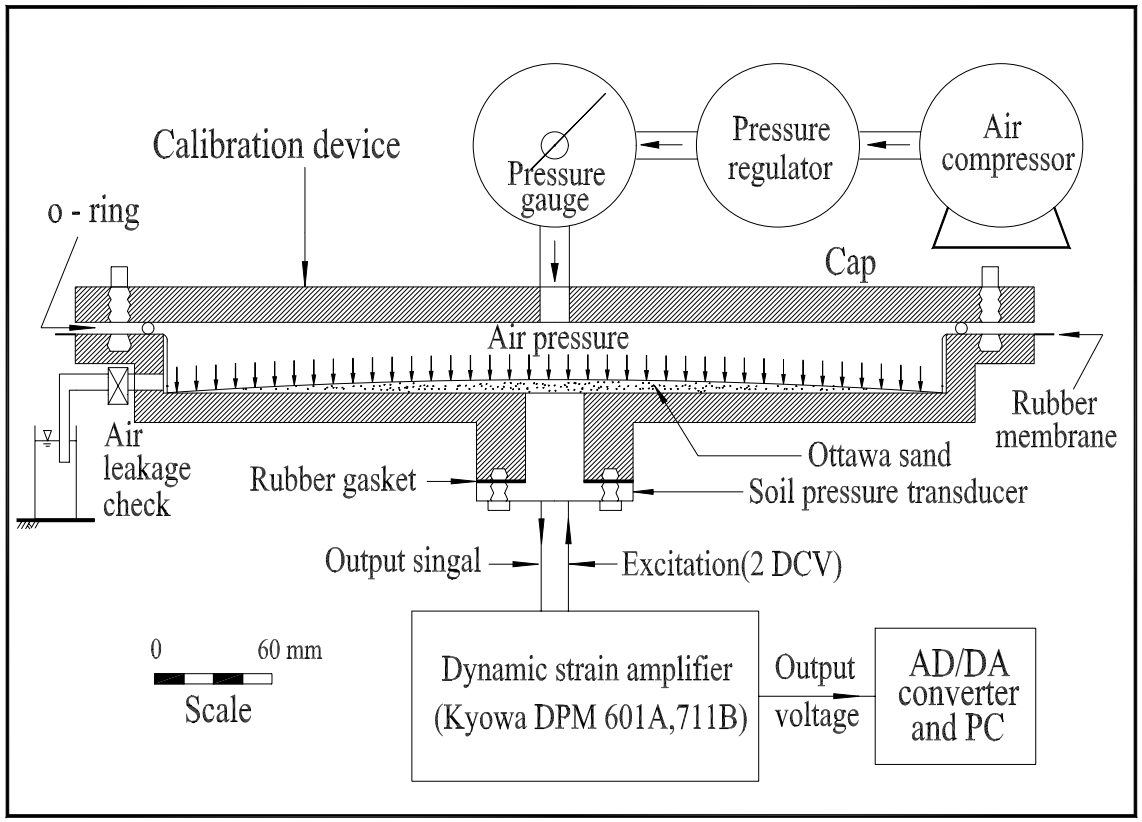

Fig. A.1 Schematic diagram of the soil pressure transducer calibration system

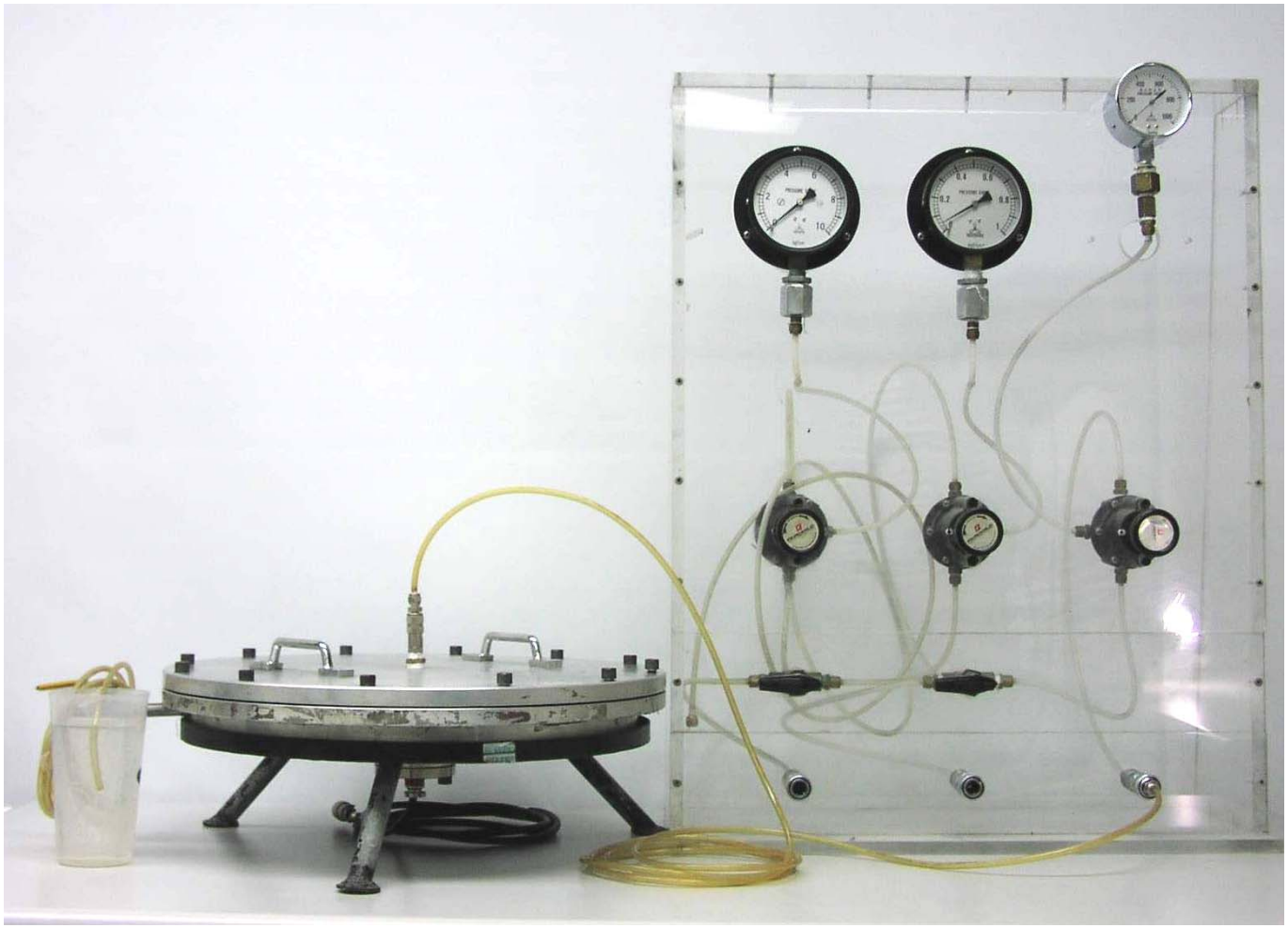

Fig. A.2. Soil pressure transducer calibration system

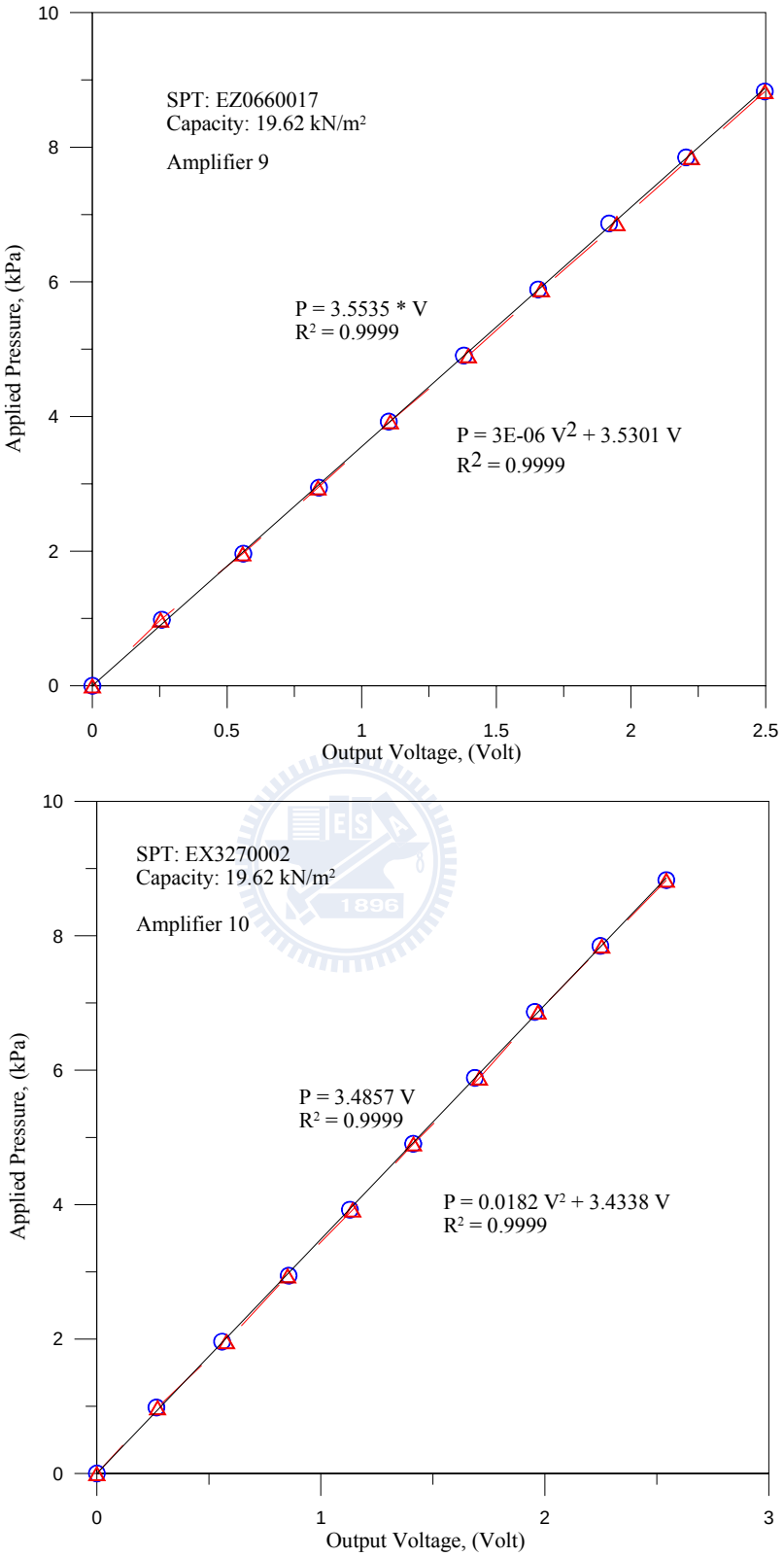

Fig. A.3. Applied pressure versus voltage output for soil pressure transducer SPT01 and SPT02

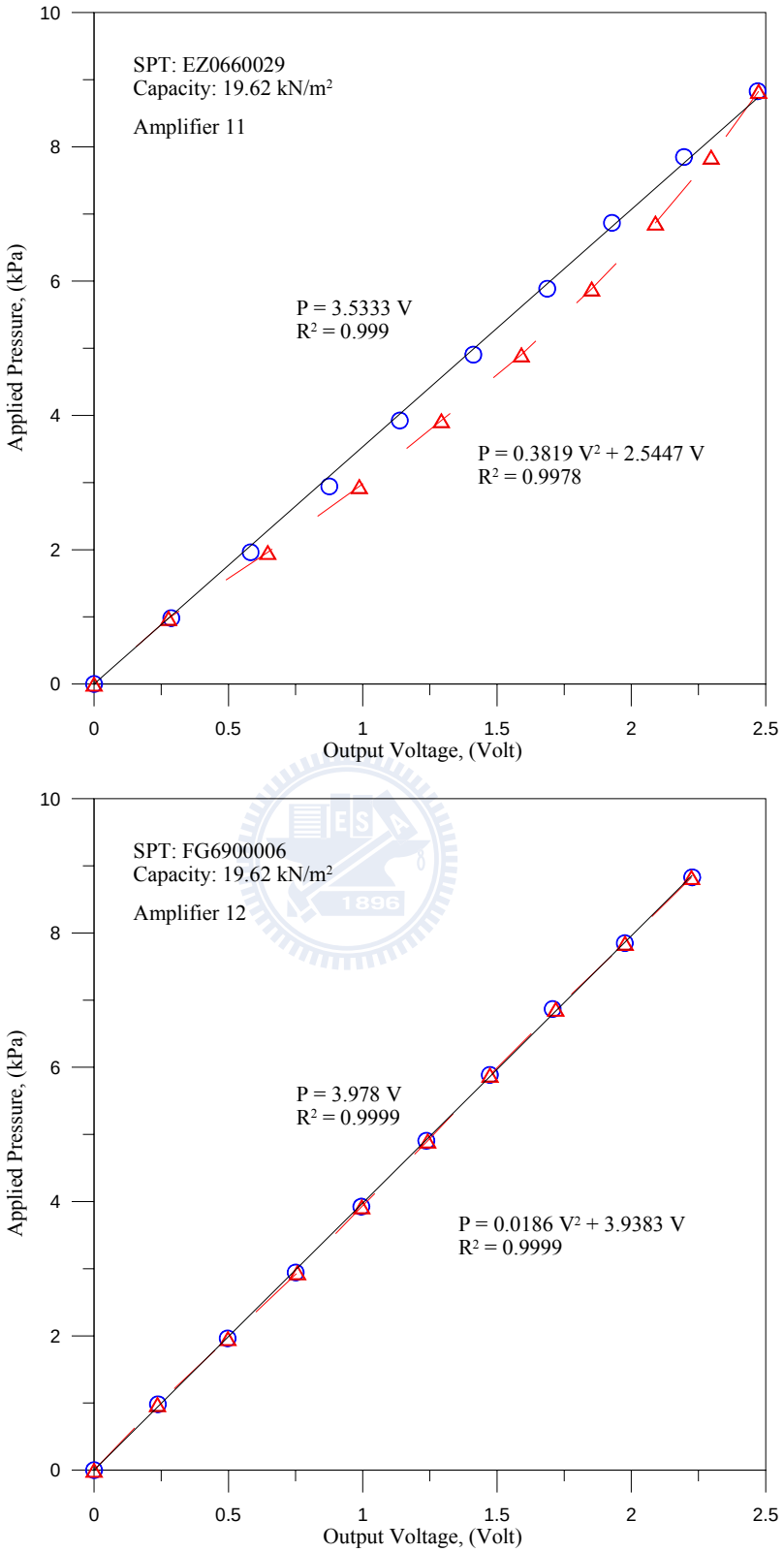

Fig. A.4. Applied pressure versus voltage output for soil pressure transducer SPT03 and SPT04

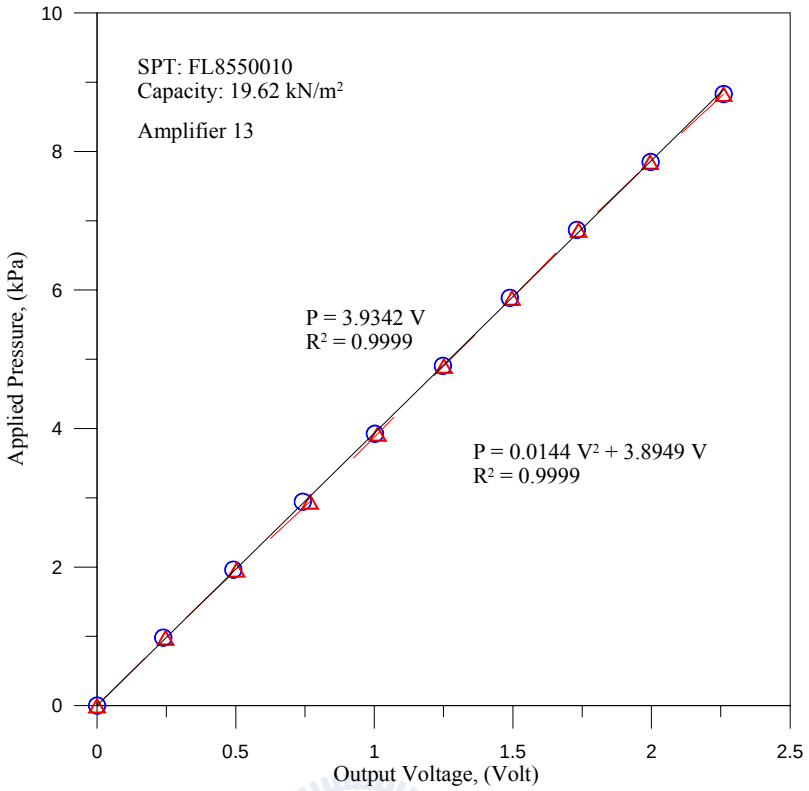

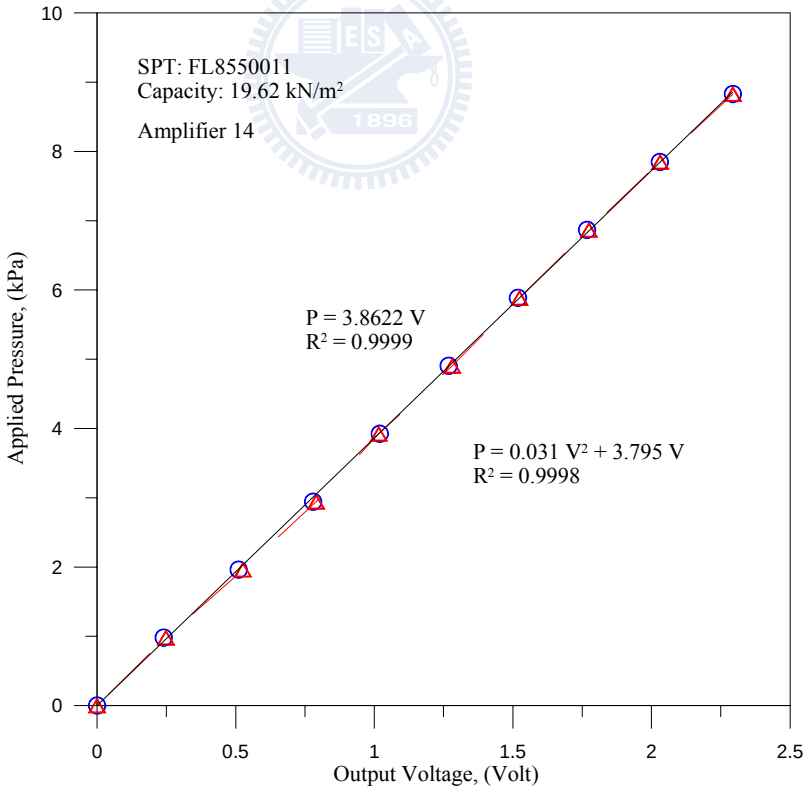

Fig. A.5. Applied pressure versus voltage output for soil pressure transducer SPT05 and SPT06

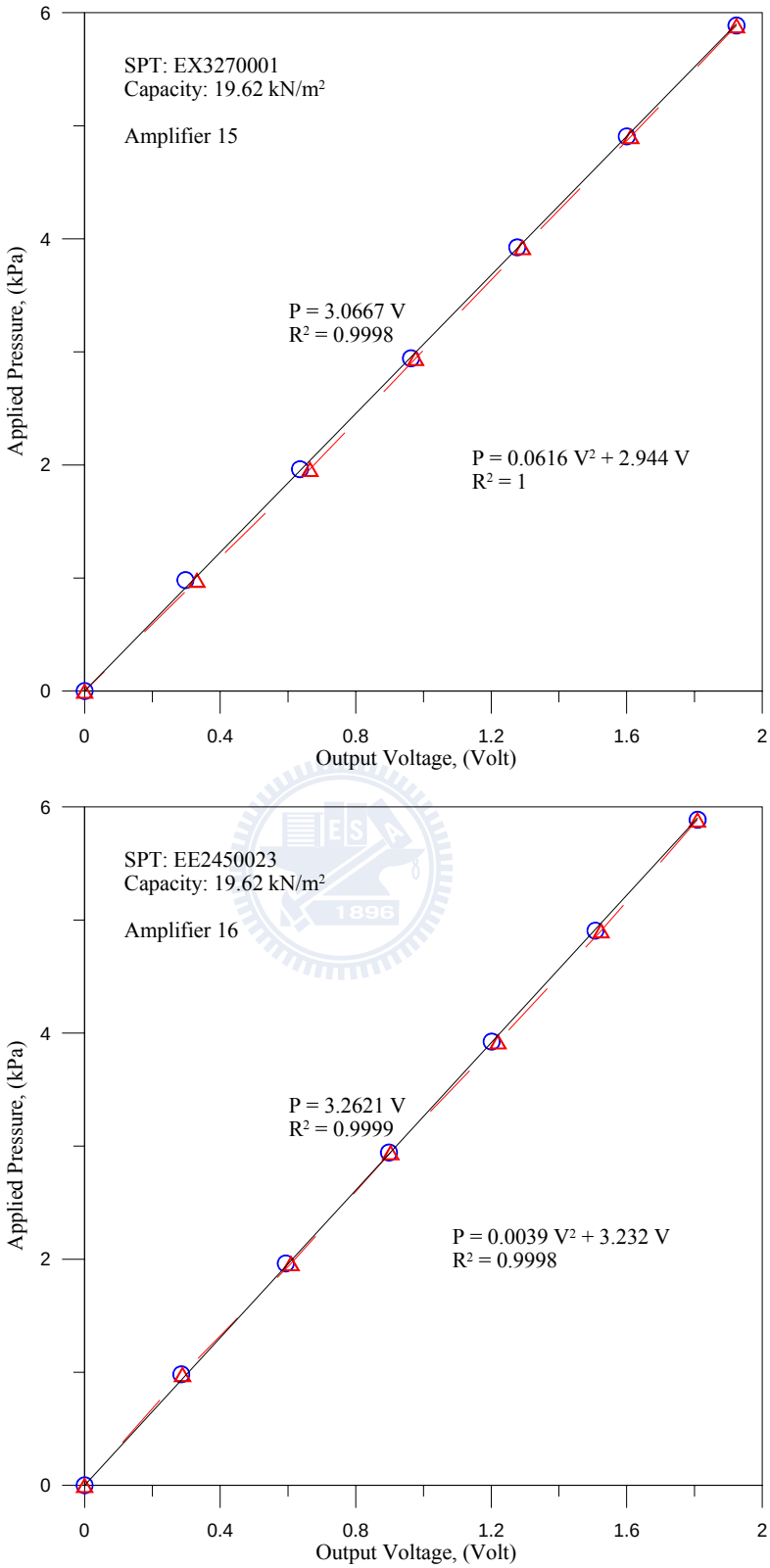

Fig. A.6. Applied pressure versus voltage output for soil pressure transducer SPT07 and SPT08

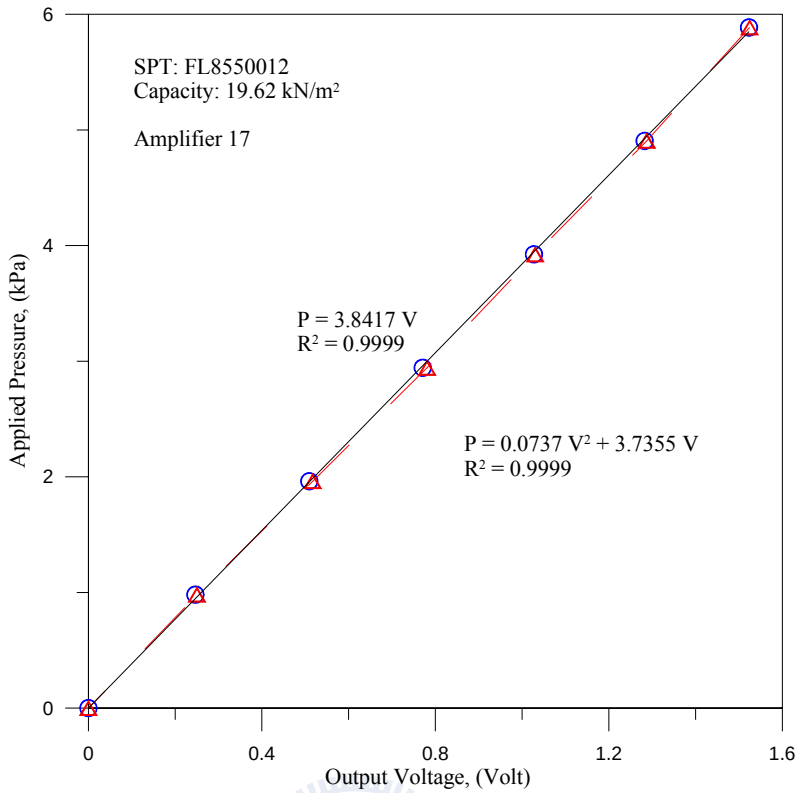

Fig. A.7. Applied pressure versus voltage output for soil pressure transducer SPT09